Applied Computational Electromagnetics Society

Journal

ACES

September 2013 Vol. 28 No. 9

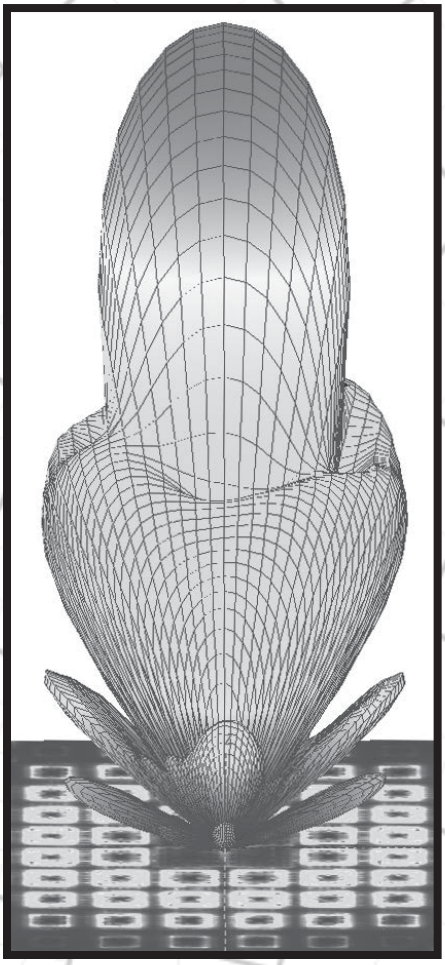

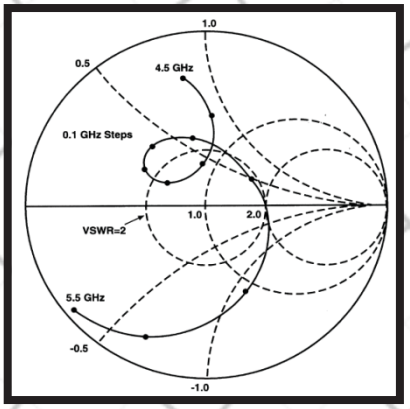

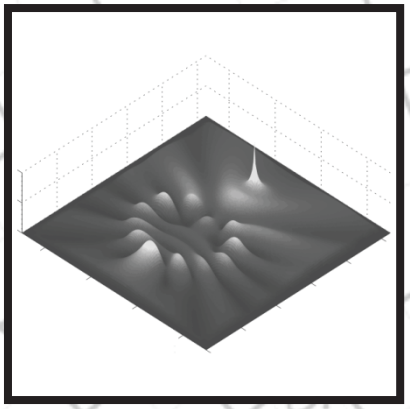

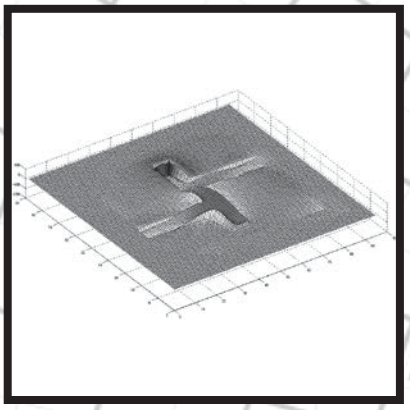

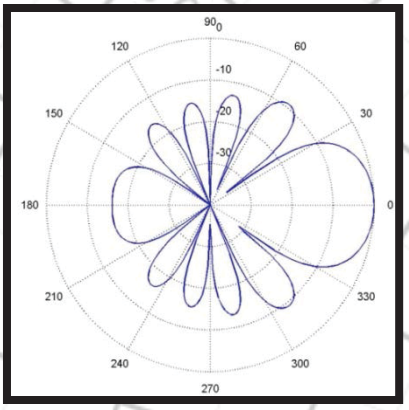

ISSN 1054-4887

GENERAL PURPOSE AND SCOPE: The Applied Computational Electromagnetics Society ***(ACES)*** Journal hereinafter known as the ***ACES Journal*** is devoted to the exchange of information in computational electromagnetics, to the advancement of the state-of-the art, and the promotion of related technical activities. The primary objective of the information exchange is to inform the scientific community on the developments of new computational electromagnetics tools and their use in electrical engineering, physics, or related areas. The technical activities promoted by this publication include code validation, performance analysis, and input/output standardization; code or technique optimization and error minimization; innovations in solution technique or in data input/output; identification of new applications for electromagnetics modeling codes and techniques; integration of computational electromagnetics techniques with new computer architectures; and correlation of computational parameters with physical mechanisms.

SUBMISSIONS: The ***ACES Journal*** welcomes original, previously unpublished papers, relating to applied computational electromagnetics. Typical papers will represent the computational electromagnetics aspects of research in electrical engineering, physics, or related disciplines. However, papers which represent research in applied computational electromagnetics itself are equally acceptable.

Manuscripts are to be submitted through the upload system of ***ACES*** web site http://www.aces-society.org See "Information for Authors" on inside of back cover and at ***ACES*** web site. For additional information contact the Editor-in-Chief:

Dr. Atef Elsherbeni
Electrical Engineering and Computer Science Department
Colorado School of Mines
310D Brown Building
1610 Illinois Street
Golden, CO 80401
Phone: (303) 273-3667
Email: aelsherb@mines.edu

SUBSCRIPTIONS: All members of the Applied Computational Electromagnetics Society are entitled to access and download the ***ACES Journal*** any published journal article available at http://www.aces-society.org. Printed issues of the ***ACES Journal*** are delivered to institutional members. Each author of published papers receives a printed issue of the ***ACES Journal*** in which the paper is published.

Back issues, when available, are $50 each. Subscription to ***ACES*** is through the web site. Orders for back issues of the ***ACES Journal*** and change of address requests should be sent directly to ***ACES*** office at:

Hank Ducey - ACES 13A
Electrical Engineering Department
The University of Mississippi
University, MS 386377 USA

Allow four weeks advance notice for change of address. Claims for missing issues will not be honored because of insufficient notice, or address change, or loss in the mail unless the ***ACES*** office is notified within 60 days for USA and Canadian subscribers, or 90 days for subscribers in other countries, from the last day of the month of publication. For information regarding reprints of individual papers or other materials, see "Information for Authors".

LIABILITY. Neither ***ACES***, nor the ***ACES Journal*** editors, are responsible for any consequence of misinformation or claims, express or implied, in any published material in an ***ACES Journal*** issue. This also applies to advertising, for which only camera-ready copies are accepted. Authors are responsible for information contained in their papers. If any material submitted for publication includes material which has already been published elsewhere, it is the author's responsibility to obtain written permission to reproduce such material.

APPLIED COMPUTATIONAL ELECTROMAGNETICS SOCIETY JOURNAL

September 2013
Vol. 28 No. 9
ISSN 1054-4887

The ACES Journal is abstracted in INSPEC, in Engineering Index, DTIC, Science Citation Index Expanded, the Research Alert, and to Current Contents/Engineering, Computing & Technology.

The illustrations on the front cover have been obtained from the research groups at the Department of Electrical Engineering, The University of Mississippi.

SEPTEMBER 2013 REVIEWERS

Arash Ahmadi
Iftikhar Ahmed
Mohamed Al-Sharkaway
Shirook Ali
Marco Arjona
Abdul Ali Babar
Mohamed Bakr
Toni Bj
Jiefu Chen
Hongwei Chen
William Coburn
Pasquale Dottorato
Grant Ellis
Luis Garcia-Castillo
Mang He
David Hill
Kai Man Luk
Antonio Orlandi
Guangdong Pan
Anil Pandey
Nirmal Paudel
Chris Railton
Mahmoud Ramezani Mayiami
Vince Rodriguez
Colan Ryan
Ramesh S
Rensheng Sun
Christopher Trueman
Ozgur Tuncer
Wei-Chung Weng
Joshua Wilson
Jing Zhao

THE APPLIED COMPUTATIONAL ELECTROMAGNETICS SOCIETY

JOURNAL

Vol. 28 No. 9 September 2013

TABLE OF CONTENTS

Modeling and Analysis of Anechoic Chamber Using CEM Tools

D. Campbell[1], G. Gampala[1], C. J. Reddy[1], M. Winebrand[2], and J. Aubin[2]

[1] EM Software & Systems (USA), Inc.
100 Exploration Way, Suite 300, Hampton, VA 23666
derek@emssusa.com

[2]ORBIT/FR, Inc.
506 Prudential Road, Horsham, PA 19044
JohnA@OrbitFR.com

***Abstract*—** Advances in computational resources facilitate anechoic chamber modeling and analysis at VHF/UHF frequencies using full-wave solvers available in commercial software such as FEKO. The measurement community has a substantial and increasing interest in utilizing computational electromagnetic (CEM) tools to minimize the financial and real estate resources required to design and construct a custom anechoic chamber without sacrificing performance. A full-wave simulation analysis such as the finite element method (FEM) provides a more accurate solution than the approximations inherent to asymptotic ray-tracing techniques such as physical optics (PO), which have traditionally been exploited to overcome computational resource limitations. An anechoic chamber is simulated with a rectangular down-range cross-section (in contrast with the traditional square cross-section) to utilize the software's capability to assess polarization performance. The absorber layout within the anechoic chamber can be optimized using FEKO for minimal reflections and an acceptable axial ratio in the quiet zone. Numerical results of quiet zone disturbances and axial ratios are included for both low- and medium-gain source antennas over a broad frequency range.

Index Terms - Anechoic chamber, axial ratio, computational electromagnetics, FEKO, finite element method, and physicaloptics.

I. INTRODUCTION

The optimum choice of anechoic chamber dimensions is crucial to ensure the minimum performance level of the quiet zone and to minimize the system cost. In many cases, however, the dimensions are predetermined (e.g., rectangular rather than square cross-section). The chamber geometry is not the only parameter limiting quiet zone performance. The quiet zone behavior depends on several factors such as absorbing material performance, layout and grades, source antenna/device under test (DUT) separation, source antenna beamwidth, DUT positioning equipment geometry and material, *etc*. A full 3D electromagnetic analysis must be performed to correctly account for all of these parameters.

To date, the industry most often analyzes anechoic chambers with a method similar to "ray tracing", which suffers from poor accuracy. The inaccuracy is especially prevalent in scenarios where the room characteristic dimensions are only a few wavelengths (i.e., a typical situation at VHF/UHF frequency bands). A few components contributing to the inaccuracy are detailed below:

- Limited data is available on the reflectivity of absorbing materials at VHF/UHF, especially at off-normal incidence.Historically, the reflection coefficient is only described by magnitude and the phase is not provided. As a result, only approximate information can be extracted from the RMS fields in the quiet zone. In some cases, assumptions were made on the reflectivity at off-normal incidence

Submitted On: April 14, 2013
Accepted On: Aug. 27, 2013

angles at VHF/UHF frequencies based on similarities to better established reflectivity curves at higher frequencies (e.g.,>2.0GHz). However, the extrapolation has been proven inaccurate for a number of VHF/UHF chambers.In other cases, the off-normal incidence data is retrieved from normal incidence reflectivity using Fresnel formulas, which are accurate for planar absorbing multi-layered structures only.

- Specular area characteristic dimensions include a few wavelengths of surface covered by absorbing material (e.g., pyramids, wedges, *etc*.), which at VHF/UHF may exceed side wall characteristic dimensions and may, therefore, span a large range of incidence angles of the illuminating rays on the specular area. Choosing the correct incidence angle and corresponding reflection coefficient at each consecutive specular point then becomes a difficult process. Upgrading the "ray-tracing" method to the "aperture integration" method is a better fit for the analysis. However, accuracy is limited by the data available for the reflectivity of absorbing materials.

Thus, the need for a more rigorous and comprehensive analysis such as a full 3D electromagnetic simulation is obvious, especially at VHF/UHF bands [1, 2].Insufficient accuracy in the chamber design has resulted in some poor chamber implementations in the past. Even identifying improper chamber performance with the VSWR test procedure is a difficult process at VHF/UHF bands. The test may show uniform field distribution in the quiet zone, while the overall chamber performance is far from optimal.

Some factors limiting the effectiveness and accuracy of the VSWR tests for chamber certification at the VHF/UHF bands are:

- Often the test zone dimensions are comparable to or less than 1λ at the lowest operating frequency. Thus, visually retrieving and/or distinguishing the ripples (period and ripple amplitude) associated with multiple reflections in the chamber interior to the fullest extent from the measured data are part of a difficult process. The chamber may even appear to achieve acceptable performance in scenarios where the reflected signal is stronger than the direct (desired) one.
- Due to geometry constraints the field probe antenna used in the free-space, VSWR procedure is typically a low- or medium-gain antenna. In cases with relatively high reflections in the shielded room, the reference measurement results may be in error. An uncertainty is then added through the entire VSWR data processing. Consequently, there could be a situation at VHF/UHF bands where the VSWR tests optimistically report the quiet zone reflectivity performance.
- The VSWR procedure is often inapplicable without modifications (e.g.,transversal cuts in elongated chambers such as tapered ones). As a result, the procedure is frequently "engineered" to exclude conflicting/confusing measurement data.

The primary manifestation of a poor elongated chamber performance includes:

- Inconsistent longitudinal trace behavior in the quiet zone over a broad frequency range.
- Significant signal level variation over a broad frequency range with the source and probe antennas rotated simultaneously (clocked) around their boresight (the chamber line of sight).

In order to assure that the chamber performs well, a significant amount of extra testing is required to be performed on the quiet zone, which might be costly or often impossible to execute. Effort has previously demonstrated an efficient method for modeling the reflectivity of absorber, while saving computational resources as compared to a full 3D EM solver [3].

A full 3D anechoic chamber simulation at VHF/UHF frequencies is a helpful tool that may be used to predict/estimate some test results and assure optimal performance. In particular, 3D anechoic chamber simulations can estimate the axial ratio accuracy, which can be achieved in the chamber with a non-square cross-section.

II. NUMERICAL METHODS

As computational resources such as memory and processors continue to experience reductions in price, state of the art CEM techniques available in commercial software packages such as FEKO [4] are becoming a more attractive option for engineers during the design phase of anechoic chambers. Full-wave techniques, such as finite-

difference time-domain (FDTD), method of moments (MoM), multi-level fast multipole method (MLFMM), and finite element method (FEM) accurately solve Maxwell's equations without approximations and are therefore becoming a popular choice with the availability of cheaper memory and CPU power. To demonstrate feasibility of anechoic chamber design at VHF/UHF frequencies using a full-wavetechnique such as FEM, we chose the commercial EM simulation tool FEKO.

FEKO is a comprehensive electromagnetic software suite that includes asymptotic solvers such as physical optics (PO), geometrical optics (GO), and uniform theory of diffraction (UTD) together with the full-wave solvers including MoM, MLFMM, and FEM. The asymptotic methods and FEM have been hybridized with MoM to assist with solving large and complex problems [5-7]. Asymptotic methods are well suited for the analysis of electrically large anechoic chambers. Apart from providing a solution with limited resources, asymptotic methods operate with underlying approximations wherein vigilance is required to model the problem well within those approximations.

In this paper, the analysis and design process for an anechoic chamber is presented. The design process utilizes both the full-wave FEM and asymptotic PO techniques, which are ideal for this electrically large, non-radiating dielectric model. FEM utilizes a volume meshing technique that employs tetrahedral elements to accurately mesh arbitrarily shaped volumes where the dielectric properties may vary between neighboring tetrahedral elements. The outer shell is meshed with triangular elements and does not require a radiation boundary. In contrast, PO utilizes a surface meshing technique that employs triangular elements to accurately mesh arbitrarily shaped surfaces where the dielectric properties are homogeneous.

III. CHAMBER AND ANTENNA MODELING

A custom anechoic chamber with a rectangular down-range cross-section (i.e., W × H) is modeled to fit within a physically limited volume. FEM was used to analyze an anechoic chamber model with a perfectly conducting outer shell. The chamber dimensions are 17″ H × 24″ W × 32.5″ L as shown in Fig. 1, where the orange color represents the outer shell modeled as PEC and the blue represents the inner absorbing material.

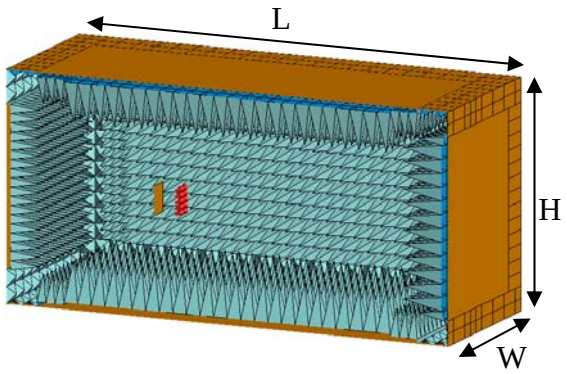

Fig. 1. Anechoic chamber model dimensions.

The center of the quiet zone is 10″ from the receiving wall and measures 6″ H × 6″ W × 6″ L. The source antenna is modeled at a 10″ separation from the center of the quiet zone (i.e., 20″ from the receiving wall) and visible left of center in Fig. 1. PO was employed to analyze an anechoic chamber model with a dielectric shell as shown in Fig. 2, because FEKO limits the analysis with PO to a single material within a given model.

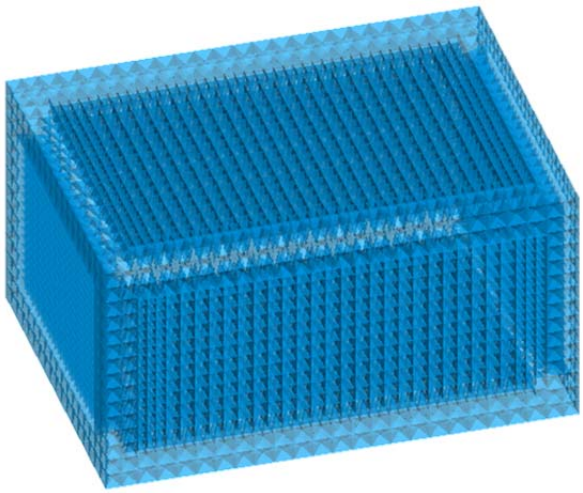

Fig. 2. Anechoic chamber analyzed with PO.

Both low- and medium-gain source antennas are modeled for vertical and horizontal polarizations with a directive gain of ~6 and 10 dBi, respectively. Any type of source antenna can be included in the model. For practical reasons, we

have chosen to generate a source antenna, similar to Fig. 3, with 25 current sources measuring λ/15 in length and arranged on a plane to achieve the desired beam widths in both the E- and H-planes, where λ is the operating wavelength. A realistic pattern is emulated by minimizing the energy radiating toward the rear of the chamber with a PEC reflector separated by λ/4 (represented by orange).

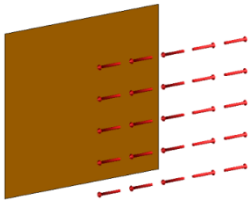

Fig. 3. Source antenna model used for analysis.

The 3dB beam widths (BW) of the source antennas are summarized below in Table II.

Table I: Source antenna of 3 dB BW.

Gain	E-Plane 3dB BW	H-Plane 3dB BW
Low	68º	111º
Medium	65º	67º

A center patch region of the two side walls, the receiving wall, the floor and ceiling were modeled with large pyramidal absorber and surrounded by small pyramidal absorber as illustrated in Fig. 4.

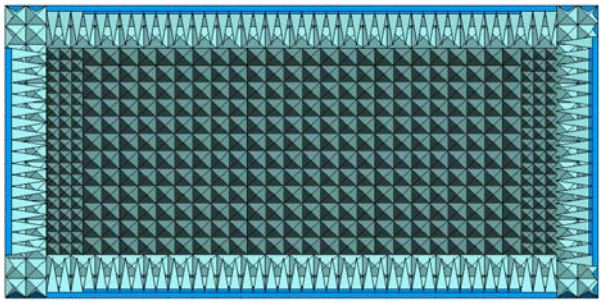

Fig. 4. Large absorber was used in center patch region of several walls.

The large pyramidal absorber is modeled with a 12″ H × 12″ W × 6″ L cuboid base below a 36″ long pyramid. The small pyramidal absorber in the surrounding area is modeled with an 8″ H × 8″ W × 4″ L cuboid base below a 24″ long pyramid as shown in Fig. 5.

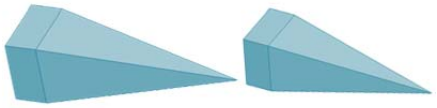

Fig. 5. Large and small pyramidal absorber models.

The real and imaginary dielectric constant for the absorbing material is illustrated in Fig. 6 and 7, respectively. The upper line indicates the maximum value, the lower line indicates the minimum value and the middle solid line indicates the average dielectric constant resulting from the manufacturing tolerances.

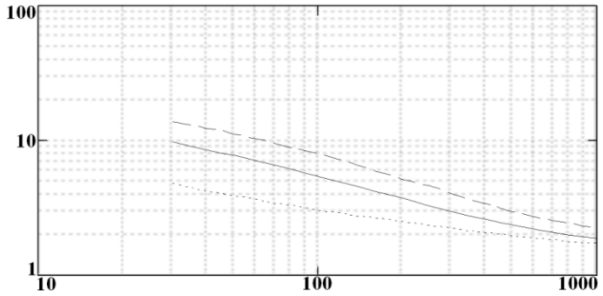

Fig. 6. Real dielectric constant for the absorber.

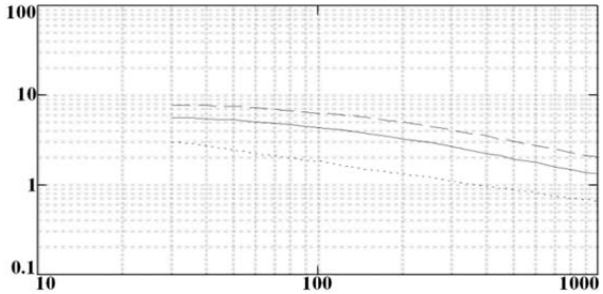

Fig. 7. Imaginary dielectric constant for the absorber.

We have elected to use the average dielectric constant and loss tangent for the absorber as summarized below in Table II for the frequencies analyzed.

Table II: Absorber material properties.

Frequency	ε'_r	ε''_r	Tan δ
150 MHz	4.758	4.467	0.93884
250 MHz	3.5	3.0	0.85714
500 MHz	2.4	1.95	0.81250
1000 MHz	1.95	1.4	0.71795
2000 MHz	1.95	1.4	0.71795

The computer memory required depends on the size of the mesh (i.e., number of tetrahedra and/or triangles), dielectric constant, and frequency as summarized in Table III and IV.

Table III: FEM mesh characterization.

Frequency	Tetrahedra	Triangles	Memory
150 MHz	1181640	43508	14 GB
250 MHz	3265760	86404	43 GB
500 MHz	12 583 444	234 684	196 GB

Table IV: PO mesh characterization.

Frequency	Triangles	Memory
500 MHz	2 364 916	10 GB
1000 MHz	7 615 698	31 GB
2000 MHz	30 035 292	123 GB

The respective run times required for this model are listed inTableV.

Table V: Simulation runtime.

Frequency	Method	Run Time
150 MHz	FEM	3 min
250 MHz	FEM	12 min
500 MHz	FEM	81 min
500 MHz	PO	27 min
1000 MHz	PO	77 min
2000 MHz	PO	271 min

Simulations were performed on a workstation with an Intel Xeon E5-2650 CPU with a total of 8 processors operating at 2.0 GHz. The workstation had 256 GB of shared memory available.

IV. ERROR ANALYSIS

Numerical results are computed for both the down-range cross-section of the fields in the center of the quiet zone and the down-range axial ratio. The quiet zone fields were then normalized with fields produced by an identical antenna radiating into free space. This process was repeated for two distinct frequencies (i.e., 150 MHz and 250 MHz). The normalized fields represent an error termproduced by energy reflecting off of the absorber,

$$\varepsilon = \left| 20 \log \sqrt{\frac{\sum |Chamber\ Field\ Components|^2}{\sum |Clear\ Site\ Field\ Components|^2}} \right|. \quad (1)$$

The down-range axial ratio,quantifies the polarization performance of an anechoic chamber by comparing the results from a simulation using a horizontally polarized antenna to the results from a simulation using a vertically polarized antenna,

$$AR = \left| 20 \log \sqrt{\frac{\sum |H\ Pol\ Field\ Components|^2}{\sum |V\ Pol\ Field\ Components|^2}} \right|. \quad (2)$$

These two equations help quantitatively validate the performance of a custom anechoic chamber configuration.

V. RESULTS

The errors produced in the central cross-section of the quiet zone have been analyzed with equation (1) for both low- and medium-gain source antennas for horizontal and vertical polarizations.

Fig. 8, 9, and 10 illustrate the results for a horizontally polarized, low-gain source antenna operating at 150 MHz, 250 MHz,and 500 MHz, respectively. The vertically polarized data sets were omitted for brevity. Fig. 11 and 12 depict the error produced when operating at 150 MHz and 250 MHz, respectively, for a vertically polarized, medium-gain source antenna. The horizontally polarized data sets were omitted for brevity.

Note the collection of plots in Fig. 8 through Fig. 12 illustrates a quiet zone error generally below 1 dB. Fig. 13 illustrates the axial ratio error from equation (2) along the length of the anechoic chamber through the center of the quiet zone for low- and medium-gain source antennas operating at 150 MHz and 250 MHz.

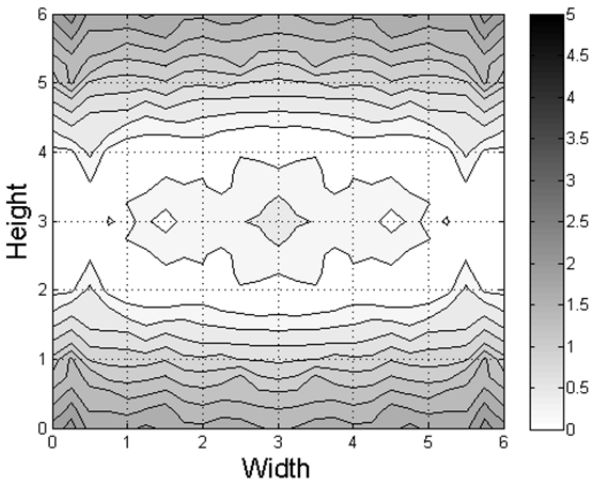

Fig. 8. Error when operating an H-polarizedlow-gain source antenna at 150 MHz.

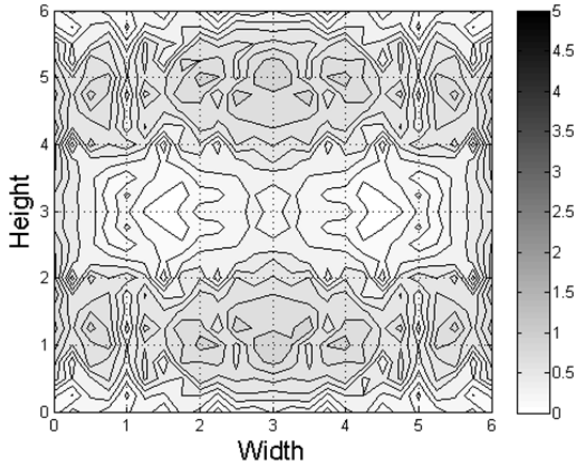

Fig. 9. Error when operating an H-polarizedlow-gain source antenna at 250 MHz.

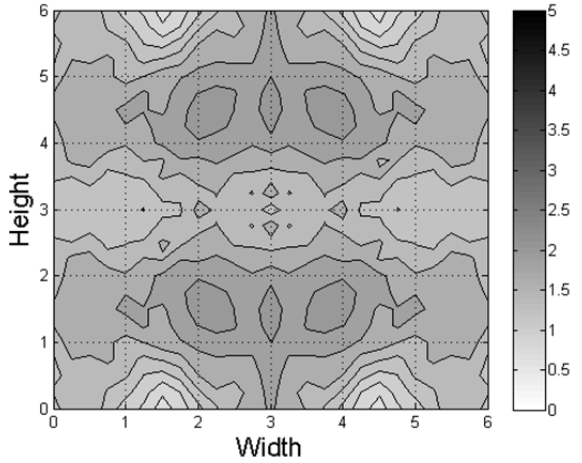

Fig. 10. Error when operating an H-polarized low-gain source antenna at 500 MHz.

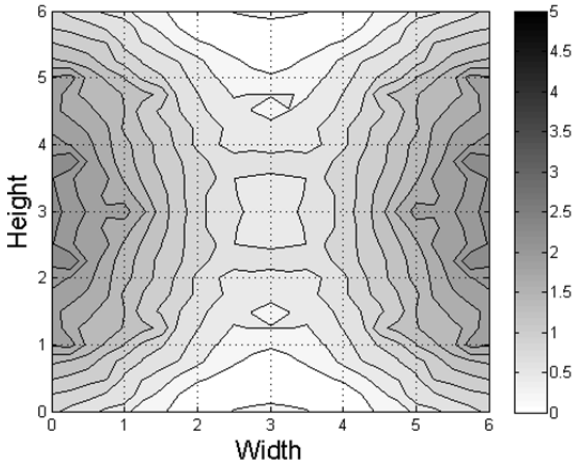

Fig. 11. Error when operating a V-polarized medium-gain source antenna at 150 MHz.

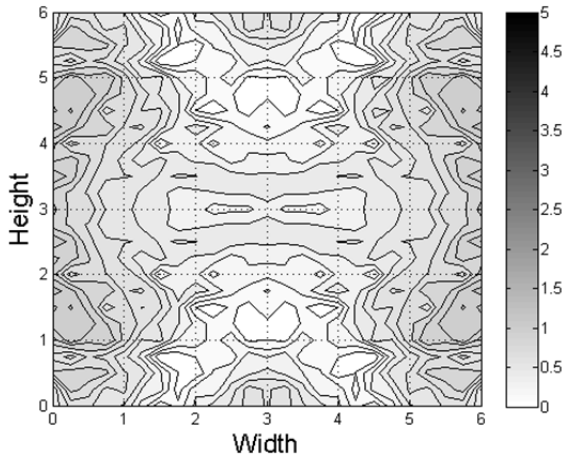

Fig. 12. Error when operating a V-polarizedmedium-gain source antenna at 250 MHz.

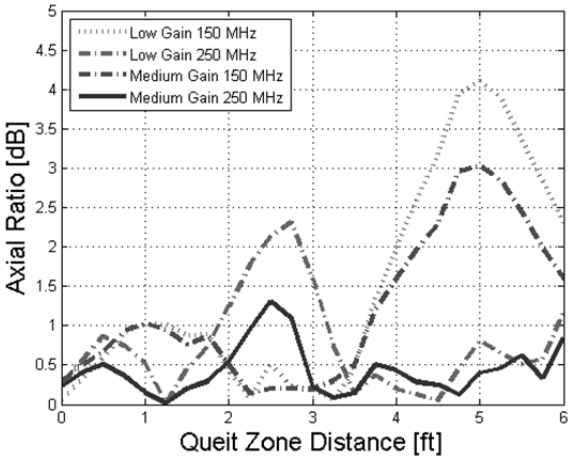

Fig. 13. Axial ratio for low- and medium-gain source antennas operating at 150 and 250 MHz.

Note the behavior of the curves in Fig. 13 is largely explained by the rectangular cross-section of the chamber resulting in:

- Different reflectivity exhibited by the side walls, the floor, and the ceiling.
- Different free space attenuation associated with different propagation distance of the reflected waves from the side walls and the floor and ceiling to the center of the quiet zone.

In theory, the axial ratio does not exist in a symmetrical chamber with a squared cross-section. If detected in a practical squared cross-section chamber, the axial ratio error is associated only with the manufacturing tolerances contributing to the error.

In addition to analyzing the anechoic chamber with FEM, the PO technique was also validated by comparing near fields in the quiet zone when operating at 500 MHz. The difference between the FEM and PO results is illustrated in Fig.14.

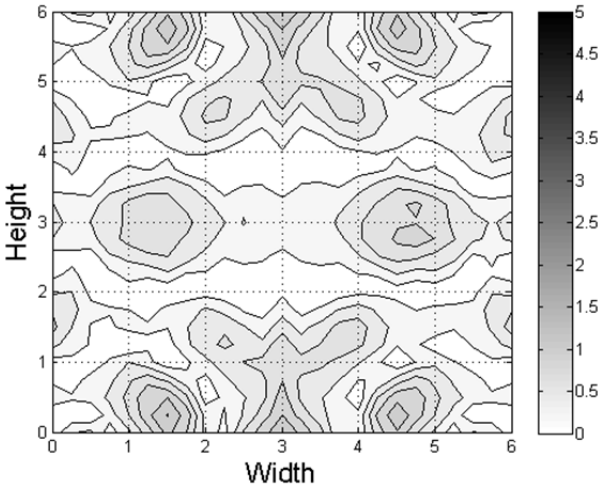

Fig.14. The difference between FEM and PO analysis results when operating at 500 MHz.

The PO technique is shown to have a maximum error of 1.0 dB when computing near fields in the quiet zone of an anechoic chamber. The additional error introduced by the physical optics method is limited, which facilitates simulating the anechoic chamber at much higher frequencies. As shown in Table IV and V, we simulated the anechoic chamber up to 2 GHz. Further increases in frequency are possible.

VI. CONCLUSION

Both full-wave and asymptotic analyses have been performed on the quiet zone of a rectangular cross-section anechoic chamber at VHF/UHF frequencies using a 3D solver within the FEKO simulation software. The results demonstrate meaningful and expected performance in the chamber with rectangular cross-section, which indicate that:

- Quiet zone performance (reflectivity) is improving as operating frequency increases.
- Quiet zone performance degrades with the increasing separation between the source antenna and quiet zone.
- A higher gain source antenna provides better quiet zone performance.
- The linear rotating polarization axial ratio is getting worse with longer separation between the source antenna and the quiet zone.
- Axial ratio is improving at higher frequencies.
- Axial ratio is improving for a higher gain source antenna.

FEKO is an effective tool for performing computational analyses of anechoic chambers at VHF/UHF frequency bands. Of particular value is the fact that one can switch from a rigorous method like FEM to an asymptotic method like PO within the same environment. Future applications of the FEKO simulation software to assist with analyzing anechoic chambers are expected.

REFERENCES

[1] M. Winebrand and J. Aubin, "Test zone performance in low frequency anechoic chambers," *Proceeding of the AMTA*, pp. 482-486, 2008.

[2] M. Winebrand and J. Aubin, "Low frequency 3-D electromagnetic analysis of anechoic chamber performance," *Microwave Journal*, October 2008.

[3] M. Agatonovic, Z. Marinkovic, and V. Markovic, "Application of ANNs in evaluation of microwave pyramidal absorber performance," *Applied Comp. Electro. Society* (*ACES*) *Journal*, vol. 27, no. 4, Apr. 2012.

[4] FEKO Suite 6.1, EM Software and Systems, 2011. www.feko.info

[5] U. Jakobus and F. M. Landstorfer, "Improved PO-MM hybrid formulation for scattering from three-dimensional perfectly conducting bodies of arbitrary shape," *IEEE Transactions on Antennas and Propagation*, vol. 43, pp. 162-169, Feb. 1995.

[6] I. P. Theron, D. B. Davidson, and U. Jakobus, "Hybridization of the method of moments with a UTD treatment of a conducting cylinder," *Proceedings of the 8th Biennial IEEE Conference on Electromagnetic Field Computation, CEFC'98*, *Tucson*, pp. 107, June 1998.

[7] M. Bingle, J. Tonder, and U. Jakobus, "Acceleration of the hybrid FEM/MoM technology in FEKO with the multilevel fast multipole method," *The 10th International Workshop on Finite Elements for Microwave Engineering*, Oct. 2010.

Derek D. Campbell was born in Marion, IN on July 23, 1983. He received the B.S. and M.S. degrees in Electrical Engineering from the Georgia Institute of Technology in 2006 and 2011, respectively.From 2002 to 2011 he served as a Research Engineer at the Georgia Tech Research Institute where he performed RCS and antenna measurements as well as analyzed geolocation algorithms. In 2012, he joined EMSoftware &Systems(USA) as an Application Engineer. His current interests are in the areas of electromagnetic theory and numerical methods primarily applied to antennas and scattering.

Gopinath Gampalajoined EM Software & Systems (USA), Inc. as an Application Engineer in 2008 and was promoted to Senior Application Engineer in November 2012. Mr. Gampala has a B.S. degree in Electronics and Communications Engineering from the Jawaharlal Nehru Technological University, Hyderabad, India. The topic of his research for his Master's degree, which he obtained from the University of Mississippi, was "Analysis and Design of Artificial Magnetic Conductors for X-Band Antenna Applications." He has experience in numerical methods for electromagnetics and during the past five years he focused on compact antenna designs using high impedance ground planes and MIMO antenna designs for LTE/4G handsets.

C. J. Reddy received M.Tech.degree in Microwave and OpticalCommunication Engineering and PhD in Electrical Engineeringfrom the Indian Institute of Technology, Kharagpur, India,in 1986 and 1988, respectively. In 1991, he wasawarded an NSERC Visiting Fellowship to conduct researchat the Communications Research Center, Ottawa, Canada. In1993, he was awarded a National Research Council (USA) Research Associate position to conduct research in computational electromagnetics at NASA Langley Research Center, Hampton, Virginia. Currently, Dr. Reddy is the President and Chief TechnicalOfficer of Applied EM Inc., a small company specializingin computational electromagnetics, antenna design, and development.At Applied EM, Dr. Reddy successfully led manysmall business innovative research (SBIR) projects from theUS Department of Defense (DoD). Dr. Reddy also serves as the President of EMSoftware & Systems (USA) Inc. At EMSS (USA), he is leadingthe marketing and support of the commercial three-dimensionalelectromagnetic software *FEKO* in North America.Dr. Reddy is a Senior Member of the IEEE and a SeniorMember of the Antenna Measurement Techniques Association (AMTA). He is a Fellow of the Applied ComputationalElectromagnetic Society (ACES), and served as a member ofits Board of Directors. He has published 35 journal papers, 54conference papers, and 17 NASA Technical Reports to date.Dr. Reddy was the General Chair of the ACES 2011 and 2013 conferences.

John Aubin currently serves as Vice President for Engineering and also as Chief Technology Officer at ORBIT/FR Inc. in Horsham, PA. Mr. Aubin received the BSEE from Virginia Tech in 1977, MBA from Temple University in 1983, and MSEE from Drexel University in 1988. He has previously been engaged in the design and implementation of high performance earth station antennas and beam waveguide systems, EW and radar antennas, monopulse tracking radars, and broadband horn antennas in addition to his work in automated antenna and RCS measurement systems. His current interests include antenna and radar cross section measurement technology, wireless systems, radar and microwave systems engineering, and antenna design. Mr. Aubin has served as principal design engineer on a number of automated antenna and radar measurement systems ranging from VHF up to millimeter waves, including a microwave imaging system for evaluation of biological tissue, a high performance low frequency radar cross section measurement system, and a dynamic radar cross section measurement system using an integrated tracking and signature measurement radar. Mr. Aubin has authored over 40 papers on antennas, radar, and measurement technology.

Study on the Matrix Pencil Method with Application to Predict Time-domain Response of a Reverberation Chamber

Song Wang, Zhan C. Wu, Lei Du, Guang H. Wei, and Yao Z. Cui

Research Institute of Electrostatic and Electromagnetic Protection
Mechanical Engineering College, Shijiazhuang, 050003, China
wansonde@gmail.com

***Abstract*—** The full wave simulation of reverberation chamber in time domain usually takes large computational time because of its resonant characteristic. This contribution makes the pioneer exploration of accelerating this kind of simulation by time-domain signal prediction. The prediction technique is based on the well known matrix pencil method (MPM). An approximation to the existing MPM is proposed to obtain a new kind of MPM, which is more computationally efficient. To conduct the prediction effectively, the signal's oversampling should be avoided and the singular values appeared in MPM should be judged appropriately. The signal can be re-sampled according to Nyquist sampling law while the singular values can be selected by the newly proposed criterion based on cavity theory. For wideband time-domain responses, it is suggested to apply digital band-pass filter before prediction to get higher precision. Using the proposed methods, the computational time can be reduced almost 50 % for the reverberation chamber's FDTD simulation.

Index Terms – Digital band-pass filter, FDTD, matrix pencil method, reverberation chamber, and signal prediction.

I. INTRODUCTION

The reverberation chamber (RC) is an essentially electrically large cavity made of highly reflective metallic walls and excited by a source. Acting as a lower cost alternative to anechoic chambers or open area test sites, RC has become an attractive electromagnetic compatibility test facility recently [1]. It has the advantages of producing a statistically uniform field within a relatively large volume, generating high-peak fields from comparatively modest input powers, and isolating the test environment from a potentially noisy ambient environment.

Numerical modeling plays an important role in the process of RC design and analysis, and there is a variety of modeling methods as reviewed in [2]. Recently, some hybrid methods both in time-domain [3] and frequency-domain [4] have attracted much attention in the field of RC's proper simulation. To sum up, a large proportion of the correlation studies adopted the time-domain methods to take advantage of wideband analysis. The finite-difference time-domain (FDTD) method [5] is the typical one because of its explicit scheme and wide applicability. However, there exists a well known problem that it is hard to reach convergence in RC's time-domain simulation because of its strong high-Q resonances [6, 7]. Using the advanced computational techniques, such as domain decomposition and parallel computation, could alleviate this contradiction to a certain degree. But a more general solution to this problem seems to be time-domain signal prediction, i.e., using the early signal records to predict the late signal response for accurate frequency domain parameter estimation. Although the RC's numerical modeling has attracted many attentions, its accelerated simulation by this way is rare to be seen.

In time-domain simulation, a Gaussian pulse excitation is usually applied whose pulse width is much shorter than the whole simulation time. Therefore, the electric field (E-field) response within the RC is almost determined by the RC's geometry. What's more, because the excitation signal has a specific frequency range, the E-field

Submitted On: March 10, 2013
Accepted On: July 26, 2013

response could be regarded as the sum of exponentially damped sinusoids with the damping rate related to RC's losses. Therefore, it is feasible to predict the remaining response using the complex exponentials extracted from the truncated response.

The matrix pencil method (MPM) is proposed to estimate parameters of exponentially damped /undamped sinusoids in noise [8], which is more computationally efficient than the polynomial method. Several modified versions of MPM have been studied since it is firstly introduced. B. Lu proposed the improved MPM using low-rank Hankel approximation [9]. Recently, MPM has attracted many attentions [10, 11] and has contributed to solving several computational electromagnetic problems [11-13].

In this contribution, the time-domain response of RC is fitted to a model of sum of complex exponentials and a new kind of matrix pencil method is proposed based on an approximation to the existing modified matrix pencil method (MMP). Through comparison, this method is demonstrated to be more computationally efficient and to retain the same precision. Before obtaining acceptable predicting results, special attention should be paid to signal's proper sampling and singular values' appropriate judgment. Fortunately, in the case for RC's time-domain response's prediction, the required major singular values for MPM could be estimated effectively according to cavity theory. Since the computing time for prediction can be neglected compared to that of RC's numerical simulation, the proposed hybrid method combing simulation and prediction can accelerate the time-domain simulation of an RC considerably.

II. MODELING RC'S TIME-DOMAIN RESPONSE

In this section, the RC's time-domain response is analysed theoretically ending up with the linear fitting model, i.e., sum of exponentially damped complex exponentials. On the one hand, the RC's stored energy U meets,

$$\frac{dU}{dt} = P_{\mathrm{t}} - P_{\mathrm{d}} = P_{\mathrm{t}} - \frac{\omega}{Q}U \tag{1}$$

where p_{t} is the net power delivered into RC, p_{d} is RC's total dissipated power, ω is the angular frequency, and Q is the quality factor embodying the overall losses of a real RC. The equation is expanded using the definition of Q [14]. Solving this differential equation leads to,

$$U = U_0 \mathrm{e}^{-\frac{t}{\tau}}, t \geq 0 \tag{2}$$

where U_0 corresponds to the stored energy when the excitation pulse is terminated and $\tau = Q/\omega$ is the time constant of RC [14]. According to the cavity theory, the amplitude of E-field strength is directly proportional to the square root of U. Moreover, the E-fields are assumed to be statistically uniform. Therefore,

$$|E_x|, |E_y| \text{ and } |E_z| \propto \sqrt{e^{-t/\tau}} = e^{-\frac{t}{2\tau}} \tag{3}$$

where $|E_x|, |E_y|, \text{and } |E_z|$ correspond to the amplitude of E-field in the $x, y, \text{and } z$ orthogonal directions, respectively. In short, the E-fields within the RC decay exponentially.

On the other hand, there exist limited resonant frequency components for a settled RC within the investigated frequency band. To sum up, the time-domain response $s(k), k = 1, 2, ..., N$ of an RC excited by a pulse can be modeled as the sum of exponentially damped complex exponentials,

$$s(k) = \sum_{i=1}^{M} c_i z_i^k, k = 1, 2, 3 \cdots N \tag{4}$$

where N is the signal's length, M is the number of major exponentials, $c_i, i = 1, 2, ..., M$ are fitting coefficients, and $z_i = e^{-\alpha_i + j\omega_i}, i = 1, 2, ..., M$ are complex exponentials with α_i being the damping factors and $\omega_i = 2\pi f_i$ the angular frequencies.

Once z_i and M are determined from the truncated early response of an RC, then $c_i, i = 1, 2, ..., M$ can be derived by solving a least-squares problem [8]. Consequently, the late response can be predicted by increasing N to be large enough.

III. DERIVATION OF A NEW KIND OF MPM

In this section, a new kind of MPM is proposed based on an approximation to the existing modified MPM.

A. Recalling the conventional MPM

The observed data (probably contaminated by noise $n(k)$) is expressed as,

$$y(k) = s(k) + n(k), k = 1, 2, ..., N. \tag{5}$$

In order to extract $z_i, i = 1, 2, ..., M$ from $y(k)$, the Hankel data matrix $\boldsymbol{Y}$ is constructed as,

$$\boldsymbol{Y} = [\boldsymbol{y}_1, \boldsymbol{y}_2, \cdots, \boldsymbol{y}_{L+1}] \tag{6}$$

where $\beta \square L/N$ is called pencil rate parameter satisfying $M < L < N - M$ and the column vector,

$$\boldsymbol{y}_l = [y(l), y(l+1), \cdots, y(N-L+l-1)]^{\mathrm{T}} \tag{7}$$

where the superscript T denotes the transpose operator. The matrices $\boldsymbol{Y}_1$ and $\boldsymbol{Y}_2$ (with the same size) are obtained by removing the last and first column of $\boldsymbol{Y}$, respectively.

The matrix pencil for $\boldsymbol{Y}_1$ and $\boldsymbol{Y}_2$ is defined as $\boldsymbol{Y}_2 - \lambda \boldsymbol{Y}_1$, with λ a complex parameter. If $n(k)=0, k = 1, 2, ..., N$, $\boldsymbol{Y}_2 - \lambda \boldsymbol{Y}_1$ can be rewritten as,

$$\boldsymbol{Y}_2 - \lambda \boldsymbol{Y}_1 = \boldsymbol{Z}_1 \boldsymbol{C} [\boldsymbol{Z}_0 - \lambda \boldsymbol{I}] \boldsymbol{Z}_2 \tag{8}$$

where

$$\boldsymbol{Z}_1 = \begin{bmatrix} z_1 & z_2 & \cdots & z_M \\ z_1^2 & z_2^2 & \cdots & z_M^2 \\ \vdots & & \ddots & \vdots \\ z_1^{N-L} & z_2^{N-L} & \cdots & z_M^{N-L} \end{bmatrix}, \tag{9}$$

$$\boldsymbol{Z}_2 = \begin{bmatrix} 1 & z_1 & \cdots & z_1^{L-1} \\ 1 & z_2 & \cdots & z_2^{L-1} \\ \vdots & & \ddots & \vdots \\ 1 & z_M & \cdots & z_M^{L-1} \end{bmatrix}, \tag{10}$$

$$\boldsymbol{Z}_0 = \mathrm{diag}\{z_1, z_2, ..., z_M\}, \tag{11}$$

$$\boldsymbol{C} = \mathrm{diag}\{c_1, c_2, ..., c_M\}. \tag{12}$$

Because $\lambda = z_i$ is the rank-reducing number of this matrix pencil, the eigenvalues of $\boldsymbol{Y}_1^{+}\boldsymbol{Y}_2$ can be regarded as $z_i, i = 1, 2, ..., M$, where + denotes the Moore-Penrose pseudo inverse operator. If $y(k)$ is contaminated by noises, the rank of $\boldsymbol{Y}_2 - \lambda \boldsymbol{Y}_1$ is probably larger than M, and the low-rank approximation to $\boldsymbol{Y}$ is proposed to suppress the noises before adopting the same procedure to derive $z_i, i = 1, 2, ..., M$ [15]. In the first step, the SVD of $\boldsymbol{Y}$ is carried out,

$$\boldsymbol{Y} = \boldsymbol{U} \begin{bmatrix} \boldsymbol{\Sigma} & \boldsymbol{O} \\ \boldsymbol{O} & \boldsymbol{O} \end{bmatrix} \boldsymbol{V}^{\mathrm{H}} \tag{13}$$

where the superscript H denotes the conjugate transpose, $\boldsymbol{U}$ and $\boldsymbol{V}$ are made up of the eigenvectors of $\boldsymbol{Y}\boldsymbol{Y}^{\mathrm{H}}$ and $\boldsymbol{Y}^{\mathrm{H}}\boldsymbol{Y}$, respectively and $\boldsymbol{\Sigma} = \mathrm{diag}(\sigma_1, \sigma_2, \cdots, \sigma_q)$ is composed of the nonzero singular values σ_i arranged in a descending sequence. In the second step, M major singular values are selected to make up,

$$\boldsymbol{\Sigma}' = \mathrm{diag}(\sigma_1, \sigma_2, \cdots, \sigma_M), M < \min(N-L, L). \tag{14}$$

Then the reduced-rank approximation (its operator $\mathcal{L}$) of $\boldsymbol{Y}$ is derived as,

$$\boldsymbol{Y}' = \mathcal{L}(\boldsymbol{Y}) = \boldsymbol{U}' \boldsymbol{\Sigma}' \boldsymbol{V}'^{\mathrm{H}} \tag{15}$$

where $\boldsymbol{U}'$ and $\boldsymbol{V}'$ are obtained by choosing the front M columns of $\boldsymbol{U}$ and $\boldsymbol{V}$, respectively. It is proved that among all the matrices with the same size of $\boldsymbol{Y}$, $\boldsymbol{Y}'$ is the one, which has the minimum Frobenius norm deviation to $\boldsymbol{Y}$, and this deviation decreases as M increases [11].

The simple criterion to determine M would be checking whether ,

$$\sigma_M / \sigma_1 <= 10^{-p} \tag{16}$$

where p is an appropriately chosen value according to the specific predicting data. These selected singular values can be regarded as the weight coefficients corresponding to the major resonant components. In contrast, those discarded ones having trivial values corresponds to the noisy components.

The same method as used in the noiseless case could be utilized to get z_i from $\boldsymbol{Y}'$, while an equivalent but more computationally efficient technique is to calculate the front M eigenvalues of ,

$$\{\boldsymbol{V}_1'^{\mathrm{H}}\}^{+} \boldsymbol{V}_2'^{\mathrm{H}} \tag{17}$$

directly to estimate z_i [15], where (in Matlab notation),

$$\boldsymbol{V}_1' = \boldsymbol{V}'(1:L, :), \boldsymbol{V}_2' = \boldsymbol{V}'(2:L+1, :).$$

The computation burden can be alleviated in this way because the operation to obtain $\boldsymbol{Y}'$ is avoided. This conventional method is named *mp*.

B. Derivation of the new kind of MPM

While $\mathcal{L}(\boldsymbol{Y})$ does not remain the Hankel structure, the reduced-rank Hankel approximation (its operator J) is introduced to derive $J(\boldsymbol{Y})$, which possesses both the Hankel structure and rank-deficient properties. This modification is helpful in suppressing noises. By the aid of $\mathcal{H}$ known as the Hankel approximation operator. An iterative algorithm of J is available where each iteration executes $\mathcal{H}$ and $\mathcal{L}$, successively. For a given matrix $\boldsymbol{X}$, the iterative algorithm of J is

$$J(\boldsymbol{X}) = (\mathcal{H}\mathcal{L})^{\infty}(\boldsymbol{X}) = \lim_{G \to \infty} (\underbrace{\mathcal{H}\mathcal{L} \cdots (\mathcal{H}\mathcal{L}}_{G}(\boldsymbol{X})) \cdots). \tag{18}$$

For more details about J, the reader can refer to [16]. The modified MPM using J is stated as below, which is named *mmp1*.

1. $\tilde{\boldsymbol{Y}} = \mathcal{J}(\boldsymbol{Y})$,

2. $\tilde{\boldsymbol{Y}}_1 = \tilde{\boldsymbol{Y}}(:, 1:L), \tilde{\boldsymbol{Y}}_2 = \tilde{\boldsymbol{Y}}(:, 2:L+1)$,

3. $\hat{\boldsymbol{Y}}_i = \mathcal{L}(\tilde{\boldsymbol{Y}}_i), i = 1, 2$,

4. Calculating the front M eigenvalues of $\{\hat{\boldsymbol{Y}}_1\}^+ \hat{\boldsymbol{Y}}_2$.

The main difference from *mp* occurred in step 1, i.e., the pre-treatment of the original master matrix $\boldsymbol{Y}$, which retains the Hankel structure in the process of filtering noise represented by operator $\mathcal{L}$. The subsequent steps resemble that of *mp*. Analyzing the computational burden of *mmp1*, $\mathcal{L}$ is the key factor because it is more time-consuming than $\mathcal{H}$ considering the SVD. In order to avoid $\mathcal{L}$, the approximation to step 3 is proposed to reduce the executions of $\mathcal{L}$ from two times to one time. That is

$$\hat{\boldsymbol{Y}} = \mathcal{L}(\tilde{\boldsymbol{Y}}), \hat{\boldsymbol{Y}}_1 = \hat{\boldsymbol{Y}}(:, 1:L), \hat{\boldsymbol{Y}}_2 = \hat{\boldsymbol{Y}}(:, 2:L+1), \quad (19)$$

in the case when $L \varepsilon 1$.

What is more, recalling the equivalent procedure mentioned above equation (17), it is preferred to derive the required M eigenvalues from matrix $\tilde{\boldsymbol{V}}$ directly, rather than rely on matrix $\hat{\boldsymbol{Y}}$ needing additional multiply operation between matrixes. To sum up, a new kind of MPM, named *mmp2*, is proposed as below,

1. $\tilde{\boldsymbol{Y}} = \mathcal{J}(\boldsymbol{Y})$,

2. obtain $\tilde{\boldsymbol{V}}$ *from* $\mathcal{L}(\tilde{\boldsymbol{Y}})$,

3. $\tilde{\boldsymbol{V}}_1 = \tilde{\boldsymbol{V}}(1:L, :), \tilde{\boldsymbol{V}}_2 = \tilde{\boldsymbol{V}}(2:L+1, :)$,

4. Calculating the front M eigenvalues of $\{\tilde{\boldsymbol{V}}_1^{\mathrm{H}}\}^+ \tilde{\boldsymbol{V}}_2^{\mathrm{H}}$.

Because the condition $L \varepsilon 1$ is usually satisfied, the method *mmp2* is assumed to get the almost identical results with *mmp1* with less computation burden.

C. Validation of the proposed method

The advantage of *mmp1* had been shown in [9] compared to *mp*. As *mmp2* is proposed based on *mmp1*, its feasibility and effectiveness is validated by comparing the simulation result from *mmp1* and *mmp2*. The similar example as in [16] is employed. M = 10, N = 1000, and β = 0.60. The symbol $\alpha_i, i = 1, 2, \ldots M$ are randomly chosen from $1.0/N$ to $1.5/N$. In Matlab notation, this is

$$\alpha = \frac{1}{N} + \mathrm{rand}(1, M) * \frac{1}{2N}.$$

Similarly, c_i are randomly chosen within [1, 2], and ω_i within [0.35*2π, 0.5*2π]. Once these parameters are determined, series $s(k)$ are built according to equation (4).

As we focus on the real-time signal prediction for RC's response, only the real parts of $s(k)$ are considered. Both the methods *mmp1* and *mmp2* are used to extract z_i under different signal-to-noise ratio (SNR), which is defined as

$$\mathrm{SNR} = 10 \times \log 10 \left(\frac{\mathrm{var}(s)}{\mathrm{var}(n)} \right). \quad (20)$$

Then, c_i are derived using the least-square method. Because the complex exponentials are used to fit the real-time series, setting the number of the selected major singular values to be 20 is optimal meaning 10 pairs of conjugate complex exponentials. The original and fitted signals are named y_o and y_s, respectively. The prediction is achieved through lengthening y_s by enlarging N. Here, both y_o and y_s are lengthened to 2000. That is to say only 1000 data are used to determine the unknown parameters, such as z_i and c_i. The second half signal is obtained through prediction. Their relative error

$$\varepsilon = \frac{\| y_s - y_o \|_2}{\| y_o \|_2}, \quad (21)$$

is regarded as the indicator for evaluating the performance of the two methods. As shown in Fig. 1, ε is exactly the same for both methods and it decreases as the SNR increases. This coincidence demonstrates the effectiveness of the approximation presented by equation (19). In fact, ε is a severe indicator, because the agreement is already quite acceptable when ε is below 0.15. In detail, the fitting and predicting performance under $\varepsilon = 0.10$ are shown in Fig. 2 and 3. As we can see, satisfactory agreement is reached.

What is more, the consumed time t_1 and t_2 of *mmp1* and *mmp2*, respectively, on a PC with a 3.0 GHz CPU is compared in Table I. Obviously, the proposed method *mmp2* is more computationally efficient than *mmp1* with the same precision. This is because $\mathcal{J}$ can reach convergence within several iterations and *mmp2* reduces the operation time of $\mathcal{L}$ effectively. Besides, the computation time increases as the SNR decreases, because lower SNRs usually correspond to more iterations in $\mathcal{J}$.

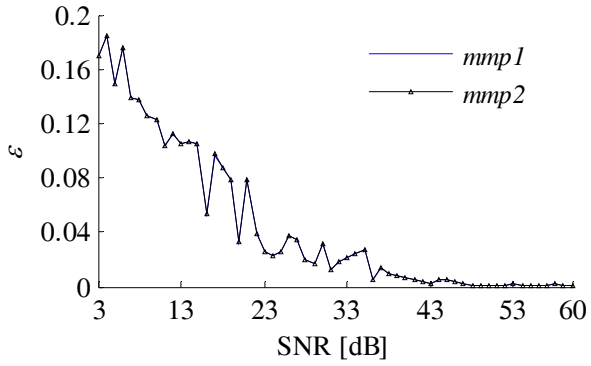

Fig. 1. ε from *mmp1* and *mmp2* versus SNR.

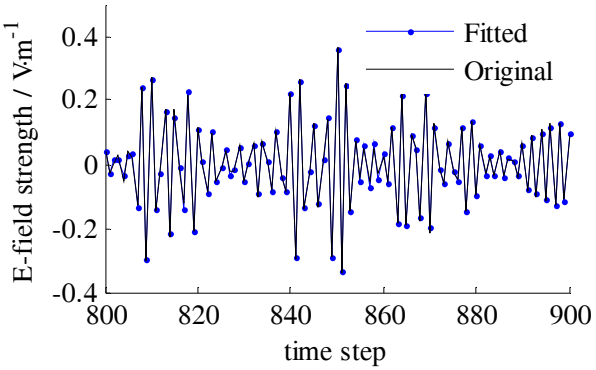

Fig. 2. Local performance of fitting.

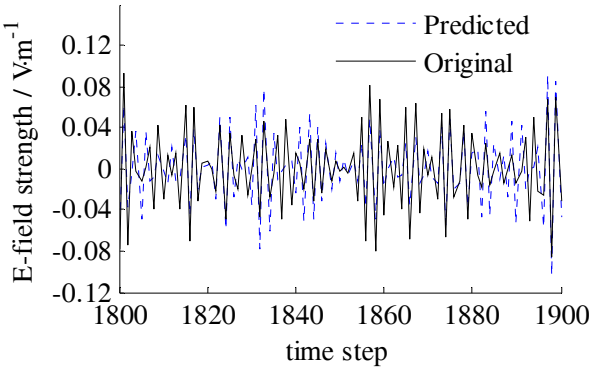

Fig. 3. Local performance of predicting.

Table. I. Comparison of t_1 (*mmp1*) and t_2 (*mmp2*).

SNR	t_1 / s	t_2 / s
5 dB	17.4	13.6
10dB	14.7	11.8
15dB	10.5	8.9
25dB	7.9	6.2
40dB	6.4	5.3

IV. APPLICATION TO ACCELERATING RC'S FDTD SIMULATION

Through predicting the RC's time-domain response from the truncated simulated signal, the RC's simulation is accelerated. Here, we focus on RC's FDTD simulation, but the prediction methodology is also applicable to the results from other time-domain simulation methods.

A. Configurations

The investigated RC's dimension is 10.5 m × 8.0 m × 4.3 m with the lowest usable frequency about 80 MHz. It is equipped with two different stirrers rotating in step-by-step mode, i.e., mechanical stirring. With the aid of the published codes in [5], it is simulated by FDTD with the spatial meshing step dx = dy = dz = 0.1 m and time step dt = 1.73 × 10^{-10}s. The transmitting antenna is a 1.6 m long dipole antenna modeled using the thin-wire technique [5]. A modulated Gaussian pulse with the specified frequency band (80~120) MHz is applied to the antenna.

On the disposal of RC's losses, treating the conductivity of the materials in numerical model as the real values is found to generate much higher electric field strength than measurement data [7] because the real RC includes many kinds of losses and they can hardly be reproduced by RC's numerical model. Alternatively, drawing on the proposition from [7], the approximation method is introduced by regarding the material of the RC as PEC and setting the air's conductivity σ_{air} to be about 1.5×10^{-5}~2×10^{-5} S/m [17]. That is to say the overall losses of the RC approximately equals to the losses on the RC's inner air volume. This value is higher than 10^{-5} S/m in [7] because our RC's material is mainly galvanized steel rather than aluminum and its reflection coefficient is lower than aluminum [17]. It is worth noting that we emphasize on the prediction on the time-domain response rather than the details about RC's numerical modeling.

The simulation runs for a number of time steps N_{ts} until the amplitude of the E-field strength is attenuated to nearly 1 % of the peak value. Eight sampling points within the RC's working volume are selected for E-field output at x, y, and z directions. The proposed method *mmp2* is adopted for the prediction.

B. Implementation issues

The RC's time-domain response from FDTD simulation is believed to possess a relatively high SNR. Acceptable agreement can be reached between the predicted response and the simulated signal for RC providing both the following issues are taken into accounts, i.e., signal re-sampling and appropriate choice of M (the number of the major singular values).

The signal re-sampling refers to ensuring the signal is sampled appropriately before prediction according to the Nyquist sampling law. Under this configuration, as the sampled frequency 1/dt is much higher than the ceiling of the investigated frequency band, these E-field signals are re-sampled at 1/20 times 1/dt with the Nyquist sampling law still satisfied. In fact, the re-sampling is crucial for good prediction results because oversampling means redundancy and additional computation burden for MMP.

Besides the signal's re-sampling, the key parameter M can no longer be determined as effortless as in section III. The simulation data show that determining M by the criterion represented in equation (16) is neither reliable nor convenient because controlling the key parameter p calls for trial and error attempts. Alternatively, since M depends on the number of resonant frequencies, it can be determined according to the number of the RC's activated resonant modes within the simulated frequency band. We manage to estimate the total number of activated resonant modes approximately based on the cavity theory. In this way, the resonant frequency (in Hz) corresponding to a potential resonant mode can be expressed as,

$$f_{m,n,p} = \frac{c}{2}\sqrt{\left(\frac{m}{L_{\mathrm{RC}}}\right)^2 + \left(\frac{n}{W_{\mathrm{RC}}}\right)^2 + \left(\frac{p}{H_{\mathrm{RC}}}\right)^2} \qquad (22)$$

where c is the velocity of light in vacuum and $L_{\mathrm{RC}}, W_{\mathrm{RC}}, H_{\mathrm{RC}}$ are the rectangular cavity's length, width, and height, respectively. Using equation (22), about 90 different resonant frequency components are determined for our simulating frequency band. So it is reasonable to set M = 180. Although, the RC equipped with some stirrers usually demonstrates more complex field distribution with a relatively larger density of resonant modes compared with the empty case, the prediction results show that it is indeed an effective approach to derive M for MPM. This can be understood considering that the number of 'activated' resonant modes in the RC with stirrers is close to that of the 'potential' resonant modes in the same RC without stirrers.

C. Results of prediction

We took two cases for results' checking. In case one, we assume an RC with the same dimensions is under low losses and set $\sigma_{\mathrm{air}}=1\times10^{-5}$ S/m. The required N_{ts} is 40000 corresponding to about 70 minutes' operation on a PC with a 3.0 GHz CPU. Each of the obtained E-fields' responses is projected to 2000 data by the re-sampling method. Similarly, the first half data are used by *mmp2* to determine the unknown parameters and the relative error ε_{t} with the same definition is used for performance checking.

According to equation (14), the span of the key parameter β should satisfy,

$$\min\{\beta N, (1-\beta)N\} > M \ . \qquad (23)$$

Through simulation optimization, the smallest ε is obtained for most sets of the E-field signals when β = 0.6. Its results are shown in Fig. 4. The fitted and predicted signal converges to zero as the same as the original simulated signal. From local checking, acceptable agreement is obtained.

Moreover, the fitting-predicting performances for all these sets of E-field signals from different locations within the working volume of the RC are shown in Fig. 5 where the 10th set corresponds to the results in Fig. 4. Acceptable performance is obtained with all ε_{t} below 15 %. The results are close to each other since all these 24 sets of sampled signals share the same RC's resonant characteristics.

In essence, only the second half signal by prediction is of significance. So additional attention is paid to the semi-simulated semi-predicted signal whose relative error between the complete simulated data is $\varepsilon_{\mathrm{tc}}$, which is certainly smaller than ε_{t} as shown in Fig. 5. Although the improvement degree from ε_{t} to $\varepsilon_{\mathrm{tc}}$ is far less than 50 %, which means the prediction is not as good as the fitting, the indispensable effect of prediction can be seen in Fig. 6. Here, the relative error in frequency-domain between the complete 2000 simulated data (after re-sampling) and the front 1000 truncated data (truncation means the rest of signal data are assigned to zeros) is denoted as ε_{f}, while the relative error between complete signal and semi-simulation semi-prediction signal is

labelled ε_{fc}. From Fig. 6, ε_{fc} is indeed smaller than ε_f, so the method combining simulation and prediction is feasible and effective.

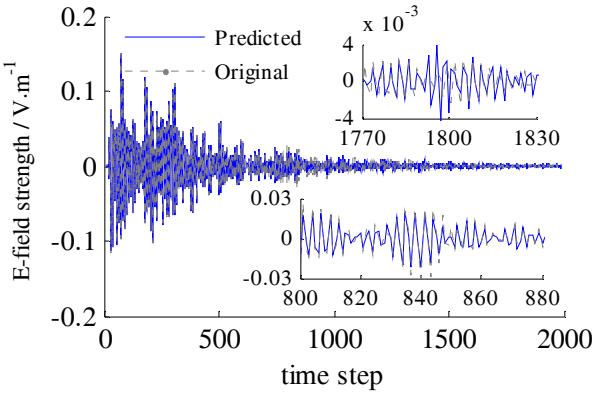

Fig. 4. Performance of fitting and predicting for RC's time-domain response.

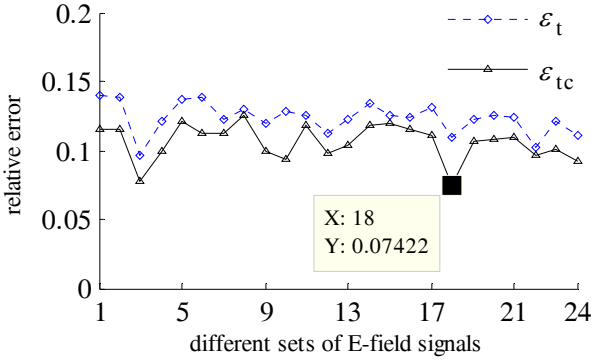

Fig. 5. Performance versus different sets of E-field signals.

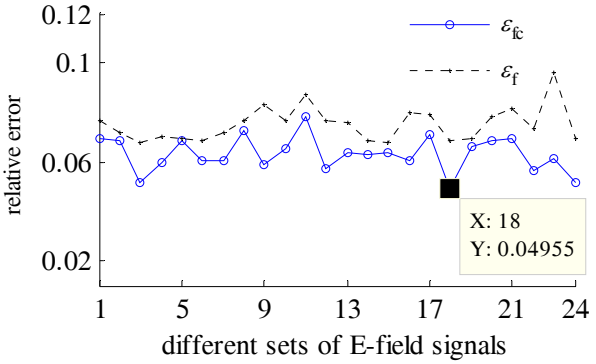

Fig. 6. Comparison of relative Error in frequency-domain.

In case two, since it had been validated that the overall losses of our RC in reality can be approximated by increasing σ_{air} to about 2.0×10^{-5} S/m [17], we took $\sigma_{air} = 2.0 \times 10^{-5}$ S/m with $N_{ts} = 26000$, which means the higher level of losses the fewer of simulation time steps. Using the same method for signal re-sampling, the length of the usable data shrunk to 1300. Similarly, the first half is used to predict the second half employing method *mmp2*, where M is also set to 180. The prediction performances are showed by the dashed line in Fig. 7, which are a little worse than that in Fig. 5. The relative error ε_{tc} for some set of the E-field signals even exceeds 30 %. The main reason is that the length of available data used in *mmp2* shrunk a lot compared with that in case one. Consequently, the formerly optimized parameter $\beta = 0.6$ is no longer the preferential choice for case two. After optimization, setting $\beta = 0.7$ can obtain quite acceptable results for all sets of the E-field signals as shown in Fig. 7.

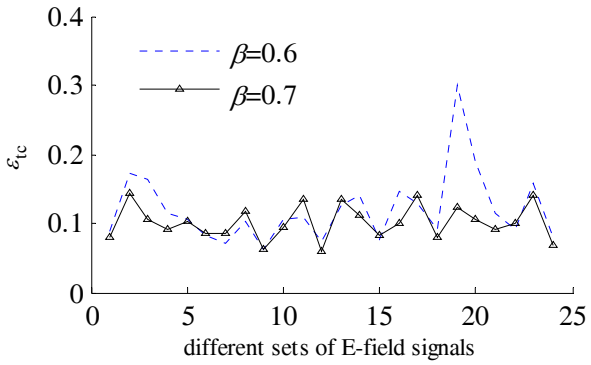

Fig. 7. Comparison of ε_{tc} with different β.

In other cases, when the investigated frequency band is enlarged, it is not easy to ensure ε_{tc} below 15 %. That is because the number of potential resonant modes will increase swiftly as the frequency band expands. From our preliminary exploration, in order to obtain acceptable prediction results, the number of properly sampled data used for prediction should be several times of the total number of resonant components. Therefore, in order to get higher precision, it is suggested to apply digital band-pass filter to the wideband time-domain responses before prediction.

V. CONCLUSION

In this contribution, accelerating RC's time-domain simulation employing signal's prediction is shown to be feasible. Since the RC's time-domain response has the characteristics of resonance and exponentially damping trend, it can be formulated as a sum of complex exponentials whose unknown parameters can be estimated effectively by the matrix pencil method. An approximation is proposed to save unnecessary reduced-rank decomposition in the MPM, which leads to a new kind of MMP, which is more computationally efficient and retains the same precision. In its application to RC's time-domain response prediction, the major singular values can be estimated appropriately by the newly proposed criterion base on the cavity theory. Simulation data show that the RC's time-domain response from FDTD modeling can be fitted and predicted effectively. Noting that the consumed computing time by MMP can be neglected compared with that by FDTD simulation, the hybrid method combining simulation and prediction can save considerable time for RC's time-domain simulation (almost 50%). Moreover, the employment of this predicting technique is independent of the RC's simulation tool. It can give reasonable results only if the under-predicting signal has an appropriate sampling rate and the major singular values are selected effectively.

REFERENCES

[1] J. H. Rudander, I.-E.-Khuda, P.-S. Kildal, and C. Orlenius, "Measurements of RFID tag sensitivity in reverberation chamber," *IEEE Antennas And Wireless Propagation Letters*, vol. 10, no. 1, pp. 1345-1348, 2011.

[2] C. Bruns and R. Vahldieck, "A closer look at reverberation chambers 3-D simulation and experimental verification," *IEEE Transactions on Electromagnetic Compatibility*, vol. 47, no. 3, pp. 612-626, 2005.

[3] S. Lallechere, P. Bonnet, S. Girard, F. Diouf, and F. Paladian, "Evaluation of FVTD dissipation and time-domain hybridization for MSRC studies," *Presented at the 23rd Annual Review of Progress in Applied Computational Electromagnetics*, Verona, Italy, 2007.

[4] H. P. Zhao and Z. X. Shen, "Efficient modeling of three-dimensional reverberation chambers using hybrid discrete singular convolution-method of moments," *IEEE Transactions on Antennas and Propagation*, vol. 59, no. 8, pp. 2943-2953, 2011.

[5] A. Z. Elsherbeni and V. Demir, *The Finite-Difference Time-Domain Method for Electromagnetics with MATLAB Simulations*, SciTech Publishing Inc., Raleigh, NC, 2009.

[6] H. Bruns, C. Schuster, and H. Singer, "Numerical electromagnetic field analysis for EMC problems," *IEEE Transactions on Electromagnetic Compatibility*, vol. 49, no. 2, pp. 253-262, 2007.

[7] F. Moglie, "Convergence of the reverberation chambers to the equilibrium analyzed with the finite-difference time-domain algorithm," *IEEE Transactions on Electromagnetic Compatibility*, vol. 46, no. 3, pp. 469-476, 2004.

[8] Y. Hua and T. K. Sarkar, "Matrix pencil method for estimating parameters of exponentially damped/umdamped sinusoids in noise," *IEEE Transactions on Acoustics*, *Speech and Signal Processing*, vol. 38, no. 5, pp. 814-824, 1990.

[9] B. Lu, D. Wei, B. Evans, and A. Bovik, "Improved matrix pencil methods," *presented at the Conference Record of the Thirty-Second Asilomar Conference on Signals, Systems & Computers*, 1998.

[10] K. Chahine, V. Baltazart, and Y. Wang, "Parameter estimation of damped power-law phase signals via a recursive and alternately projected matrix pencil method," *IEEE Transactions on Antennas and Propagation*, vol. 59, no. 4, pp. 1207-1216, 2011.

[11] Y. Liu, Z. Nie, and Q. Liu, "Reducing the number of elements in a linear antenna array by the matrix pencil method," *IEEE Transactions on Antennas and Propagation*, vol. 56, no. 9, pp. 2955-2962, 2008.

[12] J. Ritter and F. Amdt, "Efficient FDTD/matrix-pencil method for the full-wave scattering parameter analysis of waveguiding structures," *IEEE Transactions on Microwave Theory and Techniques*, vol. 44, no. 12, pp. 2450-2456, 1996.

[13] Y. Yang, S. Hu, R. Chen, H. Zhang, and T. Liu, "FDTD analysis with modified matrix pencil method for the UC-EBG lowpass filters," *Microwave and Optical Technology Letters*, vol. 44, no. 1, pp. 37-41, 2005.

[14] IEC 61000-4-21, *Electromagnetic Compatibility (EMC) - Part 4-21: Testing and Measurement Techniques - Reverberation Chamber Test Methods*, ed: International Electrotechnical Commission (IEC), pp. 40-44, 2011.

[15] T. Sarkar and O. Pereira, "Using the matrix pencil method to estimate the parameters of a sum of complex exponentials," *IEEE Antennas and Propagation Magazine*, vol. 37, no. 1, pp. 48-55, 1995.

[16] Y. Li, K. R. Liu, and J. Razavilar, "A parameter estimation scheme for damped sinusoidal signals based on low-rank Hankel approximation," *IEEE*

Trans. on Signal Processing, vol. 45, no. 2, pp. 481-486, 1997.

[17] S. Wang, Z. Wu, G. Wei, Y. Cui, and L. Fan, "A new method of estimating reverberation chamber Q-factor with experimental validation," *Progress In Electromagnetic Research Letters*, vol. 36, pp. 103-112, 2013.

Song Wang was born in 1987, Hebei province, China. He received the B.Sc. degree from Beihang university, Beijing, China, in 2010, and the M.Eng. degree from Institute of Electrostatic and Electromagnetic Protection, Mechanical Engineering College, Shijiazhuang, China. He is currently working towards the Ph.D. degree and his research interests include computational electromagnetic and electromagnetic tests in reverberation chamber.

A Shifted SSOR Preconditioner with Low-Rank Compression for Monostatic RCS Calculation

J. Chen [1, 2], Z. Liu [3, 4], B. Yong [5], Z. Jiang [6], and N. Cao [1]

[1] College of Computer and Information Engineering, Hohai University, Nanjing, China
cjq19840130@163.com

[2] Department of Space Microwave Remote Sensing System, Institute of Electronics, Chinese Academy of Sciences, Beijing, China

[3] School of Information Engineering, East China Jiaotong University, Nanchang, China

[4] State Key Laboratory of Millimeter Wave, Southeast University, Nanjing, China

[5] State Key Laboratory of Hydrology-Water Resources and Hydraulic Engineering, Hohai University, Nanjing, China

[6] Department of Communication Engineering, Nanjing University of Science & Technology, Nanjing, China

Abstract ─ Computation time and memory consumption are two crucial bottlenecks for solving large dense complex linear system arising from electric field integral equations (EFIE) formulation of monostatic scattering problems. The traditional symmetric successive over-relaxation (SSOR) preconditioner, derived from the near-field matrix of the EFIE, is widely used to accelerate the convergence rate of iterative solvers. This technique can be greatly improved by modifying the near-field matrix of the EFIE with the principal value term of the magnetic field integral equation (MFIE) operator. Additionally, the adaptive cross approximation (ACA) algorithm is applied to compress the near-field interaction matrix to save memory. Numerical experiment results indicate that the novel technique can significantly reduce both the computational time and memory significantly with low cost for construction and implementation of preconditioners.

Index Terms - Adaptive cross approximation, iterative methods, low-rank property, monostatic RCS, preconditioning techniques, and shifted technique.

I. INTRODUCTION

For electromagnetic scattering analysis, a classic problem is to compute the current distribution on the surface of an object illuminated by a given incident plane wave [1]. The formulation considered here is electric field integral equations (refer to as EFIE) since it has the most general form and does not require any assumption about the geometry of the object. The EFIE matrix equation can be solved by using iterative solvers, and the required matrix-vector product operation can be efficiently calculated by multi-level fast multi-pole algorithm (MLFMA) [2]. The use of MLFMA could reduce both the memory requirement and the computational complexity to O (NlogN) [3].

It is well-known that EFIE provides a first-kind integral equation, which is ill-conditioned and difficult to solve in a linear system [4]. Therefore, some researchers have been attempting to adopt the preconditioning method to accelerate the solution of linear systems for this problem [5-

Submitted On: Aug. 29, 2012
Accepted On: Aug. 29, 2013

7]. Simple preconditioners such as the diagonal or diagonal blocks of the coefficient matrix might be effective when the matrix has some degree of diagonal dominance. Incomplete LU (ILU) factorizations have been successfully used for nonsysmmetric dense systems [8]. However, the factorization is commonly rather ill-conditioned. Thus, this makes the triangular solvers highly unstable and the use of the ILU preconditioner might be ineffective as a whole [9]. Presently, the sparse approximate inverse (SAI) preconditioning techniques have been successfully integrated with the MLFMA [10, 11]. But the construction cost of SAI is normally higher. Relative to ILU and SAI, the symmetric successive over-relaxation (SSOR) [12, 13] preconditioner has the obvious advantage in construction cost. Furthermore, the SSOR preconditioning technique contains more information of the coefficient matrix when compared with a diagonal/block diagonal matrix, which is perhaps efficient only for very long and narrow structures. However, the conventional SSOR preconditioner is sometimes ineffective for the iterative solution of the symmetric indefinite linear systems arising from the EFIE formulation of electromagnetic scattering problems. As an attempt for a possible remedy, SSOR preconditioner combined with a tri-diagonal shift from the principal value term of MFIE operator is proposed, which is called shifted SSOR (S-SSOR) [14]. Compared to original SSOR method, this shift scheme can significantly improve the performance of the SSOR preconditioner, meanwhile it does not require much more computational and storage costs. Except that the process of monostatic scattering computation could be accelerated by S-SSOR preconditioner, another remaining bottleneck of EFIE solution is the limited memory. Some previous studies have shown that the far-field impedance matrix can be compressed by MLFMA well [2-3], while the near-field self-interaction matrix is full rank, which makes it incompressible. However, in some cases, near-field interaction matrix (excluding the self-interaction matrix) might have characteristics of low rank [15-19], such as dealing with the multi-scale problems [20]. To achieve the purpose of low memory cost, the adaptive cross approximation algorithm (ACA) [21-24] is used in this paper to compress the near-field interaction matrix.

The paper is organized as follows, section II gives a brief introduction to the EFIE formulation and the MLFMA. The shifted SSOR preconditioning technique is depicted for more details in section III. Section IV demonstrates the basic theory of low-rank decomposition strategy for near-field interaction matrix. Numerical experiments with several monostatic scattering problems are presented to verify the efficiency of the proposed method in section V. The conclusions are summarized in section VI.

II. EFIE FORMULATION AND MLFMA

The EFIE formulation of electromagnetic wave scattering problems using planar Rao-Wilton-Glisson (RWG) basis functions for surface modeling is presented in [1]. The resulting linear systems from EFIE formulation after Galerkin's testing are briefly outlined as follows,

$$\sum_{n=1}^{N} Z_{mn} I_n = V_m, \qquad m = 1, 2, ..., N \tag{1}$$

where

$$Z_{mn} = jk\int_s \mathbf{f}_m(\mathbf{r}) \bullet \int_{s'} (\bar{\mathbf{I}} + \frac{1}{k^2}\nabla\nabla\bullet)[G(\mathbf{r},\mathbf{r}')\mathbf{f}_n(\mathbf{r}')]ds ds'$$

$$V_m = \frac{1}{\eta}\int_s \mathbf{f}_m(\mathbf{r}) \bullet \mathbf{E}^i(\mathbf{r}) ds\,, \quad G(\mathbf{r},\mathbf{r}') = \frac{e^{-jk|\mathbf{r}-\mathbf{r}'|}}{4\pi|\mathbf{r}-\mathbf{r}'|}.$$

Here $G(\mathbf{r},\mathbf{r}')$ refers to the Green's function in free space and $\{I_n\}$ is the column vector containing the unknown coefficients of the surface current expansion with RWG basis functions $\mathbf{f}_m$. Also, as usual, $\mathbf{r}$ and $\mathbf{r}'$ denote the observation and source point locations. $\mathbf{E}^i(\mathbf{r})$ is the incident excitation plane wave, and η and k denote the free space impendence and wave number, respectively. Once the matrix in equation (1) is solved by numerical matrix equation solvers, the expansion coefficients $\{I_n\}$ can be used to calculate the scattered field and RCS. In the following, we use $\mathbf{Z}$ to denote the coefficient matrix in equation (1), $\mathbf{I} = \{I_n\}$, and $\mathbf{V} = \{V_m\}$ for simplicity. Then, the EFIE matrix in equation (1) can be symbolically rewritten as,

$$\mathbf{ZI} = \mathbf{V}. \tag{2}$$

The basic idea of the fast multipole method (FMM) is to convert the interaction of element-to-element to the interaction of group-to-group. Here a group includes the elements residing in a spatial box. The mathematical foundation of the FMM is the addition theorem for the scalar Green's

function in free space. Using the FMM, the matrix-vector product **ZI** can be written as,

$$\mathbf{ZI} = \mathbf{Z}_N\mathbf{I} + \mathbf{Z}_F\mathbf{I} \tag{3}$$

where $\mathbf{Z}_N$ is the near part of $\mathbf{Z}$ and $\mathbf{Z}_F$ is the far part of $\mathbf{Z}$.

In the FMM, the operation complexity to perform **ZI** is $O(N^{1.5})$. If the FMM is implemented in multilevel, the total cost can be reduced further to $O(NlogN)$ [2]. The calculation of elements in the matrix $\mathbf{Z}_N$ remains the same as in the method of moments (MoM) procedure. However, those elements in $\mathbf{Z}_F$ matrix can not be explicitly computed and stored. Hence, it is impossible to use the matrix $\mathbf{Z}_F$ directly.

III. SHIFTED SSOR PRECONDITIONER WITH LOW-RANK DECOMPOSITION STRATEGY

In the traditional SSOR preconditioning scheme, the preconditioner is chosen as follows,

$$\mathbf{M}_{SSOR} = (\tilde{\mathbf{D}} + \mathbf{L})(\tilde{\mathbf{D}})^{-1}(\tilde{\mathbf{D}} + \mathbf{U}) \tag{4}$$

where $\mathbf{Z}_N = \mathbf{L}+\mathbf{D}+\mathbf{U}$ in equation (3), **L** is the lower triangular matrix, **D** is the positive diagonal matrix, **U** is the upper triangular matrix, and $\tilde{\mathbf{D}} = (1/\omega)\mathbf{D}$, $0 < \omega < 2$ (ω is the relaxation parameter).

Although the SSOR preconditioner performs well in the case of Hermitian positive definite matrices, the performance is often poor when the matrices are indefinite or non-Hermitian, as in the case of the EFIE. The matrix of MFIE has good condition number mainly due to the existence of the principal value term [25]. Accordingly, combining the EFIE and MFIE leads to the well-conditioned combined field integral equations (CFIE). Inspired by CFIE, the principal value term of MFIE is used in order to improve the condition of EFIE matrix. More specifically, we use [14],

$$\mathbf{Z}_\tau = \mathbf{Z}_N + \alpha\mathbf{Z}_{MFIE} \tag{5}$$

to construct the S-SSOR preconditioner $\mathbf{M}_{S\text{-}SSOR}$. The impedance matrix $\mathbf{Z}_{MFIE}$ is the discretized tridiagonal matrix from the principal value term of MFIE operator and α stands for a nonnegative real parameter. It is known that $\mathbf{Z}_{MFIE}$ is a well-conditioned and very sparse real symmetric matrix. As a result, it requires a small amount of computation and storage.

In order to save memory consumption for construction of S-SSOR preconditioner, an ACA based method is proposed and the methodology is discussed in this section. The ACA decomposition is used to the near-field sub-matrices (exclude the self-interaction sub-matrices) [15]. Although the efficiency of ACA filled the near-field sub-matrices is not better than that of the ACA filled the far-field sub-matrices, it is still a little more efficient than that of direct fill.

In the FMM, the near-part matrix $\mathbf{Z}_N$ can be rewritten as,

$$\mathbf{Z}_N = \mathbf{Z}_{NS} + \mathbf{Z}_{NI} \tag{6}$$

where $\mathbf{Z}_{NS}$ is near-field self-interaction matrix and $\mathbf{Z}_{NI}$ is near-field interaction matrix. According to the theory of FMM, the near impedance can not be decomposed. However, if the diagonal part is removed from the near impedance matrix, it can be decomposed by low-rank decomposition method. As $\mathbf{Z}_{NI}$ denotes the near impedance matrix excluding the diagonal part, the matrix $\mathbf{Z}_{NI}$ could be divided into many sub-matrices by a tree data structure in MLFMA. Obviously, each none-zero sub-matrix of $\mathbf{Z}_{NI}$ denotes the near action. Accordingly, the adaptive cross approximation approach is used and the sub-matrix of $\mathbf{Z}_{NI}$ can be approximated by two small sub-matrices $\mathbf{U}_{ACA}$ and $\mathbf{V}_{ACA}$. Denoting the sub-matrix of $\mathbf{Z}_{NI}$ with $\mathbf{Z}'$, we have [21],

$$[\mathbf{Z}']_{QM} \approx [\mathbf{U}_{ACA}]_{Qk} \cdot [\mathbf{V}_{ACA}]^H_{Mk} \tag{7}$$

where M and Q are the dimensions of matrix $\mathbf{Z}'$. The symbol k is the rank of the matrix $\mathbf{Z}'$, which is much smaller than M and Q. According to equation (7), the memory requirement of the matrices $\mathbf{U}_{ACA}$ and $\mathbf{V}_{ACA}$ is much less than that of the direct filling of $\mathbf{Z}'$. The procedure of the ACA algorithm is present as follows [22]:

First, let $\mathbf{U}_{ACA}$ = NULL in order to save the selected columns and $\mathbf{V}_{ACA}$ = NULL in order to save the selected rows.

Step1: Choose the first column $\mathbf{u}_1$ randomly and let $\mathbf{U}_{ACA} = \mathbf{U}_{ACA} \cup \{\mathbf{u}_1\}$. Find the maximum value u_{1k} in $\mathbf{u}_1$. Then choose the first row $\mathbf{v}_1$, which is located at the kth row in the matrix. Let $\mathbf{V}_{ACA} = \mathbf{V}_{ACA} \cup \{\mathbf{v}_1\}$.

Step 2: Find the maximum value v_{ik} in $\mathbf{v}_i$. Then choose the $(i + 1)$th column $\mathbf{u}_{i+1}$, which is located at the kth column in the matrix.

Step 3: Let $\mathbf{U}_{ACA} = \mathbf{U}_{ACA} \cup \{\mathbf{u}_{i+1}\}$.

Step 4: Find the maximum value $\mathbf{u}_{i+1,k}$ in $\mathbf{u}_{i+1}$. Then choose the $(i + 1)$th row $\mathbf{v}_{i+1}$, which is located at the kth row in the matrix.

Step 5: $\mathbf{v}_{i+1} = \mathbf{v}_{i+1} - \sum_{j=1}^{i} u_{j,i}\mathbf{v}_j$, and let $\mathbf{V}_{ACA} = \mathbf{V}_{ACA} \cup \{\mathbf{v}_{i+1}\}$.

Step 6: If $\frac{\|\mathbf{u}_{i+1}\|\|\mathbf{v}_{i+1}\|}{\|\mathbf{u}_1\|\|\mathbf{v}_1\|} < \varepsilon$, the algorithm will stop, otherwise, go to Step 2. The low-rank decomposition form of near-field interaction matrix is $\mathbf{Z}_{NI} \approx \mathbf{U}_{ACA} \cdot \mathbf{V}_{ACA}^{H}$.

This algorithm produces a sequence of decompositions of a matrix into a sum of low-rank matrix and error matrix. Neither the original matrix nor the error matrix will be computed completely. The decision of the tolerance error ε needs a trade-off between accuracy and effectiveness. If the tolerance error is set too high, the solution results will lead to less accurate or even wrong. In contrast, a too-low tolerance error will degrade the compression effect. By classic ACA reference [23], as well as our numerical experiments, $\varepsilon = 10^{-3}$ is appropriate for most cases. Furthermore, single precision is used in the remaining part of this paper.

When ACA technique is used, the near impedance matrix can be compressed to save the memory. Moreover, the computation time to fill the near impedance will be saved. However, the diagonal part of the near impedance can not be compressed due to its full rank. This part should be computed by conventional MoM procedure. Since the ACA technique is only for compression, the SSOR accelerated iterative solver will not be affected by ACA. Accordingly, the SSOR and ACA can be integrated to improve the efficiency.

IV. NUMERICAL EXAMPLES

In this section, numerical results based on on-site experiments will demonstrate the accuracy and efficiency of the proposed method for fast calculation of monostatic RCS. In our experiments, the restarted version of GMRES algorithm [12] is used as the iterative solver, and the dimension of Krylov subspace is set to be 30 in this paper. All experiments are performed on a Core(TM)II E8400 with 3 GHz CPU and 3.24 GB RAM in single precision. Additional details and comments on the implementation are given below:

- zero vector is taken as initial approximate solution for all examples,
- the iteration process is terminated when the normalized backward error is reduced by 10^{-3} for all examples,
- the dimension of Krylov subspace is taken to be 30,
- 1.0 is taken as the relaxation parameter (ω) for building both SSOR and S-SSOR preconditioner mentioned in this paper,
- 3.0 is taken as the shift parameter for building S-SSOR preconditioner.

Although CFIE shows higher efficiency for objects with closed structure than EFIE, it fails for geometries with open structure [26]. As a result, proposed technique in this paper is a suitable choice to alleviate this difficulty due to its fast iteration capability and less memory requirement. The performance of the proposed method is investigated on three examples with open structure for monostatic RCS calculation. As shown in Fig. 1, we consider a cube-plate perfect electrical conductor (PEC) scatterer consisting of a plate of size (1 m × 0.5 m) placed on a 1 m × 1 m × 1 m cube with 4867 unknowns at 400 MHz. The second example, as shown in Fig. 2, is a 1 m × 1 m × 1 m open cavity with 8101 unknowns at 500 MHz and the final structure in Fig. 3, is a disk (radius is 2 m) with 4280 unknowns at 300 MHz.

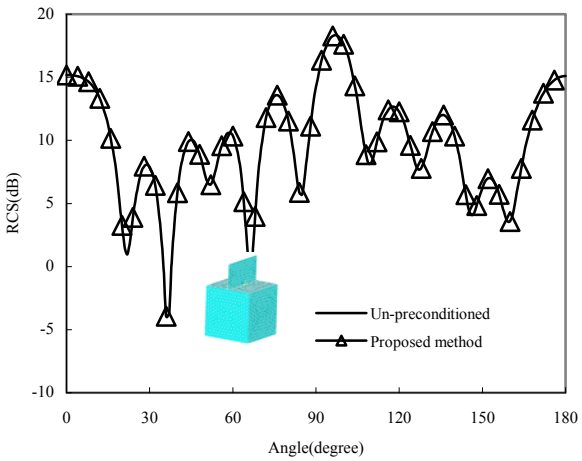

Fig. 1. The monostatic RCS for a cube-plate scatterer using the proposed method.

The sets of angles of interest for the monostatic RCS vary from 0 to 180 degree for the first two examples and 0 to 89 degree for the last

instance in pitch direction when azimuth angle is fixed at 0 degree. The RCS curve computed with repeated solution at each angle are taken as reference values. The accuracy of the compressed S-SSOR preconditioner can be seen from its agreement with the reference values.

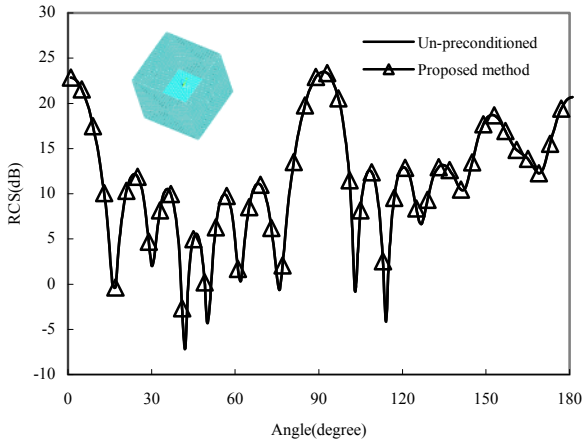

Fig. 2. The monostatic RCS for an open cavity using the proposed method.

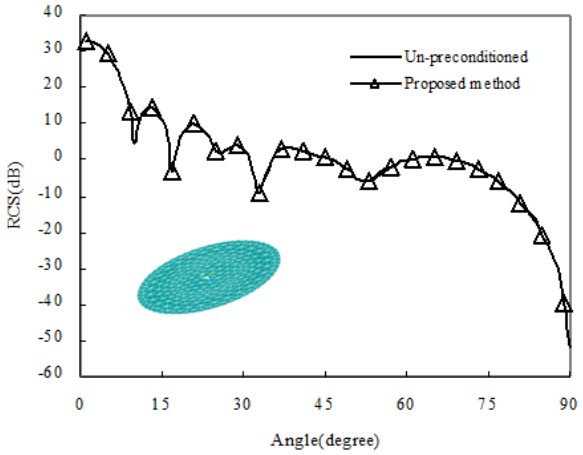

Fig. 3. The monostatic RCS for a disk using the proposed method.

Figures 4, 5, and 6 show number of iteration in each pitch angle of GMRES with unpreconditioned GMRES method, SSOR preconditioner and the proposed preconditioner for three geometries, respectively. It can be observed that the novel operator has the highest convergence rate for each example. Table 1 lists the computation time for all angles to cover the entire monostatic RCS curve on these three examples. Similar improvements can also be found in comparison with the conventional SSOR methods in terms of computational time. Compared with the unpreconditioned GMRES algorithm, the compressed S-SSOR technique decreases the computational time by a factor of 3.11 on the cube-plate scatterer example, 2.78 on the open cavity example, and 3.26 on the disk example, respectively.

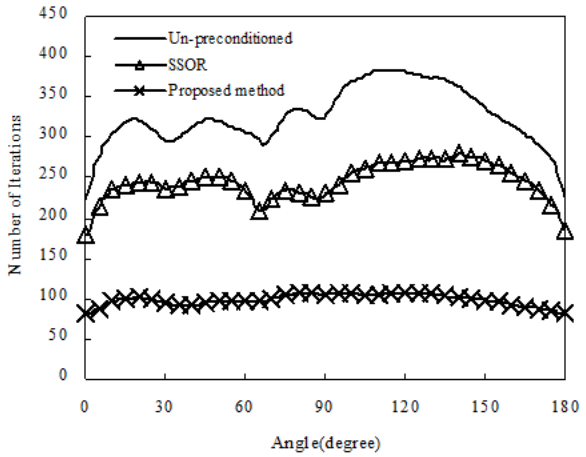

Fig. 4. Iterative number for a cube-plate scatterer with unpreconditioned GMRES method, SSOR preconditioner, and the proposed method.

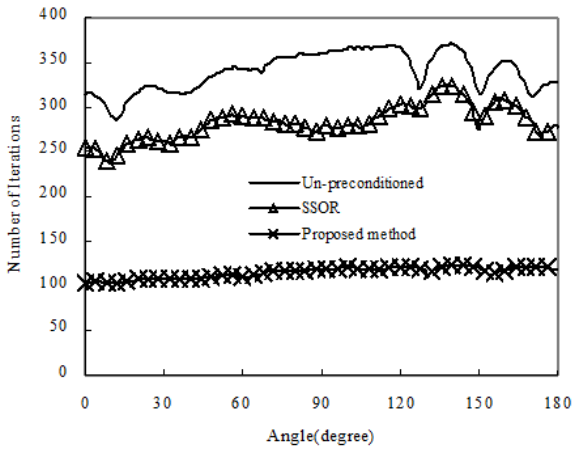

Fig. 5. Iterative number for an open cavity with unpreconditioned GMRES method, SSOR preconditioner, and the proposed method.

Table 2 demonstrates the compression effect of near-field interaction memory of the three examples. The proposed method could effectively reduce the near-field interaction memory consumption by a factor of 2.09 on the cube-plate scatterer example, 2.05 on the open cavity example, and 2.95 on the disk example,

respectively. The time for compressed operation is also listed in Table 2. It is obvious that compression time is much smaller than solution time. Summarizing the discussions we can see that, our proposed technique outperforms the conventional techniques in terms of the efficiency and memory consumption.

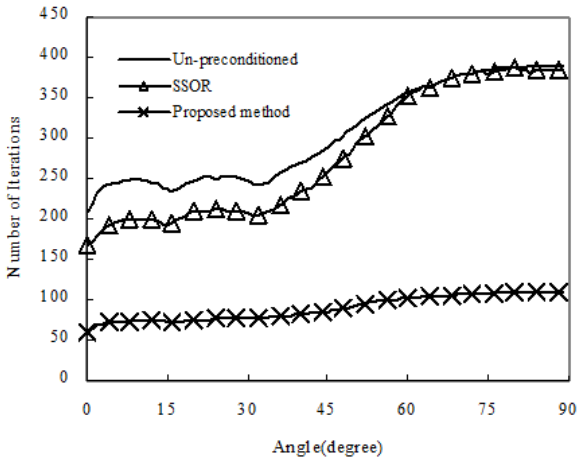

Fig. 6. Iterative number for a disk with unpreconditioned GMRES method, SSOR preconditioner, and the proposed method.

Table 1: Comparison of solution time (in seconds) with unpreconditioned GMRES method, SSOR preconditioner, and the proposed method on three different examples.

	Solution time (s)		
Geometry	**No**	**SSOR**	**S-SSOR**
Cube-plate	7972.92	6383.61	2566.77
Open cavity	12590.05	11123.44	4533.09
Disk	4952.08	4700.38	1516.77

Table 2: Compression effect of near-field interaction memory on three different examples.

Object	**Compression time(s)**	**Near-field interaction memory before compression (MB)**	**Near-field interaction memory after compression (MB)**
Cube-plate	55.13	57.41	27.45
Open cavity	77.30	78.70	38.38
Disk	37.94	55.11	18.69

The SSOR technique can accelerate the convergence of the iterative solver while the GMRES method is used in this paper. Besides, the ACA technique can save memory consumption by the near impedance matrix. Numerical results show that the ACA technique will not affect the accuracy and efficiency of the SSOR preconditioner. An "ACA-only" technique will cost large computation time for iterative solution without using the SSOR preconditioner.

V. CONCLUSION

In this paper, a new compression scheme is developed and used to construct the robust shifted SSOR preconditioners for efficiently solving the electromagnetic scattering problems existed in the non-Hermitian linear systems derived from EFIE formulation. The new method can significantly reduce both calculation time and memory consumption without compromising the accuracy of the final result. Several numerical experiments for validation are performed. Compared to the traditional SSOR preconditioner, the novel compressed shifted SSOR preconditioner is more efficient and robust.

ACKNOWLEDGMENT

The authors would like to thank the assistance and support of the National Natural Science Foundation of China (No: 61301025), Jiangsu Provincial Natural Science Foundation of China (No: BK20130853), China Postdoctoral Science Foundation (No: 2013M541035), Youth Science Foundation of Jiangxi Provincial Department of Science and Technology (No: 20122BAB211018), and Youth Science Foundation of Jiangxi Provincial Department of Education (No: GJJ13321).

REFERENCES

[1] S. Rao, D. Wilton, and A. Glisson, "Electromagnetic scattering by surfaces of arbitrary shape," *IEEE Transactions on Antennas and Propagation*, vol. 30, no. 3, pp. 409-418, 1982.

[2] W. Chew, J. Jin, E. Midielssen, and J. Song, *Fast and Efficient Algorithms in Computational Electromagnetics*. Boston, MA: Artech House, 2001.

[3] J. Song, C. Lu, and W. Chew, "Multilevel fast multipole algorithm for electromagnetic scattering by large complex objects," *IEEE Transactions on*

Antennas and Propagation, vol. 45, no. 10, pp. 1488-1493, 1997.

[4] Z. Fan, M. Chen, R. Chen, and D. Ding, "An efficient parallel FE-BI algorithm for large-scale scattering problems," *ACES Journal*, vol. 26, no. 10, pp. 831-840, Oct. 2011.

[5] X. Hu, R. Chen, D. Ding, Z. Fan, and Y. Xu, "Two-step preconditioner of multilevel simple sparse method for electromagnetic scattering problems," *ACES Journal*, vol. 27, no. 1, pp. 14-21, Jan. 2012.

[6] Z. Liu, J. Chen, and R. Chen, "An adaptive preconditioning technique using Fuzzy controller for efficient solution of electric field integral equations," *ACES Journal*, vol. 26, no. 6, pp. 512-518, June 2011.

[7] M. Chen, R. Chen, Z. Fan, and D. Ding, "Accelerating the multilevel fast multipole method with parallel preconditioner for large-scale scattering problems," *ACES Journal*, vol. 26, no. 10, pp. 815-822, Oct. 2011.

[8] K. Sertel and J. Volakis, "Incomplete LU preconditioner for FMM implementation," *Microwave and Optical Technology Letters*, vol. 26, no. 7, pp. 265-267, 2000.

[9] E. Chow and Y. Saad, "Experimental study of ILU preconditioners for indefinite matrices," *J. of Comput. Appl. Math*, vol. 86, pp. 387-414, 1997.

[10] J. Lee, J. Zhang, and C.-C. Lu, "Sparse inverse preconditioning of multilevel fast multipole algorithm for hybrid integral equations in electromagnetics," *IEEE Transactions on Antennas and Propagation*, vol. 52, no. 9, pp. 2277-2287, Sep. 2004.

[11] B. Carpentieri, "An adaptive approximate inverse-based preconditioner combined with the fast multipole method for solving dense linear systems in electromagnetic scattering," *ACES Journal*, vol. 24, no. 5, pp. 504-510, Oct. 2009.

[12] Y. Saad, *Iterative Methods for Sparse Linear Systems*, PWS Publishing Company, 1996.

[13] R. Chen, K. Edward, N. Yung, C. Chan, and D. Fang, "Application of SSOR preconditioned conjugate gradient algorithm to edge-FEM for 3-dimensional full wave Electromagnetic boundary value problems," *IEEE Transactions on Microwave Theory and Techniques*, vol. 50, no. 4, pp. 1165 -1172, April 2002.

[14] J. Chen, Z. Liu, K. Xu, D. Ding, Z. Fan, and R. Chen, "Shifted SSOR preconditioning technique for electromagnetic wave scattering problems," *Microwave and Optical Technology Letters*, vol. 51, no. 4, pp. 1035-1039, April 2009.

[15] A. Heldring, J. Rius, J. Tamayo, J. Parron, and E. Ubeda, "Multiscale compressed block decomposition for fast direct solution of method of moments linear system," *IEEE Trans. Antennas Propag.*, vol. 59, no. 2, pp. 526-536, Feb. 2011.

[16] A. Heldring, J. Rius, J. Tamayo, J. Parron, and E. Ubeda, "Fast direct solution of method of moments linear system," *IEEE Trans. Antennas Propag.*, vol. 55, no. 11, pp. 3220-3228, Nov. 2007.

[17] A. Heldring, J. Rius, J. Tamayo, and J. Parron, "Compressed block-decomposition algorithm for fast capacitance extraction," *IEEE Transactions on Computer-Aided Design of Integrated Circuits and Systems*, vol. 27, no. 2, pp. 265-271, Feb. 2008.

[18] A. Heldring, J. Rius, J. Tamayo, and J. Parron, "Multilevel MDA-CBI for fast direct solution of large scattering and radiation problems," *Antennas and Propagation Society International Symposium*, 2007.

[19] A. Heldring, J. Tamayo, J. Rius, J. Parron, and E. Ubeda, "Multiscale CBD for fast direct solution of MoM linear system," *Antennas and Propagation Society International Symposium*, 2008.

[20] Z. Jiang, Z. Fan, D. Ding, R. Chen, and K. Leung, "Preconditioned MDA-SVD-MLFMA for analysis of multi-scale problems," *ACES Journal*, vol. 25, no. 11, pp. 914-925, 2010.

[21] M. Bebendorf, "Approximation of boundary element matrices," *Numer. Math.*, vol. 86, no. 4, pp. 565-589, June 2000.

[22] S. Kurz, O. Rain, and S. Rjasanow, "The adaptive cross-approximation technique for the 3-D boundary element method," *IEEE Trans. Magn.*, vol. 38, no. 2, pp. 421-424, March 2002.

[23] K. Zhao, M. Vouvakis, and J. Lee, "The adaptive cross approximation algorithm for accelerated method of moments computations of EMC problems," *IEEE Trans. Electromagnetic Compatibility*, vol. 47, no. 4, pp. 763-773, Nov. 2005.

[24] Z. Liu, R. Chen, J. Chen, and Z. Fan, "Using adaptive cross approximation for efficient calculation of monostatic scattering with multiple incident angles," *ACES Journal*, vol. 26, no. 4, pp. 325-333, April 2011.

[25] J. Hu and Z. Nie, "Improved electric field integral equation (IEFIE) for analysis of scattering from 3-D conducting structures," *IEEE Transactions on Electromagnetic Compatibility*, vol. 49, no. 3, pp. 644-648, August 2007.

[26] P. Rui, R. Chen, Z. Fan, J. Hu, and Z. Nie, "Perturbed incomplete ILU preconditioner for efficient solution of electric field integral equations," *IET Microwave Antennas Propagation*, vol. 5, no. 1, pp. 1059-1063, 2007.

Jiaqi Chen was born in Gansu, China. He received the B.S. and Ph.D. degrees in communication engineering from Nanjing University of Science and Technology (NUST), Nanjing, China, in 2005 and 2011, respectively. He was with the Center for Sensorsystems (ZESS), University of Siegen, Siegen, Germany, as a visiting scholar in 2009. He is currently working at College of Computer and Information Engineering, Hohai University. His research interests include computational electromagnetics, SAR imaging and precipitation radar.

Zhiwei Liu was born in Jiangxi Province, P. R. China in 1982. He received B.S. degree in computer science from Nanjing University of Science & Technology in 2003, M.S. degree in Nanjing Institute of Electronics & Technology in 2006, and Ph.D. degree in Nanjing University of Science & Technology in 2011, respectively. He was with the Department of Electrical Engineering, Iowa State University, as a visiting scholar in 2009. He is currently working at Department of Information Engineering, East China Jiaotong University. His research interests focus on theory of electromagnetic scattering and inverse scattering.

Zhaoneng Jiang was born in Jiangsu Province, the People's Republic of China. He received the B.S. degree in physics from Huaiyin normal college in 2007, and is currently working toward the Ph.D. degree at Nanjing University of Science and Technology (NUST), Nanjing, China. His current research interests include computational electromagnetics, antennas and electromagnetic scattering and propagation, electromagnetic modeling of microwave integrated circuits.

Bin Yong was born in Anhui, China. He received the B.S. degrees in Computer Science and Technology, Hefei University of technology, Hefei, China and the Ph.D. degree in Cartography and Geography Information System, Nanjing University, Nanjing, China. He is currently a Professor with State Key Laboratory of Hydrology-Water Resources and Hydraulic Engineering, Hohai University, Nanjing, China. His research areas mainly includes: 1) Remote Sensing Precipitation (radar, satellite, multi-sensor, multi-platform); 2) Application of NASA multi-satellite products; and 3) Surface Water and Hydrological System Analysis. Dr. Yong is currently the American Geophysical Union member.

An Efficient Hybrid Model in Analyzing Nonlinearly Loaded Dipole Antenna above Lossy Ground in the Frequency Domain

S. R. Ostadzadeh

Department of Engineering
University of Arak, Arak, Iran
s-ostadzadeh@araku.ac.ir

Abstract ─ In this paper, a hybrid model is proposed for including lossy ground effect on scattering response from nonlinearly loaded dipole antenna. In this model, at first the input admittance and induced current at dipole antenna situated over lossy ground are efficiently modeled based on the fuzzy inference concepts. Volterra series model is then applied to compute the induced voltage across nonlinear load at different frequency harmonics. Numerical examples show not only the accuracy of the proposed hybrid model but also a high computational efficiency in comparison with previous hybrid models.

Index Terms ─ Dipole antenna, fuzzy inference, lossy ground, and nonlinear load.

I. INTRODUCTION

Nonlinear loads are connected to antennas terminal so as to protect devices against strong-strength exciting waves. A typical nonlinearly loaded antenna vertically suited above ground plane as well as its microwave equivalent circuit is shown in Fig. 1. In Fig. 1 (b), Y_{in} is the input admittance of the dipole antenna and I_{sc} is the short circuit current due to incidence of exciting waves. There are several methods for analyzing such structures in frequency domain [1-7] and time domain [8-11]. Time-domain-based analyses lead to accurate results; however, they are both relatively time-demanding, and they cannot be easily used to include the effect of lossy ground. Analysis in frequency domain on the other hand is based on solving microwave circuit in Fig. 1 (b), so that the numerical method of moments [12], MoM, for computing Y_{in} and I_{sc}, and methods of analyzing nonlinear microwave circuits [13] for computing induced voltage across nonlinear load are combined. It is well known that these hybrid models, suffer from repetitive and time consuming computations due to changing parameters of exciting waves and lossy ground.

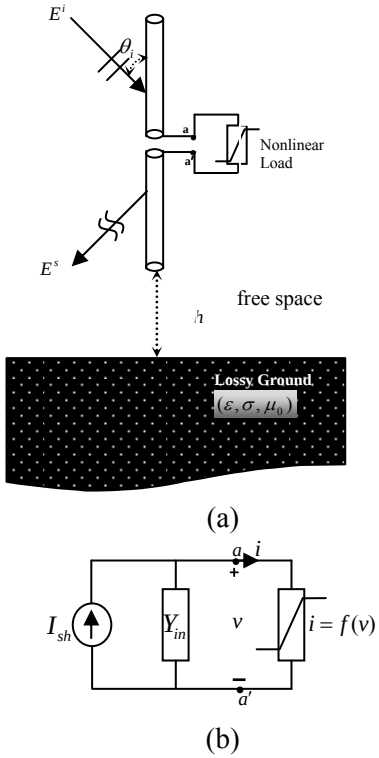

Fig. 1. (a) Schematic diagram of nonlinearly loaded dipole antenna over lossy ground and (b) microwave equivalent circuit.

Up to the author's knowledge, there is no comprehensive closed form solution for including lossy ground effect on wire antennas except in [14], restricted to $h > 0.25\lambda_0 / \sqrt{|\varepsilon_r|}$ where ε_r is

Submitted On: Sept. 18, 2012
Accepted On: Aug. 26, 2013

relative complex dielectric constant of ground and in [15], which is valid for $\varepsilon_r > 10$.

In order to overcome these mentioned drawbacks and restrictions, the novel model based on fuzzy inference introduced by Tayarani et al. [16] can be taken into considerations. In the previous study [17], the behavior of the dipole antenna in free space was considered as simple membership functions as shown in Fig. 2, and using that Y_{in} and I_{sc} were well predicted in free space. However, analysis of this problem in the presence of lossy ground was not addressed.

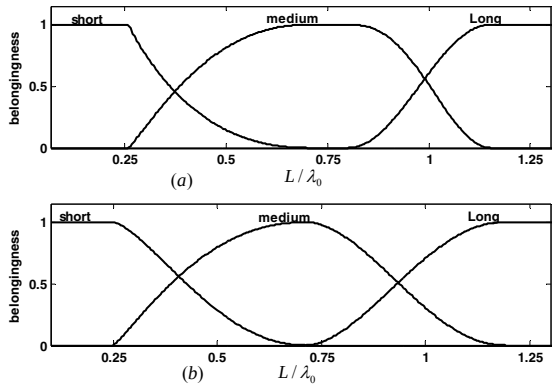

Fig. 2. The membership functions representing the behavior of the dipole antenna in free space, for (a) modeling circular movement and (b) modeling partial phase.

In this paper, at first using approximating the behavior of the dipole antenna in the presence of lossy ground with the one in free space, the effect of lossy ground on Y_{in} and I_{sc} are then easily extracted as very simple curves, and hence complete models of Y_{in} and I_{sc} in the presence of lossy ground are achieved. Volterra series model [6] is finally applied to Fig. 1 (b), so that the induced voltage at different frequency harmonies is computed.

In section II, formulation of the intelligent method [16] is briefly explained. Modeling Y_{in} and I_{sc} based on this model is given in section III. Substituting these methods in microwave equivalent circuit of Fig. 1 (b) and solving it by Volterra series is in section IV. Finally, conclusion is given in section V.

II. FORMULATION OF FUZZY MODEL

Instruction of the fuzzy-based model according to [16], for a problem is briefly explained as below:

1. Plot amplitude versus phase of output in polar plane to observe circular movement, and then find basic circles making this movement.
2. Choose three-point sets as starting points on each basic circle and then fit a circle and line on each three-point set as fuzzy inputs.
3. Define membership function for each fitted circle. These functions have belongingness one on each fitted circle and smoothly decreasing to zero on the neighbor fitted circles by the following equation,

$$\alpha(v)=\begin{cases}\frac{1}{2}(1+\cos\pi(\frac{v-a_1}{a_2-a_1})^{\beta_1}) & v:a_1\to a_2\\ \frac{1}{2}(1-\cos\pi(\frac{v-a_1}{a_2-a_1})^{\beta_2}) & v:a_1\to a_2\end{cases} \quad (1)$$

where β_1 and β_2 represents optimizations parameters and v is input value. Also a_1 and a_2 are points where fitted circles are completely fitted on the circular movement.

4. Infer a circle for each input value using the following inference equation,

$$\begin{cases}x(v)=\sum_{i=1}^{n}x_i\alpha_i(v)\\ y(v)=\sum_{i=1}^{n}y_i\alpha_i(v)\\ r(v)=\sum_{i=1}^{n}r_i\alpha_i(v)\end{cases} \quad (2)$$

in which $x_i, y_i, r_i \quad i=1,2,...n$ are center coordinates and radius of the fitted circles, respectively and x, y, and r as fuzzy outputs are center coordinates and radius of inferred circles for each input value. Also α_i is a membership function obtained in the previous step.

5. Fit lines on the three-point sets and infer a line for each input value to model partial phase (as defined in [16]) the same as circular movement.
6. Compute center coordinates and radius of the fitted circles for a few values of parameter, and then fit simple curves on

them to estimate the characteristics of fitted circles and lines for new values of parameter. These simple curves denote the effect of this parameter lonely on output.

7. Repeat the above steps for the other parameters.

III. MODEL OF DIPOLE ANTENNA BASED ON QUALITATIVE CONCEPTS

A. Modeling input admittance

Consider a dipole antenna of length 20 cm vertically situated above a lossy ground. The ground effect is characterized by three parameters, i.e., relative dielectric constant ε_r, conductivity σ and vertical spacing h.

To extract the effect of the ground dielectric constant lonely, it is assumed the other ground parameters is constant (σ = 0 and h = 0.01 m). Hence, the amplitude versus phase of the input admittance in the frequency interval of 0.1 GHz – 2.3 GHz is shown in Fig. 3.

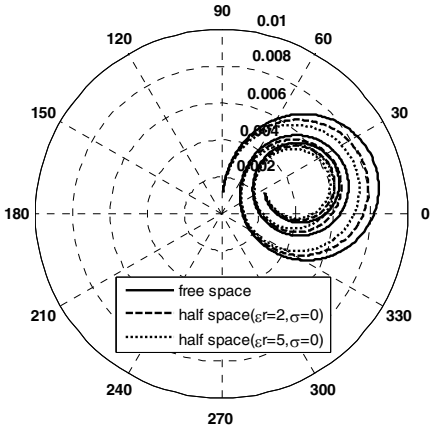

Fig. 3. The amplitude versus phase of input admittance (S) of dipole over ground for different values of ε_r.

As it is seen in Fig. 3, circular movements including three basic circles for different values of ε_r are observed. It seems that the only difference among them is center coordinates and radius of basic circles.

Therefore, at the beginning of modeling, the behaviour of the problem over lossless ground is approximated with the one in free space (Fig. 2), and then center coordinates (x_i, y_i) and radius (r_i) of fitted circles for a few values of ε_r are computed by MoM and simple curves are finally fitted on them as shown in Fig. 4.

Mean while in order to show the effect of the ground with respect to free space, they are normalized to individual ones in free space denoted by (X_n, Y_n) and R_n.

Now using these simple curves as fuzzy inputs and the problem behaviour (Fig. 2), the input admittance (actual output) for each new value of relative dielectric constant is predicted. Figure 5 shows the input admittance for ε_r = 2.5.

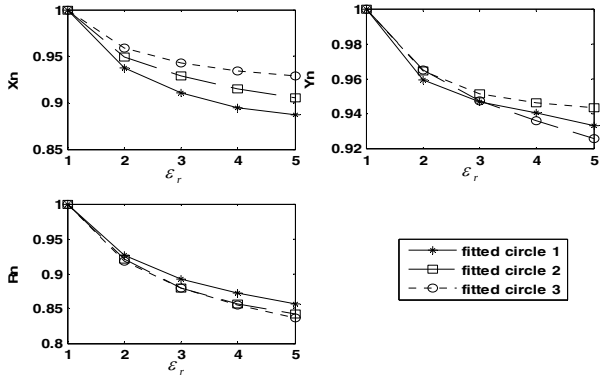

Fig. 4. The effect of the dielectric constant of ground on the input admittance using simple curves.

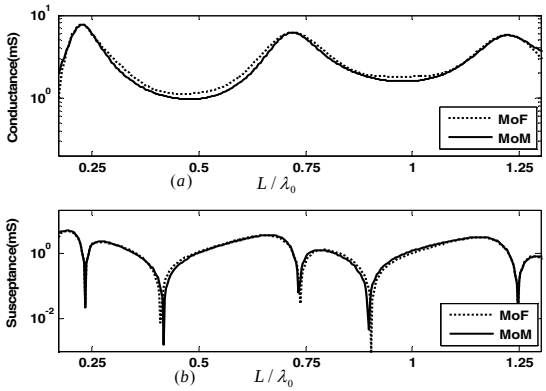

Fig. 5. The input admittance (mS) of dipole antenna suited 0.01 m away from lossless ground (ε_r = 2.5, σ = 0), for (a) conductance (mS) and (b) susceptance (mS).

As it is seen, comparing the results of method of fuzzy (MoF) with accurate ones (MoM) shows excellent agreement while the run-time is considerably reduced. To include the conductivity effect of the ground on the input

admittance lonely, it is assumed that ε_r = 1, h = 0.01 m, and the amplitude versus phase of the input admittance for a few values of conductivity is plotted in Fig. 6. Extracting the conductivity effect on input admittance is the same as the dielectric constant and shown in Fig. 7. Once more, using the achieved simple curves as fuzzy inputs and the behavior of the problem, the input admittance of dipole over lossy ground for each new value of conductivity is easily predicted. Meanwhile in Fig. 7, σ_n is normalized conductivity in decibel ($\sigma_n = 10\log(\sigma/0.0001)$).

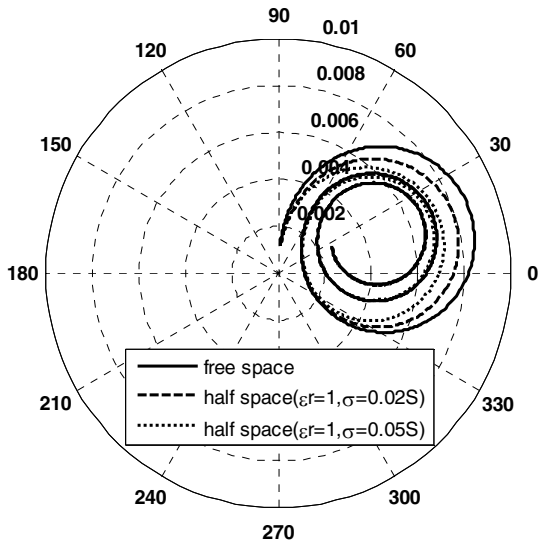

Fig. 6. The amplitude versus phase of the input admittance (S) over ground for different conductivity values.

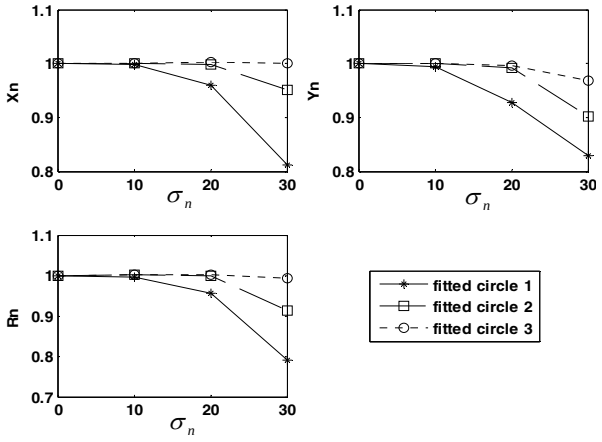

Fig. 7. The effect of conductivity on the input admittance.

In a similar manner, the effect of vertical spacing can be extracted from Fig. 8 under assuming ε_r = 1, σ = 0.0001 (S/m), and h as a varying parameter. According to [18], spatial membership functions can be used to combine the effects of more than two parameters but they cannot be viewed as a figure. Thus, in this paper without loss of generality, the two effects of ε_r and σ are combined as follows,

$$\alpha_i(\varepsilon_r,\sigma_n)=\begin{cases}\dfrac{1}{2}\left(1-\cos\pi\left[\dfrac{\varphi-\varphi_2}{\varphi_1-\varphi_2}\right]^{\beta_1}\right) & for\ \ \varphi:\varphi_1\to\varphi_2\\ \dfrac{1}{2}\left(1+\cos\pi\left[\dfrac{\varphi-\varphi_2}{\varphi_1-\varphi_2}\right]^{\beta_1}\right) & for\ \ \varphi:\varphi_1\to\varphi_2\end{cases} \quad (3)$$

in which

$$\varphi=\tan^{-1}\left(\frac{\varepsilon_r}{\sigma_n}\right), \qquad \beta_1,\beta_2 = optimizing\ \ parameters$$

and $i=\varepsilon_r,\sigma_n$.

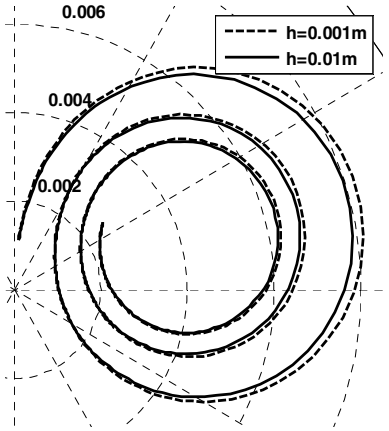

Fig. 8. The amplitude versus phase of the input admittance (S) over ground for different spacings under assuming ε_r = 1 and σ = 0.0001 (S/m).

The spatial membership functions in this case are shown in Fig. 9. In this figure, two fuzzy sets for the two independent parameters (ε_r, σ_n) are seen in which each one has belongingness value of one at its individual axis and it is smoothly decreasing to zero at the other axis.

The following inferred equations can be used to extract the fitted circles versus simultaneous effects of ε_r and σ_n,

$$x_j(\varepsilon_r,\sigma_n)=\frac{x_j(\varepsilon_r)\alpha_{\varepsilon_r}(\varepsilon_r,\sigma_n)+x_j(\sigma_n)\alpha_{\sigma_n}(\varepsilon_r,\sigma_n)}{\alpha_{\varepsilon_r}(\varepsilon_r,\sigma_n)+\alpha_{\sigma_n}(\varepsilon_r,\sigma_n)}$$

$$y_j(\varepsilon_r,\sigma_n)=\frac{y_j(\varepsilon_r)\alpha_{\varepsilon_r}(\varepsilon_r,\sigma_n)+y_j(\sigma_n)\alpha_{\sigma_n}(\varepsilon_r,\sigma_n)}{\alpha_{\varepsilon_r}(\varepsilon_r,\sigma_n)+\alpha_{\sigma_n}(\varepsilon_r,\sigma_n)} \quad (4)$$

$$r_j(\varepsilon_r,\sigma_n)=\frac{r_j(\varepsilon_r)\alpha_{\varepsilon_r}(\varepsilon_r,\sigma_n)+r_j(\sigma_n)\alpha_{\sigma_n}(\varepsilon_r,\sigma_n)}{\alpha_{\varepsilon_r}(\varepsilon_r,\sigma_n)+\alpha_{\sigma_n}(\varepsilon_r,\sigma_n)}$$

where $x_j(i)$, $y_j(i)$, $r_j(i)$, $i = \varepsilon_r, \sigma_n$, j = 1, 2, 3 are center coordinates and radii of fitted circles extracted in Figs. 3 and 5. Also, $\alpha_{\varepsilon r}$ and $\alpha_{\sigma n}$ are spatial membership functions in Fig. 9. Finally, $x_j(\varepsilon_r,\sigma_n), y_j(\varepsilon_r,\sigma_n), r_j(\varepsilon_r,\sigma_n)$ are the inferred coordinates and radii of fitted circles, respectively representing simultaneous effects of the two parameters on the input admittance as shown in Fig. 10.

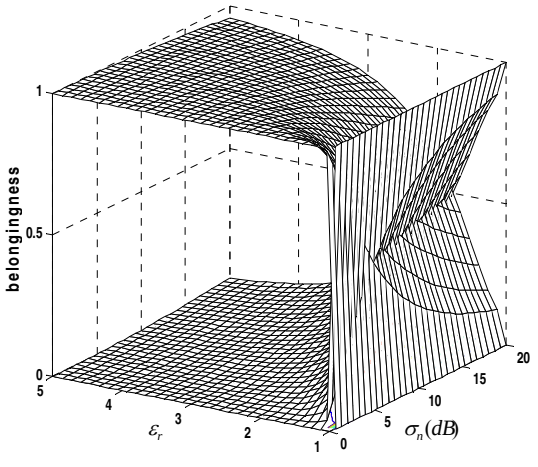

Fig. 9. Spatial membership functions for combining effects of ε_r and σ_n.

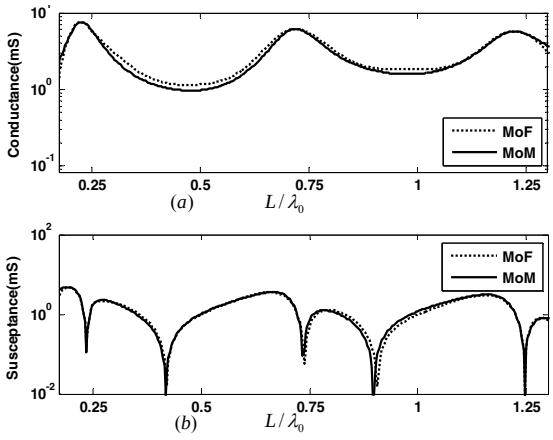

Fig. 10. The input admittance (mS) of dipole antenna suited 0.01 m away from lossy ground (σ = 0.01 S/m, ε_r = 2.5) for (a) conductance and (b) susceptance.

From now on, using these inferred spatial fuzzy inputs and the behavior of dipole antenna in free space (Fig. 2), the input admittance of the dipole antenna over lossy ground for each value of ε_r, σ, and h is efficiently predicted.

B. Modeling induced current

Modeling the induced current is the same as the input admittance, thus the dielectric constant effect is only extracted. Figure 11 shows the amplitude versus phase of the induced current on the dipole antenna over lossless ground illuminated by a plane wave with incident angle $\theta_i = 50^\circ$.

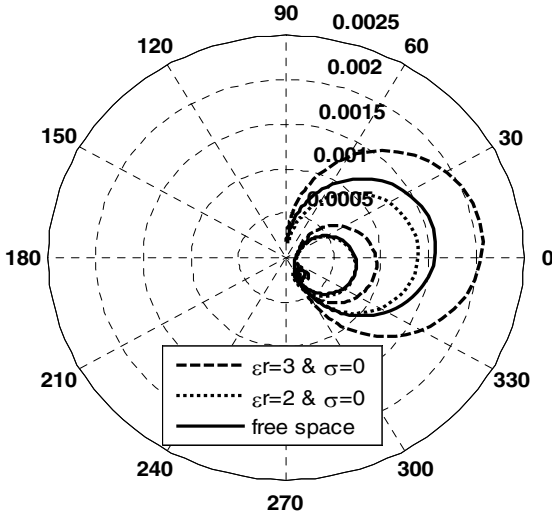

Fig. 11. The amplitude versus phase of induced current (A) for different values of dielectric constant.

In this figure, the circular movements for the induced current are observed. Hence, again approximating the behaviour of the dipole antenna over lossy ground with the one in free space (Fig. 2), the dielectric constant effect on the induced current can be easily extracted as shown in Fig. 12.

The created fuzzy system is run for $\varepsilon_r = 2.5$ and $\varepsilon_r = 10$. The predicted results (MoF) in addition to the accurate ones (MoM) are shown in Figs. 13 and 14, respectively. As it is seen in Fig. 13, good agreement is achieved while run-time is vanishingly short, but Fig. 14 shows considerable error between the two methods around $L/\lambda_0 = 0.45$.

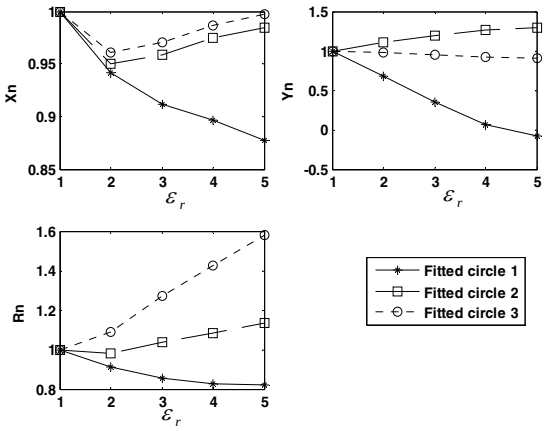

Fig. 12. Extracted relative dielectric constant effect on the induced current.

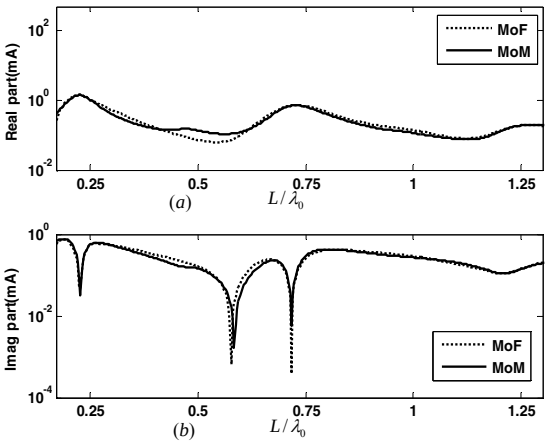

Fig. 13. The induced current computed by MoF and MoM for ε_r = 2.5 for (a) real part (mA) and (b) imaginary part (mA).

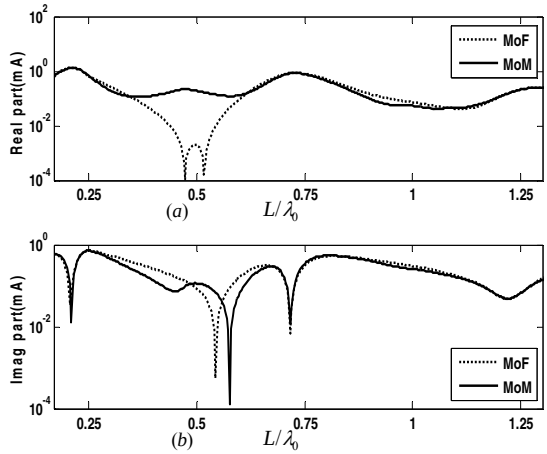

Fig. 14. The induced current computed by MoF and MoM for ε_r = 10 for (a) real part (mA) and (b) imaginary part (mA).

To know what happens around $L/\lambda_0 = 0.45$, look exactly at the Fig. 15 showing the amplitude versus phase of the induced current for $\varepsilon_r = 5$ and $\varepsilon_r = 10$. According to Fig. 15, increasing relative dielectric constant, a new circle between the first and second circles is getting formed. It means that in order to predict exactly the induced current around $L/\lambda_0 = 0.45$, a fitted circle and line around $L/\lambda_0 = 0.45$ should be added (in equations (2) and (3)). Hence, according to step (3), the new membership functions for modeling circular movement and partial phase are considered and shown in Fig. 16. These new membership functions represent the behavior of the problem for high dielectric constants.

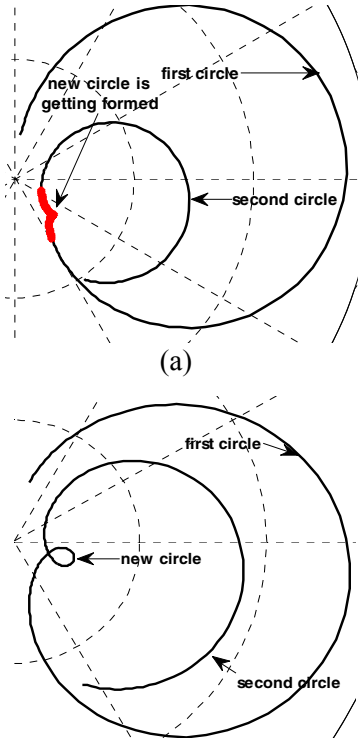

Fig. 15. The amplitude versus phase of the induced current in polar plane for, (a) $\varepsilon_r = 5$ and (b) $\varepsilon_r = 10$ (to distinguish circles better, the third basic circle is not shown).

Comparing Fig. 16 with Fig. 2 shows a new membership function around $L/\lambda_0 = 0.45$

representing presence of a new circle and line in this region. Now, with the use of these new membership functions, and four fitted circles and line as fuzzy inputs, the induced current for $\varepsilon_r = 10$ is well predicted as shown in Fig. 17. Similar to Fig. 12, center coordinates and radius of the new fitted circle for high dielectric constants can be extracted as shown in Fig. 18.

IV. COMPUTING INDUCED VOLTAGE ACROSS NONLINEAR LOAD

Consider a dipole antenna illuminated by a plane wave with amplitude E_i = 1 V/m, incident angle $\theta_i = 50^\circ$ and suited 0.01 m away from a lossy ground ($\varepsilon_r = 10, \sigma_n = 10dB$). This antenna is centrally loaded to a nonlinear conductance with following $(i-v)$ characteristic,

$$i = \frac{1}{75}v + 4v^3 \ . \qquad (5)$$

Now substituting the predicted outputs (MoF), i.e., Y_{in} and I_{sh}, in Fig. 1 (b), and applying Volterra series [6] to it, the induced voltage across nonlinear load at frequency harmonies is computed. Figure 19 shows the induced voltage at different harmonics by two hybrid approaches.

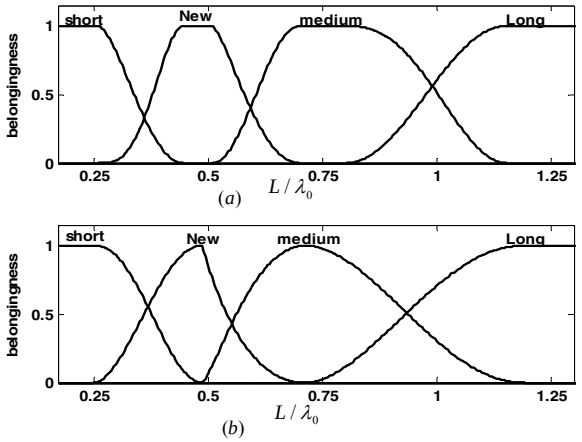

Fig. 16. The membership functions representing the problem behavior for $\varepsilon_r > 5$, for (a) modeling circular movement and (b) modeling partial phase.

Table I compares the run-times of the two hybrid approaches. As it is seen, the run-time by proposed hybrid approach is considerably reduced. Meanwhile, the run-times by the proposed model in Table I is valid after the effect of ground parameters by MoF is extracted.

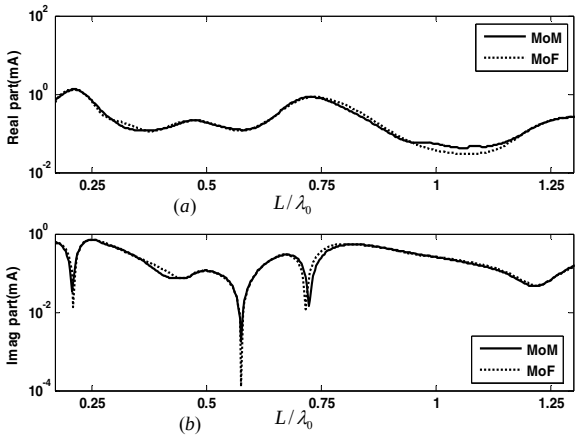

Fig. 17. The predicted induced current (mA) for $\varepsilon_r = 10$ by new membership functions for (a) real part (mA) and (b) imaginary part(mA).

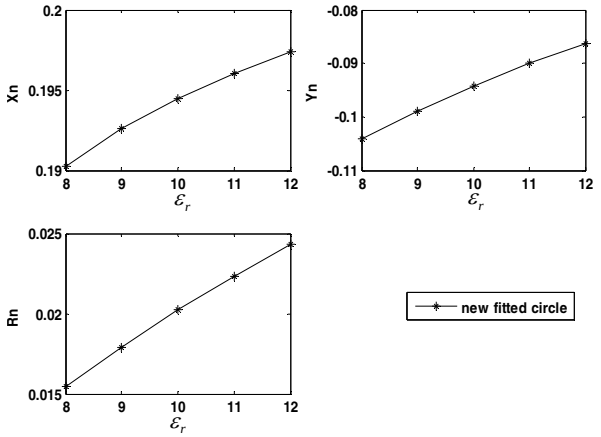

Fig. 18. Center coordinates and radius of the new fitted circle versus ε_r.

Table I. Comparing run-times of the two hybrid approaches for computing the induced voltage at different frequency harmonies.

Method **Structure**	**MoF** **+** **Volterra**	**MoM** **+** **Volterra**
Problem in free space	≈ 0.3 sec	≈ 34 sec
Problem over ground	≈ 0.45 sec	≈ 5.4 min

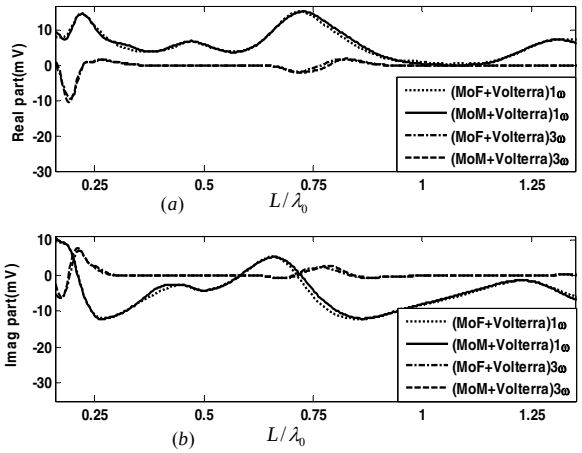

Fig. 19. Computed induced voltage (mV) at different harmonies by the two hybrid approaches for (a) real part (mV) and (b) imaginary part (mV).

V. CONCLUSION

In this paper, a combined MoF-Volterra model was proposed for analysis of nonlinearly loaded dipole antenna above imperfect ground so as to remove complex and repetitive computations. In this method, the input admittance and the induced current of the dipole antenna based upon the fuzzy inference approach was separately predicted and Volterra series was then used to compute the induced voltage at different harmonies. As a result, an efficient hybrid model is achieved. Analyzing nonlinearly loaded dipole array including mutual coupling effects is another study that can be carried out similarly.

REFERENCES

[1] C. Huang and T. Chu, "Analysis of wire scatterers with nonlinear or time-harmonic loads in the frequency domain," *IEEE Trans. Antennas Propagat.*, vol. 41, pp. 25-30, 1993.

[2] K. Lee, "Two efficient algorithms for the analyses of a nonlinearly loaded antenna and antenna array in the frequency domain," *IEEE Trans. Electromag. Compat.*, vol. 45, pp. 339-346, 2000.

[3] K. Lee, "Genetic algorithm based analyses of nonlinearly loaded antenna arrays including mutual coupling," *IEEE Trans. Antennas Propagat.*, vol. 51, pp. 776-781, 2003.

[4] K. Lee, "Mutual coupling mechanisms within arrays of nonlinear antennas," *IEEE Trans. Electromag. Compat.*, vol. 47, pp. 963-970, 2005.

[5] K. Lee, "Application of neural networks and its extension of derivative to scattering from a nonlinearly loaded antenna," *IEEE Trans. Antennas Propagat.*, vol. 55, pp. 1126-1132, 2007.

[6] T. Sarkar and D. Weiner, "Analysis of nonlinearly loaded multiport antenna structures over an imperfect ground plane using the Volterra-series method," *IEEE Trans. Electromag. Compat.*, vol. 20, pp. 278-287, 1978.

[7] K. Sheshyekani, S. Sadeghi, and R. Moini, "A combined MoM-AOM approach for frequency domain analysis of nonlinearly loaded antennas in the presence of a lossy ground," *IEEE Trans. Antennas Propagat.*, vol. 56, pp. 1717-1724, 2008.

[8] H. Schuman, "Time-domain scattering from a nonlinearly loaded wire," *IEEE Trans. Antennas Propag.*, vol. 22, no. 4, pp. 611-613, July 1974.

[9] J. Landt, "Network loading of thin-wire antennas and scatterers in the time domain," *Radio Sci.*, vol. 16, pp. 1241-–1247, Nov. 1981.

[10] M. F. Pantoja, et al, "Transient analysis of thin-wire antennas over Debye media," *Applied Computational Electromagnetic Society (ACES) Journal*, vol. 27, no. 3, March 2012.

[11] H. R. Karami, et al, "Transient response of nonlinearly loaded antennas above a lossy dielectric half-space: A modified AOM approach," *IEEE Trans. Electromag. Compat.*, vol. 20, pp. 1-9, March 2012.

[12] R. Harrington, *Field Computation by Moment Methods*, Macmillan, New York, 1968.

[13] S. Mass, *Nonlinear Microwave Circuits*, Artech House, Norwood, MA, 1988.

[14] T. Sarkar and B. Strait, "Analysis of arbitrarily oriented thin wire antenna arrays over imperfect ground planes," *Syracuse University, Syracuse, NY, Contract F19628-73-C-0047, Tech. Report TR-75-15*, 1975.

[15] P. Barnes and F. Tesche, "On the direct calculation of a transient plane wave reflected from a finitely conducting half-space," *IEEE Transaction on Electromag. Comp.*, vol. 33, pp. 90-96, 1991.

[16] M. Tayarani and Y. Kami, "A qualitative analysis in engineering electromagnetics; an application to general transmission lines," *IEICE Trans. Elect.*, vol. E83-C, pp. 85-97, 2001.

[17] S. Ostadzadeh, M. Tayarani, and M. Soleimani, "A hybrid model in analyzing nonlinearly loaded dipole antenna and finite antenna array in the frequency domain," *International Journal of RF and Microwave*, vol. 19, pp. 512-518, 2009.

[18] S. Shouraki and N. Honda, "Outlines of a soft computer for brain simulation," *5th International Conference on Soft Computing and Information / Intelligent Systems*, pp. 545-550, 1998.

Unconditionally-Stable Meshless Methods Using Different Split-Step Techniques and Their Phase Velocity Considerations

F. Ansarizadeh [1] and M. Movahhedi [2]

[1] Department of Electrical Engineering,
Shahid Bahonar University of Kerman, Kerman, Iran
f.ansarizadeh@eng.uk.ac.ir

[2] Department of Electrical and Computer Engineering,
Yazd University,Yazd, Iran
movahhedi@ieee.org

Abstract ─ In this paper, new unconditionally-stable meshless methods based on different split-step methods are proposed. Moreover, comparison of the phase velocities of two different split-step meshless methods and that of alternative-direction-implicit meshless (ADI-ML) method is presented. Here we show how employing split-step (SS) technique using radial point interpolation meshless (RPIM) method results in an unconditionally stable scheme. Symmetric operators and uniform splitting are utilized simultaneously to split the classical Maxwell's matrix into four and six submatrices. Also, for more accurate approximations Crank-Nicolson (CN) scheme that is a fully implicit scheme has been applied for implementation of these schemes. It has been demonstrated, these proposed methods produce even more effective unconditionally stable responses than those of alternating-direction-implicit meshless time-domain ADI-MLTD methods. Eventually, in order to prove the advantage of the proposed method, a comparison has been made between these novel meshless methods and their finite-difference counterparts. More smoothed phase velocities in proposed meshless methods imply a reduction in dispersion error in comparison with their analogous cases in finite-difference time-domain (FDTD) method.

Index Terms - Meshless methods, phase velocity, radial basis function (RBF), split-step (SS), and unconditionally stable.

I. INTRODUCTION

Over two recent decades special attention has been allocated to solve Maxwell's curl equations in time-domain. The main reason can be attributed to the unique capability of time-domain in solving ultra wide band (UWB) problems in only a single run and also modeling medium, which possesses nonlinear properties or/and consists of different materials and consequently different permittivity coefficients. Unfortunately, if the geometry of the problem domain is too complicated, demanding high resolution, dependency of time step size on the smallest space step leads in a time-consuming simulation process that is undesirable [1].

Meshless methods have newly been proved to be appropriate alternatives to the finite-element (FE) methods, due to their property of avoiding meshing and remeshing, in addition to the capability of effective treatment of complicated geometries [2]. Using meshless methods, it is simply possible to locate more nodes in the regions that have fast variations of fields and this way capture these variations to ameliorate the accuracy. On the other hand, in the regions fields have slow changes fewer nodes can be located that is so economical in aspects of CPU usage time and the memory needed [3]. Amidst the diverse meshless methods, the radial basis function (RBF), which brought forward by Kansa [4] in 1990, is the most prevailing technique in solving partial differential equations (PDEs) due to its accuracy, consistency and ease of implementation [5]. Applying RBF in meshless methods, unknown

Submitted On: Jan. 28, 2013
Accepted On: Sept. 12, 2013

functions of PDEs or integral equations are interpolated at the scattered nodes and point matching method is applied to the equation at the collocation nodes [6].

As mentioned before, choosing small time-step size leads in a time-consuming simulation process that is not desirable. The possibility of choosing larger time-step size helps to reduce the computational and simulation time, that is why searching for unconditionally stable schemes that permit several order larger time step size have been the aim of many studies and researches lately. Using meshless methods to solve time domain electromagnetic problems with large time steps, acquire advantages of both meshless and unconditionally stable methods simultaneously. Recently an unconditionally stable method based on leapfrog alternating-direction-implicit scheme using radial point interpolation meshless (RPIM) method in three-dimensional (3-D) has been presented in [7] that outperforms the LOD-RPIM method in terms of computational effort [8]. In 2011, a new unconditionally stable scheme based on (RPIM) method using the weighted Laguerre polynomials has been introduced in [3]. Through this technique, which is marching-on-in-degree method instead of marching-on-in-time one, the time step is used only to calculate the Laguerre expansion coefficients of sources done only at the start of the computations. Thus, the stability is not affected by the time step size any more.

Here, the split-step scheme, which divides a complete time step into several identical sub steps, for example 6 sub steps (6 SS), has been chosen to reach an unconditionally stable meshless method. Using uniform splitting operators in a special way, which explained later, 6 SS and 4 SS have the same formulations but different coefficients. To clarify the proposed technique, 6 SS-MLTD discussed in details and the same goes for 4 SS-MLTD scheme.

II. CONSTRUCTION OF SPLIT-STEP TECHNIQUE

Dealing with 6 SS-MLTD, for each time step we need only to advance six one-dimensional (1-D) equations, permitting high computational speed together with unconditional stability. Here for simplicity a TE_z wave is considered in order to implement the proposed method. It is completely clear that this simplification does not affect the generality of the method adversely.

A. Split step technique

According to the explained situation Maxwell's equations can be written down in matrix form as,

$$\frac{\partial \vec{u}}{\partial t} = \mathbf{M}\,\vec{u}. \tag{1}$$

where the fields' vector and Maxwell's matrix has considered as,

$$\vec{u} = \left(E_x, E_y, H_z\right)^{\mathrm{T}}. \tag{2}$$

$$\mathbf{M} = \begin{bmatrix} 0 & 0 & \frac{\partial}{\varepsilon \partial y} \\ 0 & 0 & -\frac{\partial}{\varepsilon \partial x} \\ \frac{\partial}{\mu \partial y} & -\frac{\partial}{\mu \partial x} & 0 \end{bmatrix}. \tag{3}$$

while μ and ε are the permeability and permittivity of the medium, respectively. As mentioned before, here 6 SS-MLTD method is explained completely and 4 SS-MLTD method can be inferred from this procedure.

B. The split-step meshless methods

At first, symmetric operator and uniform splitting technique are applied to disintegrate the matrix M into six components while matrix A_x and matrix A_y illustrate spatial derivatives in the x- and y-directions, respectively

$$\mathbf{A}_x = \begin{bmatrix} 0 & 0 & 0 \\ 0 & 0 & -\frac{\partial}{\varepsilon \partial x} \\ 0 & -\frac{\partial}{\mu \partial x} & 0 \end{bmatrix}, \tag{4-a}$$

$$\mathbf{A}_y = \begin{bmatrix} 0 & 0 & \frac{\partial}{\varepsilon \partial y} \\ 0 & 0 & 0 \\ \frac{\partial}{\mu \partial y} & 0 & 0 \end{bmatrix}. \tag{4-b}$$

Exploiting the split-step technique, in this work we consider this permutation for these six sub-matrices,

$$\mathbf{M} = \left(\frac{\mathbf{A}_x}{3}\right) + \left(\frac{\mathbf{A}_y}{3}\right) + \left(\frac{\mathbf{A}_x}{3}\right) + \left(\frac{\mathbf{A}_y}{3}\right) + \left(\frac{\mathbf{A}_x}{3}\right) + \left(\frac{\mathbf{A}_y}{3}\right). \tag{5}$$

Here it is worth mentioning that there is possibility of leading to unconditionally stable schemes for other permutations of these sub-

matrices just like the FDTD counterparts of this technique [9]. Hence, the time step size is divided into six identical sub-steps. These sub-steps produce some intermediate solution that are nonphysical and just help to reach more accurate results [4]. At the bottom, two of these equations present successive odd and even sub-steps, respectively,

$$\frac{\partial \vec{u}}{\partial t} = 6.\left(\frac{\mathbf{A}_x}{3}\right)\vec{u}\,, \quad t \to t + 1/6. \tag{6-a}$$

$$\frac{\partial \vec{u}}{\partial t} = 6.\left(\frac{\mathbf{A}_y}{3}\right)\vec{u}\,, \quad t + 1/6 \to t + 2/6. \tag{6-b}$$

As time marches these equations repeat for odd and even time sub-steps.

Here in right hand side (RHS) of the equations we use Crank-Nicolson (CN) scheme, which is unconditionally stable for more accurate results [10]. In this scheme spatial derivatives replace with the average value of two adjacent moments of the spatial derivatives. This way we get these equations for two odd and even successive sub-steps, respectively

$$\left([\mathbf{I}] - \frac{\Delta t}{6}\mathbf{A}_x\right)\vec{u}^{t+1/6} = \left([\mathbf{I}] + \frac{\Delta t}{6}\mathbf{A}_x\right)\vec{u}^{t}, \tag{7-a}$$

$$\left([\mathbf{I}] - \tfrac{\Delta t}{6}\mathbf{A}_y\right)\vec{u}^{t+2/6} = \left([\mathbf{I}] + \tfrac{\Delta t}{6}\mathbf{A}_y\right)\vec{u}^{t+1/6}. \tag{7-b}$$

Now in the next stage these equations are expressed in meshless method. Before implementation of these formulations in meshless method there is a brief explanation about this technique.

III. THE CONVENTIONAL RPIM METHOD

A. Equation formatting

Here Maxwell's equations have been discretized through RBF method. In RPIM methods the value of the field variable u(x) is interpolated using the value of the field nodes those are enclosed by the encompassing of the support domain of arbitrary point x, as described in [2]. If we assume x = $(x,y)^T$ to be the arbitrary point at which u(x) is to be approximated, desired unknown can be achieved using the following equation,

$$u(\mathbf{x}) = \sum_{i=1}^{n} r_n(\mathbf{x})\, a_n + \sum_{j=1}^{m} p_m(\mathbf{x})\, b_m. \tag{8}$$

while n is the number of nodes surrounded by the support domain of arbitrary point x=$(x,y)^T$, $r_n(x)$ is the radial basis function, p_m (x) is the monomial basis function, a_n and b_m are coefficients yet to be determined. Since its derivatives are different from the original function only in a constant coefficient and thus more efficient in mathematical handling, the Gaussian function is selected as the radial basis function,

$$r_n(\mathbf{x}) = exp\left(-c\left|\frac{r}{r_{max}}\right|^2\right). \tag{9}$$

$$r = \sqrt{(x - x_j)^2 + (y - y_j)^2}. \tag{10}$$

where r_{max} and (x_i,y_i) describe the diameter of the support domain corresponding to the arbitrary point x, and location of i^{th} node within it, respectively. Here c represents the shape parameter of the Gaussian radial basis function that controls the decaying rate of the function.

B. Choosing shape parameters

Shape parameters are so influential in basis functions and consequently the results of supposed electromagnetic problem that they also called control parameters. Basically, seeking the best shape parameters maintaining a good balance between accuracy and stability, relies on trial and error that is a costly and time consuming process. In reality, the freedom to choose shape parameters is not a positive point [11]. Up to now, there has not any calculable way to find the best shape parameters, easily, and thus choosing the optimal shape parameters is an attractive research area. In this paper r_{max} chooses equal to the size of space step (ΔS) and another shape parameter, i.e., c, finds by trial and error to give the best practical results in accordance with the electromagnetic fields propagation in the time domain and desired cut-off frequency.

IV. NUMERICAL EXPERIMENT AND DISCUSSION

As mentioned, we consider a TE_z 2-D wave propagating in a homogeneous, linear, isotropic and lossless medium. Here a 1 *cm* × 1 *cm* cavity filled with air and terminated with perfect electric conductor (PEC) boundaries has been selected in the *x*-*y* plane. Thus, in order to have symmetric

excitation, a magnetic current density in the form of modulated Gaussian pulse function has been exploited as,

$$\mathbf{M}_{sz} = \mathbf{M}_0 exp\left(-\left(\frac{t-t_0}{\tau}\right)^2\right) * sin\left(2\pi f(t-t_0)\right). \quad (11)$$

For simplicity it is supposed that $a = \Delta t/6\varepsilon$ and b = $\Delta t/6\mu$. With the definition of E-nodes and H-nodes at the same location and using the central difference scheme to approximate the time derivatives, the field variables in Maxwell's curl equations can be approximated as follows:

For the first sub-step,

$$E_{x,i}^{t+1/6} = E_{x,i}^{t}, \quad (12\text{-a})$$

$$E_{y,i}^{t+1/6} = E_{y,i}^{t} - a \times\left(\sum_j \partial x \Phi_j \, H_{z,j}^{t} + \sum_j \partial x \Phi_j \, H_{z,j}^{t+1/6}\right), \quad (12\text{-b})$$

$$H_{z,i}^{t+1/6} = H_{z,i}^{t} - b \times\left(\sum_j \partial x \Phi_j \, E_{y,j}^{t} + \sum_j \partial x \Phi_j \, E_{y,j}^{t+1/6}\right). \quad (12\text{-c})$$

For the second sub-step,

$$E_{x,i}^{t+2/6} = E_{x,i}^{t+1/6} + a \times\left(\sum_j \partial y \Phi_j \, H_{z,j}^{t+1/6} + \sum_j \partial y \Phi_j \, H_{z,j}^{t+2/6}\right), \quad (12\text{-d})$$

$$E_{y,i}^{t+2/6} = E_{y,i}^{t+1/6}, \quad (12\text{-e})$$

$$H_{z,i}^{t+2/6} = H_{z,i}^{t+1/6} + b \times\left(\sum_j \partial y \Phi_j \, E_{x,j}^{t+1/6} + \sum_j \partial y \Phi_j \, E_{x,j}^{t+2/6}\right). \quad (12\text{-f})$$

It is completely clear that other odd and even sub-steps have the same formulations, but different time intervals. Namely, this procedure repeats for the other four remaining sub-steps, respectively. This way the other update equations can be attained analogously. It is worth mentioning that in all simulated schemes, space step size is selected $\Delta S = 0.5$ mm. According to the dimensions of the supposed cavity, there are 21×21 nodes under scrutiny. Based on intrinsic difference between meshless and finite-difference methods under stipulated conditions, there are 20×20 cells in finite-difference methods. Number of unknowns in all FD-TD and ML-TD methods is equal to the number of cells and nodes, respectively. The subtle point here that is worth pondering is multiplying time sub-steps in ADI-MLTD, 4SS-MLTD, and 6SS-MLTD methods by 2, 4, and 6, respectively. Field values at these sub-steps leads to intermediate solutions those have no physical meaning and just used to update the field value variations for the next sub-steps. To analyze the assumed problem, the current source excites the cavity at its center.

Tables 1, 2, and 3 show the simulation results of the cavity analysis for its dominant mode cut-off frequency. Acceptable variations of cut-off frequency and also stability of the electromagnetic field in time-domain by increasing time step size reveal that split-step meshless time-domain methods (4SS-MLTD and 6SS-MLTD methods) are unconditionally stable. Moreover in general, 6SS-MLTD method shows more accurate results for cut-off frequencies while increasing the time step size in comparison with 4SS-MLTD method and even ADI-MLTD method.

Table 1: Simulation results of cavity analysis for its dominant mode cut-off frequency and CPU time by ADI-MLTD method.

Time-step size	Time sub-steps number	Cut-off frequency TE_{z10} (GHz)	Relative error (%)	CPU time (sec)
τ	4730	15.421	2.806	251.1642
2τ	2365	15.642	4.280	129.6259
4τ	1183	15.834	5.560	68.2512
6τ	788	15.124	0.827	48.076
8τ	591	15.476	3.173	37.746

Table 2: Simulation results of cavity analysis for its dominant mode cut-off frequency and CPU time by SS4-MLTD.

Time-step size	Time sub-steps number	Cut-off frequency TE_{z10} (GHz)	Relative error (%)	CPU time (sec)
τ	9461	15.156	1.04	102.435
2τ	4730	15.184	1.227	55.066
4τ	2365	15.145	0.967	31.270
6τ	1577	15.265	1.767	23.004
8τ	1183	15.462	3.08	19.016

Table 3: Simulation results of cavity analysis for its dominant mode cut-off frequency and CPU time by SS6-MLTD.

Time-step size	Time sub-steps number	Cut-off frequency TE_{z10} (GHz)	Relative error (%)	CPU time (sec)
τ	14191	15.141	0.94	591.410
2τ	7096	15. 162	1.08	411.996
4τ	3547	15.158	1.053	288.447
6τ	2365	15.214	1.427	102.463
8τ	1773	15.248	1.653	79.488

In this paper, variation of phase velocity in different directions, which is considered as the main source of dispersion error is disserted. Phase velocity can be found via $v_p = \Delta S/\Delta t$, while ΔS is the displacement of an arbitrary point with a specific phase of propagating wave in the time interval Δt. Considering the speed of electromagnetic waves in vacuum, i.e., $c = 3\times10^8$, as the criterion of measurement, the phase velocities in all directions are normalized dividing by this specific velocity. In other words, it can be indicated as normalized phase velocities = v_p/c.

Speaking of FDTD method, the Yee space lattice represents an anisotropic medium because in such lattice, propagation velocity is dependent on the direction of wave propagation, which causes different phase velocities in different angles of propagation. In more detailed words, the phase velocity has its maximum along the grid diagonals and its minimum along the major axis of the grid. Anisotropic phase velocity plays a key role in dispersion errors [12].

Against FDTD methods, there is not any closed form formula to calculate phase velocity in meshless methods. Facing meshless methods, phase velocity in different directions must be calculated through tracing the electromagnetic wave before reflecting back from the boundaries in different time intervals in different angels of propagation. This process can be done easily for specific angels like $\varphi = 0^o, 45^o, 90^o, 135^o$, and 180^o. For other angels using more dense nodes it is possible to calculate phase velocities in other angels. Putting these phase velocities together and using interpolation, the following curves are deduced.

Figure 1 illustrates the normalized phase velocities of different split step schemes for meshless and finite-difference time-domain methods versus wave propagation angles. Here PPW stands for "point per wavelength" that is PPW = $\lambda/\Delta S$, where λ stands for wavelength. PPW has similar meaning to cell per wavelength (CPW) in finite-difference method. Moreover, Fig. 2 shows the phase velocity of ADI-MLTD and ADI-FDTD methods as a function of propagation direction. Based on Figs. 1 and 2, numerical experiments reveal this fact that using meshless methods there is not such a great difference between phase velocities in different directions. In other words, comparing these results with their counterparts in FDTD method [13] it can be concluded that modeling geometry with nodes not cells namely meshless methods instead of finite-difference methods, results in more smoothed phase velocities in different directions and consequently lower dispersion errors. It is resulted from changing shape parameters, the least dispersion error is related to optimal shape parameters and any variations in shape parameters aggrandizes dispersion errors. More investigations endorse this result for any rectangular cavity. In sense of velocity, it is completely clear that 6SS-MLTD method outperforms 4SS-MLTD method and the same goes for 4SS4-MLTD proportional to ADI-MLTD methods.

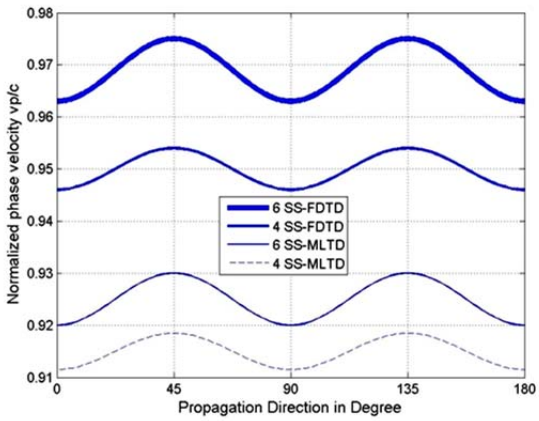

Fig. 1. Normalized phase velocities as a function of propagation angle for PPW = 41.

In these curves the smoother propagation in different directions, the less dispersion error there is in the scheme. Just like what occurred in FDTD method on examination of the phase velocity [10], ADI-MLTD method have worse anisotropy phase velocity than that of the four and six split-step

meshless methods. It means ADI-MLTD method has much larger anisotropy error in comparison with split-step methods. This fact guarantees better function of SS-MLTD methods than ADI-MLTD method. Here, all simulations are performed on an Intel Corei7 CPU with 4 GB RAM and 1.73 GHz. Memory usage in 6SS-MLTD methods is about 51% while in 4SS-MLTD and ADI-MLTD methods this factor decreases to 48%. Since the processor has to deal with more equations, it seems to be logical using higher memory in 6SS-MLTD.

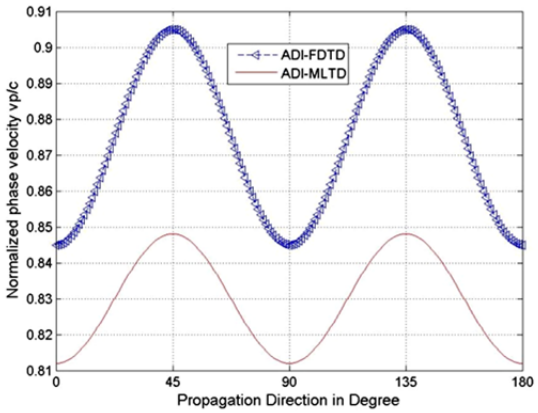

Fig. 2. Comparison between normalized phase velocities of ADI-MLTD (PPW = 40) and ADI-FDTD.

V. CONCLUSIONS

Two different split-step meshless time-domain (SS-MLTD) methods have been proposed in this paper. 4SS-MLTD and 6SS-MLTD techniques perform by splitting the Maxwell's matrix into four and six sub-matrices and simultaneously dividing the time-step into four and six equal sub-steps, respectively. These schemes brought up in this paper reduce the anisotropy of phase velocity in different directions of propagation. In other words, normalized phase velocities in SS-MLTD methods is smoother than what it is in ADI-MLTD method and as a consequence this proposed scheme lead in lower dispersion error. Additionally, it was observed just like what occurred in FDTD method, 4SS-MLTD shows more smoothed changes in different direction in respect with 6SS-MLTD method and thus less adverse dispersion errors. This will lead to useful unconditionally stable meshless methods with low dispersion error.

REFERENCES

[1] R. Mirzavand and A. Abdipour, "Unconditionally stable MFLTD method for the full-wave electromagnetic simulation," *IEEE Trans. Antennas Propagat*., vol. 60, no. 5, May 2012.

[2] G. Liu and G. Gu, *An Introduction to Meshfree Methods and Their Programming*, Springer 2005.

[3] X. Chen, Z. Chen, Y. Yu, and D. Su, "An unconditionally stable radial point interpolation meshless method with Laguerre polynomials," *IEEE Trans. Antennas Propagat.*, vol. 59, no. 10, Oct. 2011.

[4] E. Kansa, "Multiqudrics—A scattered data approximation scheme with applications to computational fluid-dynamics—I. Surface approximations and partial derivatives," *Appl. Comput. Math*., vol. 19, no. 8–9, pp. 127-145, Sept. 1992.

[5] Y. Yu, F. Jolani, and Z. (David) Chen, "An efficient meshless approach to multi-scale modeling in the time-domain," *Applied Computational Electromagnetic Society (ACES) Journal*, vol. 27, no. 6, June 2012.

[6] S. Lai, B. Wang, and Y. Duan, "Meshless radial basis functions method for solving Hallen's Integral equation," *Applied Computational Electromagnetic Society (ACES) Journal*, vol. 27, no. 1, Jan. 2012.

[7] Y. Yu and Z. Chen, "Towards the development of an unconditionally stable time-domain meshless method," *IEEE Trans. Microw. Theory Tech.,* vol. 58, no. 3, pp. 578-586, March 2010.

[8] Y. Yu and Z. Chen, "Towards the development of unconditionally stable time-domain meshless numerical methods," in *IEEE MTT-S Int. Microw. Symp. Dig.,* Boston, MA, pp. 309-312, 7-12 June 2009.

[9] Q. Chu and Y. Kong, "Three new unconditionally-stable FDTD methods with high-order accuracy," *IEEE Trans. Antennas Propagat.,* vol. 57, no. 9, Sept. 2009.

[10] G. Sun and C. Trueman, "Unconditionally stable Crank-Nicolson scheme for solving two-dimensional Maxwell's equations," *Electronics Lett.,* 3rd vol. 39, no. 7, April 2003.

[11] G. Fasshuar and J. Zhang, "On choosing optimal shape parameters for RBF approximation," *Mathematics Subject Classification* 65D05. 65D15.65M70, 2000.

[12] A. Taflove and S. Hangess, *Computational Electrodynamtics: The Finite-Difference Time-Domain Method*, Boston, MA: Artech House, 2005.

[13] M. Kusaf and A. Oztoprak, "An unconditionally stable split-step FDTD method for low anisotropy,"

IEEE Microwave and Wireless Compo. Lett., vol. 18, no. 4, pp. 224-226, April 2008.

Fatimah Ansarizadeh received the B.Sc. and M.Sc. in Electrical Engineering from Shahid Bahonar University of Kerman, Kerman, Iran in 2007 and 2013. Her current research interest is using Meshmfree methods to solving electromagnetic problems.

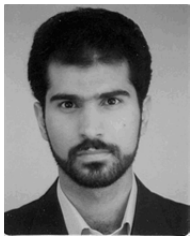

Masoud Movahhedi was born in Yazd, Iran, in 1976. He received the B.Sc. degree from Sharif University of Technology, Tehran, Iran, in 1998, the M.Sc. degree from Amirkabir University of Technology (Tehran Polytechnic), Tehran, Iran, in 2000, both in Electrical Engineering, and also Ph.D. degree in Electrical Engineering at the same University in 2006. In December 2005, he joined the Institute for Microelectronics, Vienna University of Technology, Vienna, Austria, as a Visiting Student and now is an Assistant Professor in Electrical and Computer Engineering Department at Yazd University. His research interests are in the areas of computer-aided design of microwave integrated circuits, computational electromagnetic, semiconductor high-frequency RF modeling, and metamaterials.

Dr. Movahhedi was the recipient of the GAAS-05 Fellowship sponsored by the GAAS Association to young graduate researchers for his paper presented at GAAS2005. He was also the recipient of the Electrical Engineering Department outstanding student award in 2006.

Adaptive Difference Beam with Low Sidelobes at Subarray Level Based on Semidefinite Programming

Jia Xu, Ying Zhang, and Xiao-Feng Shen

Department of Electrical Engineering
University of Electronic Science and Technology of China, Chengdu, 611731, China
jiaxu1988@gmail.com

Abstract ─ This paper proposes a semidefinite programming (SDP) method to form adaptive difference beam at subarray level. Its performance is investigated via computer simulations. Compared with loaded sample matrix inversion (LSMI) and constrained adaptive beam-pattern synthesis (CAPS). The proposed algorithm not only has manifest lower sidelobes in quiescent pattern control and sidelobe interference suppression, but also produces more accurate and deeper null in look direction when mainbeam interference deforms the pattern.

Index Terms ─ Adaptive at subarray level, difference beam, low sidelobe, and semidefinite programming.

I. INTRODUCTION

In search-track system, antennas are usually required to generate sum and difference beams simultaneously. However, the implementation of two independent excitations for the sum and difference modes of operation is generally unacceptable because of the costs and complexity [1]. Thus, it is necessary to form the two types of beams at subarray level. Since the sum pattern is used in both signal transmission and reception, the most common way to solve the problem is to generate an optimal sum pattern and suboptimal difference pattern [2]. Therefore, when element tapering is in favor of sum beam, sidelobe reduction contributed by element tapering is not effective for difference beam. Nevertheless, it is desirable to obtain low sidelobes in the adaptive beams to aid the performance against clutter [3]. Moreover, difference pattern is required to have deep slope at boresight to improve the radar sensitivity [1].

The minimum variance distortionless response (MVDR) is a popular algorithm used for adaptive beamforming. However, its high sidelobe level is an issue when practical sample covariance matrix is used [4]. The loaded sample matrix inversion (LSMI) [5] is a modification of sample matrix inversion (SMI), which suppresses sidelobes by adding a small value on the diagonal of the covariance matrix. However, there is no closed-form solution for the optimal loading value and it is usually obtained by simulation trials or empirical experience [4]. A new projection based algorithm, constrained adaptive beam-pattern synthesis (CAPS), combines advantages of subspace and penalty function (PF) approaches [3], and its performance is similar to LSMI except for very low sidelobe antennas and severe jamming situations [6]. Another approach based on optimization is realized by second-order cone (SOC) programming [7], but a hard threshold needs to be preset and the proper choice of threshold is difficult [4]. Besides, sidelobe areas have to be delimited previously for optimization. Some research has been done on adaptive difference beam at subarray level in [8-9]. However, in [8], interests go to the influence of subarray configuration on adaptive sum and difference beam. Sidelobe reduction of difference beam in [9] is mainly contributed by element tapering, especially in quiescent pattern control, which rises remarkably when element tapering is designed for sum beam (e.g. Taylor taper). References [1, 2] have investigated the effects of subarray configuration and subarray level weights on optimum sum and difference pattern. Although,

Submitted On: Feb. 26, 2013
Accepted On: July 26, 2013

suboptimum difference beams were achieved, they were aimed at non-adaptive beamforming.

In this paper, we propose semidefinite programming (SDP) method to form adaptive difference beam at subarray level in linear array while Taylor tapering is applied at element level for sum beam. Sidelobe reduction of sum beam can be achieved by element tapering, thus is not considered here. The proposed algorithm is based on the thought of matching reference difference weights with given subarray configuration. Besides, we impose constraints on interferences suppression and null depth in look direction so that deep null depth and adaption are achieved. The feasibility and advantages of the novel algorithm are verified via numerical simulations.

II. PROBLEM FORMULATION

Consider a uniform linear array with $N = 2M$ omnidirectional antennas spaced with $d = \lambda / 2$, receiving N narrowband signals $\vec{s}(t) \in C^{N\times 1}$, where λ is the carrier wave length, as shown in Fig. 1. The array is assumed to be symmetrical about the origin. When K signals impinge on the array, the n^{th} snapshot received data vector $\vec{x}_{ele}(n) \in C^{N\times 1}$ is given by [10],

$$\vec{x}_{ele}(n) = A\vec{s}(n) + \vec{v}(n), \quad (1)$$

where $\vec{v}(n)$ is a noise vector, characterizing additive Gaussian white noise. A is the array manifold matrix, which is the combination of all possible steering vectors [10],

$$A = \left[\vec{a}(\theta_1), \vec{a}(\theta_2), \ldots\ldots, \vec{a}(\theta_K)\right], \quad (2)$$

where $\vec{a}(\theta_k)$ is the steering vector for the k^{th} $(0 \le k \le K)$ signal from θ_k and is defined as,

$$\vec{a}(\theta_k) = [e^{-j\frac{2\pi d}{\lambda}\left(n-\frac{N+1}{2}\right)\sin\theta_k}]^T,\ 1 \le n \le N. \quad (3)$$

Assume an amplitude weight vector $\vec{w} = \left[w_{-M}\ w_{-M+1} \ldots w_M\right]^T$ is applied at element level to control sidelobe for the quiescent sum beam. Besides, the array is divided into L subarrays. Sub-arraying is symmetrical about the array center. The subarray geometry is shown in Fig. 2. The element to subarray transformation matrix can be described by an $N \times L$ matrix [11],

$$T_d = D_{\theta_0} \cdot D_w \cdot T, \quad (4)$$

where $D_{\theta_0} = diag\left(\vec{a}_0\right)$, $D_w = diag\left(\vec{w}\right)$, θ_0 is the look direction. T describes how different the array elements are arranged into L subarrays [11]. Then the interferences plus noise received data and the $L \times L$ disturbance covariance matrix at subarray level can be given by equations (5) and (6), respectively,

$$\vec{x}_{sub} = T_d^H \vec{x}_{ele} \quad (5)$$

$$R_{sub} = T_d^H E\left[\vec{x}_{ele}\vec{x}_{ele}^H\right]T_d = T_d^H R_{ele} T_d. \quad (6)$$

In practice, the covariance matrix R_{ele} is unknown and we replace it with its maximum likely-hood estimation [6],

$$\hat{R}_{ele} = \frac{1}{N_{sap}} \sum_{n=1}^{N_{sap}} \vec{x}_{ele}(n)\vec{x}_{ele}^H(n),$$

where N_{sap} is the sampling rate and $N_{sap} = 2N$ in this paper. If $\vec{w}_{sub}$ indicates weighting at subarray level, then the pattern with subarray configuration is given by,

$$f(\theta) = \left[diag\left(\vec{w}\right) \cdot T \cdot \vec{w}_{sub}\right]^H \left[\vec{a}(\theta) \circ \vec{a}^*(\theta_0)\right] \quad (7)$$

where "$\circ$" and "$*$" denote Hadamard product and conjugate, respectively.

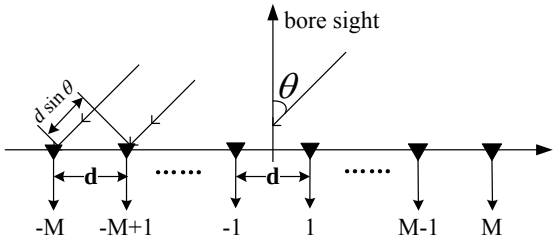

Fig. 1. The uniform linear array of $N = 2M$ sensors.

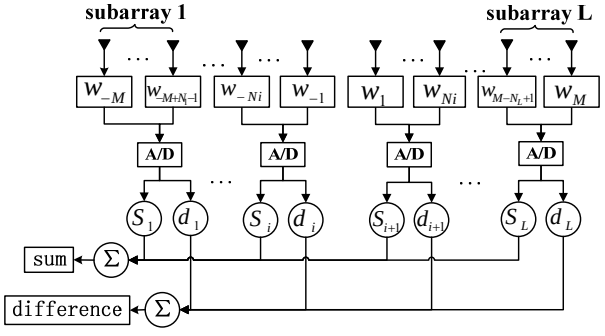

Fig. 2. Linear array with subarray configuration.

It is known that adaptive beamforming is data-dependent [12]. In this paper, we achieve adaption at subarray level. Adaptive weighting is calculated with the output from all subarray channels. A general block diagram of adaptive beam former is shown in Fig. 3.

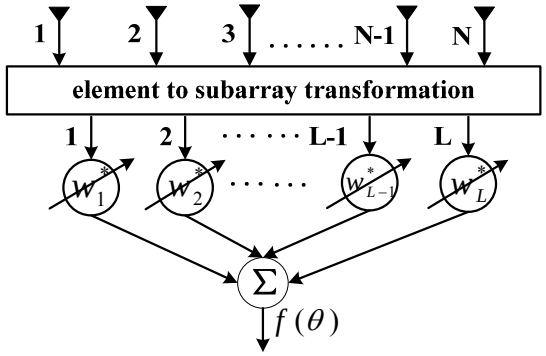

Fig. 3. Adaptive beamforming block.

A. Loaded sample matrix inversion

In reference [9], the steering vector of difference beam at subarray level $\vec{s}_\Delta(\theta_0)$ is given by,

$$\vec{s}_\Delta(\theta_0) = T_d^H\left[\vec{g}\circ\vec{a}(\theta_0)\right], \tag{8}$$

where $\vec{g} = [\underbrace{-1,...,-1}_{M}, \underbrace{1,...,1}_{M}]^T$.

The adaptive weighting at subarray level based on LSMI [6] is,

$$\vec{w}_{LSMI} = \left(\hat{R}_{sub} + \delta I\right)^{-1}\vec{s}_\Delta(\theta_0). \tag{9}$$

I denotes the identity matrix and δ is a positive constant, we choose $\delta = 4\sigma^2$ for simplification [6], where σ^2 is the power of noise.

B. Constrained adaptive beam-pattern synthesis

The adaptive weighting based on CAPS algorithm [6] is,

$$\vec{w}_{CAPS} = \vec{w}_{SMI} - X_\perp\left(X_\perp{}^H C X_\perp\right)^{-1} X_\perp{}^H C\left(\vec{w}_{SMI} - \vec{s}_\Delta\right) \tag{10}$$

where $\vec{w}_{SMI} = \hat{R}_{sub}^{-1}\vec{s}_\Delta \Big/ \left[\vec{s}_\Delta^{\,H}\hat{R}_{sub}^{-1}\vec{s}_\Delta\right]$. The columns of the matrix $X_\perp$ span the space orthogonal to $\left[J, \vec{s}_\Delta\right]$. J is a unitary $L\times K$ matrix with columns spanning the interference subspace(ISS). L and K are the number of subarray channels and interferences, respectively. J can be estimated from the received data by eigen decomposition of $\hat{R}_{sub}$. After eigen decomposition of $\hat{R}_{sub}$, we rank its eigenvalues in descending order as $\lambda_1 \ge \lambda_2 \ge ... \ge \lambda_K > \lambda_{K+1} \ge ... \ge \lambda_L$, and their corresponding eigenvectors are $\vec{u}_1,...\vec{u}_K, \vec{u}_{K+1},...\vec{u}_L$, among which $\vec{u}_1,...\vec{u}_K$ span the ISS when interference to noise ratio (INR) is large [13]. To determine the dimension of ISS (i.e., to obtain K), we use the Akaike information criterion (AIC) [14],

$$AIC(k) = -2\ln\left[\frac{\prod_{i=k+1}^{L}\lambda_i^{\frac{1}{L-k}}}{\frac{1}{L-k}\sum_{i=k+1}^{L}\lambda_i}\right]^{(L-k)N_{sap}+2k(2L-k)}.$$

$$\hat{K} = \min\left\{AIC(k), k = 0,1,...,L-1\right\} \tag{11}$$

Overestimation of dimension of ISS causes signal to interference and noise ratio (SINR) loss while underestimation results in insufficient suppression of interferences. Incorrect estimation may occur in complicated scenarios or the situations where noise power of each subarray channel differs considerably. Diagonal loading can improve the robustness of AIC against errors [6]. Therefore, we replace $\hat{R}_{sub}$ with $\hat{R}_{sub} + 4I$ in our simulation. C is a directional weighting function, and $C \approx I$ for no directional weighting, thus the CAPS weight vector used in this paper is [6],

$$w_{CAPS} = \vec{s}_\Delta + P_{[J,\vec{s}_\Delta]}\left(\vec{w}_{SMI} - \vec{s}_\Delta\right), \tag{12}$$

where $P_{[J,\vec{s}_\Delta]}$ denotes the projection onto space $\left[J, \vec{s}_\Delta\right]$.

III. THE PROPOSED METHOD

There are some algorithms such as Taylor tapering, Dolph-Chebyshev synthesizing, for low sidelobe sum pattern synthesis [15]. In terms of difference pattern, Bayliss weighting is used to achieve low side lobes [16]. Despite the fact that Taylor tapering is exploited as element excitation for sum beam, we may try to minimize the difference between $\vec{w}_{ref}$ and $T_w\vec{w}_{sub}$ with constraint of interference suppression, where

$\vec{w}_{ref}$ is the optimum difference excitations for sidelobe reduction. $T_w\vec{w}_{sub}$ is the equivalent element weight vector with subarray configuration, and $T_w = diag(\vec{w})\cdot T$. $\vec{w}_{sub}$ is the weight vector at subarray level, which we are looking for. In addition, we can impose constraints on the null in look direction for difference beam synthesis.

Suppose Taylor tapering $\vec{w}_{Taylor}$ is applied at each element for sumbeam forming. To form adaptive difference beam at subarray level, we design an optimization problem, given as follows,

$$\begin{aligned} &\vec{w}_{sub} = \arg\min_{\vec{w}_{sub}} \left\| T_w\vec{w}_{sub} - \vec{w}_{ref} \right\|_2^2 \\ &s.t.:\ \left(T_d\cdot\vec{w}_{sub}\right)^H \vec{a}_0 = 0 \\ &\quad \left(T_d\cdot\vec{w}_{sub}\right)^H \vec{a}\left(\theta_k\right) = 0, \\ &\quad\quad k = 1,2,...,K < L \end{aligned} \quad , \qquad (13)$$

where $\left\|\vec{x}\right\|_2$ is the Frobenius norm of vector $\vec{x}$. θ_k denotes the direction of the k^{th} interference. Interferences are assumed incoherent with each other. However, in general, we have no prior information of interferences, i.e., θ_k is unknown. Nevertheless, in the situation of strong interferences and small signal, the optimal weight vector tends to be orthogonal to the interference subspace [6]. Thus, we can modify equation (13) as,

$$\begin{aligned} &\vec{w}_{sub} = \arg\min_{\vec{w}_{sub}} \left\| T_w\vec{w}_{sub} - \vec{w}_{ref} \right\|_2^2 \\ &s.t.:\ \left(T_d\cdot\vec{w}_{sub}\right)^H \cdot\vec{a}_0 = 0 \\ &\quad \vec{w}_{sub}^H\cdot J = 0 \end{aligned} \quad . \qquad (14)$$

Assume $P\left(\vec{v}\right) = \| T_w\vec{v} - \vec{w}_{ref} \|_2^2$, $\vec{v}\in C^{L\times 1}$. It can be easily shown that $P(\vec{v})$ satisfies the following inequality for all $0\le\alpha\le 1$,

$$P\left(\alpha\vec{\gamma} + (1-\alpha)\vec{v}\right) \le P\left(\alpha\vec{\gamma}\right) + (1-\alpha)P\left(\vec{v}\right) \quad (15)$$

where $\vec{\gamma}\in C^{L\times 1}$. Thus, the objective function in equation (14) is convex [17]. As its constraint functions are affine, equation (14) is a quadratic program [17]. We can introduce a non-negative auxiliary variable t that serves as an upper bound on the objective [18],

$$\begin{aligned} &\min_{t,\vec{w}_{sub}} \ t \\ &s.t.:\left(T_d\cdot\vec{w}_{sub}\right)^H\cdot\vec{s}_0 = 0 \\ &\quad \vec{w}_{sub}^H J = 0 \\ &\quad \left\| T_w\vec{w}_{sub} - \vec{w}_{ref} \right\|_2^2 \le t \end{aligned} \quad . \qquad (16)$$

Equation (16) satisfies the standard form of second-order cone programming [17]. When t reaches its minimum, we get the optimal $\vec{w}_{sub}$.

SDP is a subfield of convex optimization concerned with the optimization of a linear objective function over the intersection of the cone of positive semidefinite matrices. The typical form of SDP is given by [18],

$$\begin{aligned} &\min \vec{c}^T\vec{x} \\ &s.t.\ A\vec{x} = b \\ &\quad F_0 + x_1F_1 + ... + x_pF_p \ge 0 \end{aligned} \quad , \qquad (17)$$

where $\vec{x} = [x_1, x_2, ..., x_p]^T$ is the vector to be optimized, and $F_0, F_1, ..., F_p$ are semidefinite matrices with the same order. The inequality sign $F\left(\vec{x}\right)\ge 0$ means that $F\left(\vec{x}\right)$ is positive semidefinite.

We can reformulate the nonlinear convex problem of equation (16) as the semidefinite programming of equation (18) in the variables $\vec{w}_{sub}$ and t [18],

$$\begin{aligned} &\min_{t,\vec{w}_{sub}} t \\ &s.t.:\left(T_d\cdot\vec{w}_{sub}\right)^H\cdot\vec{s}_0 = 0 \\ &\quad \vec{w}_{sub}^H J = 0 \\ &\quad \begin{bmatrix} I_{N\times N} & T_w\vec{w}_{sub} - \vec{w}_{ref} \\ \left(T_w\vec{w}_{sub} - \vec{w}_{ref}\right)^H & t \end{bmatrix} \ge 0. \end{aligned} \quad . \qquad (18)$$

This semidefinite program has dimensions $m = L+1$ and $n = N$. The number of iterations required to solve a semidefinite program grows with problem size as $O(\sqrt{n})$ and it requires $O(m^2n)$ operations per iteration [18]. Several specialized tools are available to solve it such as SeDuMi [19], YALMIP [20], etc. YALMIP is used in this work. However, YALMIP called

SeDuMi as external solver in our simulation. It usually converges after 10~13 iterations.

IV. SIMULATION RESULT

Let us consider a uniform linear array of 102 antennas with half-wavelength spacing. Look direction is set as $\theta_0 = 0^o$. The subarray configuration is [22, 8, 5, 4, 4, 4, 4, 4, 4, 4, 4, 5, 8, and 22], so that equal noise levels in all subarray channels are achieved approximately. We compare three approaches, LSMI, CAPS and SDP in scenarios of interference free, mainbeam interference and sidelobe interferences. In all simulations, a Taylor tapering with constrained side lobe level (SLL) = -30 dB and $\bar{n} = 8$ is impinged on each element, and difference beam is formed at subarray level digitally. INR is set to 30 dB. In SDP, Bayliss tapering with SLL = -30 dB and $\bar{n} = 8$ is set as the reference weights $\vec{w}_{ref}$. Signal of interest is neglected since it is usually possible to form the interference covariance matrix with signal absent in radar applications [21].

Figure 4 shows the adaptive patterns in the absence of interference obtained by the three algorithms. Although LSMI and CAPS suppress SLL effectively in [11], they deteriorate when we form difference beam at subarray level instead of sum beam. Nevertheless, SLL is remarkably low with SDP. Null depth in look direction, expressed as N_0, and SLL of each pattern are given in Table I.

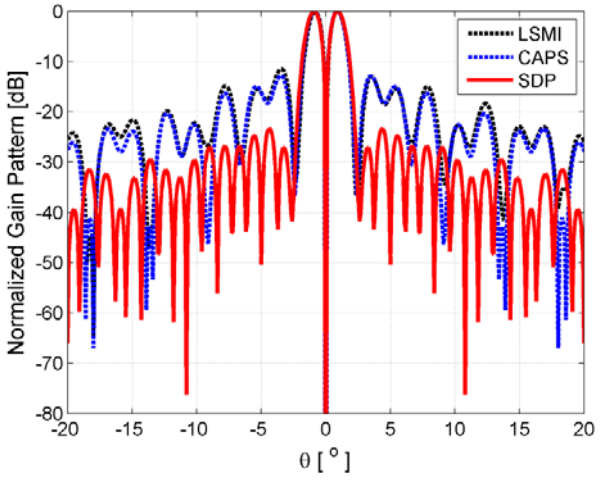

Fig. 4. Normalized pattern in absence of interference (noise only).

Figure 5 demonstrates adaptive patterns in the presence of one main lobe interference from 1.5°. SDP performs slightly better in sidelobe control, but it forms deep null exactly in look direction. Meanwhile, the other two have 0.1° deviation caused by disturbance of the main lobe interference.

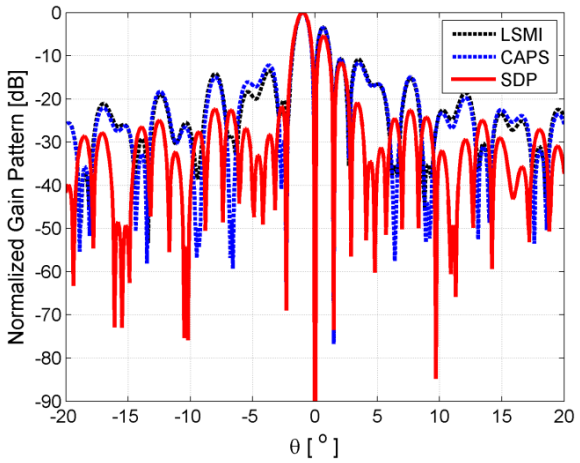

Fig. 5. Normalized pattern with one main lobe interference at 1.5°.

Figure 6 illustrates adaptive patterns in presence of two sidelobe interferences in direction of -5° and 10°. Three algorithms can suppress interference effectively, lower than -67 dB. However, compared with LSMI and CAPS, SDP reduces sidelobe dramatically and has a deeper null in look direction.

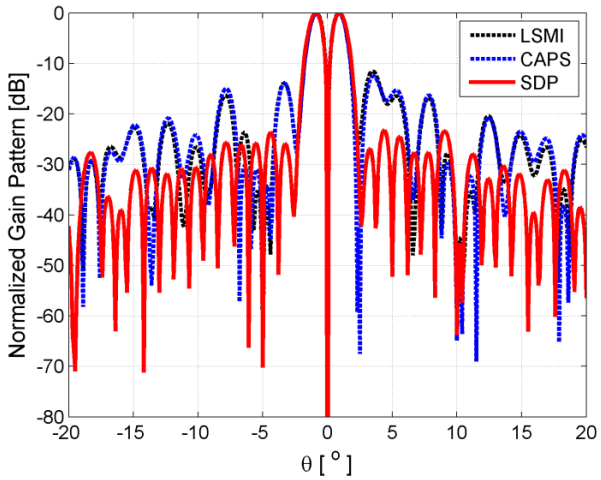

Fig. 6. Normalized pattern with two side lobe interferences at -5° and 10°.

From Table I, we can see that in situations of noise only and sidelobe interferences, SDP outperforms the other two algorithms in side lobe reduction and null depth in look direction manifestly. When the pattern is disturbed by main lobe interference, SDP can still maintain accurate deep null in look direction. This is due to the first equality constraint in equation (18).

Figure 7 and Table II depict the comparison of SINR of each approach versus θ. LSMI has the highest SINR. SDP has a small SINR loss, 0.68 dB compared with LSMI and 0.49 dB compared with CAPS, as shown in Table II. Thus, slight SINR loss is the cost of using SDP.

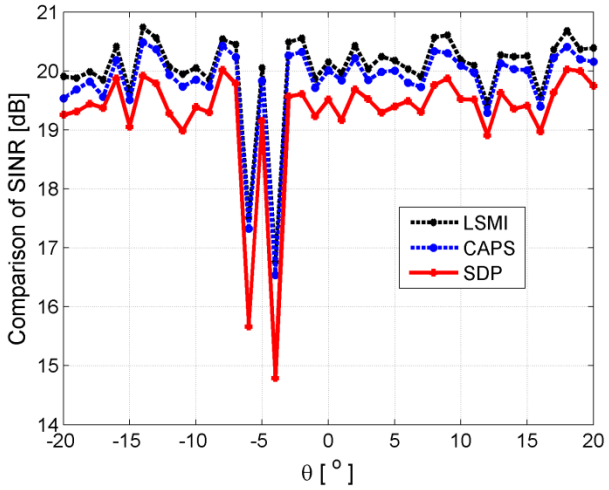

Fig. 7. SINR of three methods, interference at–5^0.

In our simulations, patterns using LSMI and CAPS differ slightly, which agrees with the conclusion in [6]. Although Taylor tapering is used at element level both in [6] and this paper, sum beam is formed at subarray level in [6] while difference beam is formed in this paper. In this case, SDP performs considerably well in suppressing sidelobe and producing accurate deep null in look direction.

As discussed in section III, the computational complexity is closely related to the size of the array and its subarrays. Thus, when we utilize the proposed algorithm to compute adaptive weights, the size of array and the amount of subarrays should be taken into consideration according to the practical requirement of real-time.

Table I: Null depth in θ_0 and SLL for LSMI, CAPS, and SDP [dB].

	absence of interference		**Mainlobe interference**		**sidelobe interference**	
	N_0	SLL	N_0	SLL	N_0	SLL
LSMI	-24	-11.1	-21*	-11.0	-24	-12.1
CAPS	-328	-12.8	-19*	-10.7	-44	-12.5
SDP	-134	-23.4	-135	-11.6	-135	-23.2

*: denoting 0.1^o deviation.

Table II: SINR and SINR Loss for LSMI, CAPS, and SDP [dB].

	SINR	**SINR Loss**
LSMI	20.17	+0.68
CAPS	19.98	+0.49
SDP	19.49	

V. CONCULSIONS

In this paper, a semidefinite programming method is proposed to form adaptive difference beam at subarray level when element excitations are for optimum sum pattern. The proposed method realizes sidelobe reduction in adaptive difference beamforming via optimization. Compared with LSMI and CAPS, the proposed method has the merits of reducing sidelobe considerably and producing an accurate deep null in look direction. The aforementioned merits of the proposed method have been verified by computer simulations. Meanwhile, it suffers from a small SINR loss, which is the cost of SDP algorithm. Thus, a tradeoff should be considered in practical situations.

ACKNOWLEDGMENT

This work was supported by a grant from the National Natural Science Foundation for Young Scholars of China (Grant No.61101094).

REFERENCES

[1] L. Manica, P. Rocca, A. Martini, and A. Massa, "An innovative approach based on a tree-searching algorithm for the optimal matching of independently optimum sum and difference excitations," *IEEE Trans. Antennas Propagat.*, vol. 56, no. 1, Jan. 2008.

[2] D. A. McNammara, "Synthesis of sub-arrayed monopulse linear arrays through matching of independently optimum sum and difference excitations," *Proc. Inst. Elect. Eng. H*, vol. 135, no. 5, pp. 371-374, 1988.

[3] G. M. Herbert, "A new projection based algorithm for low sidelobe pattern synthesis in adaptive arrays," *Radar 97*, publication no. 449, pp. 14-16, Oct. 1997.
[4] J. Wang, R. L. Krlin, and X. Lu, "Sidelobe control using optimization methods in adaptive beamforming," *Adaptive Antenna Arrays: Trend and Applications*, Berlin, July 2004.
[5] B. D. Carlson, "Covariance matrix estimation errors and diagonal loading in adaptive arrays," *IEEE Trans. Aerospace and Electronic Systems*, vol. 24, no. 4, pp. 397-401, 1988.
[6] U. Nickel, "Principle of adaptive array processing," *Advanced Radar Systems, Signal and Data Processing*, no. 5, pp. 1-20, 2006.
[7] J. Liu, et al, "Adaptive beamforming with Sidelobe control using second-order cone programming," *Pro. Of IEEE Sensor Array and Multichannel Signal Processing Workshop*, pp. 461-464, Aug. 2002.
[8] U. Nickel, "Subarray configurations for digital beamforming with low sidelobes and adaptive interference suppression," *Proc. IEEE International Radar Conference*, Alexandria, USA, pp. 714-719, May 1995.
[9] H. Hang and Z. Hao, "Study on ADBF for difference beam at subarray level with sidelobe level," *IEEE International Symposium on Microwave, Antenna, Propagation, and EMC Technologies for Wireless Communication*s, 2007.
[10] R. M. Shubair, "Improved smart antenna design using displaced sensor array configuration," *Applied Computational Electromagnetics Society (ACES) Journal*, vol. 22, no. 1, pp. 83-87, March 2007.
[11] P. Lombardo and D. Pastina, "Pattern control for adaptive antenna processing with overlapped sub-arrays," *IEEE In. Radar Conference*, pp. 188-193, Sep. 2003.
[12] A. Kulaib, R. Shubair, M. Al-Qutayri, and J. Ng, "Robust localization techniques for wireless sensor networks using adaptive beamforming algorithms," *27th Annual Review of Progress in Applied Computational Electromagnetics Society*, pp. 843-848, Williamsburg, Virginia, March 2011.
[13] R. O. Schmidt, "Multiple emitter location and signal parameter estimation," *IEEE Trans. Antennas Propagat.*, vol. 34, no. 3, pp. 276-280, March 1986.
[14] M. Wax and T. Kailath, "Detection of signals by information theoretic criteria," *IEEE Trans., Acoustics, Speech and Signal Processing*, pp. 387-392, Apr. 1985.
[15] R. C. Hansen, "Array pattern control and synthesis," *Proceedings of IEEE*, vol. 80, no. 1, pp. 141-151, January 1992.
[16] T.-S. Lee and T.-K. Tseng, "Subarray-synthesized low-side-lobe sum and difference patterns with partial common weights," *IEEE Trans. Antennas Propagat.*, vol. 41, no. 6, June 1993.
[17] S. Boyd and L. Vandenberghe, *Convex Optimization*, New York, 2009.
[18] L. Vandenberghe and S. Boyd, "Semidefinite programming," *SIAM Review*, vol. 38, no. 1, pp. 49-95, March 1996.
[19] J. F. Strum, "Using SeDuMi 1.02, MATLAB toolbox for optimization over symmetric cones," *Optimization Method and Software*, vol. 11, pp. 625-653, 1999.
[20] J. Löfberg, "YALMIP: A toolbox for modeling and optimization in MATLAB," *Proceedings of IEEE international symposium on Computer Aided Control Systems Design*, Taipei, Taiwan, China, pp. 284-289, Sep. 2004.
[21] L. Rees, J. Mallett, and L. Brennan, "Rapid convergence rate in adaptive arrays," *IEEE Trans. Aerospace and Electronic systems,* vol. 10, no. 6, pp. 853-863, Nov. 1974.

Jia XU received her B.Eng. degree in Electronics Engineering (EE) from University of Electronic Science and Technology of China (UESTC) in 2011. Since then, she has been working towards her Master's degree in UESTC. Her research interests include adaptive beamforming and wideband beamforming.

Performance of Vivaldi Antennas in Reflector Feed Applications

Nurhan T. Tokan

Department of Electronics and Communications Engineering
Yıldız Technical University, Istanbul, Esenler, 34220, Turkey
nturker@yildiz.edu.tr

Abstract ─ When a wideband antenna is to be used as a reflector feed, the phase center variation with frequency introduces an error on the phase of the primary field impinging on the reflector surface. This is because the antenna phase center will be coincident with the focus only at one particular frequency and displacement at other frequencies, which will result as the phase error losses due to axial defocusing. Tapered slot antennas are the most utilized antennas in ultra wide band (UWB) high-performance applications. In this work, performance of the UWB Vivaldi antennas (exponentially tapered slot antennas) in reflector feed applications is investigated. A long Vivaldi is designed, manufactured, and its phase center movement with frequency is measured. The correspondent phase error loss is estimated.

Index Terms ─ Astigmatism, axial defocusing, phase error loss, reflector feed, ultra wide band, and Vivaldi antenna.

I. INTRODUCTION

Nowadays, there is an increasing interest in extremely large bandwidth high-performance applications. Such applications range from deep space investigation to commercial telecommunication links and radars with high spatial resolutions [1-3]. Square kilometer array (SKA) is an international project aimed at building a huge radio telescope covering the frequency range of 70 MHz – 10 GHz. It will provide two orders of magnitude increase in sensitivity as compared to existing ones. The SKA will be an interferometric array of individual antenna stations, synthesizing an aperture with diameter up to several thousand kilometers. Several configurations are under consideration to distribute the one million square meters of collecting area. There are many different suggestions for antennas, ranging from a few tens of very large single reflectors to large arrays of tapered slot antennas or Luneberg lenses [3]. Although, there have been different suggestions for antennas, nowadays it is likely that the final array design for SKA will utilize Vivaldi antennas for the individual elements [4-7]. Vivaldi antennas are the most utilized antennas in ultra wide band (UWB) high-performance applications. They are travelling wave type antenna with a directional radiation along its aperture [8, 9]. Its time domain characteristics are investigated and proved to be weakly-dispersive in [10, 11]. In [12], the time domain radiation properties of the Vivaldi antenna are analyzed with angular dependence with respect to the signal transmitted at the main beam direction.

In a reflector system, long elements are required to achieve a sufficiently high directivity. For such long elements high phase-center instability causes considerable phase error losses due to axial defocusing and astigmatism. Phase center location wanders with changes in the frequency and in any wide band application phase error losses due to variation in phase center location are expected. This is because the antenna phase center will be coincident with the focus only at one particular frequency and when displaced at other frequencies, phase error losses will increase. If it was possible to build a feed antenna with a unique phase center and it is placed at the focus of a perfect parabolidal reflector, it would be possible to eliminate phase error losses.

To determine the phase center location of a radiating element, spherical measurements of the antenna are mostly used [13]. The phase center is determined experimentally by finding the

Submitted On: March 25, 2013
Accepted On: June 14, 2013

equiphase sphere in the radiation direction of the antenna. The center of the surface corresponds to the phase center of the antenna under test. In literature, phase centre variations of general types of antennas are investigated. These include planar loop antenna, coupled planar dipole antenna, horn antenna, and radial line helical array antennas [14-19]. In this work, the phase centre variations of the Vivaldi antenna to be used as reflector feeds are investigated. In [20], Vivaldi antenna fed reflector system is compared with traditional reflector systems and its superiorities are stated. For the determination of the phase centres, the phases of the measured patterns within the 10 dB beamwidth are observed both in E and H-planes. Phase error losses of a reflector system fed by a Vivaldi antenna are investigated. For this aim, a directive Vivaldi antenna operating in the 6:1 band is designed, simulated and measured. Its phase center locations in E and H-planes are found for every frequency within the band. The losses due to axial defocusing and astigmatism are investigated. The paper is structured as follows: in the next section, the concept of phase center variation is defined in details. In the third section, the design and phase center analysis of the antenna together with the measurement results are given. The considerations on the results are given in the last section.

II. UWB ANTENNAS IN REFLECTOR FEED APPLICATIONS

In practice, the phase center of an antenna can be defined as the point on the feed that leads to minimum phase error loss [21]. A unique phase center at the focus of the reflector would eliminate phase error losses. However, phase center location changes with changes in the frequency and in any wide band application, phase error losses are unavoidable. As an example, Vivaldi antenna is demonstrated in Fig. 1. The red dots are the phase center positions at the highest and lowest frequencies. The blue line is the focus point of the paraboloidal reflector. With its current positioning, it would be possible to use the reflector system perfectly at low frequencies of the band. However, at high frequencies there will be distance between the phase center location and the focus point of the reflector. This will result in phase error losses in the system.

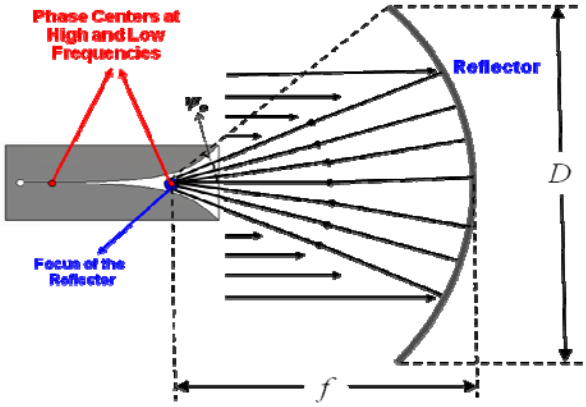

Fig. 1. Phase centre positions of the Vivaldi antenna at high and low frequencies.

Due to the variation in phase center location with frequency as shown in Fig. 1, the feed phase centre cannot be placed at the focus in UWB applications and this results as axial defocusing. We can estimate the phase error loss (*PEL*) due to axial defocusing by approximating the distribution with a quadratic aperture phase distribution. Given z as the axial defocusing, the maximum phase deviation in cycles is [21],

$$S = \frac{z}{\lambda}\left[1-\cos(2\tan^{-1}\frac{1}{4f/D})\right]. \qquad (1)$$

The half subtended angle of the reflector, ψ_o is related with f/D by,

$$\psi_o = 2\tan^{-1}\frac{1}{4f/D}. \qquad (2)$$

Phase error loss is given by

$$PEL = \frac{\rho^2\left[1-2e^{-\rho}\cos(2\pi S)+e^{-2\rho}\right]}{\left[\rho^2+(2\pi S)^2\right]\left(1-e^{-\rho}\right)^2}, \qquad (3)$$

where ρ is the distance from the focus to the reflector. These are approximate formulations for calculating *PEL*. For the exact solution, the integral with the feed pattern should be used to evaluate the phase error losses

$$PEL = \frac{\left|\int_0^{2\pi}\int_{\psi_b}^{\psi_o} E(\psi,\varphi)\tan(\psi/2)\,d\psi\,d\varphi\right|^2}{\left[\int_0^{2\pi}\int_{\psi_b}^{\psi_o}\left|E(\psi,\varphi)\right|\tan(\psi/2)\,d\psi\,d\varphi\right]^2}, \qquad (4)$$

where $E(\psi,\varphi)$ is the feed pattern and $\psi_b = 2\tan^{-1}[b/(2f)]$ where b is the central blockage radius of the feed antenna.

Phase centre locations of an UWB antenna can be obtained from simulation or measurement results. It is the location where almost constant phase within 10 dB beamwidth is obtained. This is demonstrated in Fig. 2 for a Vivaldi antenna at 8 GHz.

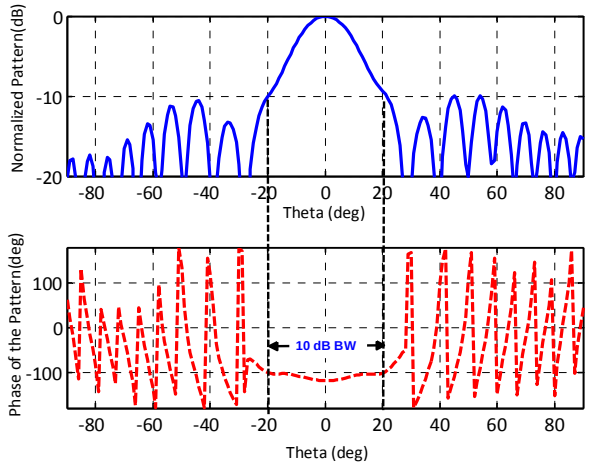

Fig. 2. Radiation pattern and phase of a Vivaldi antenna in *H*-plane at 8 GHz at its phase center.

Unequal phase centre locations in E and H-planes introduce phase error losses due to astigmatism. It is detected by the depth of the nulls in the E and H-planes. Phase error loss due to astigmatism is not as severe as the losses due to axial defocusing [21].

III. VIVALDI FED REFLECTOR IMPULSE RADIATING ANTENNA

A. Design of the feed antenna

Vivaldi is an end fire radiator usually supported on a thin, low ε_r substrate. Despite the completely planar geometry of Vivaldi, it can produce almost symmetric radiation patterns in the E and H-planes. As the length of the antenna increases, its beam width narrows and the directivity increases. Thus, to obtain high directivity, a long Vivaldi is designed as shown in Fig. 3 with its dimensions. The antenna is designed to operate in the band of 2 GHz – 12 GHz (6:1 bandwidth). The length of the exponential tapering is 2.13 wavelengths at the lowest frequency and its exponential flaring is given by $S(z) = (W_{slot}/2)\, e^{az}$ where a = 0.018 and W_{slot} = 0.43 *mm*. A quarter wavelength open circuit stub is used for UWB matching. Its dimensions are given in Fig. 3 (b). The dielectric constant of the dielectric material of the antenna is chosen ε_r = 2.33 and the thickness of the substrate is t = 0.635 *mm*.

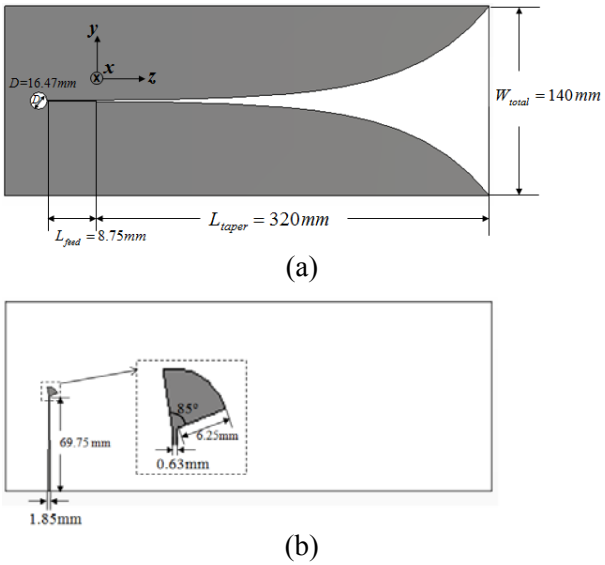

Fig. 3. UWB Vivaldi Antenna with its dimensions (a) front view and (b) back view.

B. Measurement results

The manufactured Vivaldi antenna is given in Fig. 4. The designed antenna has also been simulated by means of the commercial code CST [22] based on the FIT (Finite Integration) method. In Fig. 5, measured and simulated return loss variations of the antenna are given comparatively. In measurements, the antenna has the band of 1.5 GHz to approximately 12 GHz (8:1 band). The phase centre variations of the antenna are investigated in the frequency range of 2 GHz – 12 GHz. The measured and simulated directivities of the Vivaldi antenna are given in Fig. 6.

Fig. 4. Vivaldi antenna in measurement setup.

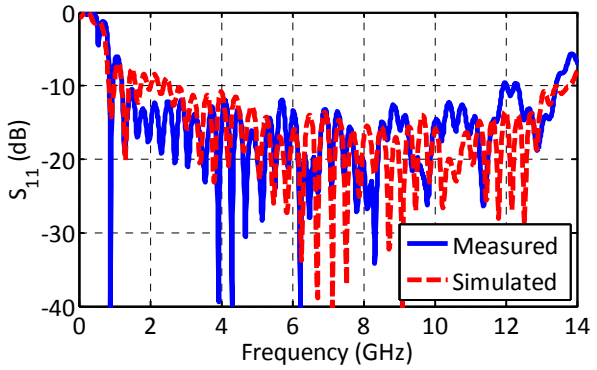

Fig. 5. Measured and simulated return losses of the Vivaldi antenna.

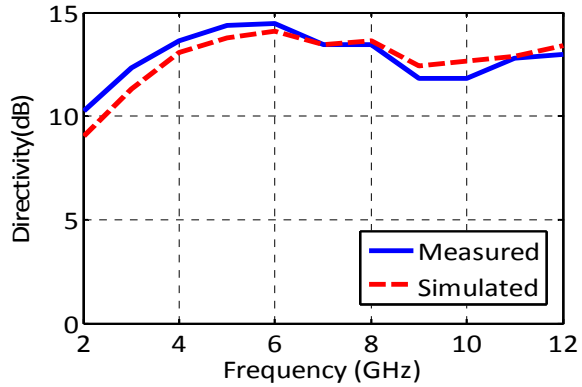

Fig. 6. Measured and simulated directivities of the Vivaldi antenna.

The co-polarised radiation patterns in E- and H-planes are given in Figs. 7 (a) and (b), respectively. 2D coloured views of the radiation patterns are preferred to demonstrate the radiation performance of the Vivaldi antenna with respect to frequency and azimuth angle.

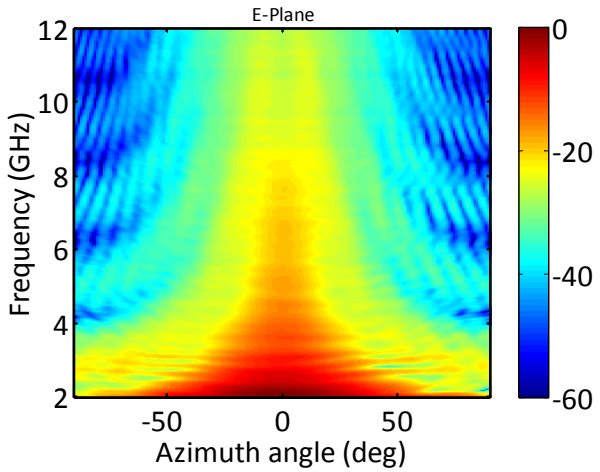

(a)

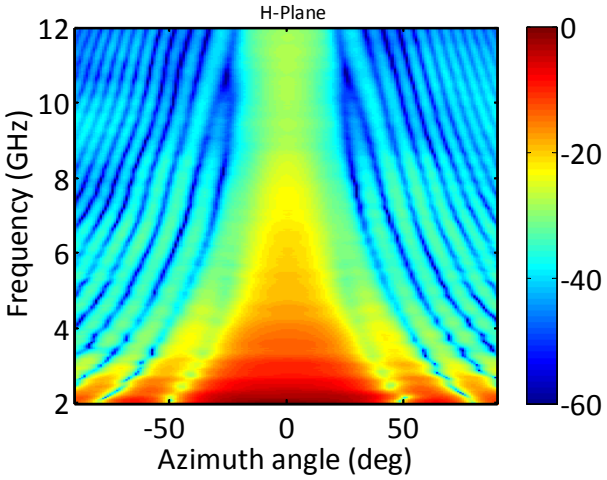

(b)

Fig. 7. (a) E-plane and (b) H-plane co-polarised radiation patterns of the Vivaldi antenna.

C. Phase error losses of the Vivaldi fed paraboloidal reflector

At the phase centre of an antenna, the electromagnetic radiation spreads spherically outward, with the phase of the signal being equal at any point on the sphere. Thus, phase centres are obtained from measurement results by detecting the locations where almost constant phase within 10 dB beamwidth is obtained on the antenna for the frequency of interest. Phase center locations varies with frequency. In Fig. 8, the phase center variations of the Vivaldi are given at E- and H-planes. In E-plane, phase centre location is at $\boldsymbol{z}$ = 22 *cm* at the lowest frequency where it is at $\boldsymbol{z}$ = 12.5 *cm* at the highest frequency. Similarly, it is at $\boldsymbol{z}$ = 25 cm and $\boldsymbol{z}$ = 8 cm in H-plane at the lowest and highest frequencies, respectively. Here, $\boldsymbol{z}$ is the axis along the tapering of the feed antenna. The reference point for $\boldsymbol{z}$ axis is the starting point of the exponential tapering as indicated in Fig. 3 (a). The variation between the lowest and highest frequencies in H-plane is 17 *cm*, which is 6.8 wavelengths at the highest frequency. It is 9.5 *cm* in E-plane, which is equal to 3.8 wavelengths at 12 GHz. This distance between phase centre locations at lowest and highest frequencies will cause the phase error loss due to axial defocusing. An appropriate location for the positioning of the feeding antenna should be determined giving the lowest phase error losses within the whole operation band. The 10 dB beamwidth in H-plane varies from 85° to 37° between 2 GHz and 12

GHz. Similarly, the beamwidth in E-plane varies with frequency between 90° and 60°. Thus, a reflector is designed with the feed subtended angle of 70°. This results in the focal length to reflector diameter ratio (f/D) of approximately 0.8. In Fig. 9, *PEL* due to axial defocusing of the feed is given at E and H-planes. These errors are determined from measured patterns at E and H-planes separately by using the wavelength and beamwidth of the corresponding frequency. Different positioning of the UWB feed antenna in the reflector system result in different *PEL* levels. Placing the centre of the feed antenna to the focus of the reflector may result in very high *PEL*s (up to 10 dB in some cases). Thus, the positioning of the Vivaldi feed antenna is determined as the location giving the lowest *PEL*s in E and H-planes. The phase centre locations at every frequency within the band are tried. The location giving the minimum (lower than 1 dB for the whole frequency band) *PEL*s both in E and H-planes is chosen as point to be placed at the focus of the reflector. It is determined as $\boldsymbol{z}$ = 14.5 *cm*, which is the phase centre location approximately at 4 GHz, in E and H-planes. The losses are obtained by both the approximate formulation given in equation (3) and integration of the radiation pattern in Fig. 9. The solid lines are obtained from the approximate formulations and dashed lines are obtained by the integration of the measured feed patterns. In Fig. 9, it can be observed that phase error losses of the Vivaldi fed reflector system due to axial defocusing are less than 1 dB for the whole frequency band.

In optimization process, besides phase error losses due to axial defocusing, losses due to astigmatism should also be considered. Astigmatism is the result of unequal phase center positions in E and H-planes. Phase error loss due to astigmatism is not as high as the losses due to axial defocusing. For the measured Vivaldi antenna, it is calculated as less than 0.1 dB for the whole frequency band. This conclusion together with Fig. 9 proves that Vivaldi antenna, with its low *PEL*s can be successfully used in reflector applications.

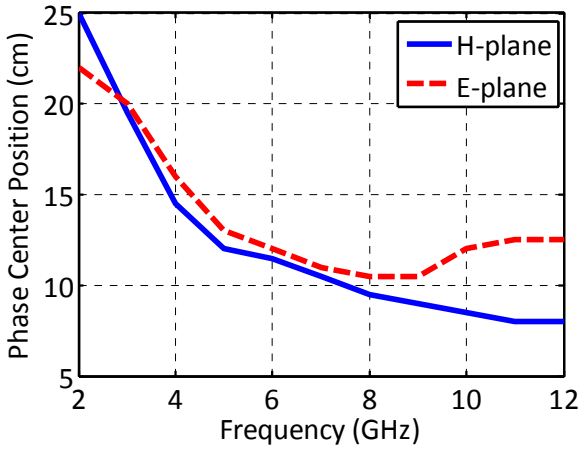

Fig. 8. Phase centre positions of the Vivaldi antenna at E and H-planes.

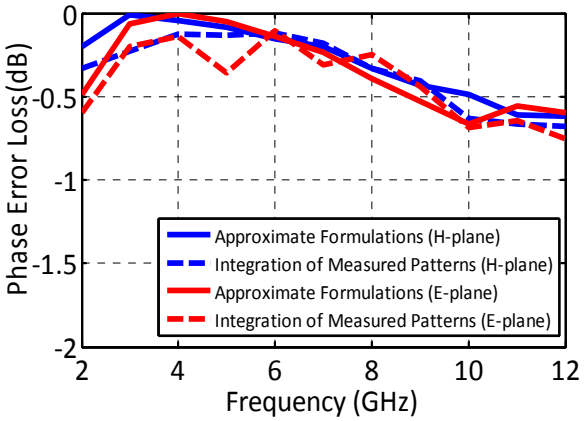

Fig. 9. Parabolloidal reflector phase error loss of the Vivaldi antenna due to axial defocusing of the feed.

IV. CONCLUSION

In reflector applications, it is desirable to have a single feed that covers the entire frequency band of operation with a symmetric, directive pattern, dual-linear polarization, and frequency invariant phase centre and radiation pattern [23]. To obtain a highly directive antenna, the size of the feed antenna should be enlarged, which results with more phase centre movement with the change in the frequency. Long antenna elements exhibit high phase-center instability, which is very undesirable characteristic when the antenna is used to illuminate a reflector. A trade-off is necessary between directivity and phase errors. In order to avoid phase-center instability, short elements can be used but then higher losses for spillover are obtained.

Vivaldi antennas are widely used antenna elements for the state-of-art applications of reflector antennas. In this work, performance of the Vivaldi antenna used as reflector feed is investigated. A long Vivaldi with high phase center variation in terms of wavelength is designed, manufactured, measured, and its consequent phase error losses are investigated. The results of the antenna analysis show that by appropriate positing of the feed antenna in the reflector system, the phase error losses due to axial defocusing and astigmatism resulting from the phase center variation with frequency can be lowered down to 1 dB levels. This proves the use of Vivaldi antennas in reflector applications.

REFERENCES

[1] U. Schwarz, F. Thiel, F. Seifert, R. Stephan, and M. A. Hein, "Ultrawideband antennas for magnetic resonance imaging navigator techniques," *IEEE Trans. Antennas Propagat*., vol. 58, no. 6, pp. 2107-2112, June 2010.

[2] N. Chahat, M. Zhadobov, R. Sauleau, and K. Ito, "A compact UWB antenna for on-body applications," *IEEE Trans. Antennas Propagat*., vol. 59, no. 4, pp. 1123-1131, April 2011.

[3] A. Ardenne, B. Smolders, and G. Hampson, "Active adaptive antennas for radio astronomy; results of the initial R&D program toward the square kilometer array," *Proceedings SPIE Conference 4015 Radio Telescope,* Munich, Germany, 2000.

[4] D. H. Schaubert, A. Ardenne, and C. Craeye, "The square kilometer array (SKA) antenna," *IEEE International Symposium on Phased Array Systems and Technology*, MA, USA, 2003.

[5] P. Hall, *The Square Kilometer Array: An Engineering Perspective*, Springer, 2005.

[6] C. Carilli and S. Rawlings, *Science with the Square Kilometre Array*, Elsevier, December 2004.

[7] J. Weem, Z. Popovic, and B. Notaros, "Vivaldi antenna arrays for SKA," *IEEE Antennas and Propagation Society International Symposium*, Utah, USA, 2000.

[8] P. Gibson, "The Vivaldi aerial," *Proc. of 9th European Microwave Conference*, pp. 101-105, 1979.

[9] T. Namas and M. Hasanovic, "Ultrawideband antipodal Vivaldi antenna for road surface scanner based on inverse scattering," *28th Annual Review of Progress in Applied Computational Electromagnetics (ACES)*, pp. 882-887, Columbus, Ohio, April 2012.

[10] E. Pancera, *Strategies for Time Domain Characterization of UWB Components and Systems*, Dissertation in Universität Karlsruhe (TH) Fakultät für Elektrotechnik und Informationstechnik, Germany, 2009.

[11] A. Mehdipour, K. Mohammadpour-Aghdam, and R. Faraji-Dana, "Complete dispersion analysis of Vivaldi antenna for ultra wideband applications," *Progress In Electromagnetics Research*, vol. 77, pp. 85-96, 2007.

[12] E. Pancera, T. Zwick, and W. Wiesbeck, "Spherical fidelity patterns of UWB antennas," *IEEE Trans. Antennas Propagat.*, vol. 59, pp. 2111-2119, 2011.

[13] P. Li and L. Jiang, "The far field transformation for the antenna modeling based on spherical electric field measurements," *Progress In Electromagnetics Research*, vol. 123, pp. 243-261, 2012.

[14] Q. Wu, B. Jin, L. Bian, Y. Wu, and L. Li, "An approach to the determination of the phase center of Vivaldi-based UWB antenna," *Proc. IEEE Antennas Propag. Society Int. Symp.*, Albuquerque, USA, 2006.

[15] H. Schantz, "Dispersion and UWB antennas," *Int. Workshop on UWB System Joint with Conf. on UWB Syst. and Tech.*, Huntsville, USA, 2004.

[16] C. Zhao, "Analysis on the properties of a coupled planar dipole UWB antenna," *IEEE Antennas and Wireless Propag. Lett.*, vol. 3, pp. 317-320, 2004.

[17] H. Moheb, A. Sebak, and L. Shafai, "Phase centre analysis of array antennas and its significance for microwave landing system," *IEE Conference on Antennas and Propagation*, York, UK, 1991.

[18] K. Jadoon, S. Lambot, E. Slob, and H. Vereecken, "Analysis of horn antenna transfer functions and phase-center position for modeling off-ground GPR," *IEEE Trans. Geoscience and Remote Sensing*, vol. 49, pp. 1649-1662, 2011.

[19] L. Li, J. Zhang, and X. Li, "Theoretical calculation and simulation of phase center of a radial line helical array antenna," *Int. Conf. on Microwave and Millimeter Wave Tech.*, Chengdu, China, 2010.

[20] M. Manteghi and Y. Rahmat-Samii, "Improved feeding structures to enhance the performance of the reflector impulse radiating antenna (IRA)" *IEEE Trans. Antennas Propagat*., vol. 54, no. 3, pp. 823-834, 2006.

[21] T. A. Milligan, *Modern Antenna Design*, Wiley-IEEE Press, 2005.

[22] The homepage of CST Microwave Studio http://www.cst.com/

[23] K. Lee, C. Chen, and R. Lee, "UWB dual-linear polarization dielectric horn antennas as reflector feeds," *IEEE Trans. Antennas Propagat*., vol. 55, pp. 798-804, 2007.

Nurhan Turker Tokan received her B.Sc. degree in Electronics and Communications Engineering from the Kocaeli University in 2002 and her M.Sc. and PhD degree in Communication Engineering from Yıldız Technical University (YTU), Istanbul, Turkey, in 2004 and 2009, respectively. From May 2003 to May 2009, she worked as a research assistant in the Electromagnetic Fields and Microwave Technique Section of the Electronics and Communications Engineering Department of YTU, Istanbul, Turkey. Since 2009, she is working as an Assistant Professor in the Electronics and Communications Engineering Department of YTU. From October 2011 to October 2012, she was Postdoctoral researcher in the EEMCS Department of Delft University of Technology, Delft, Netherlands. Since October 2012, she is a Postdoctoral Fellow at the Institute of Electronics and Telecommunications (IETR), University of Rennes 1, Rennes, France. She is the author or coauthor of more than 30 papers published in peer-reviewed international journals and conference proceedings. Her current research interests are analysis and design of antennas with emphasis on dielectric lens antennas, wideband antennas, and microwave circuits.

A Novel Antenna With Dual Band-Notched Characteristics using Shorting Pin and Z-Shaped Slot on Conductor Backed

M. Khodaee [1], M. Akbari [2], and S. Zarbakhsh [2]

[1] Faculty of Engineering, Department of Electrical Engineering
Shahid Beheshti University, Tehran, Iran
meghdadkhodaee2006@gmail.com

[2] Young Researchers and Elite club, Central Tehran Branch,
Islamic Azad University, Tehran, Iran
akbari.telecom@gmail.com and samanzarbakhsh@yahoo.com

Abstract ─ In this paper, a novel UWB antenna with dual notched bands is presented. The antenna consists of a square patch and a ground plane with a Ω-shaped slot, which increase the bandwidth from 2.7 GHz to 11.3 GHz. To achieve two bands stop, both Z-shaped slot on conductor backed plane and strip ended up a shorting pin are used. The designed antenna has a small size of 15 × 22 mm^2 while indicating the band-stop performance in the frequency bands of 3.1 GHz to 3.8 GHz and 5.1 GHz to 6.1 GHz in order.

Index Terms ─ Antennas, DGS (defected ground structure), notch band, and UWB (ultra wide band).

I. INTRODUCTION

In UWB communication systems, the design of a compact planar antenna whilst providing wideband characteristic over the whole operating band is one of main subjects. Consequently, plenty of microstrip antennas with various configurations have been experimentally characterized. Meanwhile, various strategies to rise the impedance bandwidth have been investigated [1-4]. However, The frequency range for UWB systems between 3.1 GHz and 10.6 GHz will cause interference to the existing wireless communication systems, namely, the wireless local area network (WLAN) for IEEE 802.11a operating at 5.15 GHz – 5.35 GHz and 5.725 GHz – 5.825 GHz, the IEEE 802.16 WiMAX system 3.3 GHz – 3.69 GHz, 5.25 GHz – 5.85 GHz, therefore, UWB antenna with a dual band stop performance is needful. To achieve the frequency band-notch function antenna, modified planar monopole antennas have been recently presented [5-8]. In this manuscript, a novel dual band-notch antenna is proposed. Related to it, to increase impedance bandwidth is used with an Ω-shaped slot in the ground plane. Also, based on electromagnetic coupling theory (ECT), single band-notched function is provided by inserting a Z-shaped slot on conductor backed plane. In addition, dual band-notch characteristic is obtained by using a strip ended up shorting pin. Good VSWR and radiation pattern characteristics are obtained in the frequency band of interest. Simulated and measured results are presented to validate the usefulness of the antenna structure for UWB applications.

II. ANTENNA DESIGN

Figure 1 exhibits the geometry of the proposed antenna. The antenna is fabricated on FR4 substrate with ε_r = 4.4, h = 1 mm, fed by a microstrip line and has a size of 15 × 22 mm^2. The microstrip feed line is designed for a 50 Ω characteristic impedance with fixed 1.9 mm feed line width and 7.5 mm length. It means that the antenna is connected to a 50 Ω SMA connector for signal transmission. The antenna contains a square patch with Wp = 10 mm and Lp = 13.5 mm, and a partial ground plane with length Lg = 5 mm. By cutting a novel Ω-shaped slot into the ground

Submitted On: Feb. 19, 2013
Accepted On: June 14, 2013

plane, as illustrated in Fig. 1, and carefully adjusting its parameters, impedance bandwidth enhancement may be achieved because they can adjust the electromagnetic coupling effects between the patch and the ground plane, and it can improve the impedance bandwidth without any cost of size or expense. Meanwhile, to obtain two notched bands has been used two different techniques, the former DGS (defected ground structure), and the latter shorting pin that will more be examined. Regarding to DGS, by inserting a Z-shaped slot in the conductor backed plane, a notched band at centre frequency 5.5 GHz can be earned while by using a strip line, with length W8 + L8, ended up shorting pin, another band stop at centre frequency 3.5 GHz is obtained.

III. ANTENNA PERFORMANCE AND DISCUSSION

In this section, the square monopole antenna with different design parameters are constructed, and the numerical and experimental results of the input impedance and radiation characteristics are presented and discussed. The parameters of this proposed antenna are studied by changing one parameter at a time and fixing the others. The simulated results are achieved using the Ansoft simulation software high-frequency structure simulator [9]. Table I gives optimal dimensions of the designed antenna. Figure 2 shows the structure of two different square antennas. As illustrated in Fig. 3, VSWR (voltage standing wave ratio) characteristics for both antennas shown in Fig. 2 is compared to each other. It is quite apparent that by inserting an Ω-shaped slot in the ground plane, it can adjust the electromagnetic coupling effects between the patch and the ground plane, which result in creating the third resonance at nearly 11 GHz and increasing the impedance bandwidth.

Figure 4 illustrates three antenna structures indicating major elements of creator filtering properties in the WiMAX/WLAN bands stop-bands including the Z-shaped slot in the conductor backed plane and the strip line ended up a shorting pin. Figure 5 shows the VSWR characteristics for the three mentioned antennas shown in Fig. 4. From the results, it is found that the Z-shaped slot in the conductor backed plane have main effect on the notched band at center frequency 5.5 GHz. Whereas the strip line ended up a shorting pin creates a stop band at center frequency 3.5 GHz to filter WLAN and WiMAX bands in order. Meanwhile, it is found out that both notches are autonomous than each other. It means that they have no effect on each other. It is interesting to note that by adjusting the length of the set of parameters, the centre frequencies of the notched bands can be controlled. Figure 6 illustrates the VSWR of the antenna for different values of W7. As shown in Fig. 6, parameter W7 has a considerable influence on frequency shifting in a way that by varying W7, the centre frequencies of the notched bands can be finely tuned. By selecting the optimum parameter W7 = 9.1 mm, the frequency notched-band centered at 5.5 GHz can be achieved.

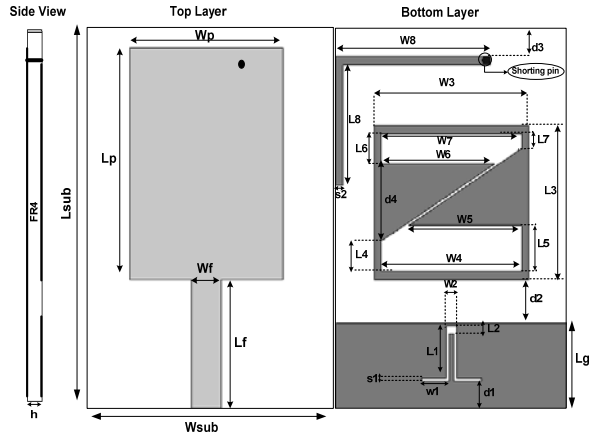

Fig. 1. Geometry of the proposed antenna.

Table I: Optimal parameter values of the antenna.

Wsub	Lsub	Wp	Lp	Wf	Lf	Lg	W1
15	22	10	13.5	1.9	7.5	5	1.8
L1	W2	L2	W3	L3	W4	L4	W5
3	0.7	0.4	10	9	9.1	1.75	7.35
L5	W6	L6	W7	L7	W8	L8	d1
2.65	7.35	1.75	9.1	0.85	10	7	1.6
d2	d3	d4	S1	S2	h	ε_r	δ
2.5	0.5	4.5	0.2	0.5	1	4.4	0.02

As mentioned before, in this study, to obtain the band-stop performance on WiMAX band with center frequency 3.5 GHz, a strip line is used with length W8+L8 that has been connected to a shorting pin. The simulated VSWR curves with different values of L8 are plotted in Fig. 7. As shown in Fig. 7, when L8 increases, the center frequency of the notched band is fallen and vice versa. Therefore, the optimized L8 is 7 mm. From

these results, we can conclude that the notch frequencies are controllable by changing values W7 and L8.

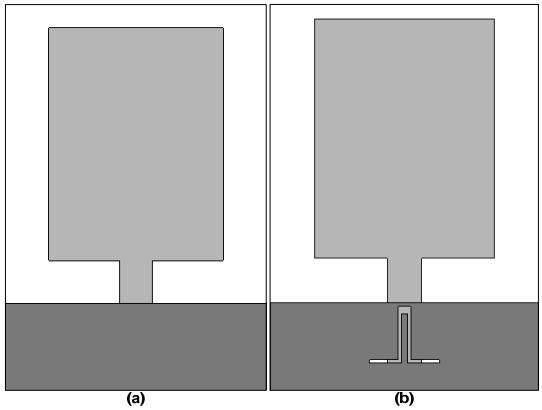

Fig. 2. (a) The simple square antenna and (b) the antenna with an Ω-shaped slot in the ground plane.

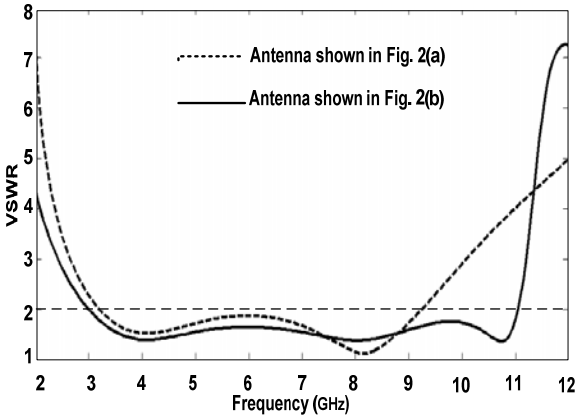

Fig. 3. Simulated VSWR characteristics for the diverse square antennas shown in Fig. 2.

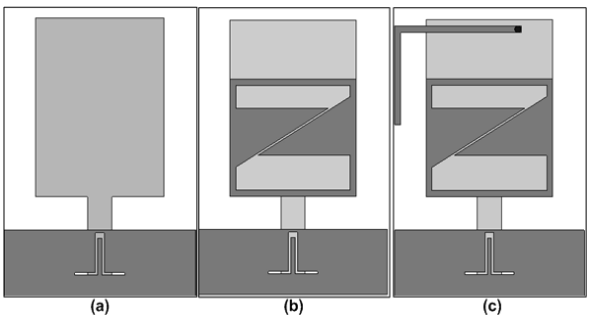

Fig. 4. (a) The simple square antenna, (b) the square antenna with a Z-shaped slot in the conductor backed plane, and (c) the proposed antenna.

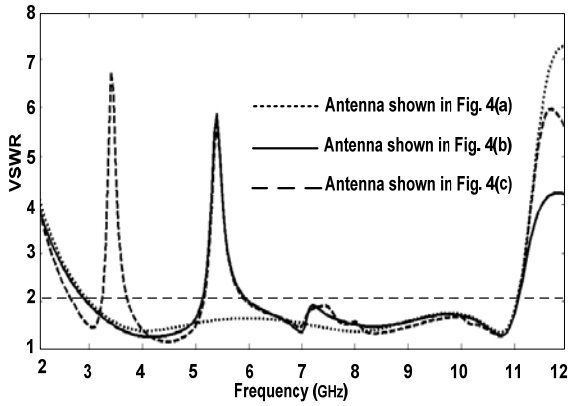

Fig. 5. Simulated VSWR characteristics for the antennas shown in Fig. 4.

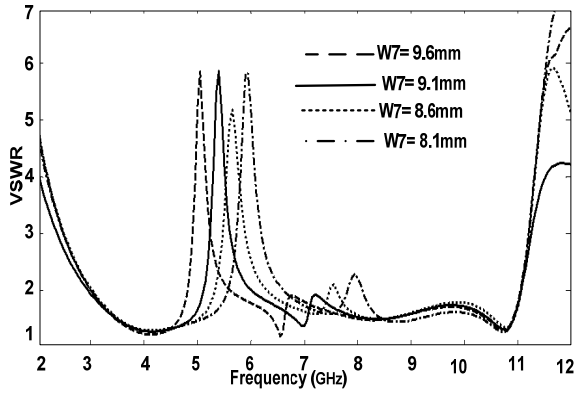

Fig. 6. Simulated VSWR characteristics of the antenna with a Z-shaped slot in the conductor backed plane with different values of W7.

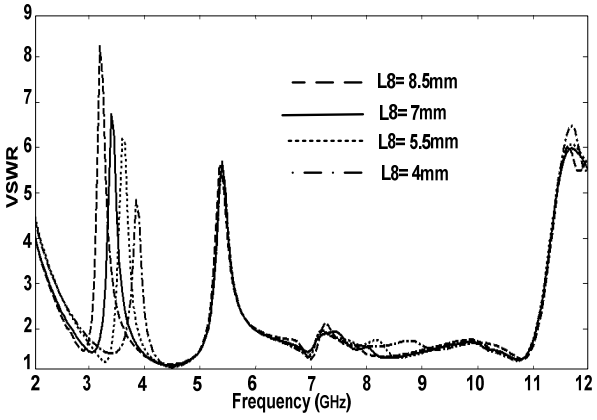

Fig. 7. Simulated VSWR characteristics of the antenna with a strip line ended up shorting pin with different values of L8.

To be clear more, Fig. 8 is used indicating the simulated current distributions on the antenna. It can be observed that at 5.5 GHz the greatest current is concentrated in the conductor backed plane with Z-shaped slot while at 3.5 GHz the most current distribution is seen on the strip line.

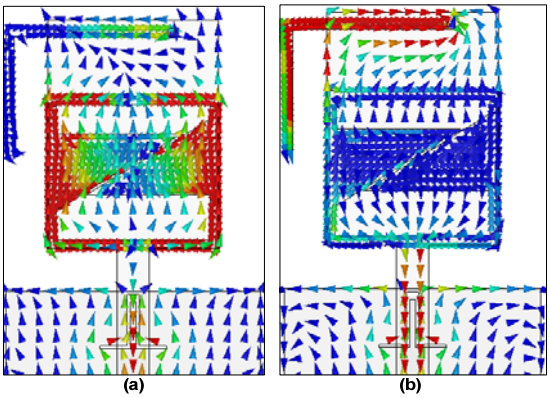

Fig. 8. Simulated surface current distributions (a) on the conductor backed plane at 5.5 GHz and (b) on the strip line at 3.5 GHz.

The photo of the fabricated antenna with optimal design is exhibited in Fig. 9. Besides, the antenna was tested in the antenna measurement laboratory at Iran Telecommunication Research Center. The measured VSWR of the proposed antenna, using an Agilent 8722ES vector network analyzer, is also shown in Fig. 10. It can be seen that the designed antenna has a wideband performance from 2.7 GHz to 11.3 GHz for VSWR $\leq$ 2, with dual notched bands of 3.1 GHz – 3.8 GHz and 5.1 GHz – 6.1 GHz. As shown in Fig. 10, there is a discrepancy between measured data and simulated results, and this could be due to the effect of the SMA port. To confirm the accurate VSWR characteristics for the designed antenna, it is recommended that the manufacturing and measurement process need to be performed carefully.

Figure 11 depicts the measured gain of the proposed antenna with and without notched bands. A sharp drop of gain is displayed in the notched frequencies band at 3.5 GHz and 5.5 GHz. For other frequencies outside the notched frequency band, the antenna gain with the slot is similar to those without it. Figure 12 exhibits simulated radiation efficiency of the proposed antenna. Radiation efficiency for over band is more than 90 % except two stop bands, which these results are exactly reasonable. On the other hand, Fig. 13 shows the measured normalized far-field radiation patterns in both H-plane (x–z plane) and E-plane (y–z plane) at frequencies 6.5 GHz and 8.5 GHz. It can be observed that the radiation patterns in the x–z plane are approximately omni-directional for the two frequencies whilst radiation pattern in the y-z plane are nearly a dipole-like.

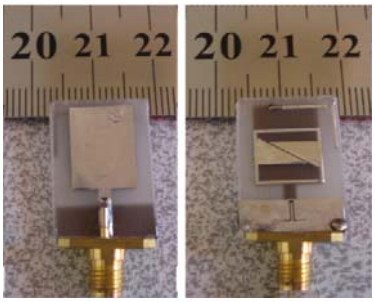

Fig. 9. Photograph of the fabricated antenna.

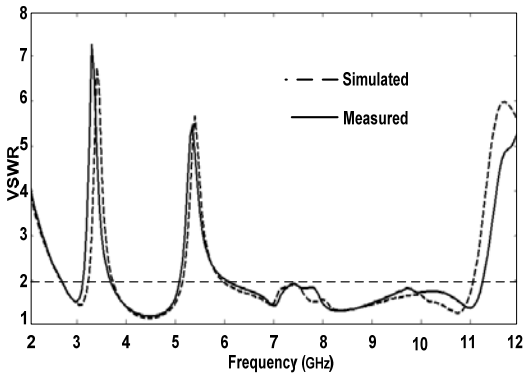

Fig. 10. Measured and simulated VSWR characteristics for the proposed antenna.

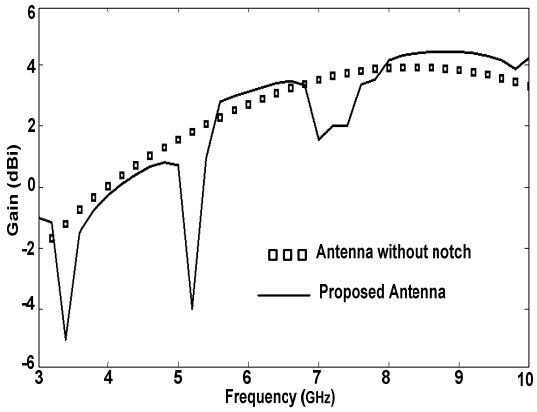

Fig. 11. Measured antenna gain of the proposed antenna without and with stop bands.

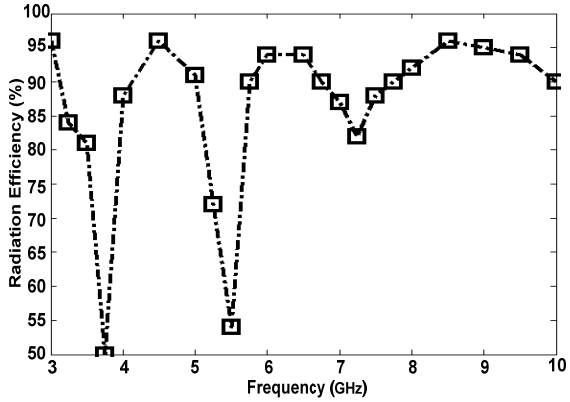

Fig. 12. Simulated radiation efficiency of the proposed antenna.

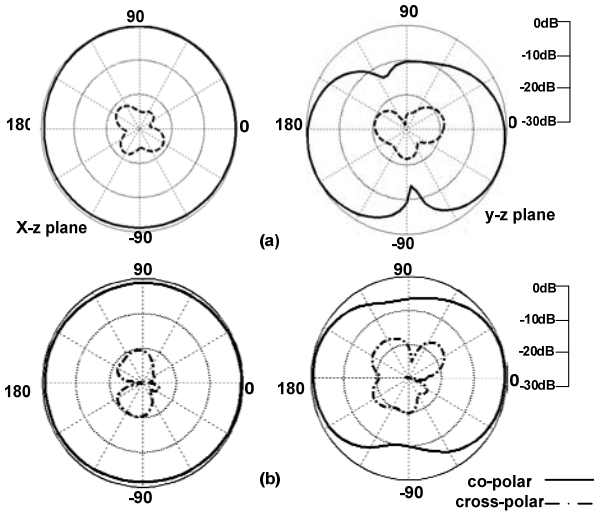

Fig. 13. Measured radiation patterns of the proposed antenna at (a) 6.5 GHz and (b) 8.5 GHz.

IV. CONCLUSION

A novel compact UWB antenna with dual band-notched characteristics has been proposed and discussed. In this design, by using an Ω-shaped slot, a wide impedance bandwidth from 2.7 GHz to 11.3 GHz with VSWR ≤ 2 is achieved. Furthermore, by applying a conductor backed plane with Z-shaped slot on it and a strip line ended up shorting pin, two frequency notched bands of 3.1 GHz – 3.8 GHz and 5.1 GHz – 6.1 GHz are obtained. The designed antenna has a small size of 15 × 22 mm^2. The good impedance matching characteristic, constant gain, and omni-directional radiation patterns makes this antenna a good candidate to be used in UWB applications and systems.

REFERENCES

[1] M. Mighani, M. Akbari, and N. Felegari, "Design of a small rhombic monopole antenna with parasitic rectangle into slot of the feed line for SWB application," *The Applied Computational Electromagnetics Society (ACES) Journal*, vol. 27, no. 1, pp. 74-79, 2012.

[2] M. Akbari, M. Koohestani, Ch. Ghobadi, and J. Nourinia, "Compact CPW-fed printed monopole antenna with super wideband performance," *Microwave Opt. Techn. Lett.*, vol. 53, pp. 1481-1483, 2011.

[3] M. Akbari, M. Koohestani, Ch. Ghobadi, and J. Nourinia, "A new compact planar UWB monopole antenna," *International Journal of RF and Microwave Computer-Aided Engineering*, vol. 21, pp. 216-220, 2011.

[4] M. Mighani, M. Akbari, and N. Felegari, "A CPW dual band notched UWB antenna," *The Applied Computational Electromagnetics Society (ACES) Journal*, vol. 27, no. 4, pp. 352-359, 2012.

[5] M. Abdollahi, H. Oskouei, M. Akbari, and M. Mighani, "A novel compact UWB antenna with triple band-notches for WiMAX/ WLAN/ ITU bands," *The Applied Computational Electromagnetics Society (ACES) Journal*, vol. 27, no. 12, pp. 1014-1021, 2012.

[6] A. A. Eldek, "Numerical analysis of a small ultra wideband microstrip-fed tap monopole antenna," *Prog. Electromag. Research (PIER)*, vol. 65, pp. 59-69, 2006.

[7] M. Ojaroudi, Gh. Ghanbari, N. Ojaroudi, and Ch. Ghobadi, "Small square monopole antenna for UWB applications with variable frequency band-notch function," *IEEE Antennas Wirel. Propag. Lett.*, vol. 8, pp. 1061-1064, 2009.

[8] R. Rouhi, Ch. Ghobadi, J. Nourinia, and M. Ojaroudi, "Ultra-wideband small square monopole antenna with band notched function," *Microwave Opt. Technol. Lett.*, vol. 52, pp. 2065-2069, 2010.

[9] Ansoft High Frequency Structure Simulation (HFSS), Ver. 10, Ansoft Corporation, Pittsburgh, PA, 2005.

Meghdad Khodaee was born in Ilam, Iran, in 1986. He received B.Sc. degree in Electrical Engineering from Zanjan University, Zanjan, Iran and M.Sc. degrees in Electrical Engineering at Shahid Beheshti Univesity, Tehran, Iran. His research interests include antenna theory, microwave active circuits and RF communication links.

Mohammad Akbari was born on February 3, 1983 in Tehran, Iran. He received his B.Sc. degree in Electrical Engineering at Bahonar University of Kerman, Iran, in 2007 and M.Sc. degrees in Electrical Engineering at Urmia University, Urmia, Iran, in 2010. His research interests include analysis and design of antennas, design and modeling of microwave structures, radar systems, and electromagnetic theory. He has taught courses in microwave engineering, antenna theory, and fields and waves, and electromagnetic in Aeronautical University, Tehran, Iran. He is author and coauthor of approximately 30 journals and international conference papers.

Saman Zarbakhsh was born on January 7, 1984 in Tehran, Iran. He received his B.Sc. degree in Electrical Engineering at Azad university of South Tehran University, Tehran, Iran, in 2007 and M.Sc. degrees in Electrical Engineering from Urmia University, Urmia, Iran, in 2010. His research interests contain antenna design, antenna miniaturization and broadband circular polarized antennas. He has taught courses in Electronics at Azad university of Shahr Rey University, Tehran, Iran.

CPW-Fed Slot-Like Sleeve-Monopole Antenna with Bandwidth Enhancement for UWB Wireless Communications

S. Bashiri [1], Ch. Ghobadi [1], J. Nourinia [1], and M. Ojaroudi [2]

[1] Department of Electrical Engineering
Urmia University, Urmia, Iran
st_s.bashiri@urmia.ac.ir, ch.ghobadi@urmia.ac.ir, and j.nourinia@urmia.ac.ir

[2] Young Researchers Club
Ardabil Branch, Islamic Azad University, Ardabil, Iran
m.ojaroudi@iauardabil.ac.ir

Abstract ─ This paper proposes a novel slot-like sleeve-monopole antenna for ultra wideband applications with multi-resonances performance. The antenna consists of a CPW-fed sleeve monopole antenna with a coupled inverted U-shaped strip, surrounded by a pair of folded strips, which provides a wide usable fractional bandwidth of more than 120 % (3.09 GHz - 12.86 GHz). By adding a coupled inverted U-shaped strip with variable dimensions on the radiating patch and also by inserting two folded strips, additional resonances are excited and hence much wider impedance bandwidth can be produced, especially at the higher band. The designed antenna has a small size of 30 × 30 mm^2. Simulated and experimental results obtained for this antenna show that it exhibits good radiation behavior within the UWB frequency range.

Index Terms ─ Coupled inverted U-shaped strip, slot-Like sleeve-monopole antenna, and ultra wideband communications.

I. INTRODUCTION

Commercial UWB systems require small low-cost antennas with omnidirectional radiation patterns and large bandwidth [1]. It is a well-known fact that planar monopole and slot antennas present really appealing physical features, such as simple structure, small size, and low cost. Due to all these interesting characteristics, planar monopoles and slots are extremely attractive to be used in emerging UWB applications, and growing research activity is being focused on them.

In UWB communication systems, one of the key issues is the design of a compact antenna while providing wideband characteristic over the whole operating band. Consequently, number of printed microstrip slot and monopole antennas with different geometries have been experimentally characterized [2, 3] and automatic design methods have been developed to achieve the optimum planar shape [4, 5]. Moreover, other strategies to improve the impedance bandwidth have been investigated [6-9].

A simple method for designing a novel and compact CPW-fed slot-like sleeve-monopole antenna with multi resonance performance for UWB applications has been presented. In the proposed structure, based on electromagnetic coupling theory (ECT), by inserting a coupled inverted U-shaped strip, surrounded by a pair of folded strips, on the sleeve monopole antenna, additional resonances are excited and the bandwidth is improved that achieves a fractional bandwidth with multi resonance performance of more than 120 %. Good return loss and radiation patterns characteristics are obtained in the frequency band of interest. Simulated and measured results are presented to validate the usefulness of the proposed antenna structure for UWB applications.

Submitted On: July 27, 2012
Accepted On: Aug. 29, 2013

II. ANTENNA DESIGN

The proposed slot-like sleeve-monopole antenna fed by a 50 Ω coplanar waveguide (CPW) line is shown in Fig. 1, which is printed on an FR4 substrate of thickness 1.6 mm and permittivity 4.4. The basic antenna structure consists of a CPW-fed monopole antenna with a pair of sleeves and a coupled inverted U-shaped strip, surrounded by a pair of folded strips. The proposed antenna is connected to a 50 Ω SMA connector for signal transmission.

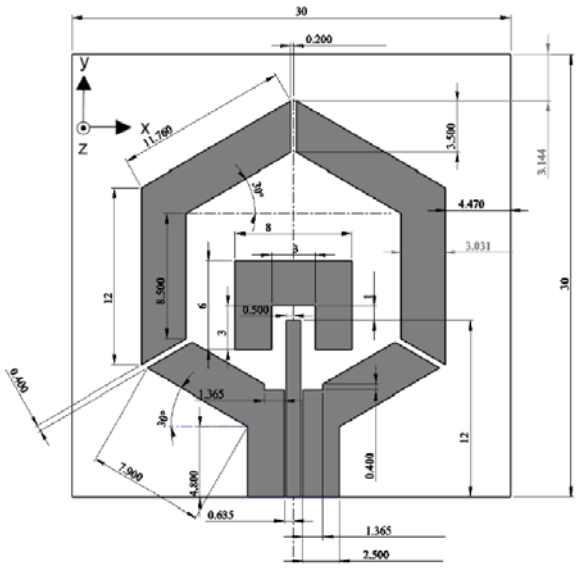

Fig. 1. Geometry of the proposed antenna (unit: mm).

In this study, the modified inverted U-shaped coupled strip act as an impedance matching element to control the impedance bandwidth of the proposed antenna, because it can creates additional surface current paths in the antenna therefore, additional resonance is excited and hence, much wider impedance bandwidth can be produced, especially at the higher band [10]. The electrical current for the exited resonance frequency does change direction along the surface of the coupled strip. Additionally, based on electromagnetic coupling theory, the folded parasitic strips, are placed around the coupled inverted U-shaped strip, and act as parasitic half-wave resonant structure electrically coupled to the sleeve monopole antenna with a coupled inverted U-shaped strip. They perturb the resonant response and also act as a half-wave resonant structure. At the new resonance frequencies, the current flows are more dominant around the parasitic elements [10].

III. RESULTS AND DISCUSSIONS

In this section, the proposed antenna with various design parameters were constructed, and the numerical and experimental results of the input impedance and radiation characteristics are presented and discussed. The simulated results are obtained using the Ansoft simulation software high-frequency structure simulator (HFSS) [11]. Figure 2 shows the structure of various antennas used for multi-resonance performance simulation studies. Return loss characteristics for ordinary CPW-fed monopole antenna (Fig. 2 (a)), with a pair of rectangular sleeves (Fig. 2 (b)), with a pair of rectangular sleeves and a coupled inverted U-shaped strip (Fig. 2 (c)), and the proposed antenna structure (Fig. 2 (d)) are compared in Fig. 3. As shown in Fig. 3, it is observed that by using these coupled elements including a coupled inverted U-shaped strip, and by inserting a pair of coupled folded strips on the sleeve monopole antenna, additional third and fourth resonances are excited, respectively, and hence the bandwidth is increased.

As shown in Fig. 3, in the proposed antenna configuration, the ordinary sleeve monopole can provide the fundamental and next higher resonant radiation band at 4.5 GHz and 8.48 GHz, respectively, in the absence of the coupled elements. To design a novel antenna, also in order increase the upper frequency bandwidth, a coupled inverted U-shaped strip is inserted in the radiating patch of the sleeve monopole antenna as displayed in Fig. 1. The upper frequency bandwidth is significantly affected by using the coupled inverted U-shaped strip. This behavior is mainly due to the change of the surface current path by the dimensions of the inverted U-shaped strip as shown in Fig. 4 (b). This figure shows that the electrical current for the third resonance frequency (9.8 GHz) does change direction along the coupled inverted U-shaped strip. Therefore, the antenna impedance changes at this frequency, the radiating power and bandwidth will increases. Furthermore, the radiation efficiency will increase. However, the resonant resistance is decreased [6]. In addition, by inserting two coupled folded strips the impedance bandwidth is effectively improved at the upper frequency [10]. The inverted coupled

folded strips can be regarded as a parasitic resonator electrically coupled to the sleeve monopole with the coupled inverted U-shaped strip. It is found that by inserting these folded strips of suitable dimensions at the antenna; much wider impedance bandwidth can be produced, especially at the higher band. As shown in Figs. 4 (a) and (c), the current is concentrated on the edges of the interior and exterior of the coupled folded strips at second (6.15 GHz) and fourth (12.2 GHz) resonance frequencies, respectively.

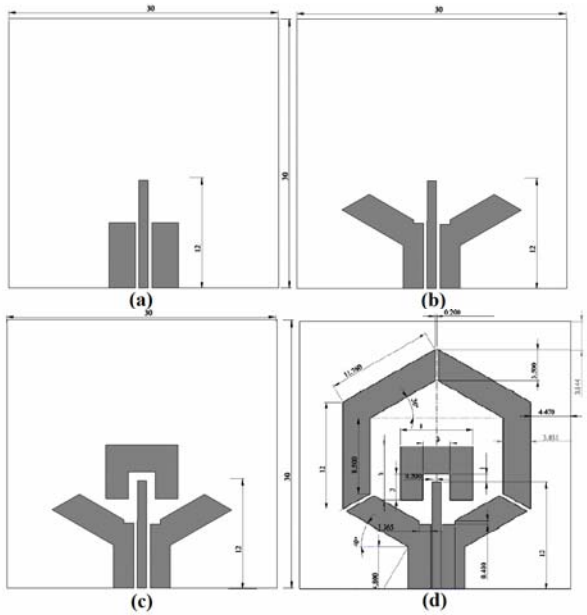

Fig. 2. (a) The basic structure (CPW-fed monopole antenna), (b) the sleeve monopole antenna, (c) sleeve monopole antenna with a coupled inverted U-shaped strip, and (d) the proposed antenna.

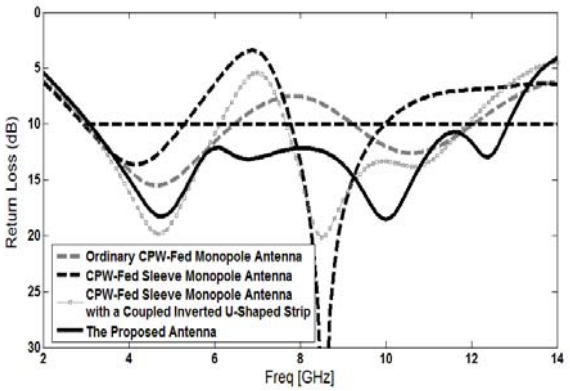

Fig. 3. Simulated return loss characteristics for the antennas shown in Fig. 2.

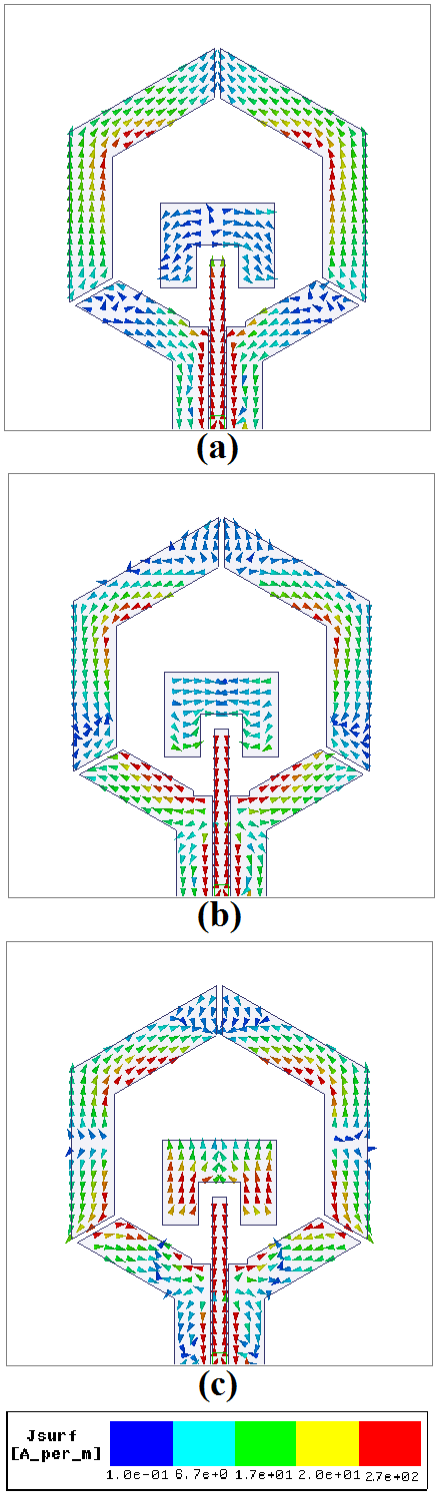

Fig. 4. Simulated surface current distributions for the proposed antenna shown in Fig. 1 at new exited resonance frequencies, (a) 6.15 GHz (second resonance frequency), (b) 9.8 GHz (third resonance frequency), and (c) 12.2 GHz (fourth resonance frequency).

The simulated radiation efficiencies of the proposed antenna are shown in Fig. 5. Results of the calculations using the software HFSS indicated that the proposed antenna features a good efficiency, being greater than 82 % across the entire radiating band. The proposed antenna with optimal design, as shown in Fig. 6, was built and tested in the antenna measurement laboratory at Iran Telecommunication Research Center (ITRC). Figure 7 shows the measured and simulated return loss characteristics of the proposed antenna. The fabricated antenna has the frequency band of 3.09 GHz to over 12.86 GHz. As shown in Fig. 7, there exists a discrepancy between measured data and the simulated results. This discrepancy between measured and simulated results is mostly due to a number of parameters such as the fabricated antenna dimensions as well as the thickness and dielectric constant of the substrate on which the antenna is fabricated, the wide range of simulation frequencies and also the effect of SMA soldering. In order to confirm the accurate VSWR characteristics for the designed antenna, it is recommended that the manufacturing and measurement process need to be performed carefully, besides, SMA soldering accuracy and FR4 substrate quality needs to be taken into consideration. In conclusion, as the slot is a short radiator, the SMA connector can modify its impedance matching [4, 5].

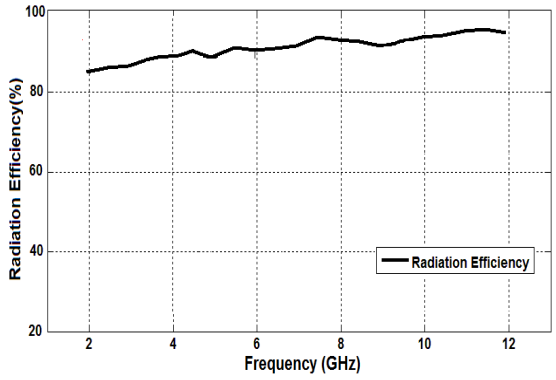

Fig. 5. Simulated radiation efficiency values of the proposed monopole antenna.

Fig. 6. Photograph of the realized printed slot-like sleeve monopole antenna.

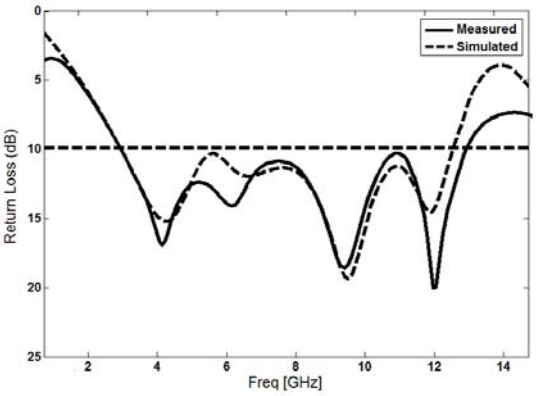

Fig. 7. Measured and simulated return loss characteristics of the proposed antenna.

Figure 8 shows the measured radiation patterns including the co- and cross-polarized in the *H*- (*x*-*z* plane) and *E*-planes (*y*-*z* plane). The main purpose of the radiation patterns is to demonstrate that the antenna actually radiates over a wide frequency band. It can be seen that the radiation patterns in the *x*-*z* plane are nearly omnidirectional even at higher frequencies, and also the cross-polarization level is low for the three frequencies.

Figure 9 shows the simulated and measured maximum gain of the proposed antenna in the *z*-axis direction (*x*-*z* plane). As shown in Fig. 9, the proposed structure has a gain that is low at 2 GHz and increases with frequency [8]. Reasonable agreement between simulations and measurements is demonstrated.

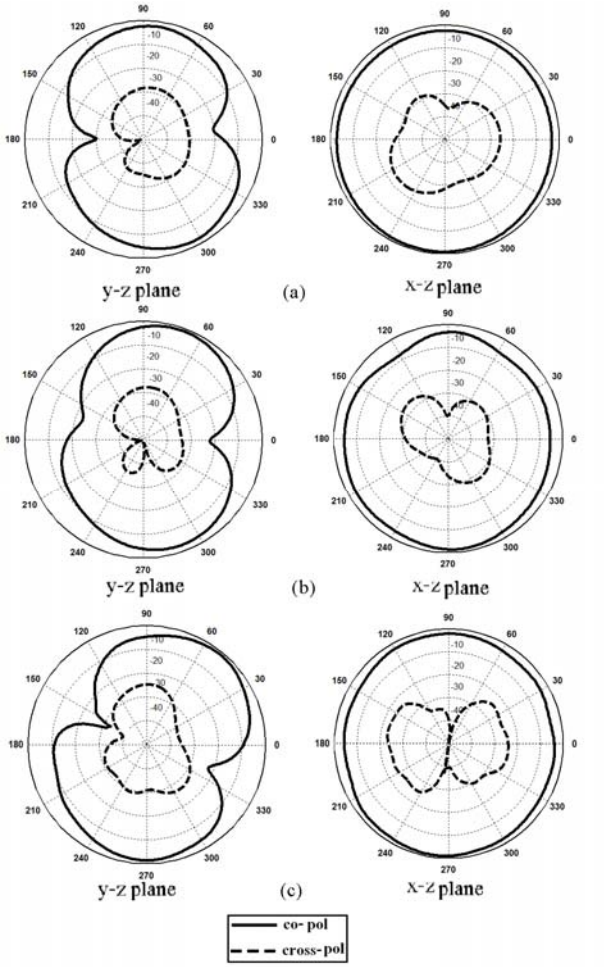

Fig. 8. Measured radiation patterns of the proposed antenna at (a) 6.15 GHz (second resonance frequency), (b) 9.8 GHz (third resonance frequency), and (c) 12.2 GHz (fourth resonance frequency).

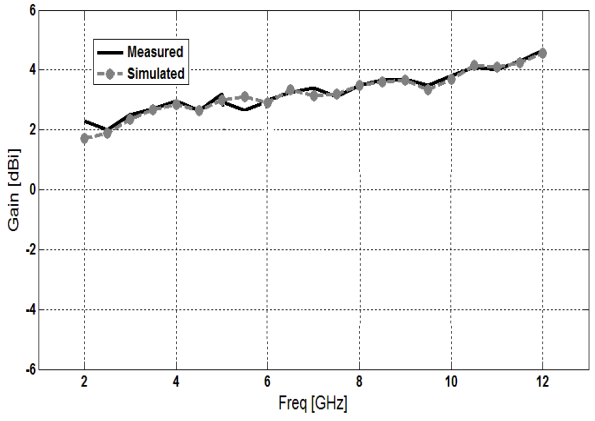

Fig. 9. Measured and simulated maximum gain of the proposed antenna in the *z*-axis direction (*x*-*z* plane).

IV. CONCLUSION

In this paper, a novel slot-like sleeve monopole antenna with multi-resonance characteristics and wide bandwidth capability for UWB applications is proposed. In this design, the proposed antenna can operate from 3.09 GHz to 12.86 GHz. By adding a coupled inverted U-shaped strip and also by inserting a pair of coupled folded strips with variable dimensions on the radiating patch of a CPW-fed sleeve monopole antenna, additional resonances are excited and hence much wider impedance bandwidth can be produced, especially at the higher band. The designed antenna has a small size. Good return loss and radiation pattern characteristics are obtained in the frequency band of interest. Simulated and experimental results show that the proposed antenna could be a good candidate for UWB applications.

ACKNOWLEDGMENT

The authors are thankful to Microwave Technology (MWT) Company staff for their beneficial and professional help (www.microwave-technology.com).

REFERENCES

[1] M. Ojaroudi and A. Faramarzi, "Multi-resonance small square slot antenna for ultra-wideband applications," *Microwave and Optical Tech. Letters*, vol. 53, no. 9, Sep. 2011.

[2] M. Partovi, N. Ojaroudi, and M. Ojaroudi, "Small slot antenna with enhanced bandwidth and band-notched performance for UWB applications," *Applied Computational Electromagnetics Society (ACES) Journal*, vol. 27, no. 9, pp. 772-778, Sep. 2012.

[3] B. H. Siahkal-Mahalle, M. Ojaroudi, and N. Ojaroudi, "Enhanced bandwidth small square monopole antenna with band-notched functions for UWB wireless communications," *Applied Computational Electromagnetics Society (ACES) Journal*, vol. 27, no. 9, pp. 759-765, Sep. 2012.

[4] M. Ojaroudi, N. Ojaroudi, and Y. Ebazadeh, "Dual band-notch small square monopole antenna with enhanced bandwidth characterestics for UWB applications," *Applied Computational Electromagnetics Society (ACES) Journal*, vol. 27, no. 5, pp. 420-426, May 2012.

[5] A. Valizade, Ch. Ghobadi, J. Nourinia, N. Ojaroudi, and M. Ojaroudi, "Band-notch slot antenna with enhanced bandwidth by using Ω shaped strips protruded inside rectangular slots for

UWB applications," *Applied Computational Electromagnetics Society (ACES) Journal*, vol. 27, no. 10, pp. 816-822, Oct. 2012.

[6] G. Zhang, J. S. Hong, B. Z. Wang, and G. Song, "Switched band-notched UWB/WLAN monopole antenna," *Applied Computational Electromagnetics Society (ACES) Journal*, vol. 27, no. 3, pp. 256-260, March 2012.

[7] M. Ojaroudi, Ch. Ghobadi, J. Nourinia, and N. Ojaroudi, "Ultra-wideband small square monopole antenna with dual band notched function," *Microwave and Optical Tech. Letters*, vol. 54, no. 2, pp. 372-374, Feb. 2012.

[8] S. Yzadanifard, R. A. Sadeghzadeh, and M. Ojaroudi, "Ultra-wideband small square monopole antenna with variable frequency band-notch function," *Progress In Electromagnetics Research C*, vol. 15, pp. 133-144, 2010.

[9] X. L. Ma, W. Shao, and G. Q. He, "A novel dual narrow band-notched CPW-fed UWB slot antenna with parasitic strips," *Applied Computational Electromagnetics Society (ACES) Journal*, vol. 27, no. 7, pp. 581-586, July 2012.

[10] Z. L. Zhou, L. Li, and J. S. Hong, "A novel compact monopole antenna with triple high quality rejected bands for UWB applications," *Applied Computational Electromagnetics Society (ACES) Journal*, vol. 27, no. 8, pp. 654-659, August 2012.

[11] Ansoft High Frequency Structure Simulation (HFSS), Ver. 13, Ansoft Corporation, 2010.

Sepideh Bashiri was born on 1986 in Marand, Iran. She received her B.Sc. degree in Electrical Engineering from Tabriz University,and M.Sc. degree in Telecommunication Engineering from Urmia University in 2012 . Her research interests include analysis and design of microstrip antennas, design and modeling of microwave structures, radar systems, and electromagnetic theory. Her research interests include monopole antenna, slot antennas, microstrip antennas for radar systems, ultra-wideband (UWB) and small antennas for wireless communications, microwave passive devices and circuits, and microwave/millimeter systems.

Changiz Ghobadi was born in June, 1960 in Iran. He received his B.Sc. in Electrical Engineering-Electronic and M.Sc. degrees in Electrical Engineering-Telecommunication from Isfahan University of Technology, Isfahan, Iran and Ph.D. degree in Electrical-Telecommunication from University of Bath, Bath, UK in 1998. From 1998 he was an Assistant Professor and now he is an Associated Professor in the Department of Electrical Engineering of Urmia University, Urmia, Iran. His primary research interests are in antenna design, radar and adaptive filters.

Javad Nourinia received his B.Sc. in Electrical and Electronic Engineering from Shiraz University and M.Sc. degree in Electrical and Telecommunication Engineering from Iran University of Science and Technology, and Ph.D. degree in Electrical and Telecommunication from University of Science and Technology, Tehran Iran in 2000. From 2000 he was an Assistant Professor and now he is an Associate Professor in the Department of Electrical Engineering of Urmia University, Urmia, Iran. His primary research interests are in antenna design, numerical methods in electromagnetic, and microwave circuits.

Mohammad Ojaroudi was born in 1984 in Germi, Iran. He received his B.Sc. degree in Power Electrical Engineering from Azad University, Ardabil Branch and M.Sc. degree in Telecommunication Engineering from Urmia University. From 2010, he is working toward the Ph.D. degree at Shahid Beheshti University. Also from July 2013 he has been working, as a research visitor in Dr. Fathy laboratory in University of Tennessee, Knoxville, USA. From 2007 until now, he is a Teaching Assistant with the Department of Electrical Engineering, Islamic Azad University, Ardabil Branch, Iran.

Since March 2009, he has been the Chief Executive Officer (CEO) in the Microwave Technology (MWT) company, Tehran, Iran. From 2012, Dr. Ojaroudi is a member of the IEEE Transaction on Antennas and Propagation (APS) reviewer group and the Applied Computational Electromagnetic Society. His research interests include analysis and design of microstrip antennas, design and modeling of microwave structures, radar systems, and electromagnetic theory. He is author and coauthor of more than 120 journal and international conferences papers. His papers have more than 450 citations with 11 h-index.

A Novel Ultra-wideband Planar Antenna with Rejection of WLAN and ITU Bands

A. Subbarao and S. Raghavan

Department of Electronics and Communication Engineering
National Institute of Technology, Tiruchirappalli, 620015, India
subbarao_ka@yahoo.com and raghavan@nitt.edu

Abstract ─ A novel compact coplanar waveguide-fed ultra wideband (UWB) antenna is proposed with dual band-notched characteristics. The antenna consists of novel tapered patch and is printed on FR4 substrate with compact size of 18×23 mm^2. By inserting a novel parasitic strip in trapezoidal slot and a pair of L-shaped slots in metallic ground, dual band-notched characteristics are obtained. Parametric analysis is performed by studying the effects of geometrical parameters of antenna on various characteristics. The antenna operates from 3.1 GHz to 11.6 GHz with dual-notched bands of 5.1 GHz-6.2 GHz and 8 GHz-8.4 GHz to avoid potential interference from WLAN and ITU bands, respectively. The antenna is analyzed in both frequency and time domains. The measured results show that the antenna has stable radiation patterns, consistent gain over the entire operating band. The time domain group delay of antenna indicates good linear phase response. The main features that make the antenna suitable for UWB applications are compactness, simple configuration, and stable radiation patterns.

Index Terms ─ Dual notched bands, gain, parasitic strip, radiation pattern, trapezoidal slot, and UWB.

I. INTRODUCTION

UWB technology has become popular due to various features such as high speed data transmission of 100 Mbps to 1 Gbps and wide bandwidth. Federal communication commission (FCC) has assigned a frequency band from 3.1 GHz to 10.6 GHz for commercial UWB applications. Hence, design of UWB systems has become more attractive in both industry and academia. UWB antenna is a key component in UWB systems. The UWB antenna is popular for future applications due to ease of fabrication, compact size, and stable radiation characteristics. Small size antennas [1, 2] are required in industrial RF and microwave devices. Conventional compact microstrip antennas with ground plane exist for UWB applications. In microstrip antennas, small ground plane is present on substrate, which is on the opposite side of the patch for size reduction. The surface current on small ground plane is considerable and affects the performance of the antenna [3]. This can be solved by using coplanar waveguide (CPW) with patches such as elliptical [4], crescent [5] because feed structure, radiating patch and ground plane are constructed on the same side of the substrate and single metallic layer is present. CPW has less dispersion, large bandwidth, and low radiation leakage than microstrip line. CPW also offers low power consumption, low profile, and high data speed for transmitter. Since planar slot antennas [6-10] have attractive features such as ease of fabrication, small size and wide bandwidth, they have become popular for the design of UWB antennas. These slot antennas can be easily integrated with monolithic microwave integrated circuits (MMIC) and printed circuit boards. A non planar UWB tapered resistive horn antenna [11] is available in literature, which provides stable beam width.

UWB antenna faces serious interference problems. Several narrow band communication systems such as IEEE 802.11a wireless local area network (WLAN) bands (5.15 GHz - 5.35 GHz and 5.725 GHz - 5.825 GHz) and 8 GHz ITU band (8.025 GHz - 8.4 GHz) overlap with UWB. Hence, it is necessary to design UWB antennas with dual

Submitted On: Aug. 18, 2012
Accepted On: Aug. 27, 2013

band-notched characteristics to avoid interference between WLAN, ITU [12] bands and UWB. To meet these requirements of the UWB antenna, there are several band notched techniques like inserting arc-slot [2], square slot [13], pi-slot [14] in radiating structure, attaching bar [15], and placing parasitic elements near printed monopole [16, 17]. UWB antenna has various applications in ground penetrating radar, indoor multimedia communications, medical imaging, and radio frequency identification.

In this paper, a compact UWB slot antenna with dual band-notched characteristics is presented. By inserting a novel parasitic strip in the trapezoidal slot and a pair of L-shaped slots in the metallic ground, the interfering WLAN and ITU bands can be rejected, respectively. The configuration of the UWB antenna is introduced in section II. The effects of different geometrical parameters on the antenna are investigated and discussed in section III. The measured radiation patterns and gain of the antenna are presented in section IV. The group delay, which represents linear phase response, is analyzed. Time domain characteristics of the antenna are presented with transient behavior in section V. Section VI concludes the paper.

II. ANTENNA GEOMETRY AND DUAL BAND-NOTCHED DESIGN

The structure of the antenna is shown in Fig. 1. The antenna is printed on FR4 dielectric substrate with relative dielectric constant of ε_r = 4.4 and loss tangent of tanδ = 0.02. The antenna has tapered tuning stub at the centre, which is fed by CPW. The CPW feed has conductor width W_4 = 2 mm and dielectric height h = 2.4 mm. The CPW feed has a 50 Ω characteristic impedance and it is terminated by subminiature version A (SMA) connector. Pentagon on tapered structure indicates novel radiating patch and each side of the pentagon is 5 mm. The antenna has a compact size of 18 × 23 mm^2. It has small size when compared to [1-6, 8, 12-14, and 16-17].

A pair of L-shaped slots is inserted in the metallic ground to avoid potential interference from ITU band as shown in Fig. 1. When the length of the each L-slot is nearly equal to ¼ th of the guided wavelength λ_{g1}, the slot resonates at corresponding notch frequency $f_{ITU\text{-}notch}$ and acts like short circuit in parallel with input impedance of the antenna. This leads the pair of L-slots to behave like resonant structure and provides band-notched characteristic for proposed antenna by rejecting the band from 8 GHz to 8.4 GHz.

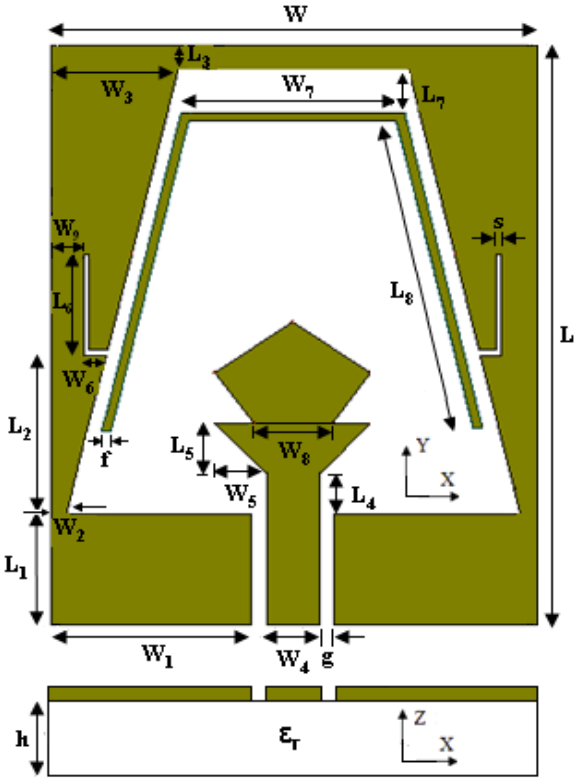

Fig. 1. Geometry of the proposed UWB antenna.

The total length of each L shaped slot is obtained by,

$$L_{L-slot} = \frac{\lambda_{g1}}{4} = \frac{c}{4 f_{ITU-notch} \sqrt{\frac{\varepsilon_r + 1}{2}}} \quad (1)$$

where λ_{g1} is the guided wavelength corresponding to the notch frequency of $f_{ITU\text{-}notch}$, c is the speed of light, and ε_r is the dielectric constant of FR4 substrate. Initially, a pair of L-slots is designed to resonate at $f_{ITU\text{-}notch}$ = 8 GHz by taking the total length of each L-slot nearly equal to $L_{L\text{-}slot}$ specified by equation (1). Practically, total length $L_{L\text{-}slot}$ of each L-slot is taken as 0.22 λ_{g1} and is represented in geometrical parameters of the antenna as $L_{L\text{-}slot}$ = W_6 + L_6. Hence, the pair of L-slots are responsible for rejection of 8 GHz - 8.4 GHz band. The ITU band-notched characteristic is

obtained by properly tuning geometrical parameters of the antenna around each L-slot.

Another band notched characteristic is obtained by inserting novel parasitic strip in the trapezoidal slot of the antenna to avoid interference from WLAN band. The total length of the parasitic strip is given by equation (2)

$$L_{strip} = \lambda_{g2} = \frac{c}{f_{strip-notch}\sqrt{\frac{\varepsilon_r + 1}{2}}}, \quad (2)$$

where λ_{g2} is the guided wavelength corresponding to the notch frequency of $f_{strip\text{-}notch}$. In this design, $f_{strip\text{-}notch}$ is 5.5 GHz. The total length L_{strip} is practically represented in parameters of the antenna as $L_{strip} = W_7 + 2\ L_8$. When L_{strip} is equal to λ_{g2} as specified in equation (2), destructive interference takes place, which makes antenna non responsive in the 5.1 GHz - 6.2 GHz band. Hence, WLAN band is rejected.

Method of moments based IE3D electromagnetic solver is used to optimize the antenna. The genetic algorithm in the solver is used to obtain the optimized values for various parameters of the proposed antenna. The optimized values of the proposed antenna are W = 18 mm, W_1 = 7.4 mm, W_2 = 0.5 mm, W_3 = 4.7 mm, W_4 = 2 mm, W_5 = 2 mm, W_6 = 0.82 mm, W_7 = 9 mm, W_8 = 5 mm, W_9 = 1 mm, L = 23 mm, L_1 = 4.4 mm, L_2 = 6.2 mm, L_3 = 0.5 mm, L_4 = 1.6 mm, L_5 = 2 mm, L_6 = 4 mm, L_7 = 2.2 mm, L_8 = 12.5 mm, g = 0.6 mm, s = 0.2 mm, and f = 0.3 mm. The voltage standing wave ratio (VSWR) of the proposed antenna is measured with Agilent E8362B network analyzer. The behavior of the antenna is specified with VSWR curve by considering lumped load at the end of the feed line. The comparison between the simulated and measured VSWR responses of the antenna is shown in Fig. 2. Both IE3D and finite element method based high frequency structure simulator (HFSS) are used to obtain VSWR curves. There is reasonable agreement between the simulated and measured VSWR responses except that there is slight difference between the curves beyond 10 GHz. The difference between the measured and simulated curves is mainly due to manufacturing tolerance of the radiating patch and imperfect soldering at the junction of the SMA connector to CPW line. The measured VSWR indicates that the impedance bandwidth of the antenna for VSWR < 2 is from 3.1 GHz to 11.6 GHz with dual notched bands of 5.1 GHz - 6.2 GHz and 8 GHz - 8.4 GHz. The measured antenna has three resonant frequencies 3.78 GHz, 4.98 GHz, and 7.2 GHz. The overlapping between these resonant frequencies leads to ultra-wide bandwidth. Good impedance matching and radiation characteristic of the antenna are obtained by proper selection for the dimensions of the novel patch and surrounding ground plane. The photograph of the fabricated antenna is shown in Fig. 3.

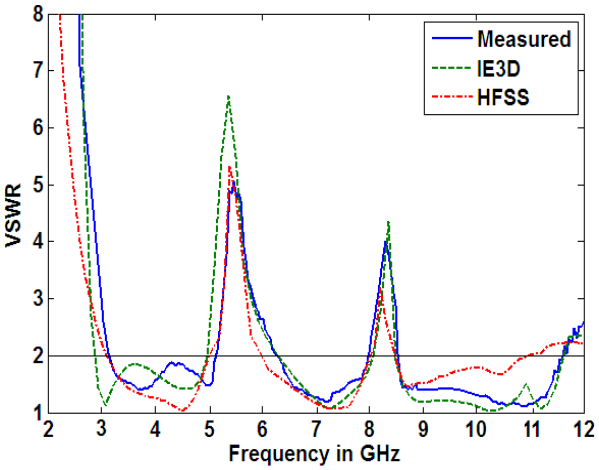

Fig. 2. Simulated and measured VSWR of the proposed antenna.

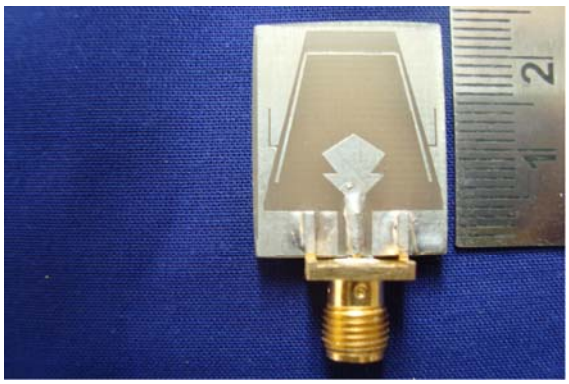

Fig. 3. Photograph of the fabricated antenna.

III. PARAMETRIC ANALYSIS

The effects of different geometrical parameters on various characteristics of the antenna are studied for the proposed antenna. This helps to design antenna with ultra-wide bandwidth. The performance of the antenna is analyzed with IE3D electromagnetic solver. The

analysis is obtained by varying one parameter and keeping the other parameters constant. The effects of most critical geometrical parameters of the antenna on different characteristics are presented here.

A. Effect of intrusion depth L_4

The intrusion depth L_4 is the most critical parameter of the antenna. This parameter leads the problem of impedance mismatching when L_4 is 0.6 mm as shown in Fig. 4. This impedance mismatching is mainly due to capacitive and inductive effects due to improper coupling between the radiating patch and the ground plane. This parameter was optimized to provide proper coupling from feed line to patch. As L_4 increases from 0.6 mm, the impedance matching is improved and the first resonant frequency almost remains constant. The second resonant frequency shifts left and the third resonating frequency also changes. The impedance bandwidth also changes. At L_4 = 2.6 mm, the bandwidth of the notched WLAN band is 5.1 GHz - 6.7 GHz, which is not desired. The antenna has good impedance matching and desired notched WLAN bandwidth of 5.1 GHz - 6.2 GHz at optimized value of L_4 = 1.6 mm.

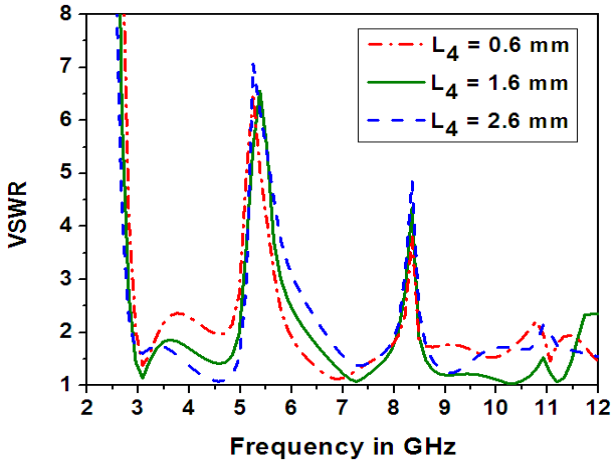

Fig. 4. Simulated VSWR curves of the antenna for different intrusion depths L_4.

B. Effect of the height L_6 of the L-slot

If L-slot height L_6 is increased from 3.5 mm to 4.5 mm, the total length of L-slot increases and the notch frequency $f_{ITU\text{-}notch}$ of ITU band decreases from 8.6 GHz to 7.9 GHz as shown in Fig. 5. The main reason is that the notch frequency $f_{ITU\text{-}notch}$ is inversely proportional to the total length of the slot $L_{L\text{-}slot}$ according to equation (1). When L_6 is 4 mm, the pair of L-slots resonates at notch frequency 8.3 GHz, which is desirable. At this frequency, ITU band is fully rejected. As L_6 changes from 4 mm, the ITU band is not fully avoided as shown in Fig. 5. The notch frequency of WLAN band is little influenced due slight interaction between L-shaped slots and parasitic strip. Hence, the notch frequency of ITU band is controlled by the slot height L_6.

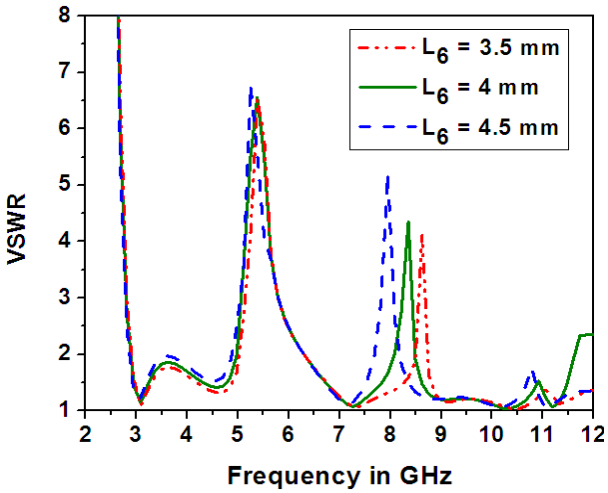

Fig. 5. Simulated VSWR curves of the antenna for different heights L_6 of the L-shaped slot.

C. Effect of the height L_8 of the parasitic strip

The parasitic strip length L_8 has significant effect on the notch frequency $f_{strip\text{-}notch}$ of WLAN band. As L_8 decreases from 13.5 mm to 11.5 mm, the total length of the strip decreases and the corresponding notch frequency $f_{strip\text{-}notch}$ increases from 4.98 GHz to 5.85 GHz as shown in Fig. 6. The desired notch frequency 5.5 GHz of WLAN band is obtained at L_8 = 12.5 mm. The notch frequency of ITU band is slightly affected. Hence, this parameter plays important role in obtaining the desired notch frequency to reject the interference from the WLAN band.

IV. RADITION PATTERNS AND GAIN

The radiation patterns of the proposed antenna are measured in anechoic chamber using double

ridge horn as transmitting antenna and the proposed UWB antenna as the receiving antenna. Figures 7 and 8 present the radiation patterns of the proposed UWB antenna in both E- and H-planes at the measured resonant frequencies 3.78 GHz, 4.98 GHz, and 7.2 GHz. In the E-plane, the antenna has a bi-directional radiation patterns at all resonant frequencies. In the H-plane, the antenna has nearly omni-directional radiation patterns, which indicates that it can receive the signals from all directions.

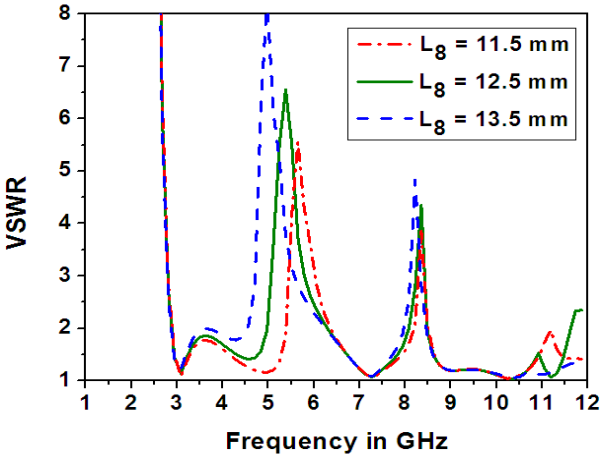

Fig. 6. Simulated VSWR of the antenna with different heights L_8 of the strip.

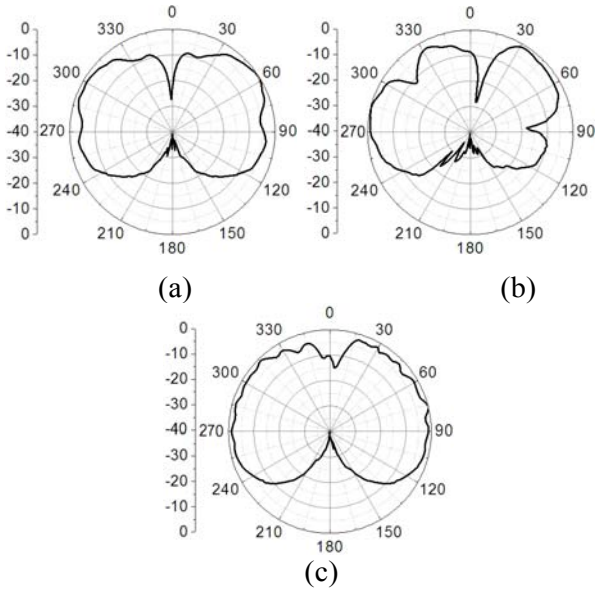

Fig. 7. Measured radiation patterns of the proposed antenna in the E-plane at (a) 3.78 GHz, (b) 4.98 GHz, and (c) 7.2 GHz.

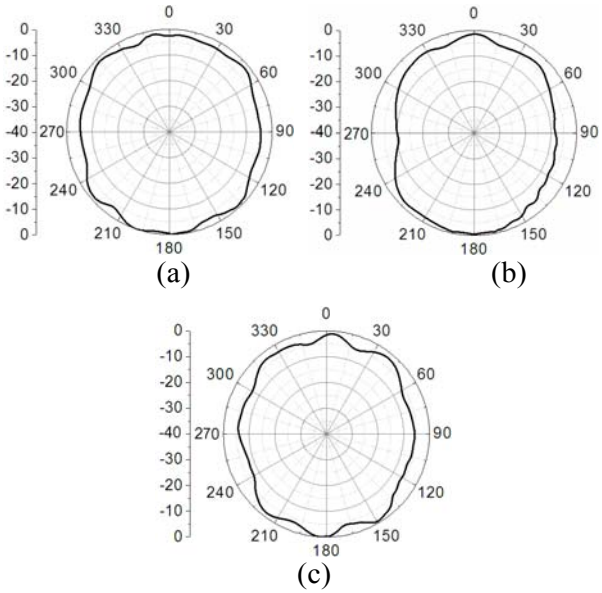

Fig. 8. Measured radiation patterns of the proposed antenna in the H-plane at (a) 3.78 GHz, (b) 4.98 GHz, and (c) 7.2 GHz.

Figure 9 represents measured gain of the antenna against frequency. The antenna has consistent gain that varies between 2.1 dBi to 4.2 dBi in the operating band. The antenna gain falls sharply to -4 dBi in WLAN band and it falls to -3.3 dBi in the ITU band. Hence, the gain curve is in good agreement with the VSWR curve, which indicates the rejection WLAN and ITU bands.

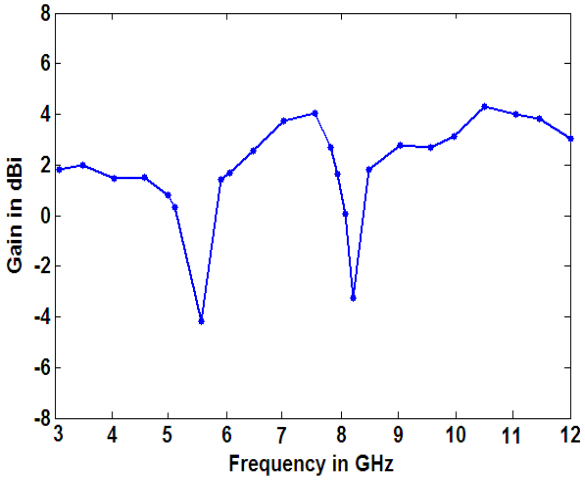

Fig. 9. Measured gain of the proposed antenna.

V. TIME DOMAIN ANALYSIS

Even though UWB antenna has large bandwidth, it does not guarantee good pulse

handling capability. To analyze this, time domain response of the antenna is required. Since group delay represents far-field phase linearity, it indicates the quality of the UWB pulse. Hence, group delay measurement is performed by placing two identical antennas at a distance of 20 cm in the far-field region. The antennas are placed in face to face orientation. The time domain group delay characteristic is shown in Fig. 10. The graph shows that the group delay variation is less than one nano second in UWB except for the notched band. This indicates linear phase response and good pulse handling capability for the proposed antenna. Hence, the antenna is useful in the UWB impulse radio and microwave imaging.

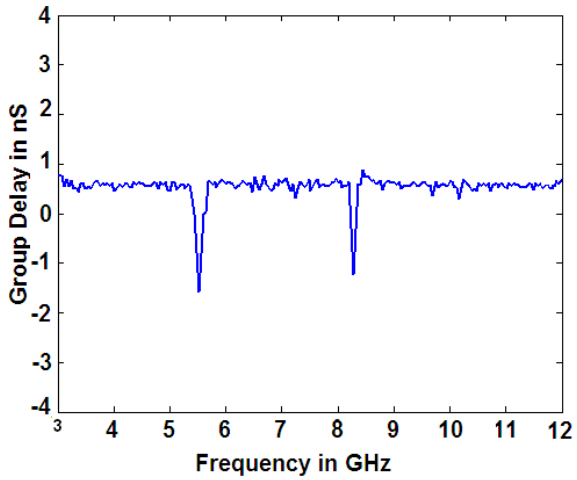

Fig. 10. Measured group delay of the proposed antenna.

Since information is transmitted through short pulses in the UWB systems, it is important to study the behavior of the transmitted pulse. The transient response of the antenna is obtained by using transfer function $H(\omega)$ [18] of the system. The channel is considered as linear time invariant (LTI) system for the transmission and reception of narrow pulses. The transmission co-efficient S_{21} is measured when two identical antennas are placed in face to face orientation in the far field. The transfer function $H(\omega)$ is computed using S_{21} parameter of the antenna as given by equation (3),

$$H(\omega)=\sqrt{\frac{2\pi RcS_{21}(\omega)e^{j\omega R/c}}{j\omega}} \qquad (3)$$

where c is the speed of light, ω is the angular frequency and R is the distance between two identical antennas. The co-sine modulated pulse is taken as input pulse with pulse width T = 228 picoseconds, centre frequency f_c = 6.85 GHz and an amplitude factor A = 1. Figure 11 shows that the proposed antenna fulfills the requirement of UWB indoor emission mask specified by the FCC. The time domain input pulse $i(t)$ is represented by equation (4),

$$i(t)=A\cos(2\pi f_c t).e^{(-t/T)^2}. \qquad (4)$$

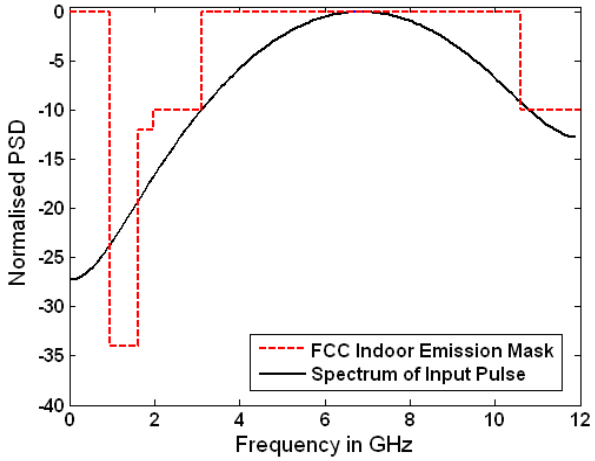

Fig. 11. FCC indoor emission mask and spectrum of the input pulse.

The received output pulse $o(t)$ is generated by the inverse Fourier transform of the product of $H(\omega)$ and the spectrum of the input signal $I(\omega)$ and is given by the novel equation shown below,

$$o(t) = F^{-1}(H(\omega).I(\omega)). \qquad (5)$$

The time domain input and output pulses are displayed in Fig. 12. The slight ringing effect in the received pulse is mainly due to the transmission characteristics of the system. The received pulse indicates that the antenna has less pulse distortion and good time domain response. Hence, the antenna is useful for UWB communications.

VI. CONCLUSION

A novel compact UWB antenna is presented with dual band-notched characteristics. By inserting a novel parasitic strip in the trapezoidal slot and a pair of L-shaped slots in

the metallic ground, the interference from WLAN and ITU bands are avoided. The antenna has impedance bandwidth from 3.1 GHz to 11.6 GHz with rejected bands of 5.1 GHz - 6.2 GHz and 8 GHz - 8.4 GHz. The effect of various parameters on the impedance bandwidth and impedance matching are investigated. The antenna has consistent gain and stable radiation patterns. The time domain group delay indicates good pulse handling capacity. The transient response of the presented antenna satisfies indoor emission criteria of the FCC. The antenna can be easily integrated with RF and microwave circuits, which makes the antenna suitable for UWB applications.

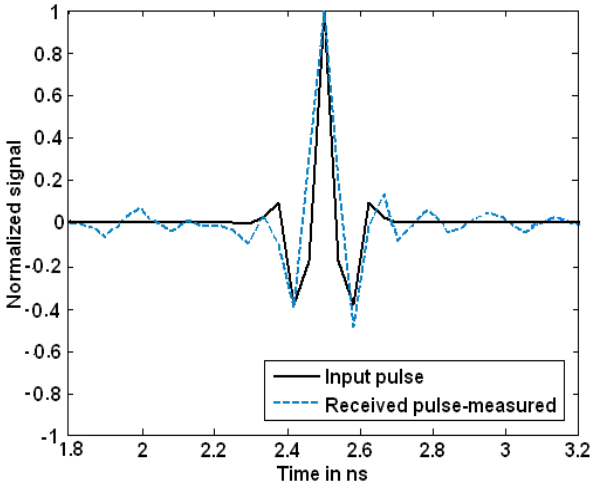

Fig. 12. Comparison of the input and output pulses.

ACKNOWLEDGMENT

The authors are thankful to the scientist, M. Balachari for providing measurement facilities in Defence Electronics Research Laboratory at Defence Research Development Organization (DRDO), Hyderabad, Govt. of India.

REFERENCES

[1] J. W. Jang and H. Y. Hwang, "An improved band-rejection UWB antenna with resonant patches and a slot," *IEEE Antennas Wireless Propag. Lett.*, vol. 8, pp. 299-302, 2009.

[2] O. Ahmed and A. R. Sebak, "A printed monopole antenna with two steps and circular slot for UWB applications," *IEEE Antennas Wireless Propag. Lett.*, vol. 7, pp. 411-413, 2008.

[3] Z. Chen, T. S. See, and X. Qing, "Small printed ultrawideband antenna with reduced ground plane effect," *IEEE Trans. Antennas Propag.*, vol. 55, no. 2, pp. 383-388, Feb. 2007.

[4] E. Angelopoulos, A. Anastopoulos, D. Kaklamani, A. Alexandridis, F. Lazarakis, and K. Dangakis, "Circular and elliptical CPW-fed slot and microstrip-fed antennas for ultra wideband applications," *IEEE Antennas Wireless Propag. Lett.*, vol. 5, pp. 294-297, 2006.

[5] M. Chen and J. Wang, "CPW-fed crescent patch antenna for UWB applications," *Electronics Lett.*, vol. 44, no. 10, pp. 613-614, May 2008.

[6] A. Subbarao and S. Raghavan, "A compact UWB slot antenna with signal rejection in 5-6 GHz band," *Microw. Opt. Technol. Lett.*, vol. 54, no. 5, pp. 1292-1296, May 2012.

[7] M. Mighani, M. Akbari, and N. Felegari, "A novel UWB small rhombic microstrip antenna with parasitic rectangle into slot of the feed line," *Applied Computational Electromagnetics Society Journal* , vol. 27, no. 1, pp. 74-79, Jan. 2012.

[8] M. Moghadasi, G. Dadashzadeh, A. Kalteh, and B. Virdee, "Design of a novel band notched slot patch antenna for UWB communication systems," *Microw. Opt. Technol. Let.*, vol. 52, no. 7, pp. 1599-603, July 2010.

[9] D. Javan and O. Ghouchani, "Cross slot antenna with U-shaped tuning stub for ultra wideband applications," *Applied Computational Electromagnetics Society Journal*, vol. 24, no. 4, pp. 427-432, Aug. 2009.

[10] W. Lui, C. Cheng, and H. Zhu, "Experimental investigation on novel tapered microstrip slot antenna for ultra-wideband applications," *IET Microw. Antennas Propag.*, vol. 1, no. 2, pp. 480-487, 2007.

[11] L. Chang and W. Burnside, " An ultra-wide-bandwidth tapered resistive TEM antenna," *IEEE Trans. Antennas Propag.*, vol. 48, no. 12, pp. 1848-1857, 2000.

[12] D. Kim and C. Kim, "CPW-fed ultra-wideband antenna with triple-band notch function," *Electron. Lett.*, vol. 46, no. 18, pp. 1246-1248, 2010.

[13] S. Hu, H. Chen, C. Law, Z. Chen, L. Zhu, W. Zhang, and W. Dou, "Backscattering cross section of ultrawideband antennas," *IEEE Trans. Wireless Propag. Lett.*, vol. 6, pp. 70-73, 2007.

[14] K. Song, Y. Yin, and L. Zhang, "A novel monopole antenna with a self-similar slot for wideband applications," *Microw. Opt. Technol. Lett.*, vol. 52, no. 1, pp. 95-97, Jan. 2010.

[15] W. Liu and S. Chen, "Ultra-wideband printed fork-shaped monopole antenna with a band-rejection characteristic," *Microw. Opt. Technol. Lett.*, vol. 49, no. 7, pp. 1536-1538, 2007.

[16] H. Zhou, B. Sun, Q. Liu, and J. Deng, "Implementation and investigation of U-shaped

aperture UWB antenna with dual band notched characteristics," *Electron. Lett.*, vol. 44, no. 24, pp. 1387-1388, Nov. 2008.

[17] A. Abbosh and M. Bialkowski, "Design of UWB planar bandnotched antenna using parasitic elements," *IEEE Trans. Antennas Propag.*, vol. 57, no. 3, pp. 796-797, Mar. 2009.

[18] V. Shameena, S. Mridula, A. Pradeep, S. Jacob, A. Lindo and P. Mohanan, "A compact CPW fed slot antenna for ultra wide band applications," *Int. J. Electron. Commun.*, vol. 66, no. 3, pp. 189-194, Mar. 2012.

A. Subbarao received the B.Tech. degree in Electronics and Communication Engineering from Nagarjuna University and M.Tech. degree in Instrumentation and control from JNTU University. He obtained his Ph.D. degree in the area of design and analysis of Ultra wide band Antennas. He has 10 years of teaching experience in a reputed engineering college. His research interest includes microwave/millimeter-wave circuits and devices, microwave integrated circuits, planar antennas, EMI/EMC, computational electromagnetics. He has published 24 research papers in various national, international journals and conferences. He is a student member in the IEICE.

S. Raghavan has 30 years of experience in teaching and research at National Institute of Technology, Tiruchirappalli, India as a Senior Professor. He completed his doctoral programme in the field of Microwave Integrated Circuits from I.I.T., Delhi, India under the guidance of Prof. Bharathi Bhat and Prof. S. K. Koul. He is a Senior Member of IEEE in MTT and EMBS, Life Fellow in BES, Fellow in IETE and IE, Life member in ISSS, MRSI, ISTE, EMC/EMI, IELTS and ILA, referee for MTT journal. His research interest includes microwave/millimeter-wave integrated circuits, antennas and microwaves in biomedical applications. He has contributed more than 40 international, national journal papers and 100 papers in international conferences. He has conducted more than 10 IEEE pre-conference tutorials.

Omni-Directional/Multi-Resonance CPW-Fed Small Slot Antenna for UWB Applications

A. Kamalvand [1], Ch. Ghobadi [2], J. Nourinia [3], M. Ojaroudi [4], and N. Ojaroudi [5]

[1] Sciences and Researches
Urmia Branch, Islamic Azad University, Urmia, Iran
asmakamalvand@hotmail.com

[2, 3] Department of Electrical Engineering
Urmia University, Urmia, Iran
ch.ghobadi@urmia.ac.ir, j.nourinia@urmia.ac.ir

[4] Young Researchers Club
Ardabil Branch, Islamic Azad University, Ardabil, Iran
m.ojaroudi@iauardabil.ac.ir

[5] Department of Electrical Engineering
Germi Branch, Islamic Azad University, Germi, Iran
n.ojaroudi@iaugermi.ac.ir

Abstract ─ In this paper, a novel multi-resonance small slot antenna with CPW feed-line and square radiating stub, for UWB applications is proposed. The proposed antenna consists of a square radiating stub with an inverted T-shaped slot and a ground plane with a T-shaped slit, which provides a wide usable fractional bandwidth of more than 145 % (1.89 GHz – 12.43 GHz). By cutting a T-shaped slit with variable dimensions on the ground plane, and an inverted T-shaped slot in the square radiating stub additional resonances are excited and hence much wider impedance bandwidth can be produced, especially at the lower and upper bands. The proposed antenna displays a good omni-directional radiation pattern even at higher frequencies. The designed antenna has a small size of 30×30 mm^2. Simulated and experimental results obtained for this antenna show that it exhibits good radiation behavior within the UWB frequency range.

Index Terms **-** CPW-fed microstrip slot antenna, multi-resonance performance, and ultra wideband application.

I. INTRODUCTION

Commercial UWB systems require small low-cost antennas with omni-directional radiation patterns and large bandwidth [1]. It is a well-known fact that printed microstrip antennas present really appealing physical features, such as simple structure, small size, and low cost. Due to all these interesting characteristics, printed microstrip antennas are extremely attractive to be used in emerging UWB applications, and growing research activity is being focused on them.

In UWB communication systems, one of the key issues is the design of a compact antenna while providing wideband characteristic over the whole operating band. Consequently, number of microstrip antenna with different geometries have been experimentally characterized [2-4] and automatic design methods have been developed to achieve the optimum planar shape [5, 6]. Moreover, other strategies to improve the impedance bandwidth, which do not involve a modification of the geometry of the planar antenna have been investigated [7, 8].

Submitted On: July 13, 2012
Accepted On: Aug. 29, 2013

In this paper, we propose a novel modified CPW-fed slot antenna with multi-resonance performance and increased impedance bandwidth, for UWB applications. In this design, the proposed antenna can operate from 1.89 GHz to 12.43 GHz and unlike other antennas reported in the literature to date, the proposed antenna displays a good omni-directional radiation pattern even at higher frequencies [6]. The modified inverted T-shaped slot acts as an impedance matching element to control the impedance bandwidth of the proposed antenna, also the inverted T-shaped slot in the ground plane can create additional surface current paths in the antenna therefore additional resonances are excited and hence much wider impedance bandwidth can be produced, especially at the lower and upper bands. Simulated and measured results are presented to validate the usefulness of the proposed antenna structure for UWB applications. The designed antenna has a small size of 30×30 mm^2. Good return loss and radiation pattern characteristics are obtained in the frequency band of interest.

II. ANTENNA DESIGN

The proposed slot antenna fed by a 50-Ohm co-planar waveguide (CPW) feed-line is shown in Fig. 1, which is printed on an FR4 substrate of thickness 1.6 mm and permittivity 4.4. The basic antenna structure consists of a square radiating stub with an inverted T-shaped slot, a CPW feed-line, and a ground plane with a T-shaped slit. The proposed antenna is connected to a 50 Ω SMA connector for signal transmission.

Based on electromagnetic coupling theory (ECT), by cutting a modified T-shaped slit of suitable dimensions at the ground plane, a new configuration can be constructed. In this structure, modified T-shaped slit of suitable dimensions at the ground plane is playing an important role in the broadband characteristics of this antenna, because it can adjust the electromagnetic coupling effects between the radiating stub and the ground plane, and improves its impedance bandwidth without any cost of size or expense. This phenomenon occurs because, with the use of a modified T-shaped slit structure, additional coupling is introduced between the upper edge of the square radiating stub patch and the ground plane [6]. The truncated ground plane is playing an important role in the broadband characteristics of this antenna, because it helps matching of the patch in a wide range of frequencies. Additionally, the modified inverted T-shaped slot acts as an impedance matching element to control the impedance bandwidth of the proposed antenna, because it can create additional surface current paths in the antenna therefore additional resonances are excited and hence much wider impedance bandwidth can be produced, especially at the lower and upper bands. This structure has a novel feeding configuration that consists of a splitting network connected to two symmetrical ports on its base. Using the theory of characteristic modes, it has been demonstrated that the insertion of two symmetric feed ports prevents the excitation of horizontal currents and assures that only the dominant vertical current mode is present in the structure [8]. As a result, an improvement in the polarization properties and impedance bandwidth of the rectangular monopole is achieved. This kind of excitation has recently been proposed for UWB application [8].

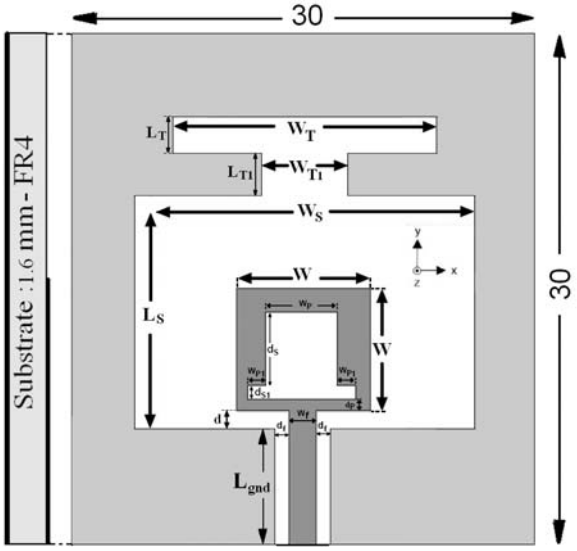

Fig. 1. Geometry of the proposed CPW-fed slot antenna.

The optimal dimensions of the designed antenna are as follows: W_S = 24 mm, L_S = 14 mm, d = 1 mm, W = 1.86 mm, d_f = 0.135 mm, W_f = 2 mm, W_T = 16 mm, L_T = 2 mm, W_{T1} = 4 mm, L_{T1} = 2 mm, W_P = 4 mm, d_P = 1 mm, W_{P1} = 1 mm, d_S = 4 mm, d_{S1} = 1 mm, and L_{gnd} = 7 mm.

III. RESULTS AND DISCUSSIONS

In this section, the CPW-fed slot antenna with various design parameters was constructed, and the numerical and experimental results of the input impedance and radiation characteristics are presented and discussed. The parameters of this proposed antenna are studied by changing one parameter at a time and fixing the others. The simulated results are obtained using the Ansoft simulation software high-frequency structure simulator (HFSS) [9].

Figure 2 shows the structure of the various antennas used for multi-resonance performance simulation studies. Return loss characteristics for ordinary CPW-fed ordinary slot antenna (Fig. 2 (a)), with a T-shaped slit in the ground plane (Fig. 2 (b)), and the proposed antenna structure (Fig. 2 (c)) are compared in Fig. 3. As shown in Fig. 3, it is observed that by using these matching elements including a coupled T-shaped slit, and an inverted T-shaped slot, additional third and fourth resonances are excited, respectively, and hence the bandwidth is increased. As shown in Fig. 3, in the proposed antenna configuration, the ordinary slot can provide the fundamental and next higher resonant radiation band at 2.4 GHz and 4.8 GHz, respectively, in the absence of these matching elements. To design a novel antenna, also in order improve the lower frequency bandwidth, a coupled T-shaped slit is cut in the ground plane as displayed in Fig. 2 (b). The upper frequency bandwidth is significantly affected by using the inverted T-shaped slot.

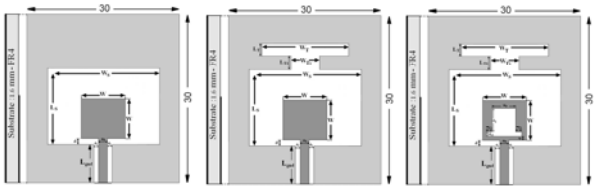

Fig. 2. (a) ordinary slot antenna, (b) antenna with a T-shaped slit in the ground plane, and (c) antenna with a T-shaped slit in the ground plane and an inverted T-shaped slot in the radiating stub.

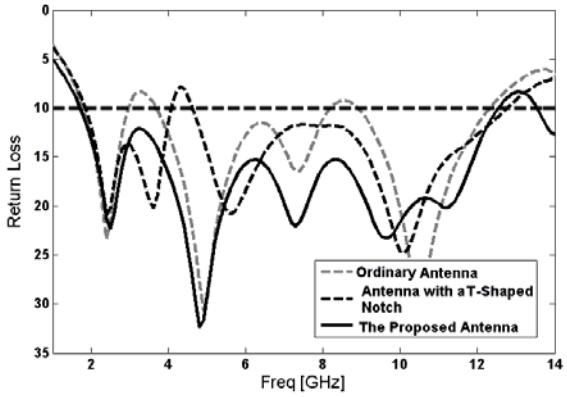

Fig. 3. Return loss characteristics for the various antenna structures shown in Fig. 2.

This behavior is mainly due to the change of surface current path by the dimensions of inverted T-shaped strip as shown in Fig. 4 (c) and (d). These figures show that the electrical current for the fourth (9.85 GHz) and fifth (11.35 GHz) resonance frequencies do change direction along the inverted T-shaped slot cut the square radiating stub. Therefore, the antenna impedance changes at these frequencies. In addition, by inserting matching elements the impedance bandwidth is effectively improved at the lower and upper frequencies [10].

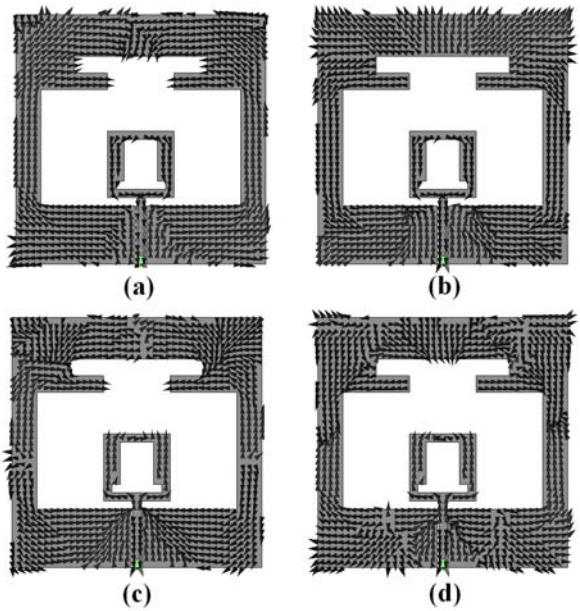

Fig. 4. Simulated surface current distributions for the proposed antenna at (a) 2.4 GHz, (b) 4.8 GHz, (c) 9.85 GHz, and (d) 11.35 GHz.

By properly tuning the dimensions of the inverted T-shaped slot, the antenna can actually radiates over a very wide frequency band. Figure 5 shows the effects of the W_{P1} on the impedance bandwidth. As illustrated in Fig. 5, the T-shaped slot is playing an important role in the broadband characteristics and in determining the sensitivity of impedance matching of this antenna [10, 11].

Another important parameter of this structure is the length L_{T1} of the T-shaped slit. By adjusting L_{T1}, the electromagnetic coupling between the top edge of the square stub and the ground plane can be properly controlled [10, 11]. Figure 6 shows the return loss characteristics simulated for different values of L_{T1}. It is seen that the upper-edge frequency of the impedance bandwidth is increased with increasing L_{T1}, but the matching became poor for larger values. Therefore the optimized L_{T1} is 2 mm.

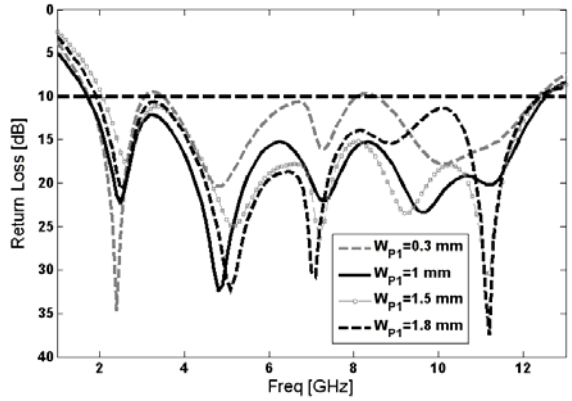

Fig. 5. Simulated return loss characteristics for the proposed antenna with different values of W_{P1}.

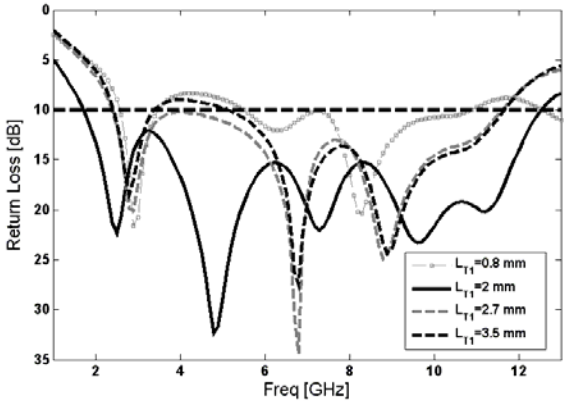

Fig. 6. Simulated return loss characteristics for the proposed antenna with different values of L_{T1}.

The proposed antenna with optimal design, as shown in Fig. 7, was built and tested. Figure 8 shows the measured and simulated return loss characteristics of the proposed antenna. The fabricated antenna has the frequency band of 1.89 GHz to over 12.43 GHz. As shown in Fig. 8, there exists a discrepancy between measured data and the simulated results this could be due to the effect of the SMA port, and also the accuracy of the simulation due to the wide range of simulation frequencies. In order to confirm the accurate return loss characteristics for the designed antenna, it is recommended that the manufacturing and measurement process need to be performed carefully.

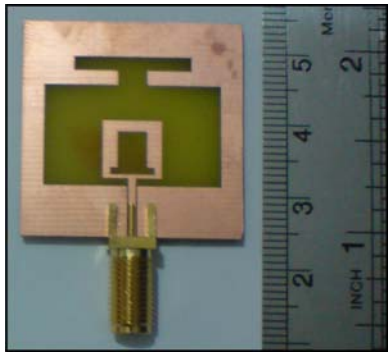

Fig. 7. Photograph of the realized printed CPW-fed slot antenna.

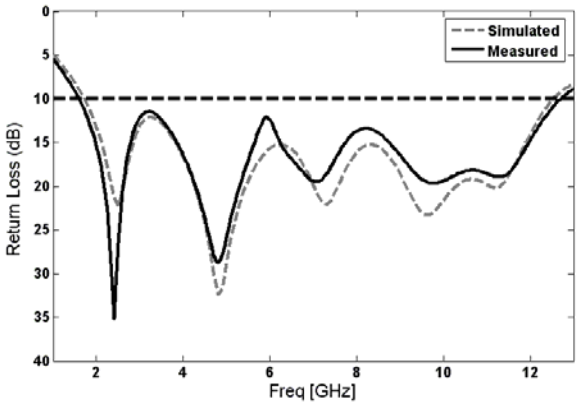

Fig. 8. Measured and simulated return loss characteristics for the proposed antenna.

Figure 9 shows the measured and simulated radiation patterns including the co- and cross-polarization in the x-z, y-z, and x-y planes. It can be seen that the radiation patterns in the x-z plane are nearly omni-directional for the three

frequencies. As shown in Fig. 9 (b) and (c), the differences between maximum and minimum co-polarized patterns are around 10 dB or more in the x-z plane at 7 GHz and 10 GHz, respectively. This discrepancy between measured and expected results is mostly due to the small ground plane effects and the change of excited surface current distributions on the system ground plane at high frequencies.

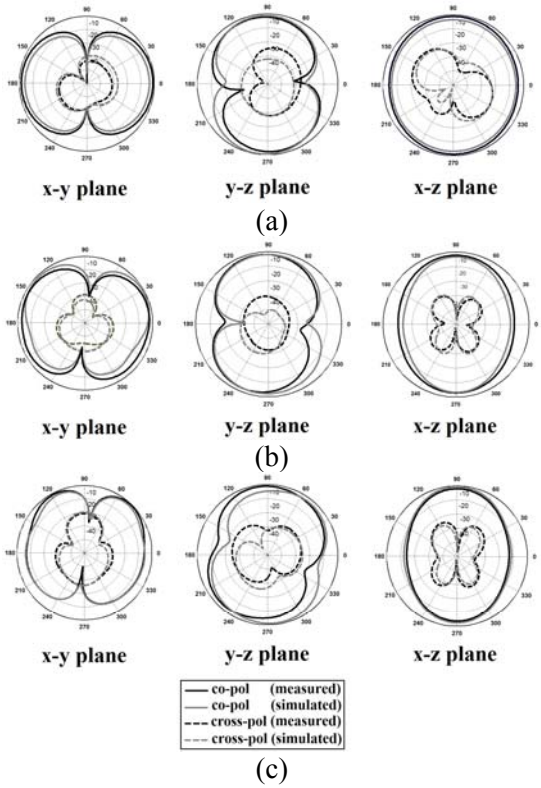

Fig. 9. Measured and simulated radiation patterns of the proposed antenna at (a) 4 GHz, (b) 7 GHz, and (c) 10 GHz.

Figure 10 shows the effects of the T-shaped slit in the ground plane and the inverted T-shaped slot in the radiating stub on the maximum gain in comparison to the same antenna without them. As shown in Fig. 10, the ordinary square antenna has a gain that is low at 3 GHz and increases with frequency. It is found that the gain of the square antenna is enhanced with the use of the inverted T-shaped slot in the radiating stub of the antenna. In addition, the ordinary square antenna with an inverted T-shaped slot has a flat gain. In this structure, inverted T-shaped slot in the radiating stub acts as a dual-fed structure, and it is created to enhance the gain of the square slot antenna at the lower and middle of the frequency band such that the gain of the proposed antenna over the complete bandwidth remains nearly constant. Another effective parameter on this structure gain is the T-shaped slit in the ground plane. It can be observed in Fig. 10 that by T-shaped slit in the ground plane, the gain of the square antenna is increased specially at the higher frequency.

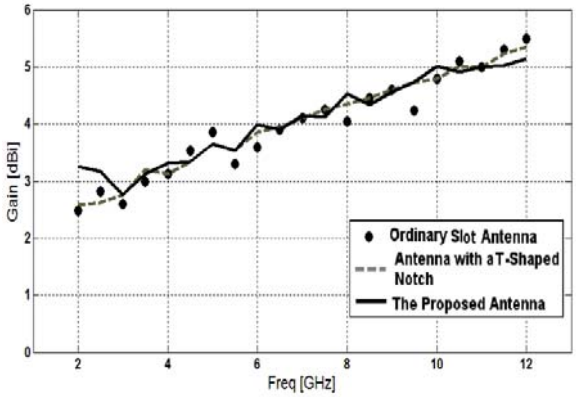

Fig. 10. Maximum gain comparisons for the ordinary square antenna (simulated), square antenna with a T-shaped slit in the ground plane (measured), and the proposed antenna (measured).

The time domain performance of UWB applications is important for pulsed based systems. In addition to radar and imaging applications, the standard has provided for their use in communications. While channel equalization is challenging for the propagation environment, the antenna features can be optimized to reduce their inherent pulse spreading effect. The group delay is defined as the negative derivative of the phase response with respect to frequency [3]. The group delay gives an indication of the time delay that the impulse signal suffers in proportion to various wavelength dimensions on the antenna. Group delays of the proposed antennas are shown in Fig. 11. The variation of the group delay of the proposed antenna is about 1 ns across the whole UWB frequency range.

IV. CONCLUSION

In this paper, a novel small slot antenna with wide bandwidth capability for UWB applications is proposed. In this design, the proposed antenna can operate from 1.89 GHz to 12.43 GHz with S_{11} < -10 dB and unlike other antennas reported in the

literature to date, the proposed antenna displays a good omni-directional radiation pattern even at higher frequencies. The designed antenna has a small size. Good return loss and radiation pattern characteristics are obtained in the frequency band of interest. Simulated and experimental results show that the proposed antenna could be a good candidate for UWB application.

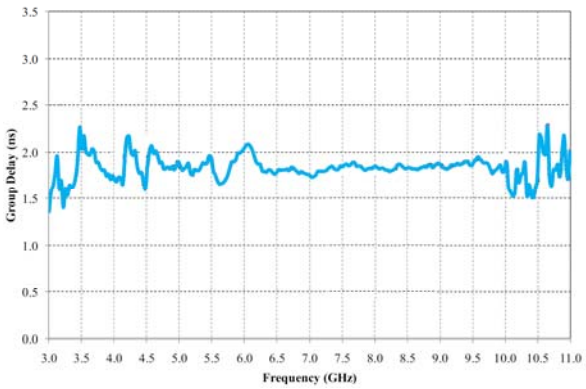

Fig. 11. Measured group delay characteristics for the proposed antenna.

ACKNOWLEDGMENT

The authors are thankful to Microwave Technology (MWT) company staff for their beneficial and professional help (www.microwave-technology.com).

REFERENCES

[1] H. Schantz, *The Art and Science of Ultra Wideband Antennas*, Artech House 2005.

[2] J. Sze and K. Wong, "Bandwidth enhancement of a microstrip line-fed printed wide-slot antenna," *IEEE Trans. Antennas Propag.*, vol. 49, pp. 1020-1024, 2001.

[3] Y. Jang, "Experimental study of large bandwidth three-offset microstrip line-fed slot antenna," *IEEE Microw. Wireless Comp. Lett.*, vol. 11, pp. 425-426, 2001.

[4] M. Kim, Y. Suh, and I. Park, "A T-shaped microstrip line-fed wide-slot antenna," in *Proc. IEEE APS Int. Symp.*, pp. 1500-1503, 2000.

[5] S. Ke, "Broadband proximity-coupled microstrip antennas with an H-shaped slot in the ground plane," *IEEE Antennas Propag. Symp. Dig.*, vol. 2, pp. 530-533, June 2002.

[6] Y. Liu, K. Lau, Q. Xue, and C. Chan, "Experimental studies of printed wide-slot antenna for wide-band applications," *IEEE Antennas Wireless Propag. Lett.*, vol. 3, pp. 273-275, Dec. 2004.

[7] Gh. Beigmohammadi, Ch. Ghobadi, J. Nourinia, and M. Ojaroud, "Small square slot antenna with circular polarisation characteristics for WLAN/WiMAX applications," *Electronics Lett.*, vol. 46, no. 10, pp. 672-673, May 2010.

[8] F. Amini, M. Azarmanesh, and M. Ojaroudi, "Small semi-circle-like slot antenna for ultra-wideband applications," *Progress In Electromagnetics Research C*, vol. 13, pp. 149-158, 2010.

[9] Ansoft High Frequency Structure Simulation (HFSS), ver. 13, Ansoft Corporation, 2010.

[10] M. Ojaroudi and A. Faramarzi, "Multiresonance small square slot antenna for ultra-wideband applications," *Microw. Opt. Technol. Lett.*, vol. 53, no. 9, pp. 2145-2149, Sep. 2011.

[11] P. Li, J. Liang, and X. Chen, "Ultra-wideband elliptical slot antenna fed by tapered microstrip line with U-shaped tuning stub," *Microw. Opt. Technol. Lett.*, vol. 47, pp. 140-143, Oct. 2005.

Asma Kamalvand was born in Khoramabad, Iran 1987. She received her B.Sc. in Electrical Engineering-Electronic from Azad University of Khoramabad, Iran, in 2009 and M.Sc. degrees in Electrical Engineering-Telecommunication from Sciences and Researches, Urmia Branch, Islamic Azad University, Urmia, Iran, in 2013. Her primary research interests are in printed microstrip antenna design.

Changiz Ghobadi was born in June, 1960 in Iran. He received his B.Sc. in Electrical Engineering-Electronic and M.Sc. degrees in Electrical Engineering-Telecommunication from Isfahan University of Technology, Isfahan, Iran and Ph.D. degree in Electrical-Telecommunication from University of Bath, Bath, UK in 1998. From 1998 he was an Assistant Professor and now he is an Associate Professor in the Department of Electrical Engineering of Urmia University, Urmia, Iran. His primary research interests are in antenna design, radar and adaptive filters.

Javad Nourinia received his B.Sc. in Electrical and Electronic Engineering from Shiraz University and M.Sc. degree in Electrical and Telecommunication Engineering from Iran University of Science and Technology, and Ph.D. degree in Electrical and Telecommunication from University of Science and Technology, Tehran Iran in 2000. From 2000 he was an Assistant Professor and now he is an Associate Professor in the Department of Electrical Engineering of Urmia University, Urmia, Iran. His primary research interests are in antenna design, numerical methods in electromagnetic, microwave circuits.

Mohammad Ojaroudi was born in 1984 in Germi, Iran. He received his B.Sc. degree in Power Electrical Engineering from Azad University, Ardabil Branch and M.Sc. degree in Telecommunication Engineering from Urmia University. From 2010, he is working toward the Ph.D. degree at Shahid Beheshti University. Also from July 2013 he has been working, as a research visitor in University of Tennessee, Knoxville, USA. From 2007 until now, he is a Teaching Assistant with the Department of Electrical Engineering, Islamic Azad University, Ardabil Branch, Iran.

Since March 2009, he has been the chief executive officer in the Microwave Technology Company (MWT), Tehran, Iran. From 2012, Dr. Ojaroudi is a member of the IEEE Transaction on Antennas and Propagation (APS) reviewer group and the Applied Computational Electromagnetic Society. His research interests include analysis and design of microstrip antennas, design and modeling of microwave structures, radar systems, and electromagnetic theory. He is author and coauthor of more than 120 journal and international conferences papers. His papers have more than 450 citations with 11 h-index.

Nasser Ojaroudi was born in 1986 in Germi, Iran. He received his B.Sc. degree in Electrical Engineering from Azad University, Ardabil Branch. From 2011, he is working toward the M.Sc. degree in Telecommunication Engineering at Shahid Rajaee Teacher Training University. Since March 2008, he has been a Research Fellow in the Microwave Technology Company (MWT), Tehran, Iran. His research interests include microstrip antennas for radar systems, ultra-wideband (UWB) and small antennas for wireless communications, microwave passive devices and circuits, and microwave/millimeter systems.

Antenna Selection Procedure for BTS Over HAPs

A. Araghi [1], M. Mayiami [1], A. Montazeri [2], A. Foudazi [1], M. Yaghubi [3], and M. Bod[4]

[1] Department of Electrical and Computer Engineering
Shahed University, Tehran, Iran
{a.araghi, ma.ramezani, foudazi}@shahed.ac.ir

[2] Iran Telecommunication Research Center, Tehran, Iran
montazeri@itrc.ac.ir

[3] Department of Electrical Engineering
University of Tehran, Tehran, Iran
m.yaghoobi@ece.ut.ac.ir

[4] Department of Electrical Engineering
Amirkabir University, Tehran, Iran
mbod@aut.ac.ir

Abstract ─ In this paper, a method is proposed to find the suitable antenna for a GSM urban macro cell covered by a base transceiver station (BTS) mounted on high altitude platform (HAP) at the stratosphere layer. To this end, an ideal cosine shape radiation pattern raised to the power of N is applied to select the appropriate antenna for achieving the optimum coverage. The optimum selection is based on minimizing the blind area, having less overlapped to total area ratio, and increasing the total coverage area, simultaneously. Our proposed scheme has two degrees of freedom; first, the values of N determining the directivity and half power beam width (HPBW), and second the angle α denoting to the mechanical tilt of the antenna elements. To find the optimum pair of (N, α), several simulations are done and the corresponding footprint contours are depicted. Simulation results show that utilizing three ideal cosine function antennas with N = 9 installed by α = 38 degrees of mechanical tilt with respect to the normal is optimum for a macro cell coverage in an urban area by using HAPs located at 17 km altitude.

Index Terms - BTS antenna, GSM, and high altitude platforms.

I. INTRODUCTION

High altitude platforms (HAPs) are spatial stations, which can hold and serve communication system instruments in the stratosphere altitude (17 km-22 km) by using an airship or aero plane [1]. Since the stratospheric layer faces with mild wind and is above the commercial air-traffic heights, it is recommended to use this altitude to have more stabilized stations [2, 3].

Using HAPs for providing the desired coverage is advantageous for a terrestrial wireless communications, which usually suffers from non-line-of-sight (NLoS) signal component. Moreover, using HAPs results in more efficient communication link in comparison with applying satellites, which suffer from delay and implementation cost.

In the common commercial wireless communication networks, global system for mobile communications (GSM) has become one of the most popular technologies for providing the voice services for these two decades [4]. Due to the large path loss for long distances (distance > 10 km) from the base transceiver station (BTS) in urban areas, the conventional BTS cannot provide such a large coverage. The GSM BTS antennas mounted on HAPs may be one of the solutions to

Submitted On: Nov. 29, 2012
Accepted On: Aug. 29, 2013

cope with this problem, since it can provide more line-of-sight (LoS) signal propagation between MS and BTS [5]. Therefore, transmitted signals experience less path loss for long distance in comparison with conventional BTS antennas. Moreover, covering larger area within a macro cell can be reliable.

Common BTS antennas (i.e., linear array of cross dipoles or slotted apertures) are installed at the height of about 30 m [6] and directed to the region of interest by using proper electrical or mechanical tilt (Fig. 1 (a)). As shown in Fig. 1 (a), the main lobe experiences the path with longer distance (results in much amount of path loss). This kind of antenna is inefficient for covering the desired circular shaped cell when it is mounted on HAP (Fig. 1 (b)). Since, the radiation pattern of the conventional BTS antennas is narrow in the yz-plane (the plane of element's placement) and wide in the xy-plane, the antenna radiation pattern has an elliptical shape footprint over the earth surface when it mounts on HAP. Thus, a large amount of desired area cannot be covered in a commonly circular macro cell, like a cell which covers urban city. For more clarity, it is useful to note that since we assume a macro cell with 20 km of radius at most, the area of the cell is very small relative to the earth surface. Hence, we assume flat earth hereafter.

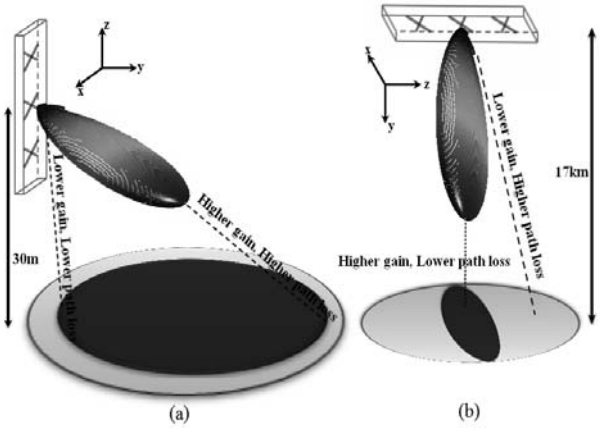

Fig. 1. Coverage area of a conventional BTS antenna (a) located at the altitude of 30 m (the direction of peak gain is electrically tilted so as to achieve the maximum possible coverage) and (b) mounted on HAP at the altitude of 17 km (without any electronical or mechanical tilt).

In this paper, to provide desired footprint contour, ideal cosine function is used to propose suitable pencil beam antennas [7, 8]. Moreover, cell sectorization [4, 6] is used for achieving a high capacity along with low signal to interference and noise ratio (SINR) within the cell.

The remainder of this paper is organized as follows; in section II, the coverage contour of conventional BTS antenna mounted on HAP is described and then an overview of antenna selection procedure is presented. Section III is devoted to the simulation and discussion of the results. Finally, in section IV, we are going through the conclusion.

II. ANTENNA SELECTION PROCEDURE FOR HAPS

In a communication system, antenna coverage depends on four independent factors: path loss, transmitted power, MS antenna gain, and BTS antenna gain, which must be considered in the link budget calculation. It is clear that in link analyzing, the first factor is an uncontrollable issue for a fixed propagation environment. Furthermore, in GSM systems, transmitted power is supposed to be selected from some specific values where most applicable transmitted power are 41 dBm for BTS transmitter (downlink) and 29 dBm for MS transmitter (uplink). Also, a typical MS antenna gain is 0 dBi and the system designer cannot control it. Considering above mentioned discussions, it seems that the only controllable factor for a system designer is BTS antenna design and configuration (the task, which is performed in this section). In subsection A, the coverage of the conventional BTS antenna mounted on HAPs is investigated and it is shown that these antennas cannot cover the urban macro cell from the altitude of 17 km. Then, the procedure of designing suitable antenna by using the ideal cosine function for covering the macro cell via HAPs is presented in subsection B.

A. Conventional BTS antenna

Suppose that a conventional BTS antenna (an array of three cross dipole antennas) is located on a platform at the altitude of 17 km and directed to the earth surface. Obviously, during the propagation, the environment has an inevitable impact on path loss. Also, path loss depends on the carrier frequency where higher frequencies result in much amount of loss. Since GSM operates in two

bands (900 MHz and 1800 MHz), to meet the worst case condition from wave attenuation point of view, in this paper f = 1800 MHz has been chosen for simulations along with uplink transmission scenario due to its lower transmitted power.

The coverage contour is computed by using the Lazgare-Penin channel model given for HAPs based systems [9]. This model is based on the fact that the total path loss can be divided into two distinguished terms: the free space loss (FSL) and the effects surrounding the terrestrial terminal that are relative to its neighboring scatterers named terrestrial loss [9]. For more clarity, HAPs is considered to be an extremely high base station that can provide a propagation path consisting of the diffraction from rooftops and multiple reflections from nearby buildings beside the mentioned FSL. The FSL only depends on the frequency and line-of-sight distance between transceivers (in this case, the altitude of platform standing). The other discussed term of loss (terrestrial loss) is entirely affected by the buildings height and street width of environment alongside with the direction of arrival.

To simulate a dense urban area, we assume that the desired area includes the building with average height of 25 m and street with of 15 m. By applying the sensitivity level of -110 dBm, 20 km radii of a circular shape area (shown in Fig. 2) cannot efficiently be covered by the conventional BTS antenna at the height of 17 km. The residual parts of the circular desired area, named blind areas, experience weak received signal leading to lack of coverage. As a result, while conventional BTS antennas provide a suitable coverage in terrestrial communication, providing a method to propose an applicable antenna based on the best footprint contour coverage at the earth surface is extremely demanded for GSM-HAPs application at the stratosphere layer.

B. The main idea: selection procedure

Large macro cell can be covered by cell sectorization. In a sectored cell, there are three types of zones in terms of coverage; (a) covered areas, (b) uncovered areas or blind areas, and (c) overlapped areas where adjacent sectors cover common region (Fig. 3).

To obtain the optimum coverage area, it is desired to decrease the blind areas as well as intersector overlapped areas. If there are no overlapped areas, several blind areas would exist and consequently more call blockage would be happened. On the other hand, by increasing the amount of total overlapped areas, the number of GSM signalling procedures, especially handover or handoff, are increased which causes signalling congestion and low quality of services in the GSM network.

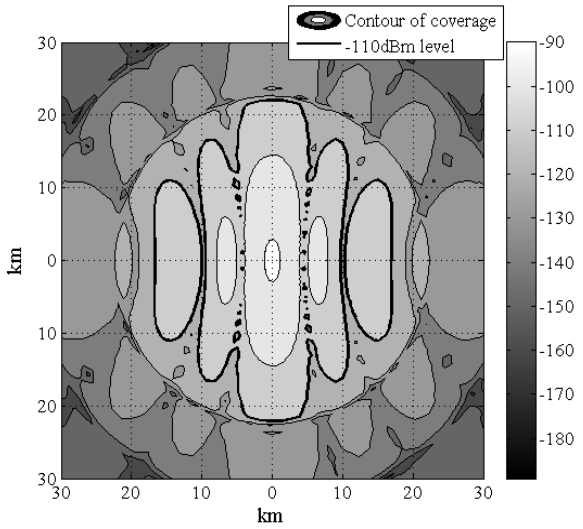

Fig. 2. Uplink coverage of a conventional BTS antenna mounted on a platform at the height of 17 km (transmitted power of MS is 29 dBm, antenna gain of MS is 0dBi, antenna gain of BTS is 17 dBi).

Therefore, we put a restriction on the amount of intersector overlapping as follows,

$$\frac{\text{Overlapped Area}}{\text{Total Area of Each Sector}} < \text{cte} \qquad (1)$$

where cte is some constant determining the signalling congestion of the network. In this paper, we suppose that the distribution of users is uniform since we do not know any priori information about the MS distribution in the cell. Also, it is assumed that the acceptable level of signaling for GSM procedure (e.g., registration, handover or handoff, and location updating) would be obtained by cte = 15 %. This is a practical assumption for GSM network manager to maintain the network quality of service appropriately. Figures 2 and 3 show that conventional BTS antenna cannot be used for satisfying this condition.

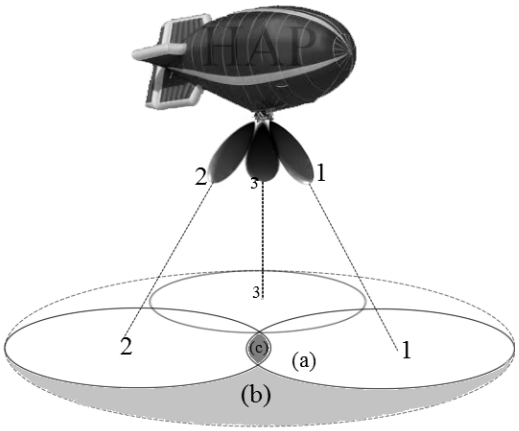

Fig. 3. The coverage zones of a three sector macro cell (a) covered area, (b) blind area, and (c) overlapped area.

Form Fig. 3 it is clear that antennas with symmetrical beam radiation pattern could satisfy the desired condition. According to [8], antennas of medium to high directivity (D) have main lobe patterns, which may conveniently be approximated by a cosine function raised to a power of N for $-\pi/2 < \theta < \pi/2$ and symmetrical properties with respect to φ as follows,

$$D = (\cos\theta)^N \frac{32\log_{10} 2}{2\left(2\arccos\left(\sqrt[N]{1/2}\right)\right)^2}. \qquad (2)$$

According to equation (2), by utilizing the higher values of N, higher directivity (and gain) and lower HPBW of radiation pattern are achieved. Figure 4 represents the radiation patterns of N = 5, 10, 15, and 20. By using these radiation patterns, directed to the area of interest, pseudo circular shaped footprints are obtained. In a covered sectored cell, as shown in Fig. 5, each sector needs to use the proposed antenna by appropriate mechanical tilt (α) with respect to the normal.

It is necessary to say that the coverage footprint is not the projections of half power beam with. The coverage of a radiation pattern is obtained via calculating the link budget for all angles θ of that radiation pattern. For more clarity, see Fig. 1 (a) where a schematic of the contour of coverage is depicted. As it is illustrated, higher amount of path loss could be compensated by higher gain of radiation pattern (provided by the main lobe) and its lower gain (provided by side lobe) is faced to shorter path (resulting in lower amount of path loss). Therefore, every angles of a radiation pattern could contribute to the coverage.

Our proposed approach is illustrated via three steps; 1) using the ideal cosine functions to model the radiation pattern of pencil beam antennas with different N and simulate the corresponding footprint on the earth surface. 2) Mechanical tilt (α) is used to fit the radiation pattern of three antennas to the cell sectors. 3) The optimum parameters, N and α, are determined (illustrated in sec. III) to satisfy the aforementioned condition.

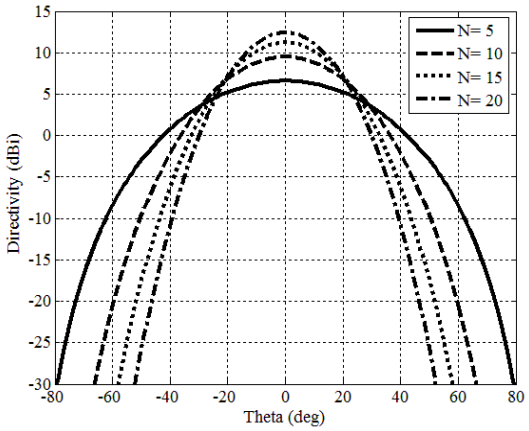

Fig. 4. Simulated radiation patterns by using the ideal cosine function for different values of N.

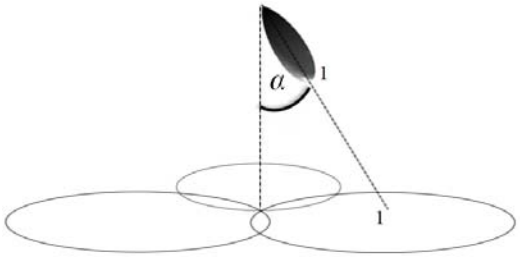

Fig. 5. Mechanical tilt by α degrees with respect to the normal.

III. SIMULATIONS AND DISCCUSIONS

The aim of this section is to find the proper values of two adjustable parameters N and α at the same time. By considering a 20 km radii circular shaped cell, which is an applicable assumption for a common urban macro cell, the proposed approach is initiated. It is assumed that the BTS antenna is mounted at the height of 17 km and other parameters are the same as in section II.

Then, parametric study has been started for different values of N and α. It has been observed that values of $10 < N < 20$ along with $30 < \alpha < 40$ result in reasonable coverage footprint. Antenna mechanical tilt leads to elliptical footprint contour instead of circular ones. The more tilt, the much resemblance to elliptical shape is occurred.

According to Tables 1 and 2, it is shown that by increasing N at a fixed tilt angle, overlapped area of two adjacent sectors as well as overlapped to total area ratio are being decreased, while the total blind area is being increased. At the same way, by increasing α for a constant N, similar results are obtained.

Table 1: Cell parameters for different pairs of N and α.

(N, α)	Overlap area of two adjacent sectors (km^2)	Overlap to total area ratio (eq. 1)	Total blind area within the cell (km^2)	Common overlap area among three sectors (km^2)
(5, 30)	324.1	%42.2	-	160.4
(5, 35)	248.4	%34.6	-	98.6
(5, 40)	183.7	%27.5	-	51.0
(10, 30)	157.5	%25.5	27.4	57.8
(10, 35)	103.9	%18.2	28.7	22.5
(10, 40)	57.1	%10.6	37.6	2.9
(15, 30)	85.3	%16.2	92.7	21.4
(15, 35)	44.5	%9.0	93.7	2.6
(15, 40)	12.2	%2.6	115.3	-
(20, 30)	48.0	%10.4	159.3	6.5
(20, 35)	16.2	%3.7	160.5	-
(20, 40)	-	-	246.1	-

For choosing the optimum pair of (N, α), the following criteria have to be satisfied; i) as is discussed in section II, part B, optimum (N, α) has to minimize both of the overlapped area of adjacent sectors and blind area, simultaneously. ii) The overlapped to total area ratio for each (N, α) has to satisfy the constraint of equation 1 with cte < 15%. iii) The optimum (N, α) should be capable of having the largest cell radius. By considering the data in Table 1, the pairs (5, 30), (5, 35), (5, 40), (10, 30), (10, 35), and (15, 30) are not suitable because they cannot satisfy equation's (1) constraint. Also, since it is required to have the minimum possible blind area and overlapped area simultaneously, all remained rows should be omitted, except for (10, 40).

As a result, it is seen that the value of (10, 40) can be a good candidate to design an appropriate antenna that can be used in three sectors macro cell in an urban area using HAP at the stratosphere layer. On the other hand, (10, 40) is a suboptimum solution since we use large steps for increasing N and α (the consecutive values of α differs in 5 degrees). For finding the optimum value of (N, α) the resolution of the simulations should be increased by decreasing the steps as much as possible. To this end, the simulations are run for all integers between $N = 5$ and $N = 20$ along with $30 < \alpha < 40$ and the results are depicted in Figs. 6 and 7. From Fig. 6, it can be concluded that the upper bound of proper (N, α) is (20, 40), since for $N \geq 20$ or $\alpha \geq 40$ the overlapped area of the two adjacent sectors is zero. Also, it is useful to mention that the flat horizontal surface of Fig. 7 shows the threshold cte = 15% of equation (1).

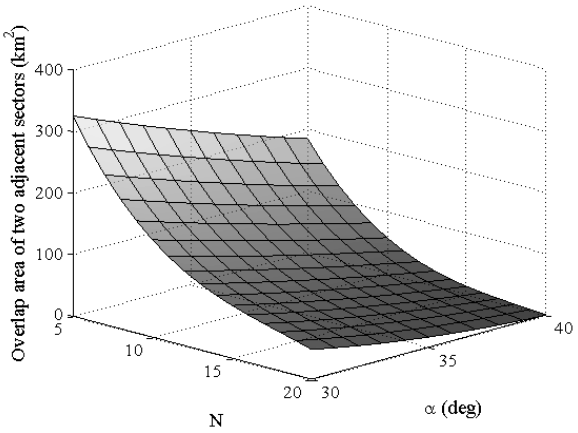

Fig. 6. The overlap area of two adjacent sectors for all $5 < N < 20$ and $30 < \alpha < 40$.

Table 2: Simulated coverage zones for different pairs of N and α.

	$\alpha = 30$	$\alpha = 35$	$\alpha = 40$
N=5	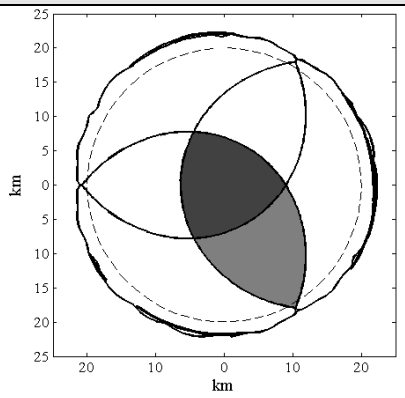	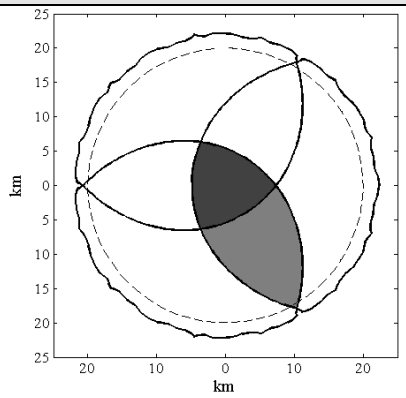	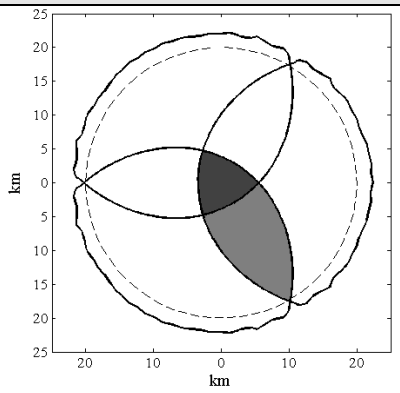
N=10	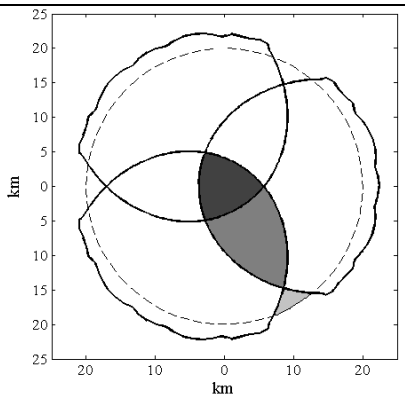	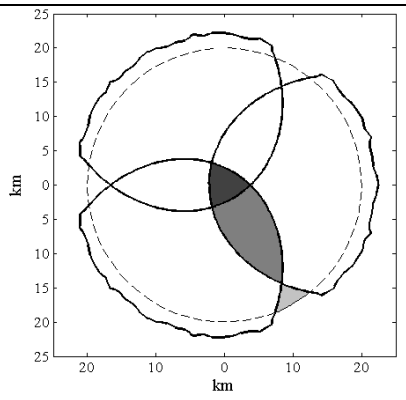	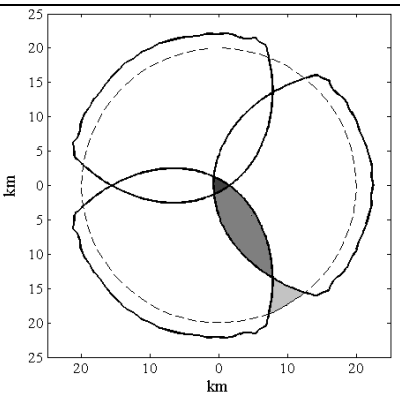
N=15	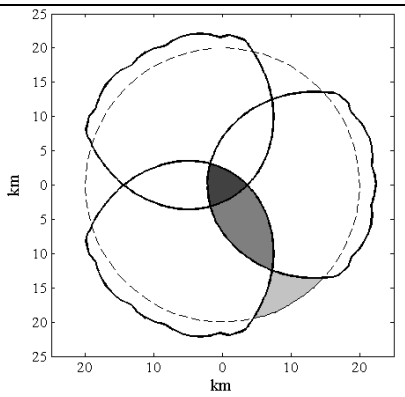	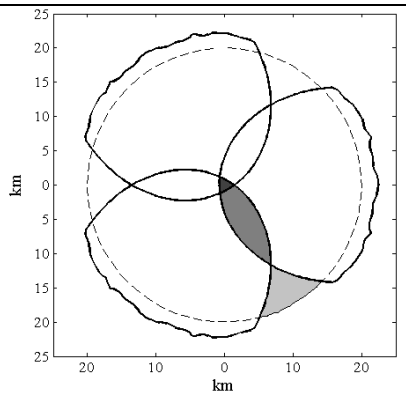	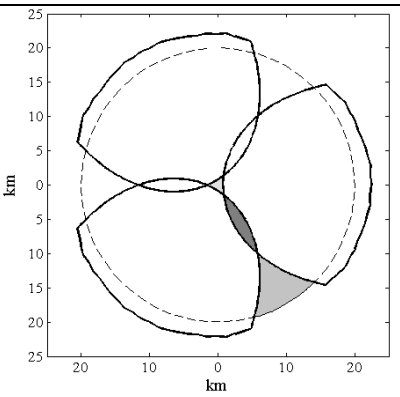
N=20	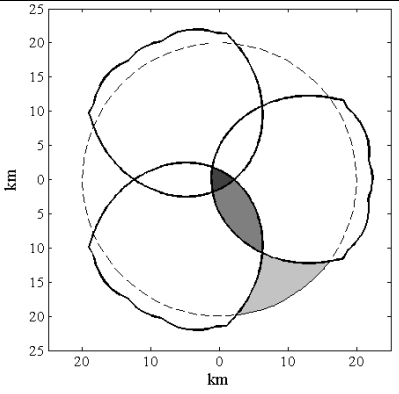	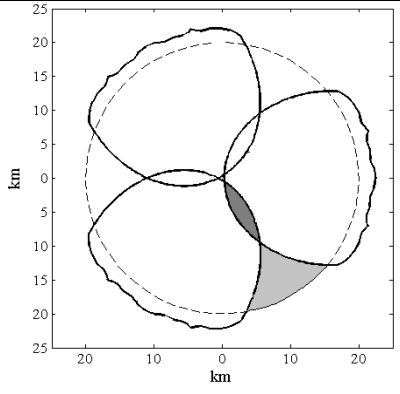	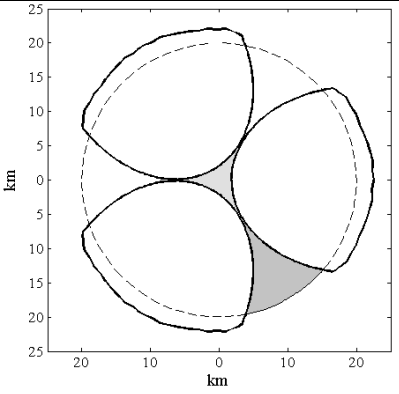

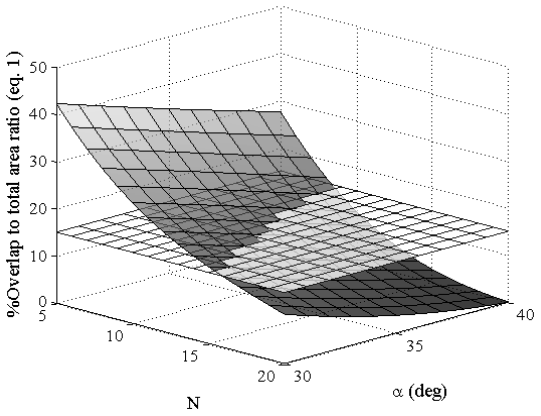

Fig. 7. The overlap to total area ratio for all $5 < N < 20$ and $30 < \alpha < 40$.

By investigating the value of (N, α) exhaustively, the pair (9, 38) is selected as the optimum point, which results in overlapped area of two adjacent sectors of 89.7 km^2, the overlapped to total area ratio of 14.9 %, the total blind area within the cell of 7.2 km^2, and common overlapped area among all three sectors of 14.4 km^2. In Fig. 5, the approximated radiation pattern of a cosine function raised to the power $N = 9$ is shown. The directivity of this radiation pattern is 9 dBi with 46 degree HPBW. Such radiation pattern with mentioned characteristics is feasible using traditional helical antennas [10] or dielectric resonator antennas (DRAs) [11], which is suitable for many applications. By mounting three of this antenna on HAP at 17 km, footprint of Fig. 8 for an urban area is attained. As you can see, the coverage of our proposed scheme is much better relative to the conventional BTS antenna depicted in Fig. 2.

It is necessary to mention that by setting $N = 9$ and $\alpha = 38$, the proportion of the common overlapped area among all three sectors to total cell area is less than 1%. Since, uniform distribution of users in the cell is considered, only 1% of users located in this area encounter with the signaling congestion, which is negligible for an urban GSM network.

IV. CONCLUSION

In this paper, a method is proposed to select the appropriate antenna mounted on high altitude platforms (HAPs) at the stratosphere altitude (17 km - 22 km) and directed to the desired GSM circular sectored macro cell for an urban area. It is shown that the conventional BTS antenna is not suitable due to its elliptical shaped footprint on the earth surface. Also, because of its low gain, the conventional antenna cannot cover the large area of a macro cell. To propose an appropriate antenna mounted on HAPs for three sectors coverage, ideal cosine function is applied. Since the radiation pattern (directivity and HPBW) of an ideal cosine function is a function of N and on the other hand, mechanical tilt (α) alters the overlapped area among three sectors, designing a sectored macro cell via HAPs has two degrees of freedom. This pair of parameters is applied to select the optimum antenna, which covers 20 km radius cell in an urban area. It is demanded to minimize blind area, to have the overlapped to total area ratio less than 15 % for two adjacent sectors, and to achieve the maximum coverage. By employing parametric study for (N, α), the optimum value of (9, 38) is obtained, which results in overlapped area of 89.7 km^2 for two adjacent sectors, the overlapped to total area ratio of 14.9%, and the total blind area of 7.2 km^2.

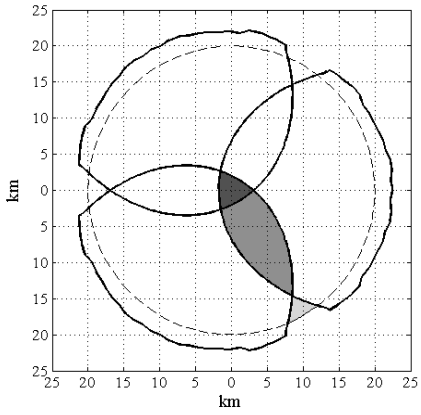

Fig. 8. Footprint of the proposed radiation pattern with (N, α) = (9, 38).

REFERENCES

[1] G. Djuknic and Y. Okunev, "Establishing wireless communications services via high-altitude aeronautical platforms – a concept whose time has come?," *IEEE Communications Magazine*, vol. 35, pp. 128-35, 1997.

[2] D. Grace and M. Mohorcic, *Broadband Communications via High Altitude Platforms*, John Wiely and Sons, 2011.

[3] T. Tozer and D. Grace, "High altitude platforms for wireless communications," *Electronics and Communication Engineering Journal*, pp. 127-137, June 2001.
[4] T. Rappaport, *Wireless Communications Principles and Practice*, 2nd Edition, Prentice Hall, 2001.
[5] J. Avlies, *High Altitude Platforms for UMTS*, Master of science thesis, Tampere University of Technology, Jan. 2007.
[6] G. Stuber, *Principles of Mobile Communication*, 2nd Edition, Kluwer Academic Publisher, 2002.
[7] C. Balanis, *Antenna Theory, Analysis and Design*, 3rd Edition, John Wiley and Sons, 2005.
[8] J. Thornton, D. Grace, M. Capstick, and T. Tozer, "Optimizing an array of antennas for cellular coverage from a high altitude platform," *IEEE Trans. on Wireless Comm.,* vol. 2, no. 3, pp. 484-492, May 2003.
[9] I. Palma-Lazgare and J. Delgado-Penin, "WiMAX HAPs-based downlink performance employing geometrical and statistical propagation channel characteristics," *Radio Science Bulletin*, no. 332, pp. 50-66, March 2010.
[10] J. Volakis, *Antenna Engineering Handbook,* 4th Edition, Chap. 12, McGraw-Hill, 2007.
[11] A. Lambrecht, J. Pontes, and W. Wiesbeck, "Investigation of dielectric resonator antennas for base station application," *23rd Annual Review of Progress in Applied Computational Electromagnetics*, pp. 1793-1800, March 2007.

Ali Araghi was born in Mashhad, Iran, in 1985. He received his B.Sc. degree from Islamic Azad University and M.Sc. degree from Shahed University, Tehran, Iran, respectively in 2009 and 2012, both in Communication Eng. Since Jan. 2012 he has been collaborating with ICT Research Institute. His research interests include the modal analysis of open structures, phase array antenna, and printed antennas with linear and circular polarization.

Mahmoud Ramezani Mayiami received his B.Sc. and M.Sc. degrees in electrical engineering, in 2008 and 2011, respectively, both from Shahed University, Tehran, Iran. Previously, he was with Iran Telecommunication Research Center and currently, he is a Ph.D. student in ECE department at Rutgers University, New Jersey, USA. His research interests span the area of wireless communications, statistical signal processing, compressive sensing and signal detection.

Ali Mohammad Montazeri was born in Isfahan, Iran, in 1981. He received the M.Sc. degree in electrical engineering in 2008 from Iran University of Science and Technology, Tehran, Iran. Currently, he has been with Iran Telecommunication Research Center, Tehran, Iran as a researcher. His research interests include wireless communication, channel estimation, and digital beamforming.

Ali Foudazi was born in Tehran, Iran, in 1986. He received his B.Sc. and M.Sc. degrees in communications engineering from Shahed University, in 2009 and 2012, respectively. He is currently Ph.D. student in Missouri University of Science &Technology. His research interests include microwave and mm-wave devices, THz technology, antenna design, and non-destructive test.

Mohsen Yaghubi-Namaad received the B.Sc. and M.Sc. degrees from the University of Tehran, Tehran, Iran, in 2009 and 2012, respectively, all in communication engineering. From 2010, he has been with the Iran Telecommunication Research Center (ITRC), where he was involved with wireless communication projects. His main research interests include wireless communications, compressive sensing and error correcting codes.

Mohammad Bod was born in 1986, in Tehran, Iran. He received the B.Sc. degree in electrical engineering, in 2009, and the M.Sc. degree in communication engineering, in 2012, both from Shahed University, Tehran, Iran. He is currently working towards the Ph.D. degree in Amirkabir University of technology (AUT). His research interests include active microwave circuits, microwave filters, phased arrays and broad-band antenna design.

Compact Oscillator Feedback Active Integrated Antenna by Using Interdigital Coupling Strip for WiMAX Applications

J. Mazloum [1], A. Jalali [1], M. Ojaroudi [2], and N. Ojaroudi [3]

[1] Faculty of Electrical and Computer Engineering,
Shahid Beheshti University, Tehran, Iran
j_mazloum@sbu.ac.ir and a_jalali@sbu.ac.ir

[2] Young Researchers Club
Ardabil Branch, Islamic Azad University, Ardabil, Iran
m.ojaroudi@iauardabil.ac.ir

[3] Department of Electrical Engineering
Ardabil Branch, Islamic Azad University, Ardabil, Iran
n.ojaroudi@yahoo.com

Abstract ─ A novel active feedback antenna for WiMAX applications is presented. By using an interdigital coupling strip in the active feedback antenna two new resonances can be achieved. Also the proposed interdigital radiating patch has a major advantage in providing tighter capacitive coupling to the line in comparison to known radiating patch. In order to generate DC isolation in the RF path, we use a pair of gap distances in the microstrip loop. Simulated and experimental results obtained for this antenna show that the proposed active integrated antenna (AIA) has a good return loss and radiation behavior within the WiMAX frequency range.

Index Terms ─ Active integrated antenna, interdigital strip, oscillator feedback structure, and WiMAX applications.

I. INTRODUCTION

Recently, the needs for active integrated antennas (AIA) have been growing significantly for mobile communication systems, such as, worldwide interoperability for microwave access (WiMAX), wireless local area network (WLAN), global positioning satellite (GPS), et al. Active integrated antennas (AIA) can provide some effective solution to various problems, such as higher transmission loss, limited source power, and reduced antenna efficiency. AIA have many advantages of reducing device size, low weight, and low fabrication cost for receiver front-end modules [1, 2]. Various techniques of active antennas, such as injection locking, cavity control, varactor tuned antenna, and oscillation feedback loop, have been presented [2]. Although the technique of using an oscillation feedback loop has improved bandwidth, gain, phase noise performance in radiated signals, simultaneously providing good power added efficiency (PAE), it still has the problem of containing design complexity and fabrication cost [1].

In the last few years, there have been rapid developments in worldwide interoperability for microwave access (WiMAX) applications. The 2.5 GHz / 3.5 GHz /5.5 GHz (2500–2690 MHz / 3400–3690 MHz / 5250–5850 MHz) bands are demanded in practical WiMAX applications. During the last years, there are various antenna designs, which enable antennas with low profile, lightweight, flush mounted, and WiMAX devices. These antennas include the planar inverted-F antennas (PIFAs) [3], planar monopole antenna

Submitted On: Aug. 19, 2012
Accepted On: Aug. 29, 2013

[4], and the printed dipole antennas [5]. In WiMAX communication systems, one of the key issues is the design of a compact active antenna while providing wideband characteristic over the whole operating band. It is a well-known fact that the active feedback presents really appealing physical features, such as simple structure, small size, and low cost. Because of all these interesting characteristics, active feedback are extremely attractive to be used in WiMAX applications and growing research activity is being focused on them [6, 7].

In this study, based on electromagnetic coupling (EC), an interdigital coupling strip in the microstrip transmission line is used to perturb two resonance frequencies at 3.5 GHz (WiMAX) and 4.2 GHz (C-band). The proposed interdigital radiating patch is shown in Fig. 1 (a). This structure has a major advantage in providing tighter capacitive coupling to the line in comparison to known radiating patch. In the proposed configuration a pair of gap distances are playing important role in the radiating characteristics of this antenna, because it can adjust the electromagnetic coupling effects between the interdigital radiating patch and the microstrip transmission line.

II. ANTENNA DESIGN AND CONFIGURATION

The proposed passive antenna fed by a 50 Ω feed line is shown in Fig. 1, which is printed on an FR4 substrate of thickness 0.8 mm, and permittivity 4.4. The numerical and experimental results of the input impedance and radiation characteristics are presented and discussed. The Ansoft simulation software high-frequency structure simulator (HFSS) [8] is used to optimize the design and agreement between the simulation and measurement.

Figure 2 shows the measured and simulated return loss and insertion loss characteristics of the proposed antenna shown in Fig. 1. The fabricated antenna has the frequency band of 3.27 GHz to over 4.38 GHz with two resonance frequencies around 3.53 GHz and 4.23 GHz. In order to understand the performance of the proposed structure in the WiMAX frequency band, the simulated current distributions on the radiating patch of the proposed antenna, are presented in Fig. 3. As shown in Fig. 3, at the resonance frequency (3.5 GHz), the current mainly concentrates on the C-shaped strips edges and also it can be seen that the electrical current does change its direction along these strips [5].

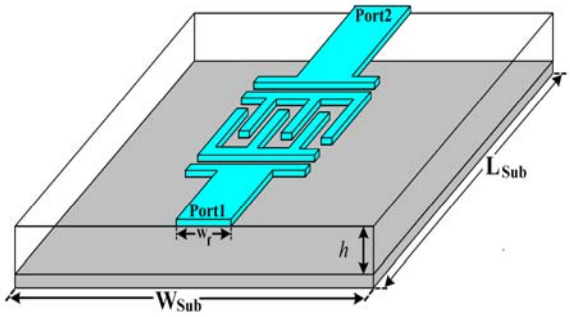

Fig. 1. The proposed antenna by using an interdigital coupling strip (W_{Sub} = 12 mm, L_{Sub} = 18 mm, W_f = 2 mm, and h = 0.8 mm).

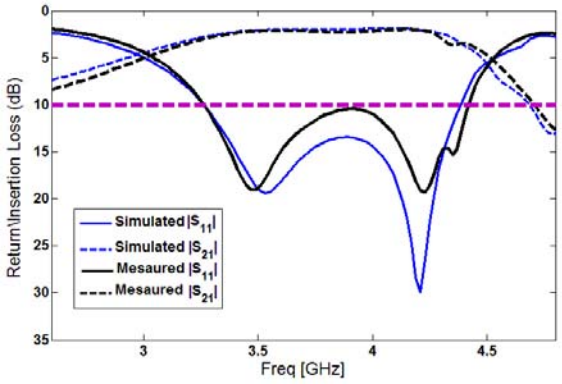

Fig. 2. Measured and simulated return loss and insertion loss characteristics for the passive microstrip antenna.

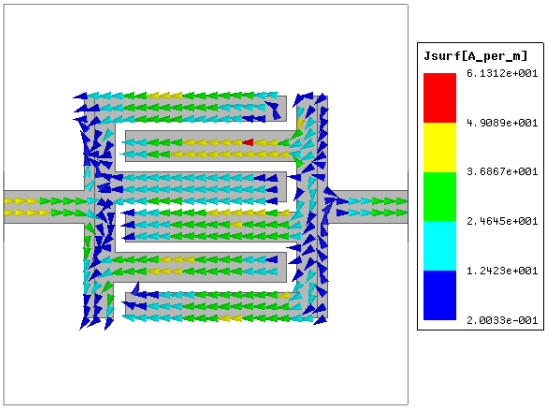

Fig. 3. Simulated surface current distributions on the radiating patch for the proposed passive antenna shown in Fig. 1, at 3.5 GHz.

The measured peak antenna gain against frequency in the range of 3.2 GHz – 4.3 GHz, are plotted in Fig. 4, showing small variations of less than 1 dBi.

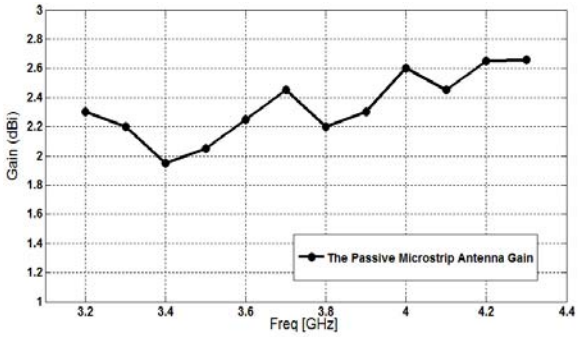

Fig. 4. Measured peak antenna gain versus frequency for the fabricated antenna in the 3.2 GHz – 4.3 GHz band.

III. OSCILLATOR DESIGN

Transistor oscillators can be designed using either bipolar or GaAs MESFET devices [9, 10]. Using the [S] parameters of the active element, the design of the microwave oscillator is performed using our full-scale computer simulation program. The stability of the device can be checked by two stability factors K and $|\Delta|$. The mathematical equations for K and $|\Delta|$ are as given in [10],

$$\Delta = S_{11}S_{22} - S_{21}S_{12} \tag{1}$$

$$K = \frac{1-\left|S_{11}\right|^2-\left|S_{22}\right|^2+\left|\Delta\right|^2}{2\left|S_{21}S_{12}\right|}. \tag{2}$$

The stability of the used transistor at the frequency of 3.5 GHz is calculated through calculation of the stability factor, K and Δ. The transistor is potentially unstable at the operated frequency 3.5 GHz (i.e., $K = 0.656$) and the stability circle at the gate-to-drain port is shown in Fig. 1. In the notation of Fig. 1, the gate-to-drain port is the terminating port,

$$R_S = \left|\frac{S_{12}S_{21}}{S_{11}^2-\Delta^2}\right| \tag{3}$$

$$C_S = conj\left(\frac{\left(S_{11}\right)-\Delta.conj\left(S_{22}\right)}{\left|S_{11}\right|^2-\left|\Delta\right|^2}\right). \tag{4}$$

Any Γ_T in the shaded stability circle region produces $|\Gamma_{in}| > 1$ (i.e., a negative resistance at the input port). We select an arbitrary point in mentioned region, at this point $\Gamma_T = 0.9\ \angle{-165}^{o}$, and the associated impedance is $Z_T = -j7.5\ \Omega$. This reactance can be implemented by an open-circuited 50 Ω line of length 0.226 λ. With Z_T connected, the input reflection coefficient is found to be $\Gamma_{IN} = 12.5\ \angle{-160}^{o}$, and the associated impedance is $Z_{IN} = -50-j3.5\ \Omega$. The load matching network is designed using equations (5) to (9), that is $Z_{IN} = 21-j2.1\ \Omega$,

$$\Gamma_{in} = S_{11} + \frac{S_{12}S_{21}\Gamma_T}{1-S_{22}\Gamma_T} \tag{5}$$

$$\Gamma_S = \Gamma_{in}^*, \tag{6}$$

$$Z_{in} = Z_0\frac{1-\left|\Gamma_S\right|^2+2j\left|\Gamma_S\right|\sin\left(\theta_{\Gamma_S}\right)}{1+\left|\Gamma_S\right|^2-2\left|\Gamma_S\right|\cos e\left(\theta_{\Gamma_S}\right)}, \tag{7}$$

$$Z_L = \frac{Real\left(Z_{in}\right)}{3} - j\ Imag\left(Z_{in}\right), \tag{8}$$

$$Y_{in} = \frac{50}{Z_L}. \tag{9}$$

The terminating circuit is designed to get maximum reflection coefficient at the transistor output. The analytical design of the terminating circuit and the output matching circuit are performed using the developed computer program [9]. As a result of the developed program and the optimization process described elsewhere [10] the lengths and widths of the termination and matching circuits are:

Terminating Circuit: Length of the open circuit series line (50 Ω) = 19.25 mm, and width of the open circuit series line = 3.2 mm.

Load matching circuit: Length of series line (50 Ω) = 1.525 mm, width of series line = 3.2 mm, length of open single shunt stub = 8.05 mm, and width of open balanced shunt stub = 3.2 mm.

In this paper, we simulated and manufactured microwave oscillator for wireless applications by using advance design system (ADS) simulator [11]. The presented miniature packaged oscillator with the matching circuit is shown in Fig. 5.

IV. ACTIVE INTEGRATED ANTENNA DESIGN

The presented active feedback antenna is shown in Fig. 6, which is printed on an FR4 substrate of thickness 1.6 mm, permittivity 4.4, and loss tangent 0.018. The proposed active

feedback antenna structure consists of an interdigital coupling strip for radiating element, a microstrip loop, and an amplifier with DC bias circuit and matching circuit for active part. The width of the 50 Ω microstrip line is fixed at 3.2 mm, as shown in Fig. 6. The matching circuit to the left and right of the device controls the degree of feedback [10]. On the other side of the substrate, a conducting ground plane is placed. In addition, to satisfy the oscillation-phase requirement, the microstrip loop is fixed to a suitable electrical length, taking the measured phases of the amplifier and passive antenna into consideration [12, 13]. The proposed antenna is connected to a 50 Ω SMA connector for signal transmission. Figure 7 presents the photograph of a realized active integrated antenna on an FR-4 substrate with the SMA connector.

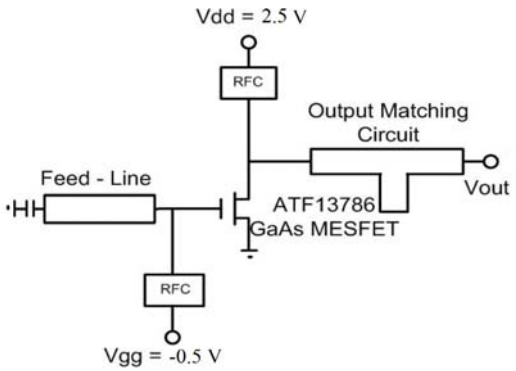

Fig. 5. Circuit layout of the proposed oscillator.

Figure 8 shows the measured return loss. The measured return losses of the active antenna shows gains of 14.3 dBi, 8.3 dBi, 4.4 dBi at each resonance frequency with the bias condition of VG = –0.2 V, VD = –0.3 V and ID = 8 mA. The magnitude of S_{11} decreases with the increase of the operating frequency. The resonant frequencies of the active antenna are correspondingly shifted by the amount of the parasitic parameters, which are caused by the transistor parameters and the layer of the active antenna. The parasitic components of the circuit pattern, printed on the substrate with copper conductors, may affect the resonant frequency, and changing the total length of the antenna. Owing to such structural errors, measured resonant frequencies are shifted from 3.5 GHz to 3.58 GHz and from 4.2 GHz to 4.31 GHz. The shift of the operating resonant frequencies becomes larger at higher operating frequency. These results may be caused by the growing effect of the added impedances at higher frequencies.

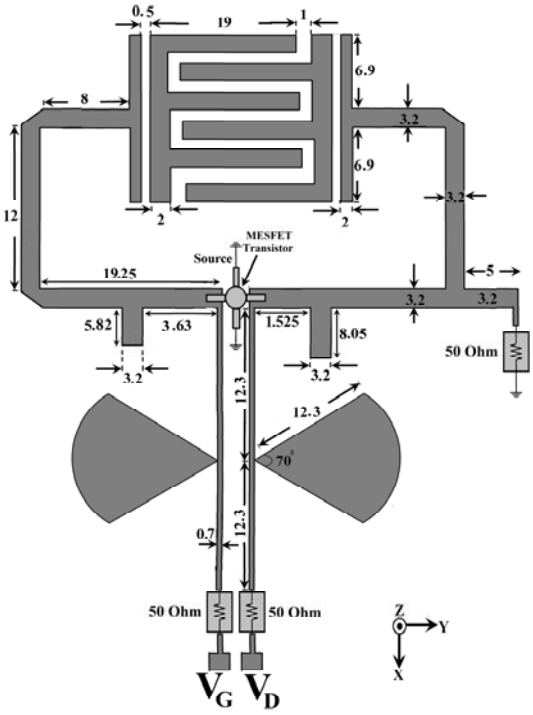

Fig. 6. Configuration of the proposed active integrated antenna with GaAs MESFET.

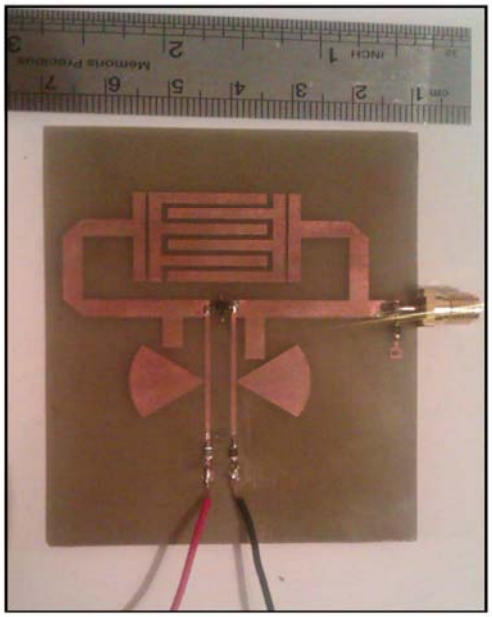

Fig. 7. Photograph of the realized active integrated antenna.

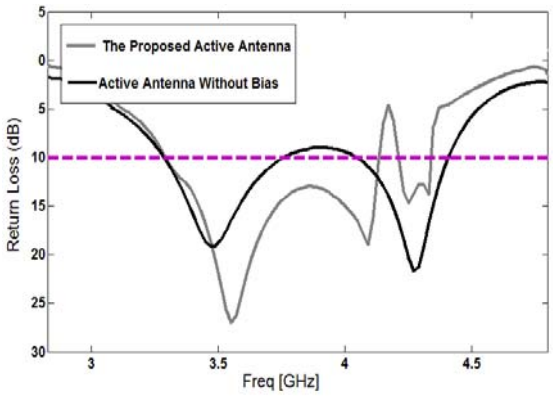

Fig. 8. Measured return losses of the active integrated antenna and the passive antenna.

The simulated radiation patterns including the co- and cross-polarizations for the E-plane (y-z plane) and H-plane (x-z plane) at the resonance frequencies are shown in Fig. 9. The simulated radiation patterns are calculated by using the gap-source technique with the commercial EM simulator HFSS, considering the complete active feedback antenna, which has same layout, except with an active transistor [9]. The received cross-polarizations in the E- and H-planes of the AIA are approximately 17 dB and 14 dB lower than the maximum co-polarized radiation, respectively. As seen in Fig. 3, the radiation pattern in the H-plane is asymmetrical due to the asymmetrical presence of the distributed oscillator-feedback circuitry. The obtained gain by the amplifier is of 11.2 dB. The designed feedback-antenna oscillator has stable oscillation and a clear spectrum at the frequency of 3.54 GHz, which is only a 0.2 % deviation from the design frequency.

Figure 10 shows the radiated output power from the fabricated active integrated antenna for the previously mentioned biasing conditions measured in anechoic chamber. The implemented oscillator exhibited output power level -33.09 dBm at frequency of 3.488 GHz. The output power is measured to be about 25.17 dBm, using an Agilent E4440A spectrum analyzer and a double-ridged horn antenna (gain 17 dBi) as a reference antenna placed at a distance of 2 m.

V. CONCLUSION

As presented above, the AIA is an interesting subject for WiMAX applications. In this paper, an active integrated antenna using an interdigital coupling strip antenna, are presented. In the proposed structure, based on electromagnetic coupling (EC), an interdigital coupling strip in the microstrip transmission line is used to perturbs two resonance frequencies at 3.5 GHz (WiMAX) and 4.2 GHz (C-band). The amplifier design based on the AIA concept has been shown to provide an efficient and successful method for designing high efficiency and compact systems. The obtained gain by the amplifier is 11.2 dB. The designed feedback-antenna oscillator has stable oscillation and a clear spectrum at the frequency of 3.54 GHz, which is only 0.2 % deviation from the design frequency.

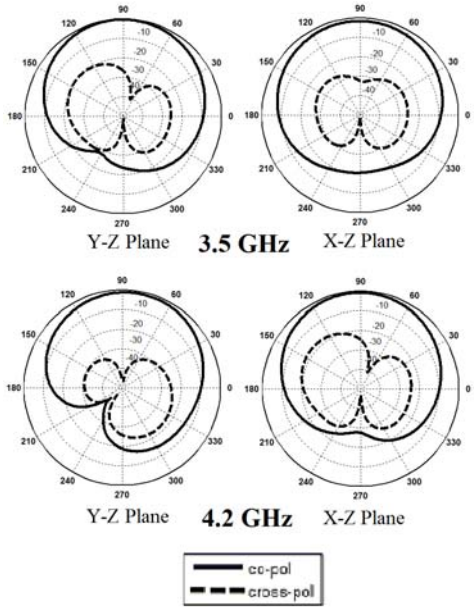

Fig. 9. simulated radiation patterns of the proposed antenna.

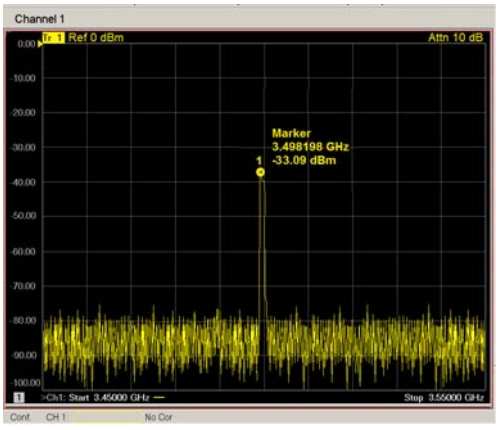

Fig. 10. Measured output power radiated from the proposed oscillator at 3.5 GHz.

ACKNOWLEDGMENT

The authors are thankful to Microwave Technology (MWT) Company staff for their beneficial and professional help (www.microwave-technology.com).

REFERENCES

[1] F. Giuppi, A. Georgiadis, M. Bozzi, S. Via, A. Collado, and L. Perregrini, "Hybrid electromagnetic and non-linear modeling and design of SIW cavity-backed active antennas," *Applied Computational Electromagnetics Society (ACES) Journal*, vol. 25, no. 8, pp. 682-689, August 2010.

[2] F. Giuppi, A. Georgiadis, M. Bozzi, S. Via, A. Collado, and L. Perregrini, "Hybrid nonlinear and electromagnetic design of an active oscillator SIW cavity backed slot antenna," *26th Annual Review of Progress in Applied Computational Electromagnetics (ACES)*, pp. 260-263, Tampere, Finland, April 2010.

[3] M. Ojaroudi, M. Hassanpour, Ch. Ghobadi, and J. Nourinia, "A novel planar inverted-F antenna (PIFA) for WLAN/WiMAX applications," *Microwave and Optical Tech. Letters*, vol. 53, no. 3, pp. 649-652, August 2011.

[4] M. Ojaroudi, N. Ojaroudi, and N. Ghadimi, "Enhanced bandwidth small square slot antenna with circular polarization characteristics for WLAN/WiMAX and C-band applications," *Applied Computational Electromagnetics Society (ACES) Journal*, vol. 28, no. 2, pp. 156-161, Feb. 2013.

[5] F. Hsiao and K. Wong, "Compact planar inverted-F patch antenna for triple-frequency operation," *Microwave and Optical Tech. Letters*, vol. 33, no. 6, pp. 459-462, 2002.

[6] V. Stoiljkovic, S. Suganthan, and M. Benhaddou, "A novel dual band center-fed printed dipole antenna," *in Proc. IEEE Antennas Propag. Soc. Int. Symp.* pp. 938-94, 2003.

[7] P. C.-Yuan, H. T.-Sheng, C. W.-Shen, and H. C.-Hsiang, "Dual wideband printed monopole antenna for WLAN/WiMAX application," *IEEE Antennas Wirel. Propag. Lett.*, vol. 6, pp. 149-151, 2007.

[8] Ansoft High Frequency Structure Simulation (HFSS), Ver. 13, Ansoft Corporation, 2010.

[9] B. Catli and M. Hella, "A low-power dual-band oscillator based on band-limited negative resistance," *IEEE Radio Frequency Integrated Circuits (RFIC) Symposium*, pp. 251-254, June 2009.

[10] G. Yun, "Compact oscillator-type active antenna for UHF RFID reader," *Electronic Letters*, vol. 43, no. 6, March 2007.

[11] Advanced Design System (ADS), Agilent Corporation, 2009.

[12] M. Ojaroudi, Sh. Yzdanifard, N. Ojaroudi, and M. N.-Moghaddasi, "Small square monopole antenna with enhanced by using inverted T-shaped slot and conductor-backed plane," *IEEE Transactions on Antenna and Propagation*, vol. 59, no. 2, pp. 670-674, Feb. 2011.

[13] J. Liu, C. Cheng, H. Chen, and P. Chen, "Active integration ring antenna/phase shifter for direct conversions," *IEE Proc. Microw. Antennas Propag.*, vol. 151, no. 4, pp. 357-361, August 2004.

Jalil Mazloum was born on 1973 in Tehran, Iran. He received his B.Sc. degree in Bioelectric Engineering from Shahid Sattari Aeronautical University of Science and Technology, Tehran, Iran, and M.Sc. degree in Bioelectric Engineering from Amirkabir University of Technology, Tehran, Iran. Since 1998, he has been a Research Fellow and a Teaching Assistant with the Department of Electrical Engineering, Aeronautical University of Science and Technology, Tehran, Iran. His research interests include design and modeling of microwave structures, radar systems, and RFID systems.

Ali Jalali received his B.Sc. in Electronic Engineering from Sharif University of Technology in 1991. He also received his M.Sc. and PhD in Electronic Engineering from Supelec University and Rennes I University, FRANCE, in 1994 and 1998, respectively. From 1998 till now he is with the Faculty of Electrical and Computer Engineering at Shahid Beheshti University, G. C., Tehran, Iran. His research interests includes low- power and low-voltage analog and digital Integrated Circuits, Digital Audio Broadcasting, and VLSI Design.

Mohammad Ojaroudi was born in 1984 in Germi, Iran. He received his B.Sc. degree in Power Electrical Engineering from Azad University, Ardabil Branch and M.Sc. degree in Telecommunication Engineering from Urmia University. From 2010, he is working toward the PhD degree at Shahid Beheshti University. Also from July 2013 he has been working, as a research visitor in Dr. Fathy laboratory in University of Tennessee, Knoxville, USA. From 2007 until now, he is a Teaching Assistant with the Department of Electrical Engineering, Islamic Azad University, Ardabil Branch, Iran.

Nasser Ojaroudi was born in 1986 in Germi, Iran. He received his B.Sc. degree in Electrical Engineering from Azad University, Ardabil Branch. From 2011, he is working toward the M.Sc. degree in Telecommunication Engineering at Shahid Rajaee Teacher Training University. Since March 2008, he has been a Research Fellow in the Microwave Technology Company (MWT), Tehran, Iran. His research interests include microstrip antennas for radar systems, ultra-wideband (UWB) and small antennas for wireless communications, microwave passive devices and circuits, and microwave/millimeter systems.

Design and Analysis of The Stub and Radial-Stub Loaded Resonator Band-Pass Filter with Cross-Shaped Coupled Feed-Lines for UWB Applications

B. Mohammadi [1], J. Nourinia [1], Ch. Ghobadi [1], and A. Valizade [2]

[1] Department of Electrical Engineering
Urmia University, Urmia, Iran
st_b.mohammadi@urmia.ac.ir, j.nourinia@urmia.ac.ir, ch.ghobadi@urmia.ac.ir,

[2] Young Researchers Club, Qaemshahr Branch
Islamic Azad University, Qaemshahr, Iran
a.valizade@sun.semnan.ac.ir

Abstract ─ In this paper, the procedure of attaining a compact microstrip ultra-wideband (UWB) band-pass filter (BPF) by the use of stub and radial stub loaded resonator and also cross-shaped coupled lines (CCLs) as feed-lines, is presented and discussed. Implementation of CCLs results in suppression of the unwanted pass-band harmonics while by loading the resonator, additional transmission zeros (TZs) are produced, which lead to improvement of the in-band performance of the BPF. Measurement results of the fabricated UWB BPF are in good agreement with simulation predictions and the presented BPF has a sharp roll-off and improved out-of-band performance in the frequency band of interest.

Index Terms ─ Band-pass filter, cross-shaped coupled lines, radial stub loaded resonator, stub loaded, and ultra-wideband applications.

I. INTRODUCTION

Since 2002 when the U.S. Federal Communications Committee (FCC) authorized the 3.1 GHz – 10.6 GHz frequency band for ultra-wideband indoor and hand-held wireless communications, tremendous efforts and researches have been carried out to develop UWB systems [1]. In UWB communication systems, designing a high performance band-pass filter with wide bandwidth, compact size, low insertion loss, and also wideband rejection is still a challenging task [2]. In order to design a wideband microstrip filter one of the common and easy to implement solutions is the use of cascaded parallel coupled sections. However, this structure suffers from spurious pass-band harmonics. In [2], defected ground structure (DGS) was used to eliminate the spurious responses. Also, to improve upper pass-band performance several other UWB filter structures based on multiple-mode resonators (MMRs) have been reported recently, which are fed by conventional quarter wavelength coupled lines and have low insertion loss, good selectivity and out-of-band rejection performance but suffer from larger circuit size and narrow upper stop-band [3-5].

In the design of UWB band-pass filters based on multiple-mode resonators, the first three resonant frequencies of the MMR should be placed in the UWB pass-band of interest almost equally. By varying the length of the center low-impedance line section or increasing the number of non-uniform sections in the MMR, UWB band-pass filters with more in-band transmission poles can be produced. On the other hand, the inevitable fourth or other higher-order resonant frequencies of the MMR may produce spurious and unwanted pass-bands at upper stop-band and degrade the performance of the resultant UWB filter. In order to overcome this intrinsic problem of the MMR-based filters, an interdigital coupled line with capacitive-ended loading and/or tapered strip

Submitted On: April 1, 2013
Accepted On: Aug. 5, 2013

shape can be implemented to the filter structure, and its first transmission zero is reallocated toward the full suppression of this fourth resonant frequency in the MMR [6]. In [7], it is shown that by the use of CCLs instead of conventional parallel coupled lines, not only the size of the microstrip filter is miniaturized but also by assigning the TZs toward the upper stop-band, the spurious harmonic pass-bands can be effectively suppressed.

This paper introduces a novel microstrip UWB BPF with improved in-band and out-of-band performances, which has sharp roll-off at both upper and lower cut-off frequencies. In the proposed structure, the sharp roll-off and high skirt selectivity is achieved by loading the resonator with a simple stub and a pair of radial stubs. These stubs produce additional TZs and resonances, which are controllable through their dimensions [5-8]. Also utilizing the radial stubs instead of the conventional stepped-stubs and forming radial stub loaded resonator (RSLR) reduces the vertical size of the filter [8].

Moreover, by implementing the CCLs instead of the conventional quarter wavelength parallel coupled lines, additional transmission zeros are added to the frequency response of the BPF, which are controllable by the dimensions of the CCLs. The out-of-band performance of the filter can be significantly improved by proper adjustment of the transmission zeros, which are produced by the CCLs toward the harmonic resonances of the multi-mode loaded resonator and eliminate the unwanted higher pass-bands. Also the size of the filter is reduced by the use of the CCLs [7]. In addition, in order to achieve tight coupling a defected ground structure (DGS) is used [9, 10]. The presented microstrip filter structure has a compact size and shows suitable performance in UWB frequency band.

II. FILTER DESIGN AND CONFIGURATION

The proposed microstrip UWB BPF with its design parameters is shown in Fig. 1. The filter substrate is Rogers (RO4003) with permittivity of 3.55, thickness of 0.8 mm, and loss tangent of 0.0027. The presented structure consists of a simple cross-shaped resonator, which is coupled with two cross-shaped meander interdigital lines, which are connected to the feed-lines. The feed-lines are connected to a 50 Ω SMA connectors for signal transmission, as shown in Fig. 1 (a). Then by loading the coupled resonator with a stub and a pair of radial stubs at its center, a stub loaded resonator (SLR) is formed, as shown in Fig. 1 (b). On the other side of the substrate, the ground plane with two symmetrical back-to-back T-shaped like defects at its center is placed, as shown in Fig. 1 (c). The defects on the ground plane perturb the current distribution and as a result the effective capacitance or inductance of the transmission lines is increased and is used here to achieve a tight coupling [8, 9].

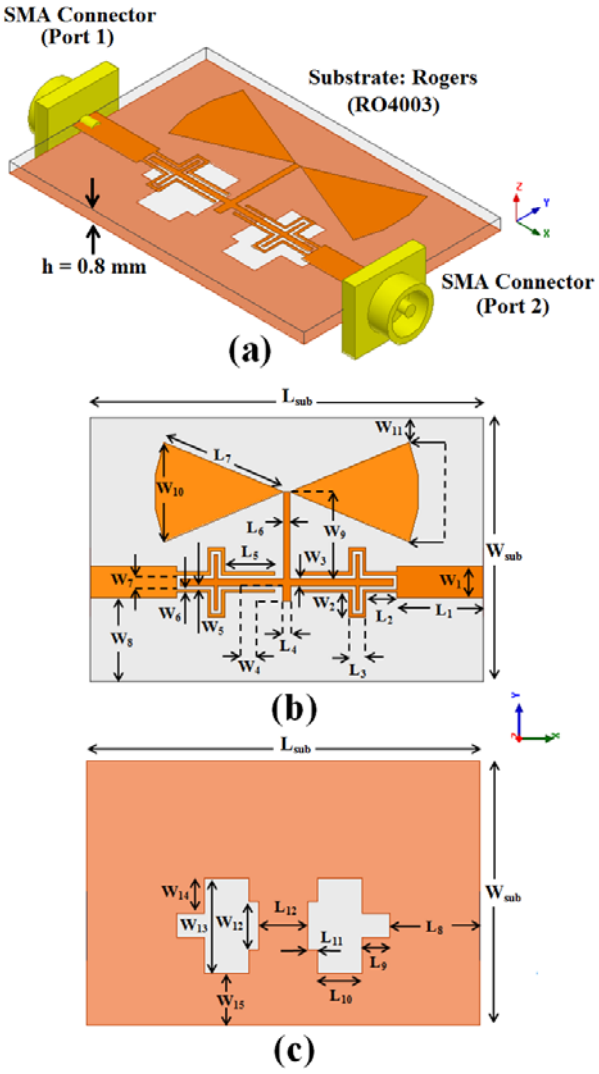

Fig. 1. Geometry and design parameters of the proposed UWB band-pass filter: (a) side view, (b) top view, and (c) bottom view.

In this study we started with a simple cross-shaped resonator. This simple resonator generates two resonances within the UWB frequency spectrum but it suffers from the presence of spurious responses, which are generated at multiples of the center frequency [2]. Then in order to eliminate the spurious harmonic pass-bands and improve the out of band performance of the filter, cross-shaped coupled lines were added to the design. The main advantage of these cross-shaped coupled lines is that they produce additional TZs, which are controllable by the dimension of the cross-shaped coupled lines. By adjusting the dimensions of the cross-shaped coupled lines and placing the first two upper stop-band TZs at the harmonic resonances of the multiple-mode resonator the unwanted pass-band is effectively rejected [7]. At the next step of the design procedure, the coupled resonator was loaded by a simple and a pair of radial stub, and thereby a stub loaded resonator (SLR) is formed. Through adding these stubs to the filter structure, additional resonances and TZs were introduced to the frequency response of the proposed BPF, which are controllable by the dimensions of the stubs. Assigning the TZs toward the cut-off frequencies and assigning the resonances toward the UWB frequency band leads to desired high skirt selectivity and improved in-band performance, respectively.

III. RESULTS AND DISCUSSIONS

The proposed UWB BPF with its final and modified design parameters was designed, fabricated, and tested and in this section its simulation and measurement results are presented and discussed. Ansoft simulation software high frequency structure simulator (HFSS) was used for simulation studies [10]. Figure 2 shows different structures, which were investigated in simulation studies and the insertion loss characteristics for the slotted ground plane filter with simple cross-shaped resonator (Fig. 2 (a)), with CCLs (Fig. 2 (b)), with CCLs and simple stub (Fig. 2 (c)), with CCLs and a pair of radial stubs (Fig. 2 (d)), and the proposed filter structure are compared in Fig. 3.

As it can be observed in Fig. 3, the simple cross-shaped resonator is a double mode resonator and generates two resonances within the UWB frequency band and has some unwanted resonances at the upper stop-band. To overcome this problem, as shown in Fig. 2 (b), cross-shaped coupled lines were added to the filter structure and by suppressing the spurious responses by two CCLs at both input and output ports, the stop-band is extended to near than 25 GHz with a rejection level of more than 20 dB, but still the frequency response of the filter is not completely tuned for UWB performance. Therefore, a simple stub and a pair of radial stubs are added to the filter structure and the proposed UWB BPF is formed. The effect of each one of these stubs on the frequency response of the filter is shown separately in Fig. 3. As it can be seen in this figure, the simple stub can improve the upper frequency band while the radial stubs have effect on both upper and lower frequency bands. By adjusting these stubs and assigning their TZs to harmonic resonances and upper/lower cut-off frequencies, an UWB BPF with improved out-of-band performance, sharp roll-off, and high skirt selectivity is designed.

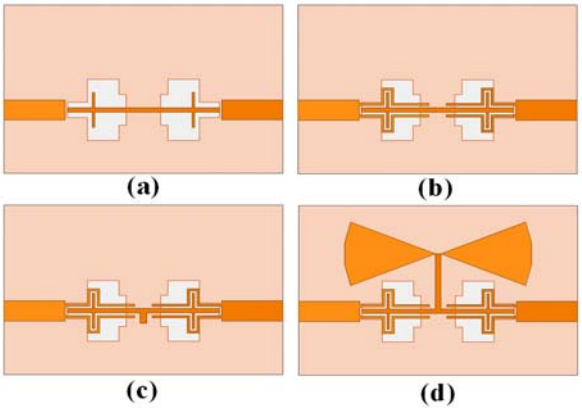

Fig. 2. Slotted ground plane filter with (a) simple cross-shaped resonator, (b) CCLs, (c) CCLs and simple stub, and (d) CCLs and a pair of radial stubs.

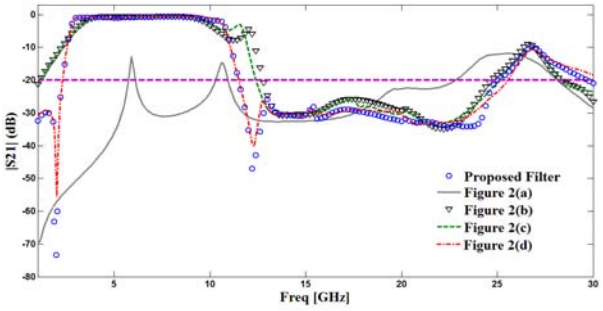

Fig. 3. Frequency responses of various filter structures shown in Fig. 2 and the proposed UWB BPF filter.

In order to modify the design parameters of the proposed filter, a parametric study was performed. The final values of the design parameters are listed in Table I. As examples of the aforementioned parametric study, the effect of two design parameters are presented and discussed here. Figure 4 shows the effect of the finger length of the CCLs (L_2 in Fig. 1) on the frequency responses of the proposed filter for different cases in Table II and compares it with the conventional parallel coupled lines. It is found that by changing the finger length, the TZs can be adjusted toward unwanted pass-bands properly. Figure 5 shows the effect of various radial stubs dimension on the return loss characteristic of the proposed UWB BPF for the cases listed in Table III. As it can be observed from this figure, the in-band performance of the filter is significantly affected by the dimensions of the radial stubs.

Table I: The final dimensions of the designed BPF.

Param.	mm	Param.	mm	Param.	mm
W_{sub}	15.25	W_{10}	5.74	L_4	0.5
W_1	1.8	W_{11}	1.43	L_5	2.9
W_2	1.4	W_{12}	2.8	L_6	0.4
W_3	0.4	W_{13}	5.5	L_7	7.5
W_4	0.9	W_{14}	2.05	L_8	5.2
W_5	0.2	W_{15}	1	L_9	1.6
W_6	0.2	L_{sub}	22.8	L_{10}	2.6
W_7	0.8	L_1	5	L_{11}	0.6
W_8	4.84	L_2	1.8	L_{12}	2.8
W_9	5	L_3	1	h	0.8

Table II: Three various cases for the finger length of CCLs.

Case	L_1(mm)
1	1.4
2	1.6
3	1.8

Another filter structure, which was compared with the presented BPF in simulation studies is shown in Fig. 6 and its frequency responses are compared with the proposed filter in Fig. 7. In this structure a smaller pair of radial stubs is used instead of the simple stub. As it is observed in Fig. 7 the frequency response of the compared filter is almost the same as the presented filter except that the presented filter has a more uniform and extended out-of-band performance but upper cut-off frequency roll-off is sharper for the compared structure.

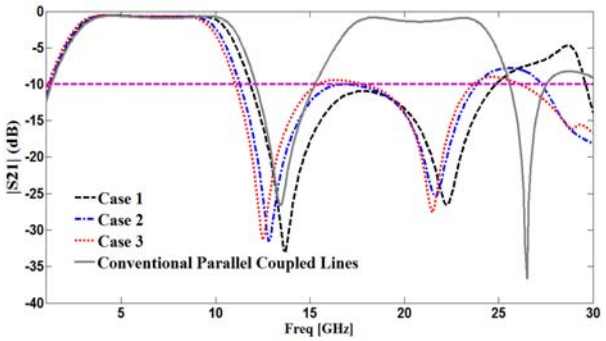

Fig. 4. Frequency responses for various radial stubs dimension listed in Table III.

Table III: Four various cases for the dimensions of the radial stubs.

Case	L_7(mm)
1	6
2	6.5
3	7
4	7.5

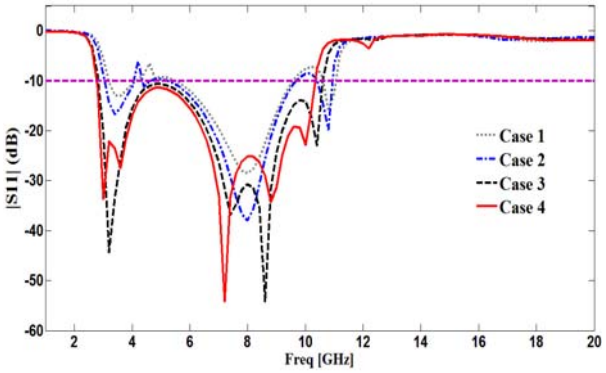

Fig. 5. Return loss characteristics for various radial stubs dimension listed in Table III.

Figure 8 shows the fabricated filter and its measured and simulated frequency responses are compared in Fig. 9. The measured results are in good agreement with the simulation data and the

fabricated UWB BPF has a 3 dB pass-band, which covers the range of 2.62 GHz – 10.67 GHz with a fractional bandwidth of 117 %. The improved out-of-band performance of this filter has an attenuation level more than 20 dB for frequencies up to 20 GHz and even more. A comparison between the proposed filter and other reported UWB BPFs is presented in Table IV. The small size and good in/out-band performances of the proposed filter are its main advantages.

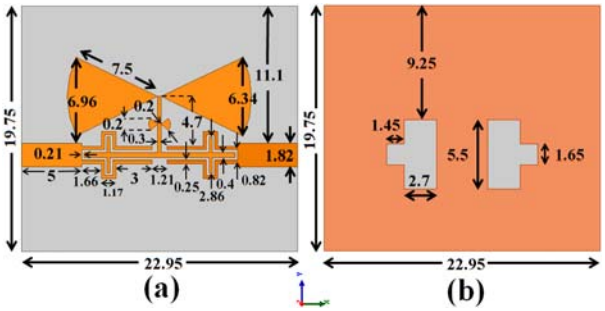

Fig. 6. Filter structure, which was used for comparison in simulation study.

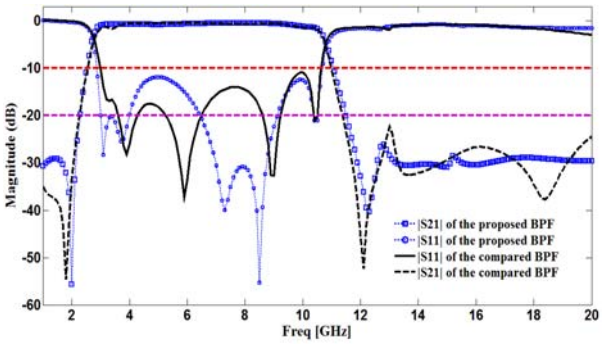

Fig. 7. Frequency responses of the filter structure shown in Fig. 6 in comparison with the proposed filter.

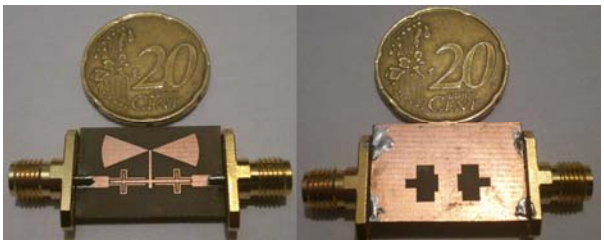

Fig. 8. The photograph of the fabricated UWB BPF.

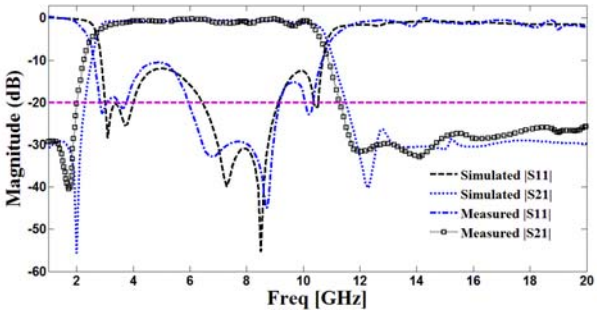

Fig. 9. Simulated and measured frequency responses of the proposed BPF.

Table IV: A comparison with reported UWB BPFs.

Ref	IL (dB)	RL (dB)	S.F.	ε_r/h (mm)	size ($\lambda_0 \times \lambda_0$)	f_c (GHz)
[3]	1.5	11	0.921	2.55/0.8	0.51×0.34	16.8
[4]	0.55	10	0.642	10.8/1.27	0.36×0.05	13.6
[5]	2	12.5	0.757	10.5/0.635	0.23×0.16	18
[6]	1.4	10	0.812	2.55/0.8	0.31×0.38	24
[7]	0.8	12	0.828	2.2/0.508	0.37×0.24	17
This Work	1	11	0.783	3.55/0.8	0.3×0.24	24

IL: insertion loss at the 6.85 GHz; RL: return loss over the whole pass-band; S.F.: selectivity factor of the pass-band (S.F. = $\Delta f_{3dB}/\Delta f_{30dB}$); Δf_{3dB}, Δf_{30dB}: 3 dB bandwidth and 30 dB bandwidth of the pass-band, respectively; ε_r: substrate relative dielectric constant; h: Substrate thickness; f_c: the upper stop-band frequency with 20 dB attenuation; λ_0 is the free space wavelength of the operating frequency at the center of the pass-band (6.85 GHz).

IV. CONCLUSION

A compact microstrip filter with sharp roll-off and improved out of band performance for UWB applications was presented and discussed. In the proposed structure cross-shaped coupled lines are used to improve the out-of-band performance of the filter while a sharp roll-off and high skirt selectivity is achieved by implementing a simple stub and a pair of radial stubs. Also by the use of this structure the overall size of the filter is

reduced. The proposed filter is cheap, easy to fabricate, and a good candidate for UWB applications.

ACKNOWLEDGMENT

The authors are thankful to Microwave Technology (MWT) Company staff for their beneficial and professional help (www.microwave-technology.com).

REFERENCES

[1] Revision of Part 15 of the Commission's Rules Regarding Ultra-Wide-band Transmission System FCC, Washington, DC, ET- Docket pp. 98-153, 2002.

[2] F. Karshenas, A. Mallahzadeh, and J. Rashed-Mohasse, "Size reduction and harmonic suppression of parallel coupled-line band-pass filters using defected ground structure," *Applied Computational Electromagnetics Society (ACES) Journal*, vol. 25, no. 2, pp. 149-155, Feb. 2010.

[3] Q. Chu, X. Wu, and X. Tian, "Novel UWB bandpass filters using stub-loaded multiple-mode resonator," *IEEE Microw. Wireless Compon. Lett.*, vol. 21, no. 8, pp. 403-405, Aug. 2011.

[4] L. Zhu, S. Sun, and W. Menzel, "Ultra-wideband (UWB) bandpass filters using multiple-mode resonator," *IEEE Microw. Wireless Compon. Lett.*, vol. 15, no. 11, pp. 796-798, Nov. 2005.

[5] H. Deng, Y. Zhao, L. Zhang, X. Zhang, and S. Gao, "Compact quintuple-mode stub-loaded resonator and UWB filter," *IEEE Microw. Wireless Compon. Lett.*, vol. 20, no. 8, pp. 438-440, Aug. 2010.

[6] S. Sun and L. Zhu, "Capacitive-ended interdigital coupled lines for UWB bandpass filters with improved out-of-band performance," *IEEE Microw. Wireless Compon. Lett.*, vol. 16, no. 8, pp. 440-442, Aug. 2006.

[7] X. Tian, Q. Chu, H. Zhu, and X. Wu, "A UWB bandpass filter with wide stopband performance using cross-shaped coupled lines," *Microwave and Millimeter Wave Technology (ICMMT) International Conference*, pp. 1-4, 2012.

[8] J. Xu, W. Wu, W. Kang, and C. Miao, "Compact UWB bandpass filter with a notched band using radial stub loaded resonator," *IEEE Microw. Wireless Compon. Lett.*, vol. 22, no. 7, pp. 351-353, July 2012.

[9] R. Habibi, C. Ghobadi, J. Nourinia, M. Ojaroudi, and N. Ojaroudi, "Very compact broad band-stop filter using periodic l-shaped stubs based on self-complementary structure for x-band application," *Electron. Lett.*, vol. 48, no. 23, pp. 1483-1484, Nov. 2012.

[10] Ansoft High Frequency Structure Simulation (HFSS), ver. 13, Ansoft Corporation, 2010.

Bahman Mohammadi was born in Divandareh, Iran 1989. He received the B.Sc. degree in Electrical Engineering from Tabriz University, Tabriz, Iran, in 2011, where he is currently working toward the M.Sc. degree in Electrical Engineering from Urmia University, Urmia, Iran. His research interests include electromagnetic computation and wideband passive microwave devices (couplers, filters, phase shifters, etc.).

Javad Nourinia received his B.Sc. in Electrical and Electronic Engineering from Shiraz University and M.Sc. degree in Electrical and Telecommunication Engineering from Iran University of Science and Technology, and Ph.D. degree in Electrical and Telecommunication from University of Science and Technology, Tehran Iran in 2000. From 2000 he was an Assistant Professor and now he is a Professor in the Department of Electrical Engineering of Urmia University, Urmia, Iran. His primary research interests are in antenna design, numerical methods in electromagnetic and microwave circuits.

Changiz Ghobadi was born on 1st of June, 1960 in Iran. He received his B.Sc. in Electrical Engineering-Electronics and M.Sc. degrees in Electrical Engineering-Telecommunication from Isfahan University of Technology, Isfahan, Iran and Ph.D. degree in Electrical-Telecommunication from University of Bath, Bath, UK in 1998. From 1998 he was an Aassistant Professor and now he is a Professor in the Department of Electrical Engineering of Urmia University, Urmia, Iran. His primary research interests are in antenna design, radar, and adaptive filters.

Arash Valizade was born in Tehran, Iran 1986. He received his B.Sc. in Electrical Engineering-Electronics from Azad University of Sabzevar, Iran, in 2008 and M.Sc. degrees in Electrical Engineering-Telecommunication from Urmia University, Urmia, Iran, in 2012, and he is currently a Ph.D. student at Semnan University, Semnan, Iran. His primary research interests are in numerical methods in electromagnetics, microstrip antenna design, microwave circuits, active integrated antenna, and reconfigurable structures.

Characteristic Parameters Determination of Different Striplines Configurations using HBEM

Mirjana T. Perić, Saša S. Ilić, Slavoljub R. Aleksić, and Nebojša B. Raičević

Department of Theoretical Electrical Engineering
University of Niš, Faculty of Electronic Engineering, Niš, 18000, Serbia
mirjana.peric@elfak.ni.ac.rs, sasa.ilic@elfak.ni.ac.rs, slavoljub.aleksic@elfak.ni.ac.rs, and nebojsa.raicevic@elfak.ni.ac.rs

Abstract ─ Different configurations of striplines are analyzed using the hybrid boundary element (HBEM) method, developed at the Faculty of Electronic Engineering of Niš. The quasi TEM analysis is applied. The effective dielectric permittivity as well as the characteristic impedance of several 2D striplines are determined. In order to validate the obtained HBEM values of the characteristic impedance, in terms of accuracy, they have been compared with the corresponding ones obtained by the finite element method. Fast convergence of the results, short computation time, and possibility to solve complex multilayered configurations of striplines, make hybrid boundary element method very efficient in the calculation of 2D striplines parameters. All results are presented in tables and graphically.

Index Terms ─ Characteristic impedance, equivalent electrodes method, finite element method, hybrid boundary element method, and stripline.

I. INTRODUCTION

Stripline is a structure having a strip sandwiched in a dielectric layer between two ground planes [1]. Such structure can be used in printed-circuit boards, ground-signal-ground transmission lines, multilayer boards, as a part of an antenna power divider, etc. Analytical solutions for centered, off-centered, and shielded striplines are given in [1]. There is mentioned that a large number of authors [2, 3] describe such configurations. In order to calculate the characteristic impedances of the striplines, different analytical and numerical techniques are used: the conformal mapping [3], the finite element method (FEM) and the method of lines (MoL) [4], the Fourier transform method [5], the method of moments (MoM) [6], the integral equation techniques [7-10], the equivalent electrodes method (EEM) [11], the generalized spectral domain analysis, etc. The integral equation method is applied in [8] for computing the capacitance and inductance matrix for a multiconductor transmission line in a multilayer dielectric region. Characteristic parameters of the stripline, placed in an anisotropic media between two ground planes, are analyzed in [11].

The purpose of this paper is to present some other configurations of striplines placed in the multilayer media and to verify the accuracy of the hybrid boundary element method [12]. This method, developed at our Department, is a combination of the equivalent electrodes method [13] and the boundary element method (BEM) [14, 15]. The EEM, which resembles the MoM [16], but is however very different from it, was successfully applied in [17-19] for solving the problems with multilayer media, as well as the problems of transmission and shielded slot lines. Generally, the application of the EEM depends on the Green's function of the observed problem, and therefore the method is based on the combination of analytical derivation of the Green's function in the closed form and the numerical procedure for solving simplified problems. In some cases, finding the Green's function in the closed form can be very difficult or even impossible. It is very important to notice that the EEM application does not require any kind of numerical integration for problem solving. In the MoM, the numerical integration is always present. That produces some prob-

Submitted On: Nov. 6, 2012
Accepted On: Aug. 29, 2013

lems in the numerical solving of non-elementary integrals having singular subintegral functions.

An improvement of the EEM has been achieved combining it with the BEM, in order to solve problems of arbitrarily shaped multilayer structures, where finding the Green's function can be very difficult or even impossible. That method is called the hybrid boundary element method (HBEM). It is based on the EEM, on the point-matching method (PMM) for the potential of the perfect electric conductor (PEC) electrodes and for the normal component of the electric field at the boundary surface between any two dielectric layers.

Until now, the method is applied to solving multilayer electromagnetic problems [12], grounding systems [20], as well as electromagnetic field determination in the vicinity of cable terminations [21]. The HBEM can be successfully applied to analysis of corona effects [22] and metamaterial structures [23]. This method can be also used to the 3D problems solving that will be presented in future papers. Through the several examples, the HBEM is applied to determine both the effective dielectric permittivity and the characteristic impedance. A computer code has been written to obtain numerical solutions for those examples of 2D striplines. The main assumption of the analysis involves quasi TEM propagation in investigated striplines. In order to test the accuracy of the developed method, the numerical results are presented for all presented examples and compared with those obtained by FEM, [24].

The theoretical approach is presented in section II. Section III is devoted to show that highly accurate results can be obtained with short computation time. Also, the obtained numerical results are given in this section. The conclusions are summarized in section IV.

II. THEORETICAL APPROACH

A cross-section of the stripline sandwiched in multilayer dielectric between two ground planes is shown in Fig. 1. According to the HBEM, an arbitrary shaped electrode can be replaced by the equivalent electrodes, and an arbitrary shaped boundary surface between any two dielectric layers can be replaced by discrete equivalent total line charges placed in the air, as seen in Fig. 2. The discretization technique is similar to the method of moments and is well known.

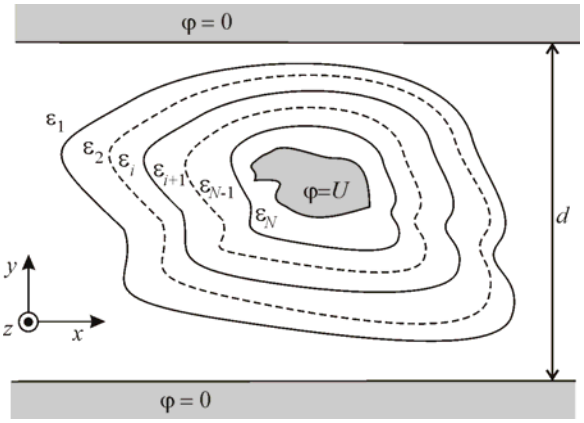

Fig. 1. Stripline in multilayer dielectric.

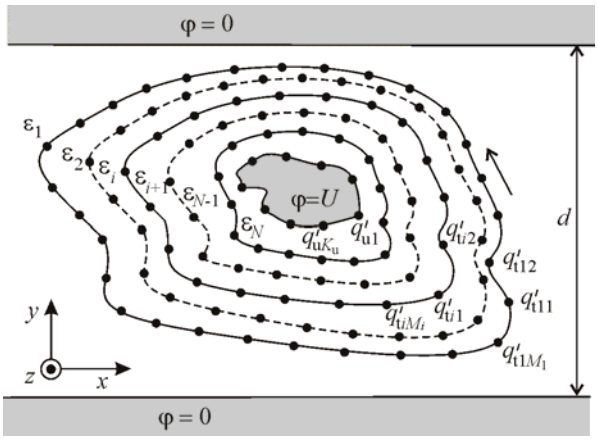

Fig. 2. Corresponding HBEM model.

Since the free surface charges do not exist on dielectric boundary surfaces (free surface charges exist only on PEC, see Fig. 2), the total surface charges between the dielectric layers are equal to the polarized surface charges. The Green's function of the line charge placed at height h, parallel to two infinite parallel ground planes is, [25],

$$G(x,y)=\frac{1}{2\pi\varepsilon}\ln\sqrt{\frac{\cosh\left[\frac{\pi}{d}x\right]-\cos\left[\frac{\pi}{d}(y+h)\right]}{\cosh\left[\frac{\pi}{d}x\right]-\cos\left[\frac{\pi}{d}(y-h)\right]}} \qquad (1)$$

where d is the distance between two planes. Using this Green's function, the electric scalar potential of the observed system from Fig. 2 is,

$$\varphi = \sum_{k=1}^{K_u} \frac{q'_{uk}}{2\pi\varepsilon_N} \ln \sqrt{\frac{\cosh\left[\frac{\pi}{d}(x-x_{uk})\right] - \cos\left[\frac{\pi}{d}(y+y_{uk})\right]}{\cosh\left[\frac{\pi}{d}(x-x_{uk})\right] - \cos\left[\frac{\pi}{d}(y-y_{uk})\right]}} +$$

$$+ \sum_{i=1}^{N-1} \sum_{m=1}^{M_i} \frac{q'_{tim}}{2\pi\varepsilon_0} \ln \sqrt{\frac{\cosh\left[\frac{\pi}{d}(x-x_{tim})\right] - \cos\left[\frac{\pi}{d}(y+y_{tim})\right]}{\cosh\left[\frac{\pi}{d}(x-x_{tim})\right] - \cos\left[\frac{\pi}{d}(y-y_{tim})\right]}},$$

$$N \geq 2, \qquad (2)$$

and the electric field is $\boldsymbol{E} = -\text{grad}(\varphi)$, where: M_i is the number of equivalent electrodes (EEs) on the i-th boundary surface between two layers. In the following examples, the total number of unknowns N_{tot}, will be denoted by,

$$N_{\text{tot}} = K_u + \sum_{i=1}^{N-1} M_i .$$

A relation between the normal component of the electric field and total surface charges is presented as,

$$\hat{\boldsymbol{n}}_{im} \cdot \boldsymbol{E}_{im}^{(0+)} = \frac{-\varepsilon_{i+1}}{\varepsilon_0(\varepsilon_i - \varepsilon_{i+1})} \eta_{tim},$$

$$\eta_{tim} = \frac{q'_{tim}}{\Delta l_{im}},\ m = 1,\ldots,M_i,\ i = 1,\ldots,N-1, \qquad (3)$$

where $\hat{\boldsymbol{n}}_{im}$ is the unit normal vector oriented from the layer ε_{i+1} towards the layer ε_i. Positions of the matching points for the potential of the PEC are,

$$x_{un} = x_{uk} + \delta_{nk} a_{euk} \hat{\mathbf{n}}_{uk} \cdot \hat{\mathbf{x}}$$

$$y_{un} = y_{uk} + \delta_{nk} a_{euk} \hat{\boldsymbol{n}}_{uk} \cdot \hat{\boldsymbol{y}},$$

$n = 1,\ldots,K_u$, $k = 1,\ldots,K_u$ and $a_{euk} = \Delta l_{uk}/4$, where δ_{nk} is the Kronecker's delta function,

$$\delta_{nk} = \begin{cases} 1, & n = k \\ 0, & n \neq k, \end{cases} \qquad (4)$$

while a_{euk} are corresponding to the EEs radii.

Boundary surface matching points for the normal component of the electric field on the i-th boundary surface are,

$$x_{tin} = x_{tim} + \delta_{nm} a_{eim} \hat{\boldsymbol{n}}_{im} \cdot \hat{\boldsymbol{x}} \text{ and}$$

$$y_{tin} = y_{tim} + \delta_{nm} a_{eim} \hat{\boldsymbol{n}}_{im} \cdot \hat{\boldsymbol{y}},$$

$i = 1,\ldots,N-1$, $n = 1,\ldots,M_i$ and $m = 1,\ldots,M_i$, where $a_{eim} = \Delta l_{im}/\pi$ are the EEs radii.

The aim is to obtain the quadratic system of linear equations with unknown free charges of PEC and total charges per unit length at the boundary surfaces between dielectric layers. Using the PMM for the potential of the conductor given by equation (2) and the PMM for the normal component of the electric field given in equation (3), it is possible to determine unknown charges. After solving the system of linear equations it is possible to calculate the capacitance per unit length of the stripline,

$$C' = \sum_{k=1}^{K_u} \frac{q'_{uk}}{U}. \qquad (5)$$

The characteristic impedance of the stripline is calculated as $Z_c = Z_{c0}/\sqrt{\varepsilon_r^{\text{eff}}}$, where $\varepsilon_r^{\text{eff}} = C'/C'_0$ is the effective dielectric permittivity, and Z_{c0} is the characteristic impedance of the stripline without dielectrics (free space). In order to compare the obtained results for the characteristic impedance, the FEM, [24], is used. A deviation between the HBEM and FEM results will be defined as,

$$\delta[\%] = \frac{\left|Z_c^{\text{HBEM}} - Z_c^{\text{FEM}}\right|}{Z_c^{\text{FEM}}} \cdot 100. \qquad (6)$$

III. NUMERICAL RESULTS AND DISCUSSION

A. Example 1

The geometry of the stripline with a circular cross-section is shown in Fig. 3. After applying the HBEM using the procedure described in section II, the unknown free charges per unit length of the conductor and the total charges per unit length on the boundary surfaces between layers are calculated.

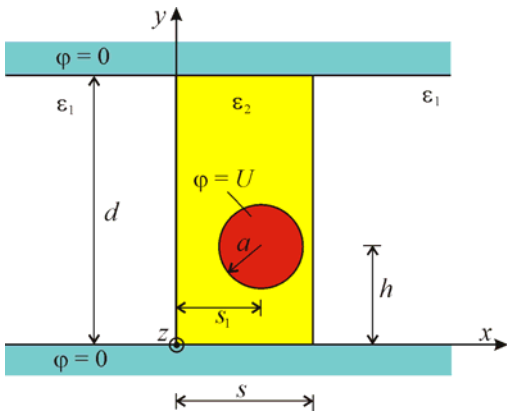

Fig. 3. Stripline with circular cross-section.

Two characteristic parameters of the stripline are determined: the effective dielectric permittivity and the characteristic impedance. Values of these two parameters and the computation time are calculated for: $\varepsilon_{r1} = 1$, $\varepsilon_{r2} = 3$, $s/d = 0.5$, $s_1/s = 0.6$, $h/d = 0.4$, and $a/s = 0.3$ and presented in Table I. N_{tot} is the total number of unknown values.

Table I: Convergence of the results and computation time.

N_{tot}	ε_r^{eff}	Z_c [Ω]	t(s)
247	2.2820	54.741	7.7
329	2.2828	54.831	13.6
413	2.2832	54.885	21.2
494	2.2835	54.918	30.6
576	2.2837	54.944	41.9
660	2.2838	54.963	54.9
741	2.2840	54.977	69.0
823	2.2841	54.989	85.3
988	2.2842	55.006	122.0
1070	2.2843	55.013	144.4
1154	2.2843	55.019	167.8

The calculation was performed on the computer with dual core INTEL processor 2.8 GHz and 4 GB of RAM. Analyzing Table I, following conclusions can be given. First, a very good convergence of values of both parameters is achieved. Increasing the number of unknown, the computation time increases linearly. The computation time is very short. For the system of 1154 unknowns we needed up to 167.8 seconds.

Equipotential contours and the normalized distribution of the polarized charges per unit length along the boundary surfaces are shown in Figs. 4 and 5, respectively for: $\varepsilon_{r1} = 1$, $\varepsilon_{r2} = 3$, $s/d = 0.5$, $s_1/s = 0.6$, $h/d = 0.4$, and $a/s = 0.3$. In order to validate the accuracy of the HBEM results for the effective dielectric permittivity and characteristic impedance of the stripline, the comparison of those values obtained by HBEM and FEM versus s_1/s and h/d for $\varepsilon_{r1} = 1$, $\varepsilon_{r2} = 3$, $s/d = 0.5$, and $a/s = 0.3$, is presented in Table II. The table shows that the numerical results for the effective dielectric permittivity and the characteristic impedance obtained using the HBEM are obviously in very good agreement with the FEM values with divergence less than 0.55 %.

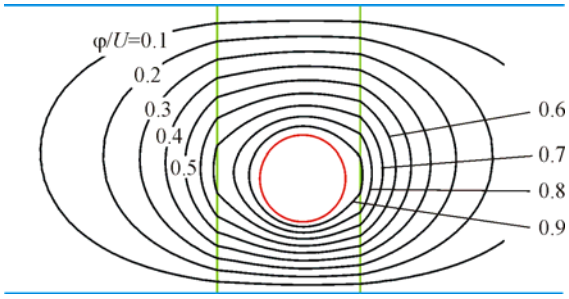

Fig. 4. Equipotential contours.

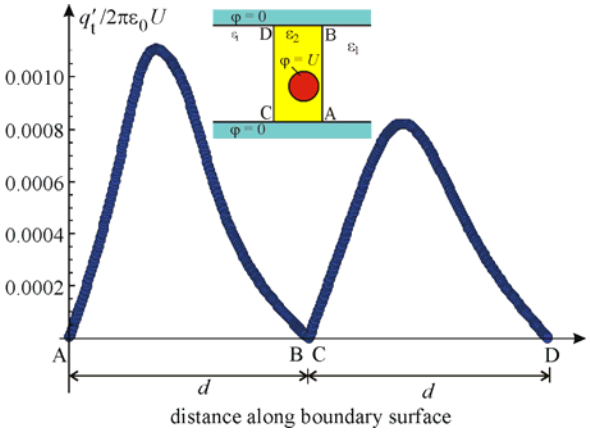

Fig. 5. Distribution of polarized charges per unit length along the boundary surfaces.

Table II: Comparison between the values of dielectric permittivity and characteristic impedance of the stripline versus s_1/s and h/d for: $\varepsilon_{r1} = 1$, $\varepsilon_{r2} = 3$, $s/d = 0.5$, and $a/s = 0.3$.

$\frac{s_1}{s}$	$\frac{h}{d}$	HBEM		FEM	
		ε_r^{eff}	Z_c [Ω]	ε_r^{eff}	Z_c [Ω]
0.35	0.2	2.5844	28.361	2.5837	28.517
	0.3	2.3532	46.713	2.3540	46.792
	0.4	2.2566	55.293	2.2577	55.349
	0.5	2.2285	57.923	2.2296	57.977
0.4	0.2	2.6183	28.176	2.6177	28.331
	0.3	2.3850	46.401	2.3857	46.480
	0.4	2.2838	54.963	2.2849	55.018
	0.5	2.2542	57.596	2.2554	57.645
0.5	0.2	2.6446	28.036	2.6441	28.190
	0.3	2.4100	46.154	2.4113	46.233
	0.4	2.3059	54.699	2.3070	54.754
	0.5	2.2751	57.332	2.2762	57.380

Increasing the parameter h/d to the center distance between the parallel planes (h/d = 0.5), the characteristic impedance increases too. After that value (h/d > 0.5), the characteristic impedance decreases. Those higher values are the same distances as for h/d < 0.5, but this time from the upper plane. An influence of the circular conductor radius on the characteristic impedance and the effective dielectric permittivity is presented in Table III. The HBEM results are compared with the corresponding FEM results. The results deviation is presented in Table III as well. This deviation parameter indicates a good results agreement between both methods.

Table III: Comparison between the values of dielectric permittivity and characteristic impedance of the stripline versus a/s for: ε_{r1} = 1, ε_{r2} = 3, s/d = 0.5, s_1/s = 0.5, and h/d = 0.25.

	HBEM		FEM		
	ε_r^{eff}	Z_c [Ω]	ε_r^{eff}	Z_c [Ω]	δ[%]
0.1	2.6670	80.106	2.6683	80.370	0.33
0.2	2.5678	55.121	2.5667	55.247	0.23
0.3	2.5038	38.854	2.5042	38.957	0.26
0.4	2.5202	24.502	2.5192	24.629	0.52

B. Example 2

Geometry of the stripline with a rectangular cross-section placed horizontally, off-centered, into the dielectric layer of permittivity ε_2, is shown in Fig. 6. Analysis of this structure is also possible using the HBEM.

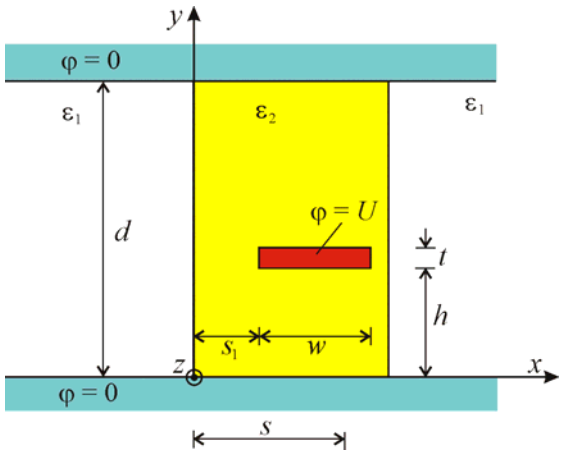

Fig. 6. Stripline with rectangular cross-section.

Applying the procedure described in section II, a computer code for the calculation of the effective dielectric permittivity and the characteristic impedance is developed. Values of the effective dielectric permittivity, characteristic impedance and the computation time for: ε_{r1} = 1, ε_{r2} = 3, s/d = 0.5, s_1/s = 0.2, h/d = 0.3, w/s = 0.5, and t/w = 0.1, are presented in Table IV. N_{tot} denotes the total number of unknowns. A good convergence of the results is achieved for the short computation time. The convergent rate is linear, as well as in example 1. The calculation was performed on a computer with dual core INTEL processor 2.8 GHz and 4 GB of RAM.

Table IV: Convergence of the results and computation time.

N_{tot}	ε_r^{eff}	Z_c [Ω]	t(s)
264	2.4871	75.239	8.5
348	2.4873	75.283	14.7
436	2.4874	75.313	23.1
520	2.4875	75.332	32.7
604	2.4876	75.346	44.4
692	2.4876	75.358	58.6
776	2.4877	75.366	73.2
858	2.4877	75.372	91.8
946	2.4877	75.379	109.5
1030	2.4878	75.384	130.2
1114	2.4878	75.388	152.9
1202	2.4878	75.392	180.0

Equipotential contours and a distribution of polarized charges per unit length along boundary surfaces are shown in Figs. 7 and 8, respectively, for: ε_{r1} = 1, ε_{r2} = 3, s/d = 0.5, s_1/s = 0.2, h/d = 0.3, w/s = 0.5, and t/w = 0.1.

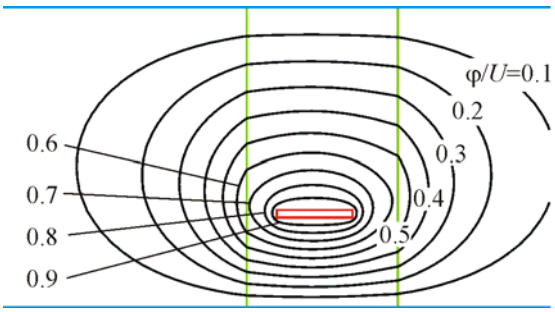

Fig. 7. Equipotential contours.

Using the FEM software, the same stripline model was created, in order to verify the accuracy of the HBEM results. In Tables V and VI, the comparison of the effective dielectric permittivity and characteristic impedance as well as a deviation between the HBEM and FEM results, are presented. The maximal deviation is 0.22 %.

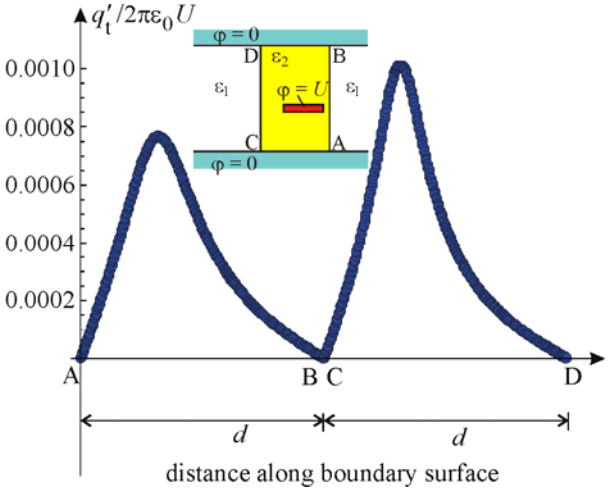

Fig. 8. Distribution of polarized charges per unit length along the boundary surfaces.

Table V: Comparison between the values of dielectric permittivity and characteristic impedance of stripline versus s_1/s and h/d for: $\varepsilon_{r1} = 1$, $\varepsilon_{r2} = 3$, $s/d = 0.5$, $w/s = 0.5$, and $t/w = 0.05$.

$\frac{s_1}{s}$	$\frac{h}{d}$	HBEM		FEM	
		ε_r^{eff}	Z_c [Ω]	ε_r^{eff}	Z_c [Ω]
0.1	0.1	2.7350	44.646	2.7348	44.634
	0.2	2.5588	65.889	2.5587	65.834
	0.3	2.4540	78.241	2.4539	78.166
	0.4	2.3985	84.833	2.3986	84.750
	0.5	2.3825	86.756	2.3825	86.666
0.2	0.1	2.7986	44.135	2.7985	44.126
	0.2	2.6214	65.097	2.6214	65.045
	0.3	2.5087	77.382	2.5087	77.307
	0.4	2.4485	83.963	2.4485	83.879
	0.5	2.4310	85.886	2.4311	85.795
0.25	0.1	2.8056	44.080	2.8055	44.069
	0.2	2.6289	65.005	2.6289	64.953
	0.3	2.5153	77.281	2.5153	77.206
	0.4	2.4545	83.860	2.4545	83.777
	0.5	2.4369	85.783	2.4370	85.695

Table VI: Comparison between the values of dielectric permittivity and characteristic impedance of stripline versus w/s for: $\varepsilon_{r1} = 1$, $\varepsilon_{r2} = 3$, $s/d = 0.5$, $s_1/s = 0.2$, $h/d = 0.3$, and $t/w = 0.05$.

$\frac{w}{s}$	HBEM		FEM		δ[%]
	ε_r^{eff}	Z_c [Ω]	ε_r^{eff}	Z_c [Ω]	
0.1	2.6304	133.670	2.6300	133.371	0.22
0.2	2.5980	109.038	2.5983	108.878	0.15
0.3	2.5746	94.713	2.5746	94.611	0.11
0.4	2.5467	84.782	2.5468	84.697	0.10
0.5	2.5087	77.382	2.5087	77.307	0.03
0.6	2.4556	71.694	2.4556	71.628	0.09
0.7	2.3817	67.310	2.3817	67.251	0.09

IV. CONCLUSION

The HBEM is applied to the 2D striplines analysis. Two quasi-static parameters are calculated: the effective dielectric permittivity and the characteristic impedance. The FEM software was applied as validation of HBEM results accuracy. The maximal results deviation is less than 0.55 %. In both examples, the corresponding FEM models of striplines were created with a few hundred of thousands of finite elements. Such large number of finite elements is necessary from the point of this software accuracy. The comparison with HBEM is given only in order to verify the accuracy of the HBEM results.

The application of HBEM is very efficient and simple in the 2D striplines analysis. Fast convergence of the results and short computation time are some of this method advantages. The method can be also successfully applied to the arbitrary number of conductors and arbitrary number of dielectric layers. A large variety of very complex 2D and 3D problems, regarding striplines with or without symmetry, can be also solved. That will be the subject of our future research.

ACKNOWLEDGMENT

The work presented here was partly supported by the Serbian Ministry of Education and Science in the frame of the project TR 33008.

REFERENCES

[1] B. C. Wadell, *Transmission Line Design Handbook*, Artech House, Inc., pp. 125-137, 1991.

[2] H. A. Wheeler, "Transmission line properties of a strip line between parallel planes," *IEEE Trans. Microwave Theory Tech.*, vol. 26, no. 11, pp. 866-876, Nov. 1978.

[3] S. Rawal and D. Jackson, "An exact TEM calculation of loss in a stripline of arbitrary dimension," *IEEE Trans. Microwave Theory Tech.*, vol. 39, no. 4, pp. 694-699, April 1991.

[4] H. H. Chen, "Finite-element method coupled with method of lines for the analysis of planar or quasi-planar transmission lines," *IEEE Trans. Microwave Theory Tech.*, vol. 51, no. 3, pp. 848-855, March 2003.

[5] K.-Y. Su and J.-T. Kuo, "An efficient analysis of shielded single and multiple coupled microstrip lines with nonuniform fast Fourier transform (NUFFT) technique," *IEEE Trans. Microwave Theory Tech.*, vol. 52, no. 1, pp. 90-96, Jan. 2004.

[6] M. Tong, "Full-wave analysis of coupled lossy transmission lines using multiwavelet-based method of moments," *IEEE Trans. Microwave Theory Tech.*, vol. 53, no. 7, pp. 2362-2370, July 2005.

[7] M. Lucido, "A new high-efficient spectral-domain analysis of single and multiple coupled microstrip lines in planarly layered media," *IEEE Trans. Microwave Theory Tech.*, vol. 60, no. 7, pp. 2025-2034, July 2012.

[8] C. Wei, R. Harrington, J. Mautz, and T. Sarkar, "Multiconductor transmission lines in multilayered dielectric media," *IEEE Trans. Microwave Theory Tech.*, vol. 32, no. 4, pp. 439-450, April 1984.

[9] J. Crane and M. Havrilla, "Effect of center-conductor misalignment on stripline characteristic impedance," *25th Annual Review of Progress in Applied Computational Electromagnetics – ACES*, Monterey, California, USA, pp. 587-592, 2009.

[10] F. Seydou, R. Duraiswami, N. A. Gumerov, and T. Seppanen, "TM electromagnetic scattering from 2D multilayered dielectric bodies – numerical solution," *ACES journal*, vol. 19, no. 2, pp. 100-107, 2004.

[11] N. Raičević and S. Ilić, "One hybrid method application on anisotropic strip lines determination," *23rd Annual Review of Progress in Applied Computational Electromagnetics – ACES*, Verona, Italy, pp. 8-13, 2007.

[12] N. Raicevic, S. Aleksic, and S. Ilic, "A hybrid boundary element method for multilayer electrostatic and magnetostatic problems," *J. of Electromagnetics*, vol. 30, no. 6, pp. 507-524, 2010.

[13] D. Veličković, "Equivalent electrodes method," *Scientific Review*, no. 21-22, pp. 207-248, 1996.

[14] C. Brebbi, J. C. Telles, and L. Wrobel, *Boundary Element Techniques. Theory and Applications in Engineering*, Berlin: Springer, 1984.

[15] J. Singh, A. Glière, and J. Achard, "A multipole expansion-based boundary element method for axisymmetric potential problem," *J. of Engineering Analysis with Boundary Elements*, vol. 33, no. 5, pp. 654-660, 2009.

[16] R. Harrington, *Field Computation by Moment Methods*, New York: Macmillan, 1968.

[17] D. Veličković, "Application of equivalent electrodes method in multilayer media," *Proc. 5th International Conf. on Applied Electromagnetics PES 2001*, Niš, Serbia & Montenegro, pp. 873-878, 2001.

[18] D. Veličković and S. Ilić, "Shielded slot line of two dielectric layers-theoretical analysis," *Proc. 6th International Conf. on Applied Electromagnetics PES 2003*, Niš, Serbia and Montenegro, pp. 297-300, 2003.

[19] D. Veličković and S. Ilić, "Shielded slot line of two dielectric layers-numerical results," *Proc. 6th International Conf. on Applied Electromagnetics PES 2003*, Niš, Serbia and Montenegro, pp. 301-304, 2003.

[20] S. Ilić, N. Raičević, and S. Aleksić, "Application of new hybrid boundary element method on grounding systems," *Proc. of 14th International IGTE'10 Symposium*, Graz, Austria, pp. 160-165, 2010.

[21] N. Raičević, S. Ilić, and S. Aleksić, "Application of new hybrid boundary element method on the cable terminations," *Proc. of 14th International IGTE'10 Symposium*, Graz, Austria, pp. 56-61, 2010.

[22] B. Petković, S. Ilić, S. Aleksić, N. Raičević, and D. Antić, "A novel approach to the positive DC nonlinear corona design," *J. of Electromagnetics*, vol. 31, no. 7, pp. 505-524, 2011.

[23] N. Raicevic and S. Ilic, "One hybrid method application on complex media strip lines determination," *Proc. 3rd International Congress on Advanced Electromagnetic Materials in Microwaves and Optics, METAMATERIALS 2009*, London, United Kingdom, pp. 698-700, 2009.

[24] D. Meeker, FEMM 4.2, Available: http://www.femm.info/wiki/Download

[25] S. Ilić, S. R. Aleksić, and N. B. Raičević, "TEM analysis of vertical broadside symmetrically coupled strip lines with anisotropic substrate," *International Journal of Applied Electromagnetics and Mechanics*, IOS Press, vol. 37, no. 2-3, pp. 207-214, 2011.

Mirjana T. Perić received Dipl.–Ing. and M.Sc. degrees in Theoretical Electrical Engineering from the Faculty of Electronic Engineering (FEE) of Niš, Serbia, in 2000 and 2006, respectively. She is currently working toward the Ph.D. degree in Theoretical Electrical Engineering at the FEE of Niš, Serbia. In 2001 she joined the Department of Theoretical Electrical Engineering at the FEE. She is a teaching assistant at the same faculty. Her researching interests are: electromagnetic field theory, analytical and numerical methods for electromagnetic field modeling, electromagnetic compatibility, and transmission and microstrip line analysis.

Ms. Perić is a member of the IEEE Microwave Theory and Techniques Society, IEEE EMC Society, ACES Society and ETRAN (Society for Electronics, Telecommunications, Computers, Automatic Control and Nuclear Engineering of Serbia).

Saša S. Ilić received Dipl.–Ing. degree in Electronics and Telecommunications in 1995 from the Faculty of Electronic Engineering (FEE) of Niš, Serbia. At the same faculty he received M.Sc. degree in Theoretical Electrical Engineering in 2001. He is currently working toward the Ph.D. degree in Theoretical Electrical Engineering at the Faculty of Electronic Engineering of Niš, Serbia. From January 1998 up to now, he has engaged to the Department of Theoretical Electrical Engineering, at the FEE. His researching areas are: lightning protection systems, low-frequency electromagnetics fields penetrated into human body, and microstrip transmission lines analysis with isotropic, anisotropic and bianisotropic media. Mr. Ilić is a member of ETRAN.

Slavoljub R. Aleksić received Dipl.–Ing., M.Sc. and Ph.D. degrees in Theoretical Electrical Engineering in 1975, 1979, and 1997, respectively from the FEE of Niš of the University of Niš, Serbia. He became a teaching assistant at the Dept. of Theoretical Electrical Engineering at the FEE after his graduating. He has been an Assistant and Associate Professor at the same Department in 1980 and 1997, respectively. He is currently a chief of Department of Theoretical Electrical Engineering. His research areas are: EM field theory, numerical methods in electromagnetics, lightning protection systems, low-frequency EM fields, microstrip transmission lines with isotropic, anisotropic and bianisotropic media, cable joints and cable terminations, permanent magnets analysis, power lines. Prof. Aleksić is a member of ETRAN.

Nebojša B. Raičević received his Dipl.–Ing., M.Sc. and Ph.D. degrees at the FEE of Niš, Serbia, in 1989, 1998, and 2010, respectively. He received the Dr.-Ing. degree with a PhD-thesis dealing with the numerical electromagnetic field calculations. He is currently an Assistant Professor at the FEE. His research interests include: cable terminations and joints, numerical methods for EM problems solving, microstrip transmission lines with isotropic, anisotropic and bianisotropic media, metamaterial structures, EMC, nonlinear electrostatic problems, magnetic field calculation of coils and permanent magnets.

Prof. Raičević is a member of the IEEE Antennas and Propagation Society, IEEE EMC Society, IEEE Dielectrics and Electrical Insulation Society, IEEE Magnetics Society and ETRAN.

Compact Branch Line Coupler using Step Impedance Transmission Lines (SITLs)

S. H. Sedighy [1] and M. Khalaj-Amirhosseini[2]

[1] School of New Technologies,
Iran University of Science and Technology, Tehran, Iran
sedighy@iust.ac.ir

[2] School of Electrical Engineering,
Iran University of Science and Technology, Tehran, Iran
khalaja@iust.ac.ir

Abstract ─ A compact branch line coupler is proposed by using the optimized step impedance transmission lines (SITLs). The proposed branch line coupler has an area reduction of more than 50% at 1 GHz. The measured results of the fabricated coupler are in good agreement with the simulation results.

Index Terms ─ Branch line, compact, coupler, and step impedance transmission line.

I. INTRODUCTION

Branch line couplers are among the important components in the microwave circuits, which have wide applications in balanced mixers, image rejection mixers, balanced amplifiers, power combiners, and power dividers. The convenience of design and implementation, compact size and high-performance of this coupler is highly demanded in microwave integrated circuits. The conventional branch line coupler is composed of four uniform quarter-wavelength transmission lines. This coupler has narrow bandwidth and large size around a single frequency [1-7].

Some efforts have been done to compact the conventional branch line couplers. Lumped elements can reduce the coupler size [8], but real lumped components are far from ideal, which resulted in some practical problems especially at high frequency. Moreover, the lumped element values are discrete and include some tolerances commercially, which limit the designer to achieve the desirable specs. The series and shunt stubs embedded in the ground or signal lines have been used in [9] to reduce the size of a branch line coupler. Also, four coupled transmission lines have been presented in [10] to reduce the size of a branch line coupler. Each quarter wavelength branch in the conventional coupler has been replaced by an equivalent circuit composed of four coupled transmission lines and two single transmission lines. A compact slow-wave microstrip branch line coupler with four microstrip high-low impedance resonant cells periodically placed inside the branch-line coupler was introduced in [11]. Another effective way to reduce the size of a branch line coupler is the replacement of straight transmission lines segments by space-filling curve segments with the same electrical characteristics [12, 13]. Moreover, nonuniform transmission line (NTL) can be used instead of the quarter wavelength uniform transmission lines to reduce the size of branch line coupler [14]. In this method, the normalized width function of the NTLs expanded in a truncated Fourier series and an optimization method applied to obtain the optimum values of series coefficients. Two unequal-length high impedance transmission lines paralleling with each other have been used in [15] instead of the branch line coupler arms to reduce the size of the branch line coupler. Planar artificial transmission line concept is another option to reduce the physical length of a transmission line. In this method, a transmission line incorporated with microstrip quasi-lumped elements is capable of synthesizing microstrip

Submitted On: Nov. 22, 2012
Accepted On: Aug. 29, 2013

lines with reduced physical length, which can be used to reduce the size of branch line coupler [16]. Also, defected ground structures and composite right/left handed (CRLH) transmission-line have been used in [17, 18] to design a compact branch line coupler.

Step impedance transmission lines and step impedance resonators (SIRs) are other ways to reduce the size of microstrip components [19]. In this paper, step impedance transmission lines (SITLs) are used to compact the conventional branch line coupler. The proposed branch line coupler is realized by the microstrip step impedance transmission lines instead of the uniform quarter wavelength branches. The impedance ratio of SITLs is considered as a variable and written as the total electrical length of the line. This additional design parameter gives us a higher degree of design freedom, which is useful to design a reduced size branch line coupler. Moreover, the folded lines are used for more size reduction. Finally, the proposed branch line coupler is fabricated. The measurement results have a good agreement with the simulation results.

II. STEP IMPEDANCE TRANSMISSION LINES (SITLs)

Generally, step impedance transmission line is a non-uniform transmission line, which can be used in microstrip circuits for size reduction, shift the spurious pass band to the higher frequency and even to suppress the multiple spurious pass bands [20, 21]. Figure 1 shows a step-impedance transmission line with three segments: Z_2 line with the electrical length of θ_2 and two Z_1 lines with electrical length of $\theta_1/2$. For equaling this SITL and uniform Z_0 transmission line with the length of $\pi/2$ at f_0 frequency, two independent elements of the ABCD matrices of both SITL and uniform line have to be equal to each other at the design frequency, f_0. Consequently, the optimum values of $k_z=Z_2/Z_1$ and Z_1 to achieve the minimum discontinuity in the SITL with total length, θ_t , can be expressed as follows [12],

$$k_{z1} = \cot^2(\theta_t/2) + \sqrt{\cot^4(\theta_t/2) - 1} \qquad (1)$$

$$k_{z2} = \frac{1}{k_{z1}} = \cot^2(\theta_t/2) - \sqrt{\cot^4(\theta_t/2) - 1}\,, \qquad (2)$$

$$\frac{Z_1}{Z_0} = \left\{ \begin{array}{l} \sin(\theta_1)\cos(\theta_2) + \\ \quad [k_z \cos^2(\theta_1/2) - k_z^{-1}\sin^2(\theta_1/2)]\sin(\theta_2) \end{array} \right\}^{-1}, \qquad (3)$$

where $\theta_1 = \theta_2 = \theta_t/2$. Figure 2 shows the k_{Z1}, k_{Z2} and Z_1/Z_0 versus the total electrical length, θ_t. As shown in Fig. 2, increasing the impedance ratio, k_{z1}, which is equal to decreasing of k_{z2}, decreases the total electrical length of the SITLs and result in more compactness in the SITL. Also, it resulted in very low Z_1 and very high Z_2 (by chosing k_{z1}) or very high Z_1 and very low Z_2 (by chosing k_{z2}). In other words, very low (ideally zero) and very high impedances (ideally infinity) are needed in the SITL configuration to acheive maximum of compactness (ideally $\theta_t=0$). Although practical limitations to achieve very high impedance lines ($w/h<<1$) and very low impedance lines ($w/h>>1$) can limit the selection of very low and high impedance ratios. In addition, very high and low impedance ratios cause high discontinuity effects and high mode excitation in high frequency.

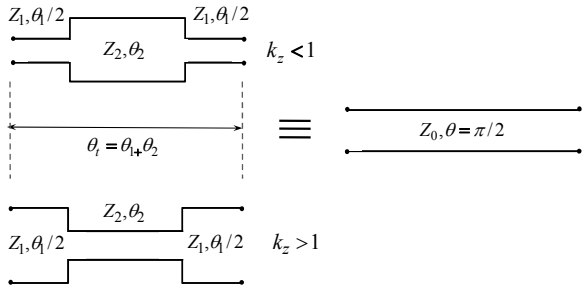

Fig. 1. The step impedance transmission line configuration (SITL).

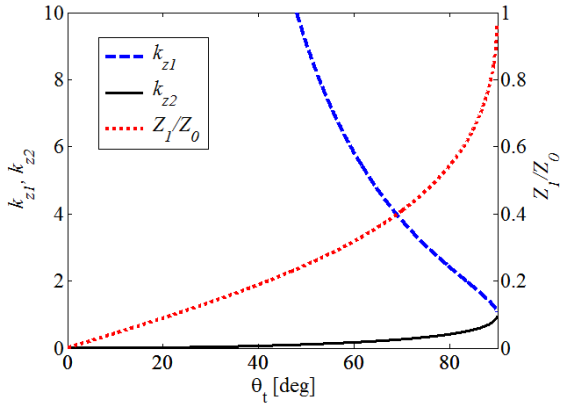

Fig. 2. Impedance ratio (k_{z1} and k_{z2}) and normalized impedance Z_1 versus total electrical length of SITL, θ_t.

III. DESIGN AND RESULTS

The conventional branch line coupler is composed of the uniform transmission lines with Z_1=35.34 Ω and Z_2=50 Ω for the horizontal and vertical branches, respectively, and the electrical length of 90 degrees for all branches. Based on section II, design of branch line coupler is started to reach the desired size reduction. Step impedance transmission lines are replaced with *λ/4* uniform transmission lines in the branch line coupler structure. The total electrical length of the vertical and horizontal lines are selected as θ_t=*67.5°*. Therefore, the impedance ratios, k_z, which are calculated from equations (1) and (2), are k_z=4.24 for the vertical branches and k_z=*1/4.24* for the horizontal ones. Then, the Z_1 impedance can be calculated using equation (3). The circuit layout of the proposed branch line coupler is shown in Fig. 3. The Z_{V1}, Z_{V2}, Z_{H1}, and Z_{H2} are 19.16 Ω, 81.3 Ω, 21.74 Ω, and 92.28 Ω, respectively. The designed coupler is fabricated by using a dielectric substrate RO4003 with a relative dielectric constant of 3.5 and a thickness of 30 mils for operation at 1 GHz. Therefore, the line widths of the SITL segments are 6.36 mm and 0.7 mm for vertical SITL and 5.45 mm and 0.53 mm for horizontal SITL.

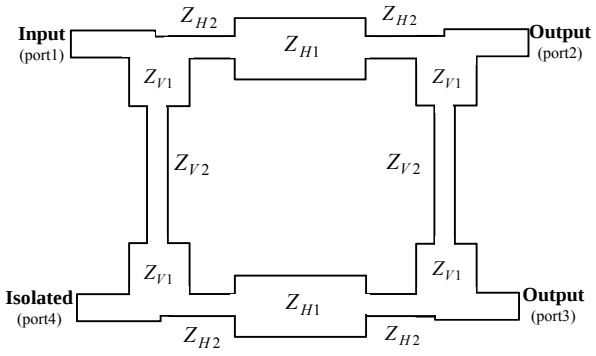

Fig. 3. Layout of the proposed SITLs branch line coupler.

The proposed coupler is theoretically simulated using MATLAB. Since the discontinuities are not accurately considered in the MATLAB simulation, we tuned the designed parameters with EM full wave simulation based on the method of moments. Figure 4 shows the photograph of the fabricated branch line coupler. The exact area of the coupler has been shown by black dash line in the figure. Also, the impedance of the vertical and horizontal segments has been added to the figure. In order to achieve more compactness, one-level folded transmission lines have been used in the high impedance segment of the vertical branches.

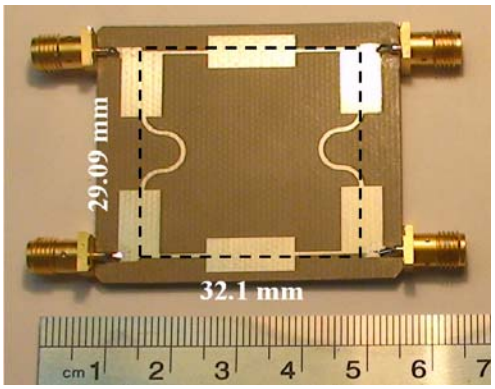

Fig. 4. The photo of the fabricated coupler.

The simulation and measurement results have been demonstrated in Fig. 5, respectively. The required circuit area for the proposed SITLs coupler is 50 % less than the circuit area of the conventional branch line coupler at the operation frequency, 1 GHz. The measured results of the fabricated coupler are in good agreement with the simulation results. There are deep nulls in the return loss and isolation at 1 GHz and the measured |S12| and |S13| are -3.36 dB and -3.4 dB, respectively. Moreover, the measured results show a good performance for the designed coupler at 1.9 GHz.

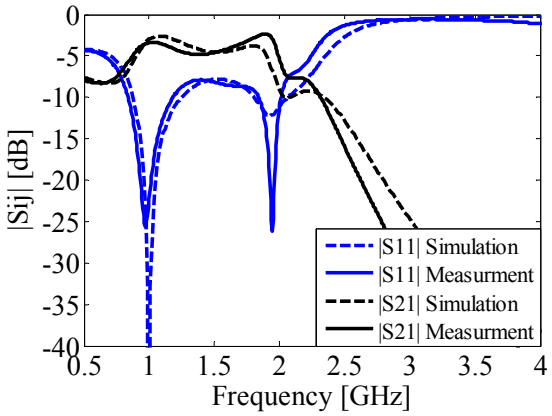

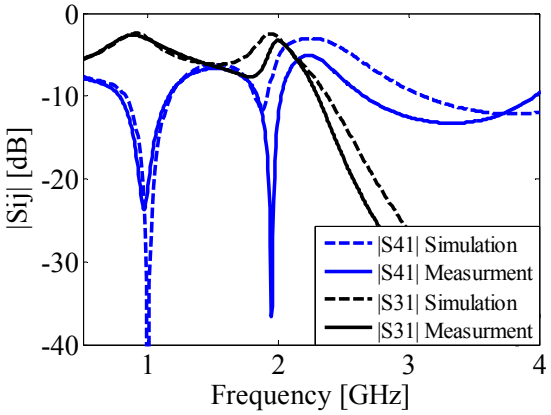

Fig. 5 Comparison of the measurement and simulation results of the branch line coupler.

IV. CONCLUSION

Branch line coupler is proposed to operate in the reduced size. The proposed structure contains step impedance transmission lines (SITLs) instead of the uniform transmission lines. A branch line coupler has been designed and fabricated at 1 GHz. More than 50 % size reduction is obtained in the proposed branch line coupler, while the coupler performance does not change compared with the conventional one at the design frequency. The measured and simulation results have a good agreement for the fabricated coupler.

REFERENCES

[1] P. Myun-Joo and L. Byungje, "Dual-band, cross coupled branch line coupler," *IEEE Microwave and Wireless Components Letters*, vol. 15, pp. 655-657, Oct. 2005.

[2] K. Tsung-Nan, L. Yo-Shen, W. Chi-Hsueh, and C. Hsiung, "A compact LTCC branch-line coupler UsingModified-T equivalent-circuit model for transmission line," *IEEE Microwave and Wireless Components Letters*, vol. 16, pp. 90-9292, Feb. 2006.

[3] C. Young-Hoon and H. Jia-Sheng, "Compact wide-band branch-line hybrids," *IEEE Transactions on Microwave Theory and Techniques*, vol. 54, pp. 704-709, Feb. 2006.

[4] J. Cui and J. Li, "Compact microstrip branch-line coupler with wideband harmonic suppression," *Applied Computational Electromagnetics Society (ACES) Journal*, vol. 27, pp. 766-771, 2012.

[5] E. Yilmaz and M. Hasanovic, "Sonnet modelling and simulation of broadband branchline coupler," *27th Annual Review of Progress in Applied Computational Electromagnetics (ACES), Williamsburg, Virginia,* pp. 398-402, 2011.

[6] A. Nosrati, S. Abbaspour, and A. Nouri, "A novel high miniaturized branch-line coupler," *24th Annual Review of Progress in Applied Computational Electromagnetics (ACES), Niagara Falls, Canada,* pp. 888-892, 2008.

[7] A. Mohra and S. Mahmoud, "New compact 3 dB 0/180 microstrip coupler configurations," *Applied Computational Electromagnetics Society (ACES) Journal*, vol. 19, pp. 108-112, 2004.

[8] C. Yi-Chyun and C. Chong-Yi, "Design of a wide-band lumped-element 3-dB quadrature coupler," *IEEE Transactions on Microwave Theory and Techniques*, vol. 49, pp. 476-479, March 2001.

[9] K. Hettak, G. Morin, and M. Stubbs, "Compact MMIC CPW and asymmetric CPS branch-line couplers and Wilkinson dividers using shunt and series stub loading," *IEEE Transactions on Microwave Theory and Techniques*, vol. 53, pp. 1624-1635, May 2005.

[10] M. Nosrati and S. Valashani, "A novel compact branch-line coupler using four coupled transmission lines," *Microwave and Optical Technology Letters*, vol. 50, pp. 1712-1714, June 2008.

[11] H. Wang, B. Wang, Y. Guo, L. Ong, and S. Xiao, "A compact slow-wave microstrip branch-line coupler with high performance," *IEEE Microwave and Wireless Components Letters*, vol. 17, pp. 501-503, July 2007.

[12] H. Ghali and T. Moselhy, "Miniaturized fractal rat-race, branch-line, and coupled-line hybrids," *IEEE Transactions on Microwave Theory and Techniques*, vol. 52, pp. 2513-2520, Nov. 2004.

[13] M. Nosrati and B. Virdee, "Realization of a compact branch-line coupler using quasi-fractal loaded coupled transmission-lines," *Progress In Electromagnetics Research C*, vol. 13, pp. 33-40, 2010.

[14] F. Hosseini, M. Hosseini, and M. Yazdany, "To compact ring branch-line coupler using nonuniform transmission line," *Microwave and Optical Technology Letters*, vol. 51, pp. 2679-2682, Nov. 2009.

[15] M. Khalaj-Amirhosseini and M. Yazdani, "To compact branch-line couplers using parallel high-impedance transmission lines," *Microwave and Optical Technology Letters*, vol. 52, no. 9, pp. 1996-1999, Sep. 2010.

[16] W. Chao-Wei, M. Tzyh-Ghuang, and Y. Chang-Fa, "A new planar artificial transmission line and its applications to a miniaturized Butler matrix," *IEEE Transactions on Microwave Theory and Techniques*, vol. 55, pp. 2792-2801, Dec. 2007.

[17] M. Maddah-Ali, H. Oskouei, and K. Forooraghi, "A compact branch-line coupler using defected

ground structures," *Microwave and Optical Technology Letters*, vol. 50, pp. 386-389, Feb. 2008.

[18] L. X. Qi, L. R. Peng, Y. X. Mi, C. J. Xin, Y. X. Xing, C. Qiang, and C. T. Jun, "Arbitrarily dual-band components using simplified structures of conventional CRLH TLs," *IEEE Transactions on Microwave Theory and Techniques*, vol. 54, pp. 2902-2909, July 2006.

[19] S. Sedighy and M. Khalaj-Amirhosseini, "Compact Wilkinson power divider using stepped impedance transmission lines," *Journal of Electromagnetic Waves and Applications*, vol. 25, pp. 1773-1782, 2011.

[20] S. Kumpang, R. Phromloungsri, M. Chongcheawchamnan, M. Krairiksh, and I. Robertson, "Design and application of microstrip parallel-coupled lines employing step-impedance transmission-line compensation," *IET Microwaves Antennas & Propagation*, vol. 3, pp. 410-415, April 2009.

[21] M. Velazquez-Ahumada, J. Martel, F. Medina, and F. Mesa, "Design of band-pass filters using stepped impedance resonators with floating conductors," *Progress in Electromagnetics Research-Pier*, vol. 105, pp. 31-48, 2010.

Seyed Hassan Seddighi was born in Qaen, South Khorasan, Iran in 1983. He received B.S., M.S. and PhD degrees in Electrical Engineering from Iran University of Science and Technology (IUST) in 2006, 2008, and 2013, respectively. He is currently an Associate Professor in Iran University of Science and Technology, IUST. His current research interests include microstrip antenna, optical transformation, design and application of metamaterials.

Mohammad Khalaj Amirhosseini was born in Tehran, Iran in 1969. He received his B.Sc, M.Sc. and Ph.D. degrees from Iran University of Science and Technology (IUST) in 1992, 1994 and 1998 respectively, all in Electrical Engineering. He is currently an Associate Professor at College of Electrical Engineering of IUST. His scientific fields of interest are electromagnetic direct and inverse problems including microwaves, antennas and electromagnetic compatibility.

An Adaptive Time-Stepping Algorithm in Weakly Coupled Electromagnetics-Thermal-Circuit Modeling

R. B. B. Ovando-Martinez, C. Hernandez, and M. A. Arjona

División de Estudios de Posgrado e Investigación
Instituto Tecnológico de La Laguna, Torreón, Coah. 27000, Mexico
ronat-13@hotmail.com, coni.hernandez@ieee.org, and marjona@ieee.org

Abstract ─ This paper presents a weakly coupled formulation for the electromagnetic and thermal fields by applying the backward differentiation formula (BDF) and the Theta algorithm for the adaptive time-stepping and variable order 2D finite-element discretization. A coupling of the electromagnetic diffusion equation (EDE) and the electrical circuit equations is also included. A minimum time step criterion is adopted and an algorithm for the time-step size and order selection is implemented. The proposed model was programmed in C language. An example is presented to show the application of the formulation.

Index Terms - Coupling, electrical circuits, electro-thermal analysis, finite elements, and time-stepping.

I. INTRODUCTION

The coupled problem analysis (CPA) involves the coupling and solution of two or more partial differential equations (PDE's) [1]. Recently, the CPA has been applied in electromagnetics, thermal and fluid flow field problems for solving power quality troubles in electrical and electronic devices [2-5]. The use of modern numerical techniques and advanced computational tools makes possible the CPA. The finite element is a numerical technique used for solving space and time domain PDE's [6, 7]. A huge amount of numerical processes take place in a transient CPA computation. Fast and efficient algorithms are required for the transient CPA. Numerical methods based on constant time steps, such as the Euler methods, are not appropriate in a transient CPA due to the high computational time that is required [8]. Instead, variable time-stepping strategies are recommended [9]. The backward differentiation formula (BDF) is a variable time-stepping method, which is A-stable and L-stable and is recommended for solving stiff problems [10, 11]. The Theta algorithm is a non-variable time-stepping method, where the parameter θ is chosen such that $0 \leq \theta \leq 1$ and different solution schemes are obtained [12, 13]. A finite element (FE) BDF-Theta strategy has been successfully implemented for solving the transient EDE [14].

In this paper, the BDF-Theta strategy reported in [14] is applied for solving a weakly coupled electro-thermal 2D-FE transient formulation. The methodology is applied using 2D first-order triangular elements. A coupling of the EDE and the electrical circuit equations is included in the model [15]. A suitable minimum FE time-step criterion is adopted to avoid small time steps and instability. An algorithm for the proper time-step and order selection is implemented. An error control criterion and an initial guess prediction algorithm are applied for convergence acceleration. The developed formulation was applied to compute the magnetic vector potential, temperature distributions, and induced electrical current in a metallic slab close to a conductor fed with a voltage source. The model formulation was programmed in C language.

II. DOMAIN EQUATIONS

A CPA is carried out for the electro-thermal analysis of an electrical device. An electro-thermal analysis is commonly required in the design of electrical motors, generators, and transformers

Submitted On: Dec. 13, 2012
Accepted On: Aug. 29, 2013

[16-18]. This paper develops an electro-thermal CPA model. Therefore, the EDE and the heat equation (HE) are the subject of this paper. The EDE and the HE are described by a diffusion type PDE as in equation (1),

$$C_1 \nabla^2 f = -S_o + C_2 \frac{\partial f}{\partial t} \tag{1}$$

where f is a function, $C_{1,2}$ are constants, S_o is a source function, and t the time. The EDE and the HE are properly obtained considering the list of symbols shown in Table I. However, in electric devices modeling some special considerations in the EDE must be considered. The electric devices may be fed by voltage sources and/or current sources (see Table I) and they present a variety of electrical connections.

Equations (2) and (3) show the formulation of the EDE for thick conductors that are fed by a voltage source [14],

$$\frac{1}{\mu}\nabla^2 A = -\sigma \frac{V}{\ell} + \sigma \frac{\partial A}{\partial t} \tag{2}$$

$$V = RI + R \int_{S_t} \sigma \frac{\partial A}{\partial t} dS_t \,, \tag{3}$$

where V is the voltage, R represents the resistance, I the current, σ the electrical conductivity, ℓ the length, and S_t the total surface of the conductor. The resistance R for thick conductors is defined as,

$$R = \frac{\ell}{\sigma S_t} \,. \tag{4}$$

Table I: Equivalent symbols for the EDE and HE.

	f	S_o	C_1	C_2
EDE	Magnetic Potential	Current density	Reluctivity	Electric Conductivity
	A (Wb/m)	J and/or $\sigma V/\ell$ (A/m^2)	υ (m/H)	σ (S/m)
HE	Temperature	Power density	Thermal Conductivity	Mass density product Specific heat
	T (°K)	q (W/m^3)	k (W/(m°K))	$P \cdot C_p$ (kg/m3, J/(kg°K))

The power loss density is calculated with equations (2) and (3). Afterwards, the HE is used to obtain the temperature distribution.

III. FINITE ELEMENT MODEL

The set of equations (1)-(4) is solved using first order triangular FE and the Galerkin residuals. Equations (5) and (6) show the FE discretization for the EDE, HE, and the electric circuit equations,

$$C_2 \left[T_{ij}\right] \left\{ \frac{\partial f_j}{\partial t} \right\} = C_1 \left[M_{ij}\right] \left\{f_j\right\} + S_o \left\{G_i\right\} \tag{5}$$

$$V = RI + \sum_m \left(\frac{R\sigma S}{3} \sum_{g=1}^{3} \left(\frac{A_g^{n+1} - A_g^n}{\Delta t} \right) \right), \tag{6}$$

where,

$$\left[T_{ij}\right] = \int_\Omega N_i N_j d\Omega \,, \tag{7}$$

$$\left[M_{ij}\right] = -\int_\Omega \left(\frac{\partial N_i}{\partial x}\frac{\partial N_j}{\partial x} + \frac{\partial N_i}{\partial y}\frac{\partial N_j}{\partial y} \right) d\Omega \,, \tag{8}$$

$$\left\{G_i\right\} = \int_\Omega N_i d\Omega \,, \tag{9}$$

where i and j stand for the nodes numbers, n is the time step number, Δt is the time-step defined as $\Delta t = t_{n+1} - t_n$, $N_{i,j}$ represents the 2D first-order triangular FE shape functions, m is the number of elements conforming a conductor, S is the area of the triangular element, and g is the local node numbering in a triangular element. By introducing a parameter θ in equation (5) such that,

$$f_j^{n+\theta} = \theta f_j^{n+1} + (1-\theta) f_j^n \tag{10}$$

$$G_i^{n+\theta} = \theta G_i^{n+1} + (1-\theta) G_i^n \,, \tag{11}$$

the theta scheme in equation (12) is obtained as follows,

$$C_2 \left[T_{ij}\right] \left\{ \frac{\partial f_j^{n+\theta}}{\partial t} \right\} = C_1 \left[M_{ij}\right] \left\{f_j^{n+\theta}\right\} + S_o \left\{G_i^{n+\theta}\right\}. \tag{12}$$

The Taylor series are used to obtain a linear approximation of the temporal partial differentiation in equation (12) as,

$$\frac{\partial f_j^{n+\theta}}{\partial t} = \frac{f_j^{n+1} - f_j^n}{\Delta t} \,. \tag{13}$$

Nevertheless, the resulting equation gives stable results for $\theta > 1/2$ as the time step $\Delta t \to 0$ [12]. The Taylor series approximation in equation (13) involves fixed time steps that lead to large computation times. An alternative approximation for the temporal partial differentiation in equation (12) is the implementation of the BDF. The BDF is a variable time-stepping algorithm that allows savings in the computational time. In addition, the BDF has good stability properties for orders less than sixth [10].

In the next section the BDF-Theta algorithm developed in [14] has been implemented to solve the weakly coupled electro-thermal problem described by equation (12).

IV. BDF-THETA ALGORITHM

The BDF-Theta includes the damping characteristics of the theta algorithm and the variable time-stepping and order algorithms of the BDF method. The effectiveness and accuracy of the BDF-Theta method is reported in [14] where the model results have been compared against an analytical solution. The arithmetic operations performed with the BDF-Theta are smaller in comparison with the Runge-Kutta methodologies [8, 14, 19-20]. Different schemes of solution depending on θ are obtained from the BDF-Theta method, e.g., the implicit scheme of the BDF-Theta method leads to the common BDF-implicit solver strategies, such as the ones used in the DASSL code [10]. The implementation of the BDF-Theta produces a nonlinear system of equations that are solved by the Newton-Raphson (NR).

Once the BDF-Theta algorithm is applied in equation (12), the residual and Jacobian are obtained by equations (14) and (15), respectively,

$$\{R_i\} = C_1[M_{ij}]\{f_j^{n+\theta}\} + S_o\{G_i^{n+\theta}\} + C_2[T_{ij}]\left\{\frac{1}{\Delta t}\sum_{g=0}^{K} f_j^{n+1-g}\alpha_g\right\} \quad (14)$$

$$[Jac_{i\beta}] = \theta C_1[M_{i\beta}] + C_2[T_{i\beta}]\left\{\frac{\alpha_0}{\Delta t}\right\}, \quad (15)$$

where K represents the order and backward data required to evaluate equation (14).

The algebraic process to obtain α_g from equations (14) and (15) is described in [11] and it is defined as,

$$\alpha_g = \frac{(t_{n+1} - t_n)}{(t_{n+1} - t_{n+1-g})}\prod_{\substack{\psi=1 \\ \psi\neq g}}^{K}\frac{(t_{n+1} - t_{n+1-\psi})}{(t_{n+1-g} - t_{n+1-\psi})} \quad (16)$$

for $0 < g \leq K$, while for $g = 0$,

$$\alpha_0 = -\sum_{\psi=1}^{K}\alpha_\psi . \quad (17)$$

Equations (16) and (17) store information at t_{n+1-K}, which is used to evaluate the temporal partial differentiation in equation (12) at each time step. The solution of equations (14) and (15) is obtained by applying equation (18) and distinct schemes of solution are allowed by varying θ,

$$[Jac_{i\beta}]\{\Delta f_\beta^{n+1}\} = -\{R_i\} \quad (18)$$

where f^{n+1} are the unknown variables and f^n the last iteration values. The initial guess prediction algorithm can be implemented in equation (18) for the convergence acceleration [11, 21].

V. THE WEAKLY ELECTRO-THERMAL MODEL

The proposed weakly modeling is obtained from equations (14) and (15). The symbols in Table I are replaced into equations (14) and (15) to obtain the EDE and the HE. The residual and Jacobian for the EDE are shown in equations (19) and (20), respectively,

$$\{R_i^{EDE}\} = \upsilon[M_{ij}]\{A_j^{n+\theta}\} + \frac{\sigma U}{\ell}\{G_i^{n+\theta}\} + \sigma[T_{ij}]\left\{\frac{1}{\Delta t}\sum_{g=0}^{K} A_j^{n+1-g}\alpha_g\right\} \quad (19)$$

$$[Jac_{i\beta}^{EDE}] = \theta\upsilon[M_{i\beta}] + \sigma[T_{i\beta}]\left\{\frac{\alpha_0}{\Delta t}\right\}, \quad (20)$$

while the residual and the Jacobian for the HE are,

$$\{R_i^{HE}\} = k[M_{ij}]\{T_j^{n+\theta}\} + q\{G_i^{n+\theta}\} + \rho C_p[T_{ij}]\left\{\frac{1}{\Delta t}\sum_{g=0}^{K} T_j^{n+1-g}\alpha_g\right\}, \quad (21)$$

$$[Jac_{i\beta}^{HE}] = \theta k[M_{i\beta}] + \rho C_p[T_{i\beta}]\left\{\frac{\alpha_0}{\Delta t}\right\}. \quad (22)$$

The solution of equations (19) to (22) is obtained from equation (18). Equations (19) to (22) were programmed in C language and solved using a sparse direct solver [22-23]. The flowchart of the programmed code is shown in Fig. 1. In a first step, the meshing, the physical parameters, the simulation time t_s, and the boundary conditions are executed. The BDF-Theta proposes a minimum time-step constraint [14]. The use of a minimum time-step in the model avoids the presence of discontinuities in the numerical results and brings numerical stability [11, 14]. Reference [14] proposes a minimum time-step constraint Δt_{min} for the EDE as,

$$\Delta t_{EDE}^{\min} = C \cdot \mu \cdot \sigma \cdot h^2 \quad (23)$$

where C is a constant chosen such that $C \leq 1$ and h is related to the minimal FE size [13, 24]. However, in a CPA a minimum time-step per phenomenon must be defined. Wherefore, this paper proposes a minimum time-step constraint for the HE as,

$$\Delta t_{HE}^{\min} = C \cdot \rho \cdot C_p \cdot h^2 \cdot \frac{1}{k}. \quad (24)$$

In a CPA model, the different time-step restrictions must be incorporated in an absolute

minimum time-step Δt_{min}. This paper proposes the absolute minimum time-step strategy defined by equation (25),

$$\Delta t_{\min} = \frac{\Delta t_{EDE}^{\min} \Delta t_{HE}^{\min}}{\Delta t_{EDE}^{\min} + \Delta t_{HE}^{\min}}. \tag{25}$$

The time-step criterion in equation (25) has been successfully used for fluid flow analysis in [13]. Once the time-step defined in equation (25) is calculated, an initial guess prediction algorithm is performed for convergence acceleration as it is indicated in [14]. The convergence in equation (18) accelerates when the predicted values Ap^{n+1} and Tp^{n+1} are near to the system solution. Equations (19) and (20) are calculated until a certain relative error ε is accomplished. Afterwards, the coupled circuit equations at equation (6) are solved. The power loss density is calculated and used for solving equations (21) and (22). The power loss density is obtained as,

$$q = \sigma\left(\frac{\partial A}{\partial t}\right)^2 + \frac{J^2}{\sigma}. \tag{26}$$

The first term at the right hand side of equation (26) represents the power loss density due to the Eddy currents. The second term in equation (26) represents the power loss density due to the current or voltage sources (see Table I). Equation (26) is used in equations (21) to (22) and the HE is solved until a predefined relative error ε is achieved. The time loop is performed while $t_{n+1} \neq t_s$. A new order and a new time-step are calculated at each iteration. The Gear's algorithm has a suitable technique to calculate Δt and the K order at each time iteration [11]. The Gear's algorithm changes the K order up or down by defining a time step ratio η_K as,

$$\eta^j{}_K = \frac{\Delta t_{new}}{\Delta t} = \frac{\Delta f_j}{f_j^{n+1} - fp_j^{n+1}} \tag{27}$$

where $\eta^j{}_K$ is the time step ratio of the K order in the node jth, f refers to the unknown variables A and T at Table I, fp are the predicted values and Δf_j is an absolute error (error control) allowed in the jth unknown variable.

In this paper, the Δf_j quantities are the last iteration values from ΔA^{n+1} and ΔT^{n+1} in the NR. The maximum time-step ratio for the next iteration is chosen as $\eta_K = \min_{j \in \mathrm{NOD}} \eta^j{}_K$ where NOD refers to the set of nodes in the FE mesh. The order K for the next iteration is obtained by comparing the quantities η_K, $\eta_{K\text{-}1}$, and η_{K+1} and selecting $\max_{K\text{-}1 \le Y \le K+1} \eta_Y$. The process to obtain the quantities η_K, $\eta_{K\text{-}1}$, and η_{K+1} is described in [11]. From the time loop, two different time steps (Δt_{EDE} and Δt_{HE}) and two orders (K_{EDE} and K_{HE}) are obtained. The order K_{EDE} is applied in equations (19) and (20) and the order K_{HE} is used in equations (21) and (22). An absolute time-step is obtained from Δt_{EDE} and Δt_{HE} using equation (25) as in equation (28),

$$\Delta t_{abs} = \frac{\Delta t_{EDE} \Delta t_{HE}}{\Delta t_{EDE} + \Delta t_{HE}}. \tag{28}$$

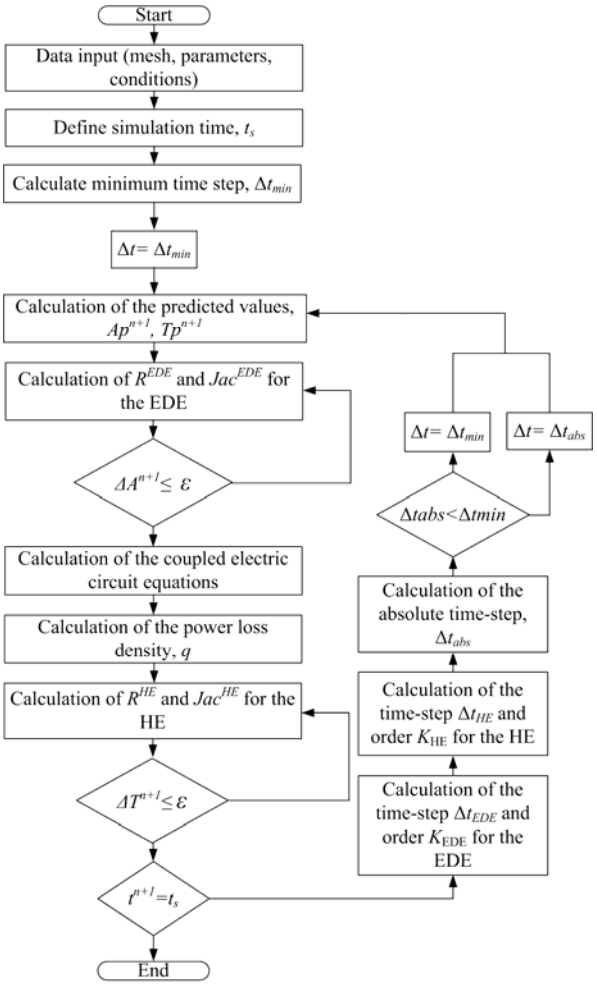

Fig. 1. Flowchart of the developed model.

Finally, the time-step Δt for the next iteration is selected as $\Delta t_{\min}$ if $\Delta t_{\mathrm{abs}} \le \Delta t_{\min}$ and selected as Δt_{abs} if $\Delta t_{\min} \le \Delta t_{\mathrm{abs}}$.

VI. NUMERICAL EXAMPLE

The problem domain and parameters for a nichrome wire placed above an aluminum slab are shown in Fig. 2. The nichrome wire is fed with a voltage source. The power loss density is generated by the electrical conductivity and the eddy currents. The power loss densities increment the temperature gradient in the domain. The Dirichlet boundary condition is used for the EDE and the HE.

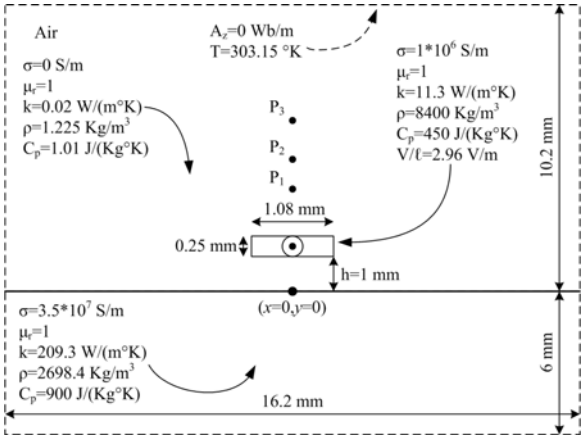

Fig. 2. Problem domain used in the numerical example.

The weakly electro-thermal CPA model shown in Fig. 1 was programmed in C language and solved for the domain illustrated in Fig. 2. The mesh has 2587 nodes and 5016 first order triangular elements. The model was executed in a laptop computer with a 2 GHz dual core processor and 2 GB RAM. Two numerical experiments were made for relative errors ε of 1E-1 and 1E-2 with θ=1. The modeling results are shown in Table II. It was found that for tighter relative errors ε the orders K_{EDE} and K_{HE} are higher and more stable as it is reported in Table II and shown in Figs. 3 and 4. It can be concluded that higher time-steps and lower time-loop iterations are attained for tighter relative errors in ε. The time-step Δt evolution throughout the simulation time is shown in Fig. 5.

It was found that the time-step is more stable for a tighter error ε. Nevertheless, the NR loop in the model causes a higher computation time for a tighter error ε. The proposed model was used to obtain the electromagnetic and thermal transient response at points P_1(0, 0.0019), P_2(0, 0.0023), and P_3(0, 0.003) shown in Fig. 2. The numerical results shown in Figs. 6 and 7 were obtained using an implicit scheme (θ=1) and a relative error of ε=1E-2. The transient solution for a simulated time of 150 *s* required 234 *s* of computation time. The steady state was attained after 1 m*s* of simulated time for the EDE and after 100 *s* for the HE. The time steps are short before the first 1 m*s* of simulated time due the small time constant of the EDE in equation (28). Afterwards, the time steps are larger due to the time constant of the HE in equation (28). The modeling results were compared against those obtained with a commercial software [25] and an error less than 1E-5 was achieved as it is shown in Figs. 6 and 7. The induced current density shown in Fig. 8 was estimated from the Eddy currents in the metallic slab and by solving the electric circuit equations given by equation (6). Finally, the potential distribution for the EDE and the HE are shown at Figs. 9 and 10. The electrical current in the nichrome wire at Fig. 2 produces the magnetic potential distribution shown in Fig. 9. The temperature distribution at Fig. 10 is caused by the Eddy currents in the metallic slab and by the power loss density obtained from the voltage source in the nichrome wire. The hot spot was located in the nichrome wire where the temperature rises 34 °K above the ambient temperature.

Table II: Numerical behavior obtained in the model for ε = 1E-1 and ε = 1E-2.

	ε=1*E*-1	ε=1*E*-2
Max K_{EDE}	5	5
Max K_{HE}	2	3
Max Δt	27.92	55.18
Time iterations	278	267
Computation time (s)	228	234

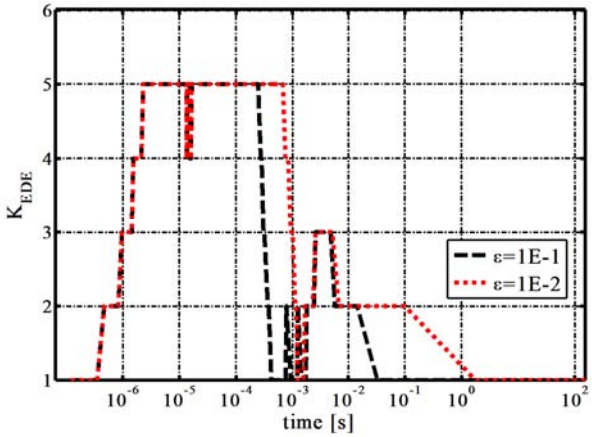

Fig. 3. Evolution of the order K_{EDE} for θ=1 and ε equals to 1E-1 and 1E-2.

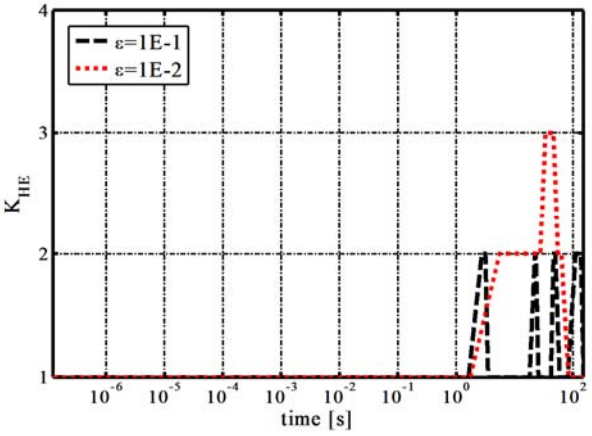

Fig. 4. Evolution of the order K_{HE} for θ=1 and ε equals to 1E-1 and 1E-2.

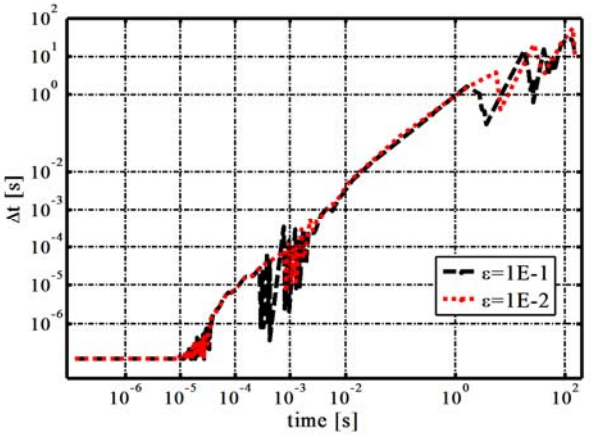

Fig. 5. Time-step Δt evolution for θ=1 and ε equals to 1E-1 and 1E-2.

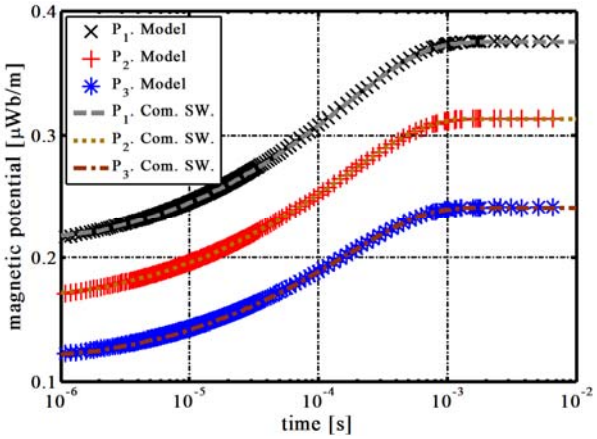

Fig. 6. Transient response of the EDE at points P_1, P_2, and P_3 for θ=1 and ε=1E-2. Results computed with the propose model (Model) and a commercial software (Com. SW.).

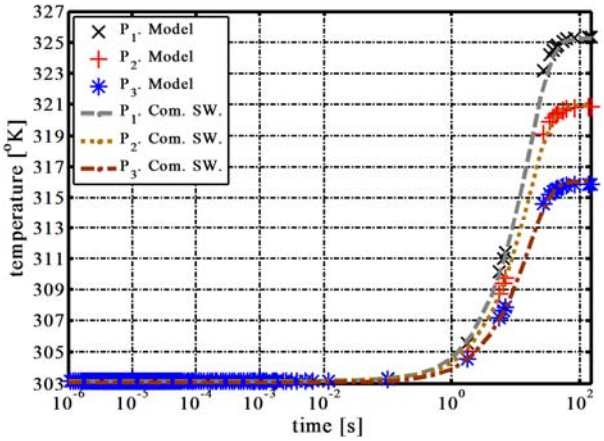

Fig. 7. Transient response of the HE at points P_1, P_2, and P_3 for θ=1 and ε=1E-2. Results computed with the propose model (Model) and a commercial software (Com. SW.).

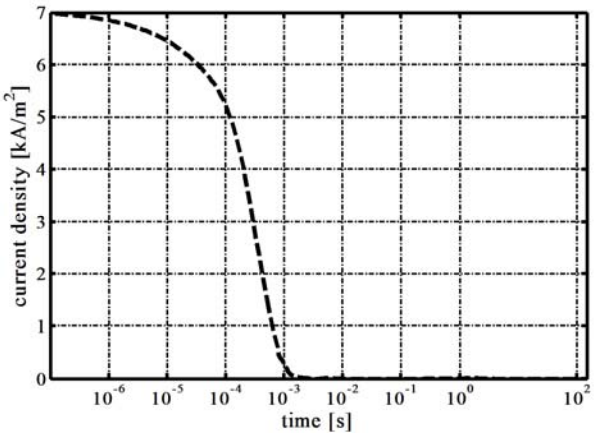

Fig. 8. Current density induced in the metallic slab.

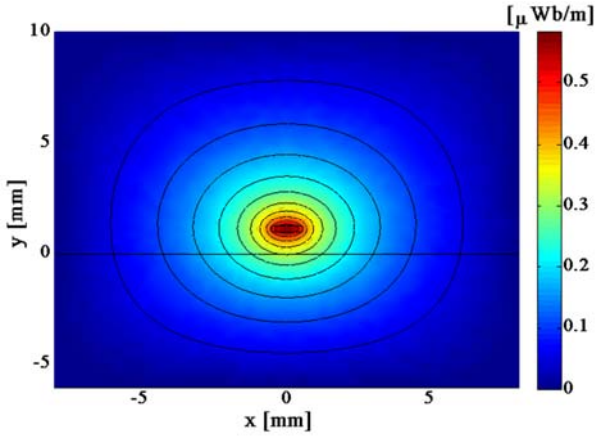

Fig. 9. Magnetic potential distribution computed at steady state for θ=1 and ε=1E-2. Max. Pot.: 5.82x10^{-7} Wb/m, Min. Pot.: 0 Wb/m.

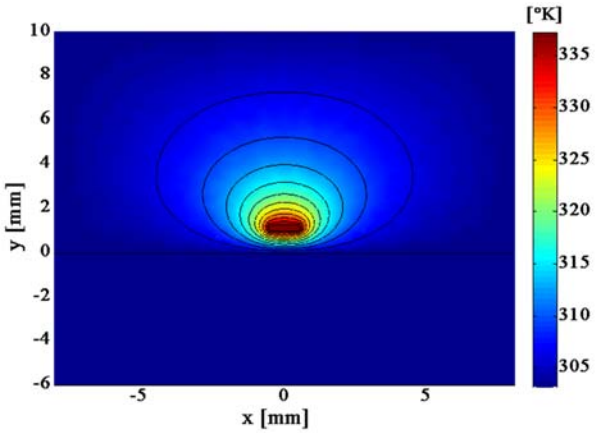

Fig. 10. Temperature distribution computed at steady state for θ=1 and ε=1E-2. Max. Temp.: 337.16 °K, Min. Temp.: 303.15 °K.

VII. CONCLUSION

The BDF-Theta algorithm for the variable time step and order has been applied for the first time to solve a weakly coupled electro-thermal formulation using 2-D first-order finite elements. The electrical power losses due to the Eddy currents and the voltage sources were computed and used in the heat equation. An electrical circuit coupled to thick conductors has been included in the model. A minimum and absolute time step criteria were proposed to incorporate the time steps restrictions from the EDE and the HE. The proposed time-step criterion avoids small time steps and model instabilities. The developed model was programmed in C language and used to solve a numerical example.

ACKNOWLEDGMENT

The authors would like to thank to CONACYT, PROMEP, DGEST, and Instituto Tecnológico de la Laguna for their financial support.

REFERENCES

[1] M. Celuch, M. Soltysiak, and U. Erle, "Computer simulations of microwave heating with coupled electromagnetic, thermal, and kinetic phenomena," *ACES Journal*, vol. 26, no. 4, pp. 275-283, April 2011.

[2] G. Henneberger, K. Sattler, and W. Hadrys, "Coupling of magnetic and fluid flow problems and its application in induction melting apparatus," *IEEE Trans. On Magn.*, vol. 29, no. 2, pp. 1589-1594, 1993.

[3] K. Preis, O. Biro, G. Buchgraber, and I. Ticar, "Thermal-electromagnetic coupling in the finite element simulation of power transformers," *IEEE Trans. On Magn.*, vol. 42, no. 4, pp. 999-102, 2006.

[4] C. Rosas, N. Moraga, V. Bubnovich, and R. Fisher, "Improvement of the cooling process of oil-immersed electrical transformers using heat pipes," *IEEE Trans. On Magn.*, vol. 20, no. 3, pp. 1955-1961, 2005.

[5] V. M. Kulkarni, K. N. Seetharamu, P. A. Aswatha Narayana, A. I. Azid, and G. A. Quadir, "Flow analysis for flip chip underfilling process using characteristic based split method," *IEEE Electronics Packaging Technology Conf.*, pp. 615-619, Feb. 2004.

[6] M. Sadiku, "A simple introduction to finite element analysis of electromagnetic problems," *IEEE Trans. On Education*, vol. 32, no. 2, pp. 85-93, 1989.

[7] J. H. Alwash and L. J. Qaseer, "Three-dimension finite element analysis of a helical motion induction motor," *ACES Journal*, vol. 25, no. 8, pp. 703-712, August 2010.

[8] I. A. Tsukerman, A. Konrad, G. Bedrosian, and M. V. K. Chari, "A survey of numerical methods for transient Eddy current problems," *IEEE Trans. On Magn.*, vol. 29, no. 2, pp. 1711-1716, Mar. 1993.

[9] Q. Wang, C. Yan, Y. Shi, D. Ding, and R. Chen, "Transient analysis of electromagnetic scattering using marching-on-in-order time-domain integral equation method with curvilinear RWG basis functions," *ACES Journal*, vol. 26, no. 5, pp. 429-436, May 2011.

[10] K. E. Brenan, S. L. Campbell, and L. R. Petzold, *Numerical Solution of Initial Value Problems in Differential-Algebraic Equations*, Society for

Industrial and Applied Mathematics, pp. 41-148, 1996.

[11] R. K. Brayton, F. G. Gustavson, and G. D. Hachtel, "A new efficient algorithm for solving differential algebraic systems using implicit backward differentiation formulas," *Proceedings of the IEEE*, vol. 60, no. 1, pp. 98-108, January 1972.

[12] G. J. Barclay, D. F. Griffiths, and D. J. Higham, "Theta method dynamics," *LMS Journal of Computation and Mathematics*, vol. 3, pp. 27-43, Feb. 2000.

[13] O. C. Zienkiewics and R. L. Taylor, *The Finite Element Method Vol. 3 Fluid Dynamics*, Butterworth Heinemann, pp. 64-90, 2000.

[14] R. B. B. Ovando-Martinez, M. A. Arjona Lopez, and C. Hernandez Flores, "A finite-element variable time-stepping algorithm for solving the electromagnetic diffusion equation," *IEEE Trans. On Magn.*, vol. 48, no. 2, pp. 647-650, 2012.

[15] J. Jin, W. Quan-di, Y. Ji-hui, and Z. Ya-li, "Wideband equivalent circuit model and parameter computation of automotive ignition coil based on finite element analysis," *ACES Journal*, vol. 25, no. 7, pp. 612-619, July 2010.

[16] M. A. Arjona, R. B. B. Ovando-Martinez, and C. Hernandez, "Thermal-fluid transient two-dimensional characteristic-based-split finite-element model of a distribution transformer," *IET Electr. Power Appl.*, vol. 6, no. 5, pp. 260-267, 2012.

[17] M. A. Taghikhani and A. Gholami, "Heat transfer in power transformer windings with oil-forced cooling," *IET Electr. Power Appl.*, vol. 3, no. 1, pp. 59-66, 2009.

[18] J. P. A. Bastos and N. Sadowski, *Electromagnetic Modeling by Finite Element Methods*, Marcel-Dekker, 2003.

[19] T. Boonen, J. Van Lent, H. De Gersem, J. Driesen, and S. Vandewalle, "Algebraic multigrid for implicit Runge-Kutta discretizations of the Eddy current problem," *IEEE Trans. On Magn.*, vol. 43, no. 4, pp. 1265-1268, April 2007.

[20] A. Nicolet and F. Delincé, "Implicit Runge-Kutta methods for transient magnetic field computation," *IEEE Trans. On Magn.*, vol. 32, no. 3, pp. 1405-1408, May 1996.

[21] L. O. Chua and P. Min, *Computer Aided Analysis of Electronic Circuits algorithms and Computational Techniques*, Prentice Hall, pp. 665-685, 1975.

[22] O. Shenk and K. Gartner, "Solving unsymmetric sparse systems of linear equations with pardiso," *Journal of Future Generation Computer Systems*, vol. 20, no. 3, pp. 475-487, 2004.

[23] O. Shenk and K. Gartner, "On fast factorization pivoting methods for symmetric indefinite systems," *Elec. Trans. On Numberical Analysis*, vol. 23, pp. 158-179, 2006.

[24] R. W. Lewis, P. Nithiarasu, and N. S. Kankanhally, *Fundaments of the Finite Element Method for Heat and Fluid Flow*, Wiley, 2004.

[25] COMSOL Multiphysics user's guide, version 3.5a, COMSOL AB, November 2008.

R.B.B. Ovando-Martinez received the B.Sc. degree in Electrical Engineering from the Instituto Tecnológico de la Laguna, Torreón, México, in 2008, the M.Sc. degree in Electrical Engineering from the Instituto Tecnológico de la Laguna, Torreón, México, in 2009. He is currently working toward his Sc.D. degree in Electrical Engineering at the Instituto Tecnológico de la Laguna. His research interest includes electromagnetic, thermal and fluid dynamics modeling of electrical machines.

C. Hernandez received the B.Sc. degree in Computer Science from the Instituto Tecnológico de Estudios Superiores de Monterrey, Monterrey, México, in 1990, the M.Sc. degree in foundations of advanced information technology from Imperial College, London, U.K., in 1995, and the Sc.D. degree in Electrical Engineering from the Instituto Tecnológico de la Laguna, Torreón, México, in 2007. She was with the Simulation Department, Instituto de Investigaciones Eléctricas from 1991 to 2000. She is currently with the Instituto Tecnológico de la Laguna, Torreón, México. Her interests are in artificial intelligence and global optimization applied to electrical machines.

M. A. Arjona received the B.Sc. degree in Electrical Engineering from the Instituto Tecnológico de Durango, Durango, México, in 1988, the M.Sc. degree in Electrical Engineering from the Instituto Tecnológico de la Laguna, Torreón, México, in 1990, and the Ph.D. degree in Electrical Engineering from Imperial College, London, U.K., in 1996. He was with the Simulation Department, Instituto de Investigaciones Eléctricas from 1991 to 1999. He is currently a Professor of electrical machines with the Instituto Tecnológico de la Laguna. His interests are in the electromagnetic design, analysis, and control of electrical machines.

Electromagnetic Analysis of a Novel Cylindrical Transverse-Flux Permanent-Magnet Linear Machine

Ping Zheng [1], Bin Yu [1], Haiyuan Yan [2], Yi Sui [1], Jingang Bai [1], and Pengfei Wang [1]

[1] School of Electrical Engineering and Automation
Harbin Institute of Technology, Harbin, 150080, China
zhengping@hit.edu.cn, yubin1983@163.com, suiyi_hitee2005@163.com, baijingangdiyi@163.com, and wpf6032@163.com

[2] China Academy of Launch Vehicle Technology, Beijing, 100076, China
yhylzx2005@sina.com

Abstract ─ Cylindrical transverse-flux permanent-magnet linear machine (TFPMLM) is a novel electric machine used for free piston energy converters. As the disadvantages of low power factor and complex manufacture exist in the conventional TFPMLM, this paper employs the staggered (not overlapped) stator teeth to reduce the flux leakage, and further increase the power factor and force density. In this paper the flux leakage and performances of two topologies are researched and compared. Then thorough analysis is made on axial 3-phase TFPMLM, which has great potential in force density and power factor. Thrust fluctuation, force density and power factor of the axial TFPMLM are analyzed. Moreover, the methods to improve force density and power factor are researched. Finally, a scheme with power factor up to 0.52, force density up to 2.17×10^5N/m^3 is developed.

Index Terms ─ Flux leakage, force density, linear machine, power factor, and transverse flux.

I. INTRODUCTION

Transverse flux permanent-magnet machine (TFPMM) is a special structure PM machine. Unlike traditional machines, the electric load and magnetic load of TFPMM are decoupled from each other. High torque/force density can be obtained by improving the electric and/or magnetic load. So scholars make further research on the theory and technology of TFPMM, and great achievements have been made. TFPMM has broad prospect of application in wind power generation, marine propeller, linear drive, magnetic levitation, etc [1].

Since Professor H. Weh designed the first prototype of transverse flux machine (TFM), the later scholars have proposed a variety of different structures of transverse flux machines to improve the performance and the processing technology [2]. A TFM with C-shaped stator core was proposed by Rolls-Royce in Britain; the stator is made of soft magnetic composite (SMC), which has poor magnetic properties and high cost [3]. A C-core TFM was proposed by Royal Institute of Technology in Sweden, which has high power factor but low torque density [4]. An E-core TFM was proposed by Aalborg University in Denmark, which is suitable for high speed application because of the less pole number [5]. A TFM with claw-pole stator and outer rotor was proposed by Aachen Institute of Technology in Germany, which has small outer diameter, with liquid cooling used for heat dissipation [6]. Similar topology was investigated by the University of Southampton in UK [7]. A reluctance type TFM was proposed by the University of Calgary in Canada, which has simple manufacturing process, but increases the amount of permanent magnets [8]. A TFM with permanent-magnet screen technology was proposed by the Electrotechnology Research Institute in Korea, which uses the permanent-magnet flux to weaken the leakage flux, and the machine performance is improved [9]. For TFMs, the problems of complicated structure, difficult manufacturability, and low power factor normally

Submitted On: Jan. 22, 2013
Accepted On: Aug. 25, 2013

exist. So a large number of researches have been developed on how to improve the power factor, simplify the structure, and optimize the parameters. The research work mainly focus on the application of new materials (SMC), optimal design methods (particle swarm design, magnetic field screen, and genetic algorithm), parameter optimizations (3-D finite element method, equivalent magnetic circuit method), control optimizations (harmonics current injection, symmetric current control), etc[10-15].

In this paper, a novel cylindrical transverse-flux permanent-magnet linear machine (TFPMLM) is proposed based on the previous research work on rectangular topology [16], which is used for a free-piston generator system. Cylindrical structure is more convenient to manufacture, and more suitable for assembling with the free-piston power generation system. Moreover, the novel cylindrical topology can solve the problems of high flux leakage and low power factor existing in the former rectangular one. Two different topologies are proposed and compared. The 3-D finite element method (FEM) (Maxwell 14.0) is used to simulate the flux distribution in different parts of the machine. With Armature and PM flux leakage considered, local optimization is used to find the best axial thickness of the stacked long stator core and pole arc coefficient. With power factor and force density considered together, parametric match optimization is used, with the combination of winding turns and pole number, the combination of air-gap length and axial length, and the overlapping cross-sectional angle of adjacent stator cores are investigated.

II. STRUCTURE AND LEAKAGE FACTOR OF THE NOVEL STAGGERED-TEETH CYLINDRICAL TFPMLM

A. Structure

Compared with traditional TFPMLM, the novel staggered-teeth cylindrical TFPMLM has a quite different stator structure. There are two kinds of arrangements of the machine structure, called axial 3-phase structure and circumferential 3-phase structure, respectively. For every pole pair, stator teeth are composed of three types of laminations arranged in the form of I, III, II, and III, successively, as shown in Figs. 1 (a) and 2 (a). I and II are defined as the stacked long stator core. Windings of each phase are wounded around the roots of the teeth. Stator structure and mover structure are shown in Figs. 1 (b) and (c) and Figs. 2 (b) and (c), respectively. For 3-phase machine, the phase windings have two ways of arrangement, namely axial and circumferential 3-phase windings. For axial 3-phase structure, the adjacent phases are arranged by 2/3 pole pitch displacement in axial direction, as shown in Fig. 1 (d). For circumferential 3-phase structure, coils around two adjacent teeth forms a phase winding, and 3-phase windings are evenly distributed circumferentially, the PMs of the adjacent phases are arranged by 2/3 pole pitch displacement in the axial direction, as seen in Fig. 2 (d).

(a) Stator laminations.

(b) Stator structure.

(c) Mover structure.

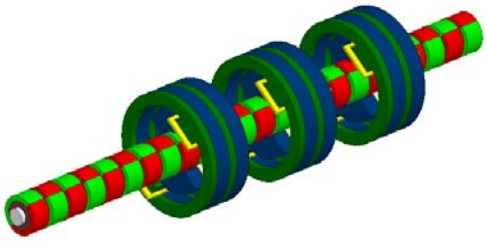

(d) 3-D FEM model.

Fig. 1. Axial 3-phase structure.

(a) Stator laminations.

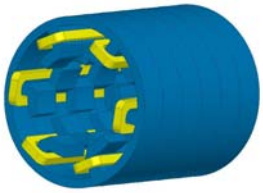

(b) Stator structure.

(c) Mover structure.

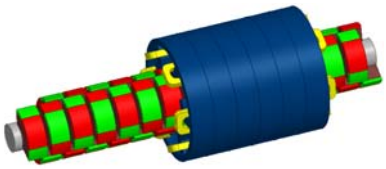

(d) 3-D fem model.

Fig. 2. Circumferential 3-phase structure.

B. General forms of flux leakage

There are PM flux leakage and armature flux leakage in TFPMLM. Leakage factor is defined as the ratio of the total flux and the main flux. Taking circumferential structure as an example, PM flux leakage includes flux leakage between transverse adjacent PMs, diagonal PM flux leakage between poles and flux leakage between longitudinal adjacent PMs, as in Fig. 3. Flux leakage between transverse adjacent PMs is defined as PM transverse leakage $\Phi_{\sigma pmt}$; the diagonal PM flux leakage between poles and the flux leakage between longitudinal adjacent PMs are defined as PM longitudinal leakage $\Phi_{\sigma pml}$. To calculate the leakage factor, the total flux and each flux leakage are calculated by 3D FEM, respectively. The flux leakage paths are shown by the solid arrow lines in Figs. 3 and 4. For each flux leakage, a yellow calculated plane is set up in the path of the flux leakage, and the flux leakage can be calculated by integrating the flux density on the plane. Both axial thickness of stacked long stator core and arc coefficient play a significant role in the PM flux.

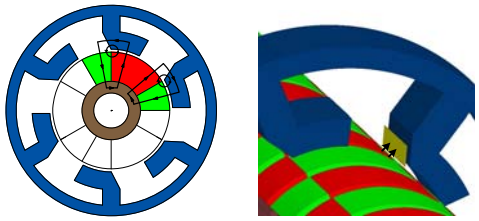

(a) Flux leakage between transverse adjacent PMs.

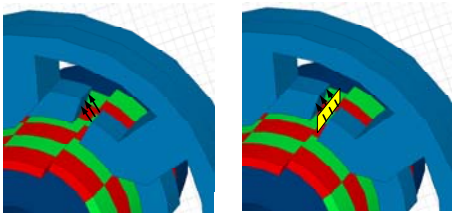

(b) Diagonal PM flux leakage between Poles.

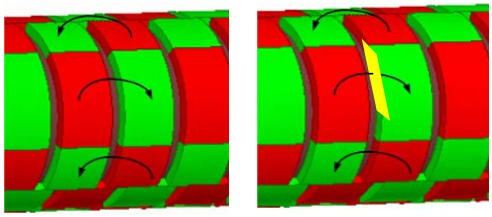

(c) Flux Leakage between Longitudinal Adjacent PMs.

Fig. 3. PM flux leakage paths and calculated planes.

Armature flux leakage includes slot flux leakage, flux leakage between teeth, and flux leakage between poles, as seen in Fig. 4. In addition, slot flux leakage and flux leakage between the teeth are defined as armature transverse leakage $\phi_{\sigma at}$; the flux leakage between poles is defined as armature longitudinal leakage $\phi_{\sigma al}$. Unlike PM flux leakage, armature flux leakage is mainly influenced by axial thickness of stacked long stator core.

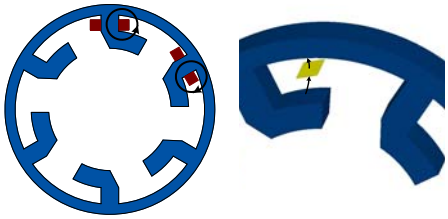

(a) Slot flux leakage.

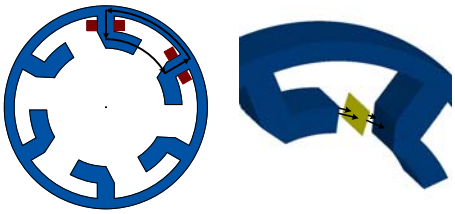

(b) Flux leakage between teeth.

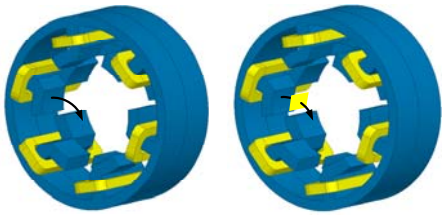

(c) Flux Leakage between Poles.

Fig. 4. Armature flux leakage paths and calculated planes.

C. Optimization of leakage factor

In this part, the topologies in Figs. 1 (d) and 2 (d) are optimized to reduce the flux leakage. Local optimization and FEM (provided by commercial software Maxwell 14.0) are used to find the best axial thickness of the stacked long stator core and pole arc coefficient.

1) *Optimization of the leakage factor of the axial three-phase type.*

The major parameters of the axial three-phase structure machine are shown in Table I.

Table I: Main parameters of axial three-phase type.

Parameters	Value	Parameters	Value
Rated power (kW)	1	Outer diameter of stator yoke	74mm
Rated velocity (m/s)	3	Inner diameter of stator yoke	60mm
Rated voltage(V)	44	Outer diameter of stator tooth	50mm
Material of the stator core	DW315-50	Inner diameter of stator tooth	26mm
Material of the mover core	DW315-50	Thickness of tooth	12mm
Permanent Magnet	N35SH	Length of air-gap	1mm
Winding	Single parallel-wounded concentrated winding	Thickness of PM	3mm
Turns per phase	52	Outer diameter of mover	18mm
Slot fill factor	70%	Outer diameter of shaft	10mm
Number of poles per phase	16	Pole pitch	15mm

The following analysis is based on the condition that the pole pitch stays unchanged. The effect of thickness of the stacked long stator core on the armature flux leakage factor is analyzed when PMs are excluded, as shown in Fig. 5. While Fig. 6 shows the effect of thickness of the stacked long stator core on the PM flux leakage factor in the case that PM singularly produces flux.

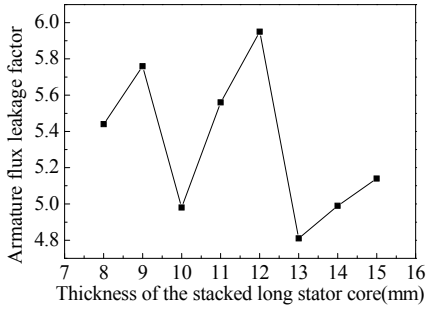

Fig. 5. Armature flux leakage factor versus axial thickness of the stacked long stator core.

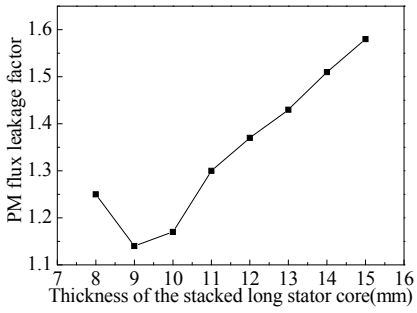

Fig. 6. PM flux leakage factor versus axial thickness of the stacked long stator core.

Considering the leakage factor of the armature and PM simultaneously, the axial thickness of the stacked long stator core is selected to be 10 mm.

The effect of arc coefficient on the PM flux leakage factor is shown in Fig. 7. It can be seen that with the increase of arc coefficient, PM longitudinal leakage increases, leading to an increase in the flux leakage factor. The PM flux leakage factor reaches a minimum of 1.17 when pole arc coefficient is 0.8, which is chosen to increase the PM utilization rate.

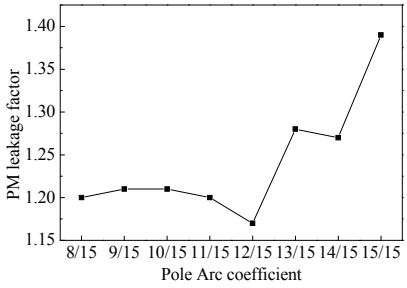

Fig. 7. PM flux leakage factor versus pole arc coefficient.

2) *Optimization of the leakage factor of circumferential three-phase type.*

The major parameters of the circumferential three-phase structure machine are shown in Table II.

Table II: Main parameters of the circumferential three-phase type.

Parameters	Value	Parameters	Value
Rated power (kW)	1	Outer diameter of stator yoke	78mm
Rated velocity (m/s)	3	Inner diameter of stator yoke	70mm
Rated Voltage(V)	44	Outer diameter of stator tooth	52mm
Material of the stator core	DW315-50	Inner diameter of stator tooth	42mm
Material of the mover core	DW315-50	Thickness of tooth	12mm
Permanent Magnet	N35SH	Length of air-gap	1mm
Winding	Single parallel-wounded concentrated winding	Thickness of PM	4mm
Turns per phase	35	Outer diameter of mover	36mm
Slot fill factor	70%	Outer diameter of shaft	18mm
Number of poles per Phase	48	Pole pitch	15mm

Due to the same structure of the stator tooth per phase in the case of axial and circumferential structure, armature flux leakage of both is similar. While PM flux leakage factor of the two differs slightly because of the different PM arrangements. The effects of thickness of stacked long stator core on armature flux leakage factor and PM flux leakage factor are shown in Figs. 8 and 9, respectively. Considering the leakage factor of the armature and PM simultaneously, the axial thickness of the stacked long stator core is selected to be 12mm.

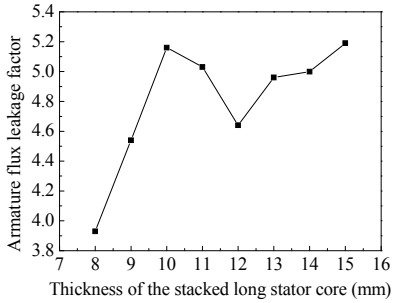

Fig. 8. Armature flux leakage factor versus axial thickness of the stacked long stator core.

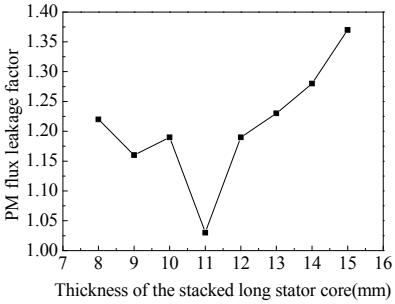

Fig. 9. PM flux leakage factor versus axial thickness of the stacked long stator core.

The trend of the PM leakage factor versus arc coefficient is shown in Fig. 10. Considering electromagnetic performances, pole arc coefficient is selected to be 12/15.

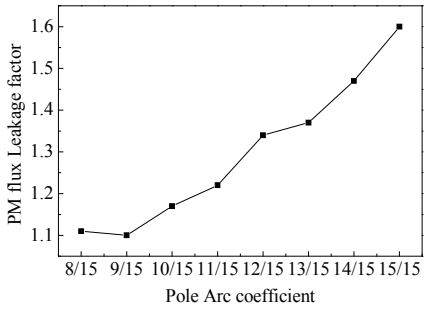

Fig. 10. The PM flux leakage factor versus the pole arc coefficient.

3) *Performance comparison between two structures.*

The key dimensions of the two types have been initially determined in the analysis above. In this part, simulation of no-load and load characteristics of the two types of machines is made by simplified 3-D FEM model, as realized in Figs. 1 (d) and 2 (d), and the results are shown as follows. The simplified model is based on equation (1),

$$E_{ph} = \sqrt{2}\pi f N p \Phi. \quad (1)$$

The thrust and back EMF of the simplified model and full model has the ratio of p_s/p, where p_s is the simplified pole pair number and p is the pole pair number in the full model. In this paper, p_s/p is 1/8. No-load characteristics of the two structures are shown in Figs. 11 and 12.

When the armature windings are fed with rated currents $I_N = I_q = 7.6$ A (d-axis current I_d is 0) and the mover moves at rated speed, load back EMF and thrust of the two structures are shown in Figs. 13 and 14. To make a clear comparison, some key performances are listed in Table III.

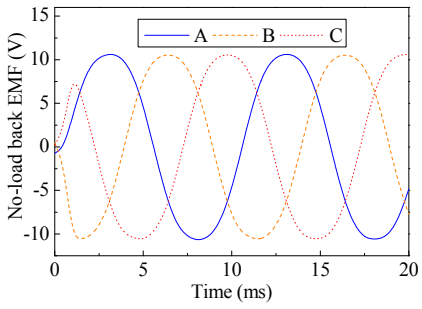

(a) No-load back EMF.

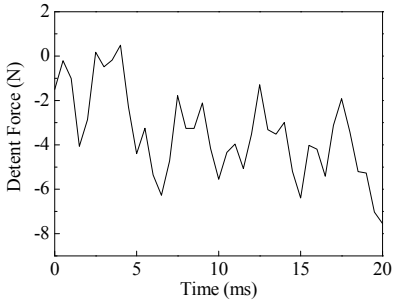

(b) Detent force.

Fig. 11. No-load performance of the axial 3-phase structure.

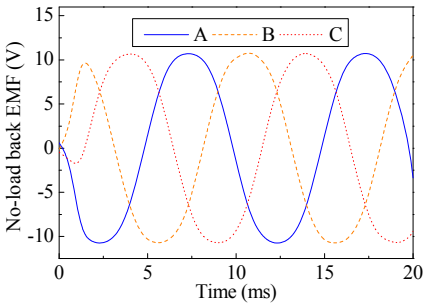

(a) No-load back EMF.

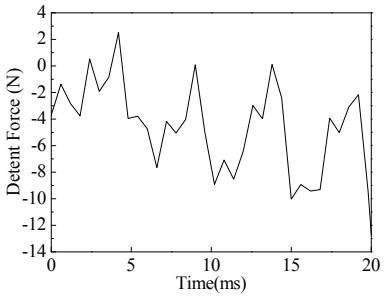

(b) Detent force.

Fig. 12. No-load performance of circumference 3-phase structure.

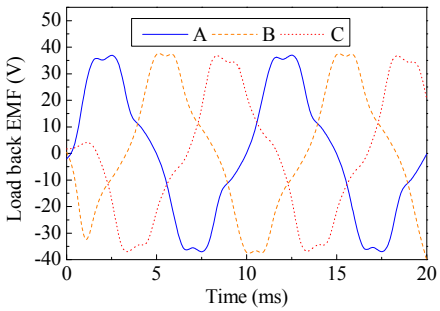

(a) Load back EMF.

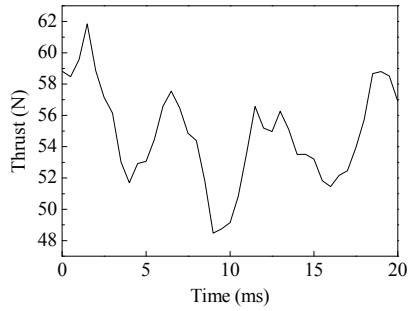

(b) Thrust.

Fig. 13. Load performance of the axial 3-phase structure.

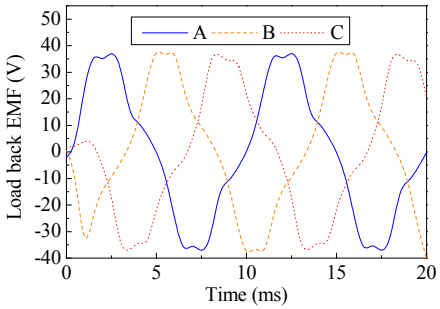

(a) Load back EMF.

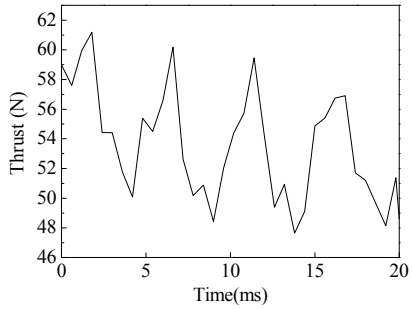

(b) Thrust.

Fig. 14. Load performance of the circumference 3-phase structure.

Table III: Performance comparison of the two structures.

	Axial 3-phase type	Circumferential 3-phase type
the aberration rate of no-load EMF	0.0667	0.3137
Detent force	3.46	4.45
Thrust fluctuation	12.12%	12.44%
Force density(N/m^3)	1.40×10^5	4.17×10^4

Compared with the circumferential structure, the axial counterpart has a lower back EMF aberration rate and detent force, but has almost the same thrust fluctuation. The latter also has a higher force density. Therefore, axial 3-phase type is chosen for further study.

III. THRUST FLUCTUATION, FORCE DENSITY AND POWER FACTOR OF AXIAL TFPMLM

A. Theoretical analysis

From the previous analysis, thrust fluctuation is as high as 12.12 % for axial structure. Thrust fluctuation results in the vibration and noise of the machine, and especially in the case of low speed, resonance [17].

Detent force is the key indicator of thrust fluctuation. For normal linear machines, detent force can be decreased by modifying the pole pitches of stator and mover [18, 19]. While in the proposed machine, this method becomes useless because the pole pitch of the stator equals to that of the mover. The decrease of the detent force can be achieved by changing the arc coefficient, since the distribution of the harmonic magnetic field varies with arc coefficient significantly.

Being the primary concern of the novel cylindrical TFPMLM, force density and power factor are analyzed for axial structure by deducing the formulae of force density and power factor. Thrust is given by equation (2),

$$F=\frac{3\sqrt{2}\pi^2}{8}NpB_\delta J\frac{l_s}{\tau}D_{si}S_c\cos\varphi. \qquad (2)$$

The symbol N is the turns-in-series per-phase, p is pole pair number, B_δ is air gap flux density, τ is the pole pitch, l_s is axial length of PM, D_{si} is the inner diameter of the stator, and S_c is the cross-sectional area of the conductor. The force density is given by equation (3),

$$F_\xi=\frac{F}{p\tau\pi(\frac{D_o^2}{4})}=\frac{3\sqrt{2}\pi}{2}NJB_\delta\frac{l_s}{\tau}\frac{D_{si}S_c\cos\varphi}{D_o^2\tau}. \qquad (3)$$

The symbol D_o refers to the outer diameter of the stator. The power factor is defined by equation (4),

$$\cos\varphi=\frac{E_{ph}}{\sqrt{E_{ph}^2+(\omega LI_q)^2}}. \qquad (4)$$

Where E_{ph} is the phase back EMF. The power factor can be further derived as shown in equation (5),

$$\cos\varphi = \frac{1}{\sqrt{1+\dfrac{32(\omega L I_q)^2}{\pi^4 (NpB_\delta v D_{si}\dfrac{l_s}{\tau})^2}}}. \quad (5)$$

From equations (3) and (5), it is obvious that the force density and the power factor depends on l_s/τ, i.e., the pole arc coefficient α. In condition that the pole arc coefficient remains constant, the axial thickness of the stacked long stator core affects the force density via utilization ratio of the PM and power factor via the armature flux leakage.

B. 3D-FEM simulation

When the axial thickness of the stacked long stator core stays 10 mm, no-load and load performances with different pole-arc coefficients are shown in Figs. 15, 16, and 17, respectively. The aberration rate of the no-load EMF and decent force decrease firstly, and then increase.

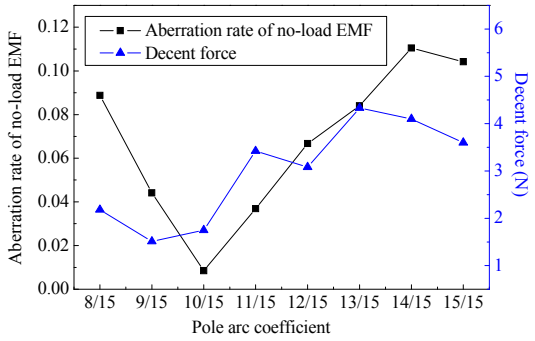

Fig. 15. The decent force and aberration rate of no-load EMF versus pole arc coefficient.

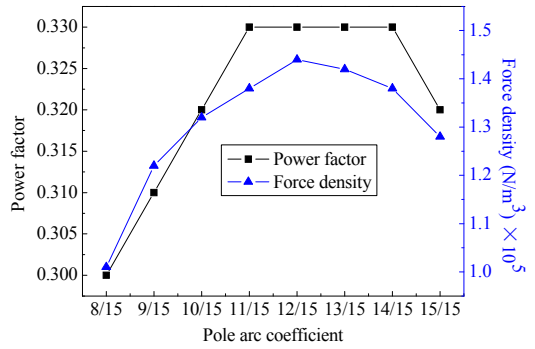

Fig. 16. Power factor and force density versus pole-arc coefficient.

The force density and power factor increase firstly, and then decrease. It can be seen that favorable no-load and load performances are achieved when pole arc coefficient is 12/15.

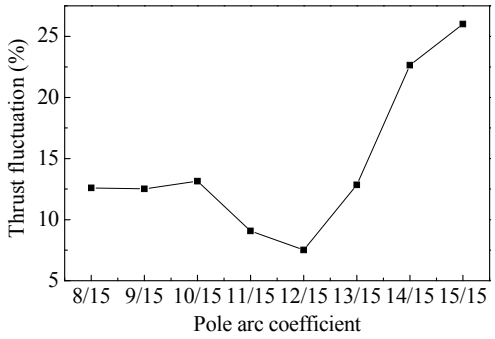

Fig. 17. Thrust fluctuation versus pole arc coefficient.

When the pole arc coefficient stays 12/15 and the axial thickness of the stacked long stator core ranges from 8 mm to 15 mm, the performances of no-load are shown in Fig. 18. The aberration rate of no-load EMF increases at first, and then decreases; the decent force has the opposite phenomena. When the axial thickness of the stacked long stator core ranges from 8 mm to 15 mm, the performances of the load are shown in Fig. 19. The force density firstly increases, and then decreases; the power factor has a descending trend. When the axial thickness of the stacked long stator core is 10 mm, the thrust fluctuation is the lowest, as shown in Fig. 20. With the performances of no-load and load taken into account, the axial thickness of the stacked long stator core is chosen to be 10 mm.

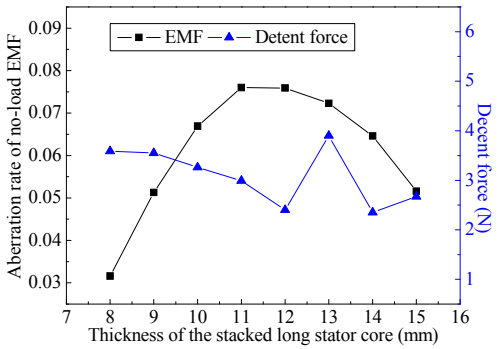

Fig. 18. The decent force and aberration rate of no-load EMF versus axial thickness of the stacked long stator core.

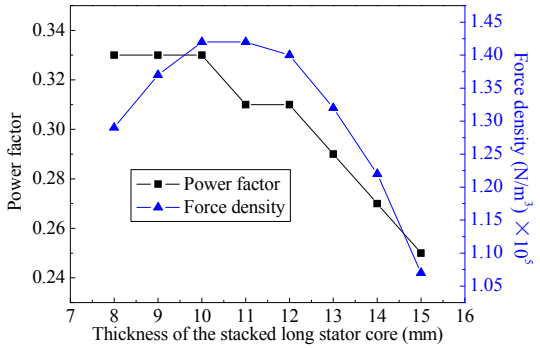

Fig. 19. Power factor and force density versus axial thickness of the stacked long stator core.

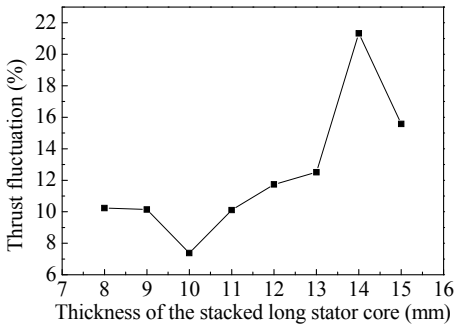

Fig. 20. Thrust fluctuation versus axial thickness of the stacked long stator core.

On the overall, when the pole-arc coefficient is 12/15 and axial thickness of the stacked long stator core is 10 mm, favorable no-load and load performances are achieved.

IV. THE METHODS TO IMPROVE FORCE DENSITY AND POWER FACTOR OF TFPMLM

Neglecting the saturation and armature reaction, thrust of the machine is given by equation (6),

$$F = m\frac{\sqrt{2}\pi p}{2\tau}\Phi_m N I_{ph}\cos\varphi. \qquad (6)$$

According to equation (6), there are three ways to improve the thrust of the preciously determined machine: increasing the air-gap flux Φ_m, increasing the armature current I_{ph}, and increasing the number of turns N. It is also necessary to take the effects on the power factor into account when implying the three methods. Power factor is determined by either equation (7) or (8) [20],

$$\cos\varphi = \cos[\tan^{-1}(\frac{\Phi_i}{\Phi_m})], \qquad (7)$$

$$\cos\varphi = \cos[\tan^{-1}(\frac{I_q X}{E_0})]. \qquad (8)$$

The symbol Φ_i is the flux that armature winding produces when armature current acts independently. The symbol Φ_m is the air-gap flux when permanent magnets act independently, X is the reactance, and E_o is the RMS value of no-load EMF. By increasing the air-gap flux Φ_m, the power factor and the force density can be increased at the same time. If the armature current I_{ph} is increased, the increased q-axis current I_q results in a lower power factor, though a higher force density can be achieved. Force density can be increased when the number of turns N is increased, but the power factor lowers dramatically as the reactance X is in proportion to the square of the number of turns N.

A. Combination of winding turns and pole number

According to the calculation results, the reactance X of the designed TFPMLM is 24.32 Ω, which is much larger than the reactance of the traditional radial-flux PM machine. Hence, a large reactance is another reason for the low power factor of TFPMLM. Besides, from equation (2) it is obvious that the number of pole pairs p needs to vary with the number of turns N in order to guarantee rated power output.

The 3D-FEM simulation results are shown in Fig. 21. It is easy to see that with the increase of the number of turns, the power factor decreases dramatically, while the force density has a very modest increase.

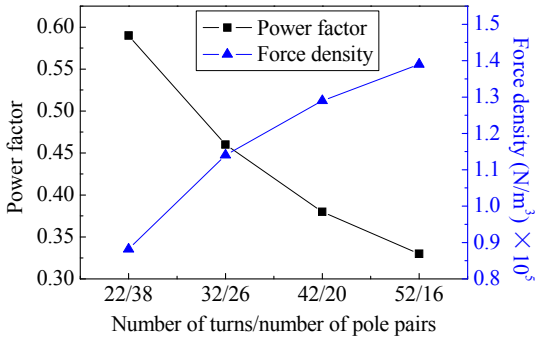

Fig. 21. Power factor and force density versus number of turns matching number of poles.

As a trade-off, the number of turns and pole pairs are chosen to be 32 and 26, respectively. And in this case, the power factor is 0.46 and the thrust density is 1.14×10^5 N/m^3.

B. Combination of air-gap length and axial length

As analyzed above, increasing Φ_m can increase the power factor and the force density simultaneously. The decrease of the air-gap length is the effective means of increasing Φ_m. A simplified FEM model for the pole-pair number being 2 and number of turns 32 is simulated. Similarly, the number of pole pairs varies with the change of air-gap length to guarantee rated power output. Figure 22 shows the trends of power factor and force density with regard to air-gap length.

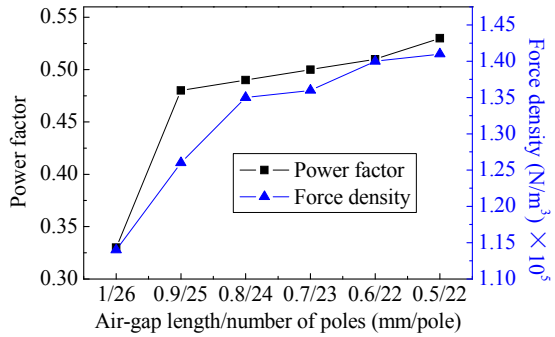

Fig. 22. Power factor and force density versus air-gap length matching number of poles.

It can be seen that the power factor and the force density both increase with the decrease of air-gap length. Thrust and thrust fluctuation are shown in Fig. 23. When the air-gap is 0.8 mm, thrust fluctuation is the lowest.

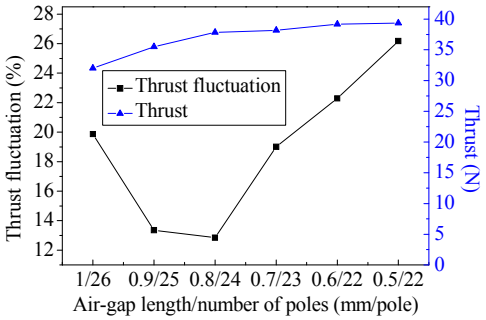

Fig. 23. Thrust fluctuation versus air-gap length / number of poles.

To ensure modest thrust fluctuation, the air-gap length is better to be 0.8 mm. The number of pole pairs is chosen to be 24. In this case, power factor is 0.49 and thrust density is 1.35×10^5 N/m^3.

C. Overlapping cross-sectional angle of adjacent stator cores

Overlapping cross-sectional angle of adjacent stator core is defined as θ as seen in Fig. 24, which can be optimized to get better power factor and force density. To reduce the axial armature-flux leakage, the adjacent stator teeth of the proposed machine are designed to be staggered. The accompanying problem is that the utilization ratio of PM is only 1/2. To compromise, overlapping cross-sectional angle of adjacent stator core can be optimized to get better power factor and force density, as is shown in Fig. 25.

Fig. 24. Overlapping cross-sectional angle of adjacent stator core.

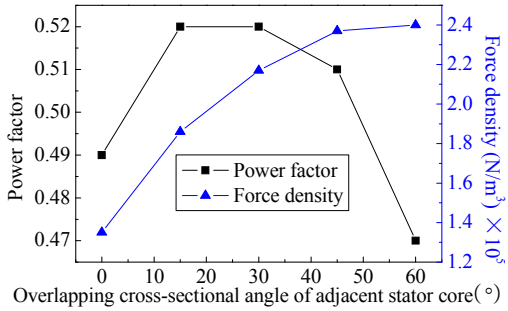

Fig. 25. Power factor and force density versus overlapping cross-sectional angle of adjacent stator core.

It can be seen that the force density keeps increasing, while the power factor first increases to the largest value, and then decreases. That is because the axial armature-flux leakage increases dramatically when overlapping cross-sectional

angle of the adjacent stator core is too large. With the variation of the overlapping angle, thrust fluctuation is shown in Fig. 26. It is observed that the thrust fluctuation first decreases, and then increases. When overlapping cross-sectional angle of adjacent stator core is 15°, thrust fluctuation reaches a minimum value.

On the overall, in order to get high power factor and force density, θ is chosen to be 30°. The final model is simulated by 3-D FEM and the results are shown in Fig. 27. The final proposed TFPMLM has power factor of 0.52 and force density of 2.17×10^5 N/m^3. The efficiency of the designed TFPMLM is 88.3%. These performances are similar to most well-designed TFMs, but the machine structure in this paper is quite simple.

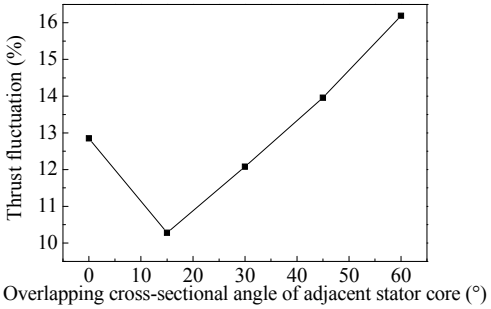

Fig. 26. Thrust fluctuation versus overlapping cross-sectional angle of adjacent stator core.

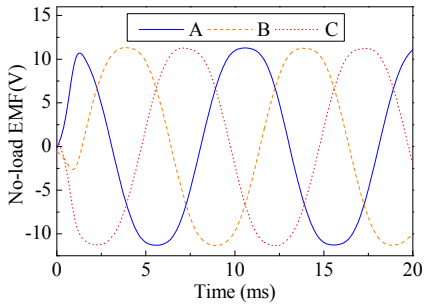

(a) No-load EMF.

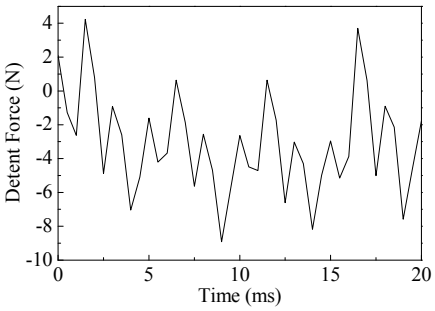

(b) Detent force.

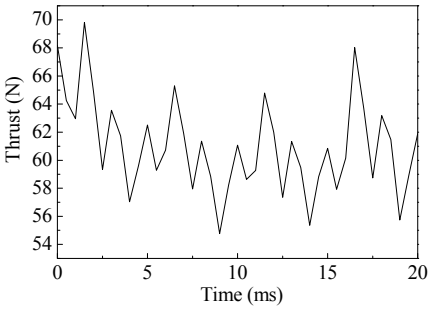

(c) Thrust.

Fig. 27. No-load and load performances of the final proposed TFPMLM.

V. CONCLUSION

A novel cylindrical transverse-flux permanent-magnet linear machine (TFPMLM) is proposed, which has axial 3-phase structure and circumferential 3-phase structure. The novel structure has the benefit of decreasing the flux leakage, which is the main factor that is affecting the performances of the TFPMLM. The axial 3-phase structure has better performances of back EMF and force density when compared to previous research. In the further study, a favorable scheme is achieved by optimizing the axial stacked stator core thickness and pole arc coefficient. In order to further improve the machine performance, the combination of number of turns and axial length, combination of air-gap length and axial length, and overlapping angle between adjacent stator teeth are reasonably matched. Finally, a scheme with power factor of 0.52, efficiency above 0.88 and force density up to 2.17×10^5 N/m^3 has been designed.

ACKNOWLEDGMENT

This work was supported in part by National Natural Science Foundation of China under Project 50877013 and 51077026, in part by the 863 Plan of China under Project 2011AA11A261, and in part by the Abroad Returnees Foundation of Harbin.

REFERENCES

[1] H. Polinder, B. Mecrow, A. Jack, P. Dickinson, and M. Mueller, "Conventional and TFPM linear generators for direct-drive wave energy conversion," *IEEE Trans. Energy Convers.*, vol. 20 , no. 2 , pp. 260-267, 2005.

[2] D. Kang and H. Weh, "Design of an integrated propulsion, guidance, and levitation system by magnetically excited transverse flux linear motor

(TFM-LM)," *IEEE Trans. Energy Convers.*, vol. 19, pp. 477-484, 2004.

[3] S. Husband and C. Hodge, "The Rolls-Royce transverse flux motor development," In *Proc. of IEEE International Electric Machines and Drives Conference (IEMDC2003)*, Madison, USA, pp. 1435-1441, June 2003.

[4] P. Anpalahan, J. Soulard, and H. P. Nee, "Design steps towards a high power factor transverse flux machine," In *Proc. of European Conference on Power Electronics and Applications*, Graz, Austria, pp. 1-6, August 2001.

[5] P. Rasmussen, G. Runolfsson, T. Thorsdottir, U. Jakobsen, and A. Pedersen, "E-core transverse flux machine with integrated fault detection system," *2011 International Conference on Electrical Machines and Systems (ICEMS2011)*, Beijing, China, pp. 1-6, August 2011.

[6] R. Blissenbach, I. Viorel, and G. Henneberger, "On the single-sided transverse flux machine design," *Electrical Machines and Power Systems*, vol. 31, no. 2, pp. 109-127, 2003.

[7] M. Harris and G. Pajooman, "Comparison of alternative topologies for VRPM (transverse-flux) electrical machines," *IEE Colloquium on New Topologies for Permanent Magnet Machines*, London, UK, pp. 2/1-2/7, June 1997.

[8] B. Hasubek and E. Nowicki, "Design limitations of reduced magnet material passive rotor transverse flux motors investigated using 3D finite element analysis," *2000 Canadian Conference on Electrical and Computer Engineering*, Halifax, NS, Canada, pp. 365-369, 2000.

[9] T. Hoang, D. Kang, and J. Lee, "Comparisons between various designs of transverse flux linear motor in terms of thrust force and normal force," *IEEE Trans. On Magn.*, vol. 46, no. 10, pp. 3795-3801, 2010.

[10] A. Shiri and A. Shoulaie, "Investigation of frequency effects on the performance of single-sided linear induction motor," *Applied Computational Electromagnetics Society (ACES) Journal*, vol. 27, no. 6, pp. 497-504, June 2012.

[11] H. Hasanien, "Particle swarm design optimization of transverse flux linear motor for weight reduction and improvement of thrust force," *IEEE Trans. Ind. Electron*., vol. 58, pp. 4048-4056, 2011.

[12] Y. Nozaki, J. Baba, K. Shutoh, and E. Masada, "Improvement of transverse flux linear induction motors performances with third order harmonics current injection," *IEEE Trans. Appl. Supercon.*, vol. 14, pp. 1846-1849, 2004.

[13] D. Kang, "Increasing of thrust force in transverse flux machine by permanent-magnet screen," *IEEE Trans. On Magn.*, vol. 41, no. 5, pp.1952-1955, 2005.

[14] A. Argeseanu, E. Ritchie, and K. Leban, "Optimal design of the transverse flux machine using a fitted genetic algorithm with real parameters," *13th International Conference on Optimization of Electrical and Electronic Equipment*, Brasov, Romania, pp. 671-678, May 2012.

[15] J. Alwash and L. Qaseer, "Three-dimension finite element analysis of a helical motion induction motor," *Applied Computational Electromagnetics Society(ACES) Journal*, vol. 25, no. 8, pp. 703-712, August 2010.

[16] P. Zheng, C. Tong, G. Chen, R. Liu, Y. Sui, W. Shi, and S. Cheng, "Research on the magnetic characteristic of a novel transverse-flux PM linear machine used for free-piston energy converter," *IEEE Trans. On Magn.*, vol. 47, pp. 1082-1085, 2011.

[17] R. Nariman and S. Abbas, "Minimizing thrust fluctuation in linear permanent-magnet synchronous motor with Halbach array," In *Proceedings of Power Electronic & Drive Systems & Technologies Conference (1st PEDSTC)*, Tehran, Iran, pp. 302-306, Feb. 2010.

[18] A. Masnoudi and A. Elantably, "A simple assessment of the cogging torque in a transverse flux permanent magnet machine," In *Proceedings of IEEE International Electric Machines and Drives Conference (IEMDC2001)*, Cambridge, MA, USA, pp. 754-759, June 2001.

[19] A. Njeh, A. Masmoudi, and A. Elantably, "3D FEA based investigation of the cogging torque of a claw pole transverse flux permanent magnet machine," In *Proceedings of IEEE International Electric Machines and Drives Conference (IEMDC2003)*, Madison, USA, pp. 319-324, June 2003.

[20] M. Harris, G. Pajooman, and S. A. Sharkh, "The problem of power factor in VRPM (transverse-flux) machines," In *Proceedings of Eighth International Electric Machines and Drives Conference*, Cambridge, UK, pp. 386-390, Sep. 1997.

Ping Zheng (M'04–SM'05) received the B.Sc., M.Sc., and Ph.D. degrees from Harbin Institute of Technology, Harbin, China, in 1992, 1995, and 1999, respectively. Since 1995, she has been with Harbin Institute of Technology, where she has become a professor in 2005.

She is the member of IEEE IAS Electric Machines Committee, IEEE Industry Applications Society and International Compumag Society. Now she is an author or coauthor of more than 130 published refereed technical papers and four books. Her current research interests include electric machines and control, hybrid electric vehicles, and unconventional electromagnetic devices.

Bin Yu received the B.Sc. degree in Electrical Engineering from Tianjin University of Science and Technology in 2005, and M.Sc. degree from North China Electric Power University in 2010. He is currently working for his Ph.D. degree in Harbin Institute of Technology, China. His research interests include the design and control of new-structure permanent-magnet linear machines for free-piston stirling engines and series hybrid electric vehicles.

Haiyuan Yan received the B.Sc. degree and the M.Sc. degree in Electrical Engineering and Automation from Harbin Institute of Technology, Harbin, China, in 2009 and 2011. After her graduation, she worked in China Academy of Launch Vehicle Technology, dedicating to electromechanical servo technology research. Her research interests include transverse flux permanent magnet linear generator used in stirling system, permanent magnet synchronous servo motor used in electromechanical servo system of rockets and missiles, and the servo control technology of PMSM.

Yi Sui received the B.Sc. degree and M.Sc. degree in Electrical Engineering from Harbin Institute of Technology, Harbin, China, in 2009 and 2011, respectively. He is currently working toward the Ph.D. degree. His research interests include fault-tolerant permanent-magnet synchronous machine system used in pure electric vehicles, permanent-magnet linear machines, and high performance servo machine system used in unconventional areas.

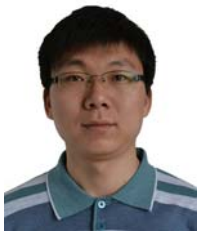

Jingang Bai received the B.Sc. degree in Electrical Engineering from Harbin University of Science and Technology in 2009, and M.Sc. degree from Harbin Institute of Technology, in 2011, where he is currently working toward the Ph.D. degree. His research interests include flux-modulated brushless compound-structure PM synchronous machine used in hybrid electric vehicles, and high power density linear machines used in stirling engine system.

Pengfei Wang received the B.Sc. and M.Sc. degrees in Electrical Engineering from Harbin Institute of Technology, Harbin, China, in 2007 and 2009, respectively, where he is currently working toward the Ph.D. degree. His research interests include fault-tolerant permanent-magnet synchronous machines, permanent-magnet linear machines, and control strategies of multiphase machines under healthy and post-fault conditions.

2013 INSTITUTIONAL MEMBERS

DTIC-OCP LIBRARY
8725 John J. Kingman Rd, Ste 0944
Fort Belvoir, VA 22060-6218

AUSTRALIAN DEFENCE LIBRARY
Northcott Drive
Canberra, A.C.T. 2600 Australia

BEIJING BOOK CO, INC
701 E Linden Avenue
Linden, NJ 07036-2495

DARTMOUTH COLLEGE
6025 Baker/Berry Library
Hanover, NH 03755-3560

DSTO EDINBURGH
AU/33851-AP, PO Box 830470
Birmingham, AL 35283

SIMEON J. EARL – BAE SYSTEMS
W432A, Warton Aerodome
Preston, Lancs., UK PR4 1AX

ENERGY KEN LIBRARY
PO Box 300613
Jamaica, NY, 11430

ENGINEERING INFORMATION, INC
PO Box 543
Amsterdam, Netherlands 1000 Am

ETSE TELECOMUNICACION
Biblioteca, Campus Lagoas
Vigo, 36200 Spain

GA INSTITUTE OF TECHNOLOGY
EBS-Lib Mail code 0900
74 Cherry Street
Atlanta, GA 30332

TIMOTHY HOLZHEIMER
Raytheon
PO Box 1044
Rockwall, TX 75087

HRL LABS, RESEARCH LIBRARY
3011 Malibu Canyon
Malibu, CA 90265

IEE INSPEC
Michael Faraday House
6 Hills Way
Stevenage, Herts UK SG1 2AY

INSTITUTE FOR SCIENTIFIC INFO.
Publication Processing Dept.
3501 Market St.Philadelphia, PA
19104-3302

LIBRARY – DRDC OTTAWA
3701 Carling Avenue
Ottawa, Ontario, Canada K1A OZ4

LIBRARY of CONGRESS
Reg. Of Copyrights
Washington DC, 20559

LINDA HALL LIBRARY
5109 Cherry Street
Kansas City, MO 64110-2498

MISSOURI S&T
400 W 14th Street
Rolla, MO 56409

MIT LINCOLN LABORATORY
244 Wood Street
Lexington, MA 02420

NATIONAL CHI NAN UNIVERSITY
Lily Journal & Book Co, Ltd
20920 Glenbrook Drive
Walnut, CA 91789-3809

JOHN NORGARD
UCCS
20340 Pine Shadow Drive
Colorado Springs, CO 80908

OSAMA MOHAMMED
Florida International University
10555 W Flagler Street
Miami, FL 33174

NAVAL POSTGRADUATE SCHOOL
Attn:J. Rozdal/411 Dyer Rd./ Rm 111
Monterey, CA 93943-5101

NDL KAGAKU
C/0 KWE-ACCESS
PO Box 300613 (JFK A/P)
Jamaica, NY 11430-0613

OVIEDO LIBRARY
PO BOX 830679
Birmingham, AL 35283

DAVID PAULSEN
E3Compliance
1523 North Joe Wilson Road
Cedr Hill, TX 75104-1437

PENN STATE UNIVERSITY
126 Paterno Library
University Park, PA 16802-1808

DAVID J. PINION
1122 E Pike Street #1217
SEATTLE, WA 98122

KATHERINE SIAKAVARA
Gymnasiou 8
Thessaloniki, Greece 55236

SWETS INFORMATION SERVICES
160 Ninth Avenue, Suite A
Runnemede, NJ 08078

YUTAKA TANGE
Maizuru Natl College of Technology
Maizuru, Kyoto, Japan 625-8511

TIB & UNIV. BIB. HANNOVER
Welfengarten 1B
Hannover, Germany 30167

UEKAE
PO Box 830470
Birmingham, AL 35283

UNIV OF CENTRAL FLORIDA
4000 Central Florida Boulevard
Orlando, FL 32816-8005

UNIVERSITY OF COLORADO
1720 Pleasant Street, 184 UCB
Boulder, CO 80309-0184

UNIVERSITY OF KANSAS – WATSON
1425 Jayhawk Blvd 210S
Lawrence, KS 66045-7594

UNIVERSITY OF MISSISSIPPI
JD Williams Library
University, MS 38677-1848

UNIVERSITY LIBRARY/HKUST
Clear Water Bay Road
Kowloon, Honk Kong

CHUAN CHENG WANG
8F, No. 31, Lane 546
MingCheng 2nd Road, Zuoying Dist
Kaoshiung City, Taiwan 813

THOMAS WEILAND
TU Darmstadt
Schlossgartenstrasse 8
Darmstadt, Hessen, Germany 64289

STEVEN WEISS
US Army Research Lab
2800 Powder Mill Road
Adelphi, MD 20783

YOSHIHIDE YAMADA
NATIONAL DEFENSE ACADEMY
1-10-20 Hashirimizu
Yokosuka, Kanagawa,
Japan 239-8686

APPLIED COMPUTATIONAL ELECTROMAGNETICS SOCIETY JOURNAL
http://www.aces-society.org

INFORMATION FOR AUTHORS

PUBLICATION CRITERIA

Each paper is required to manifest some relation to applied computational electromagnetics. **Papers may address general issues in applied computational electromagnetics, or they may focus on specific applications, techniques, codes, or computational issues.** While the following list is not exhaustive, each paper will generally relate to at least one of these areas:

1. **Code validation.** This is done using internal checks or experimental, analytical or other computational data. Measured data of potential utility to code validation efforts will also be considered for publication.

2. **Code performance analysis.** This usually involves identification of numerical accuracy or other limitations, solution convergence, numerical and physical modeling error, and parameter tradeoffs. However, it is also permissible to address issues such as ease-of-use, set-up time, run time, special outputs, or other special features.

3. **Computational studies of basic physics.** This involves using a code, algorithm, or computational technique to simulate reality in such a way that better, or new physical insight or understanding, is achieved.

4. **New computational techniques** or new applications for existing computational techniques or codes.

5. **"Tricks of the trade"** in selecting and applying codes and techniques.

6. **New codes, algorithms, code enhancement, and code fixes.** This category is self-explanatory, but includes significant changes to existing codes, such as applicability extensions, algorithm optimization, problem correction, limitation removal, or other performance improvement. **Note: Code (or algorithm) capability descriptions are not acceptable, unless they contain sufficient technical material to justify consideration.**

7. **Code input/output issues.** This normally involves innovations in input (such as input geometry standardization, automatic mesh generation, or computer-aided design) or in output (whether it be tabular, graphical, statistical, Fourier-transformed, or otherwise signal-processed). Material dealing with input/output database management, output interpretation, or other input/output issues will also be considered for publication.

8. **Computer hardware issues.** This is the category for analysis of hardware capabilities and limitations of various types of electromagnetics computational requirements. Vector and parallel computational techniques and implementation are of particular interest.

Applications of interest include, but are not limited to, antennas (and their electromagnetic environments), networks, static fields, radar cross section, inverse scattering, shielding, radiation hazards, biological effects, biomedical applications, electromagnetic pulse (EMP), electromagnetic interference (EMI), electromagnetic compatibility (EMC), power transmission, charge transport, dielectric, magnetic and nonlinear materials, microwave components, MEMS, RFID, and MMIC technologies, remote sensing and geometrical and physical optics, radar and communications systems, sensors, fiber optics, plasmas, particle accelerators, generators and motors, electromagnetic wave propagation, non-destructive evaluation, eddy currents, and inverse scattering.

Techniques of interest include but not limited to frequency-domain and time-domain techniques, integral equation and differential equation techniques, diffraction theories, physical and geometrical optics, method of moments, finite differences and finite element techniques, transmission line method, modal expansions, perturbation methods, and hybrid methods.

Where possible and appropriate, authors are required to provide statements of quantitative accuracy for measured and/or computed data. This issue is discussed in "Accuracy & Publication: Requiring, quantitative accuracy statements to accompany data," by E. K. Miller, *ACES Newsletter,* Vol. 9, No. 3, pp. 23-29, 1994, ISBN 1056-9170.

SUBMITTAL PROCEDURE

All submissions should be uploaded to ACES server through ACES web site (http://www.aces-society.org) by using the upload button, journal section. Only pdf files are accepted for submission. The file size should not be larger than 10MB, otherwise permission from the Editor-in-Chief should be obtained first. Automated acknowledgment of the electronic submission, after the upload process is successfully completed, will be sent to the corresponding author only. It is the responsibility of the corresponding author to keep the remaining authors, if applicable, informed. Email submission is not accepted and will not be processed.

EDITORIAL REVIEW

In order to ensure an appropriate level of quality control, papers are peer reviewed. They are reviewed both for technical correctness and for adherence to the listed guidelines regarding information content and format.

PAPER FORMAT

Only camera-ready electronic files are accepted for publication. The term **"camera-ready" means that the material is neat, legible, reproducible, and in accordance with the final version format listed below.**

The following requirements are in effect for the final version of an ACES Journal paper:

1. The paper title should not be placed on a separate page.

The title, author(s), abstract, and (space permitting) beginning of the paper itself should all be on the first page. The title, author(s), and author affiliations should be centered (center-justified) on the first page. The title should be of font size 16 and bolded, the author names should be of font size 12 and bolded, and the author affiliation should be of font size 12 (regular font, neither italic nor bolded).

2. An abstract is required. The abstract should be a brief summary of the work described in the paper. It should state the computer codes, computational techniques, and applications discussed in the paper (as applicable) and should otherwise be usable by technical abstracting and indexing services. The word "Abstract" has to be placed at the left margin of the paper, and should be bolded and italic. It also should be followed by a hyphen (—) with the main text of the abstract starting on the same line.

3. All section titles have to be centered and all the title letters should be written in caps. The section titles need to be numbered using roman numbering (I. II. ….)

4. Either British English or American English spellings may be used, provided that each word is spelled consistently throughout the paper.

5. Internal consistency of references format should be maintained. As a guideline for authors, we recommend that references be given using numerical numbering in the body of the paper (with numerical listing of all references at the end of the paper). The first letter of the authors' first name should be listed followed by a period, which in turn, followed by the authors' complete last name. Use a coma (,) to separate between the authors' names. Titles of papers or articles should be in quotation marks (" "), followed by the title of journal, which should be in italic font. The journal volume (vol.), issue number (no.), page numbering (pp.), month and year of publication should come after the journal title in the sequence listed here.

6. Internal consistency shall also be maintained for other elements of style, such as equation numbering. Equation numbers should be placed in parentheses at the right column margin. All symbols in any equation have to be defined before the equation appears or right immediately following the equation.

7. The use of SI units is strongly encouraged. English units may be used as secondary units (in parentheses).

8. Figures and tables should be formatted appropriately (centered within the column, side-by-side, etc.) on the page such that the presented data appears close to and after it is being referenced in the text. When including figures and tables, all care should be taken so that they will appear appropriately when printed in black and white. For better visibility of paper on computer screen, it is good to make color figures with different line styles for figures with multiple curves. Colors should also be tested to insure their ability to be distinguished after black and white printing. Avoid the use of large symbols with curves in a figure. It is always better to use different line styles such as solid, dotted, dashed, etc.

9. A figure caption should be located directly beneath the corresponding figure, and should be fully justified.

10. The intent and meaning of all text must be clear. For authors who are not masters of the English language, the ACES Editorial Staff will provide assistance with grammar (subject to clarity of intent and meaning). However, this may delay the scheduled publication date.

11. Unused space should be minimized. Sections and subsections should not normally begin on a new page.

ACES reserves the right to edit any uploaded material, however, this is not generally done. It is the author(s) responsibility to provide acceptable camera-ready files in pdf and MSWord formats. Incompatible or incomplete files will not be processed for publication, and authors will be requested to re-upload a revised acceptable version.

COPYRIGHTS AND RELEASES

Each primary author must execute the online copyright form and obtain a release from his/her organization vesting the copyright with ACES. Both the author(s) and affiliated organization(s) are allowed to use the copyrighted material freely for their own private purposes.

Permission is granted to quote short passages and reproduce figures and tables from and ACES Journal issue provided the source is cited. Copies of ACES Journal articles may be made in accordance with usage permitted by Sections 107 or 108 of the U.S. Copyright Law. This consent does not extend to other kinds of copying, such as for general distribution, for advertising or promotional purposes, for creating new collective works, or for resale. The reproduction of multiple copies and the use of articles or extracts for commercial purposes require the consent of the author and specific permission from ACES. Institutional members are allowed to copy any ACES Journal issue for their internal distribution only.

PUBLICATION CHARGES

All authors are allowed for 8 printed pages per paper without charge. Mandatory page charges of $50 a page apply to all pages in excess of 8 printed pages. Authors are entitled to a total of two, free of charge, copies of the printed journal issue in which their paper was published. These two copies will be mailed to the corresponding author. Additional reprints are available for $50. Requests for additional re-prints should be submitted to the managing editor or ACES Secretary.

Corresponding author is required to complete the online form for the over page charge payment right after the initial acceptance of the paper.

ACES Journal is abstracted in INSPEC, in Engineering Index, DTIC, Science Citation Index Expanded, the Research Alert, and to Current Contents/Engineering, Computing & Technology.